Directing the assembly of heterometallic molecular magnets using compartmental ligands

María José Heras Ojea

M.Sci.

Submitted in fulfilment of the requirements for the Degree of Doctor of Philosophy

School of Chemistry

College of Science and Engineering

University of Glasgow

Supervisor: Prof. Mark Murrie

April 2017

Abstract

The use of multinucleating ligands capable of directing the synthesis of heterometallic single−molecule magnets (SMMs) is discussed herein. To this end, we have focused on investigating the coordination chemistry of two different ligands, 2,2'−(propane−1,3−diyldiimino)bis[2−(hydroxymethyl)−propane−1,3−diol] (Bis−tris propane, H_6L) and *N,N′*−bis(2−Hydroxy−3−methoxyphenylmethylidene)-2,6−pyridinediamine (H_2L2), with 3*d* and/or 4*f* metal ion precursors.

The aminopolyalcohol ligand H_6L has been employed in the assembly of twenty−three new complexes, ranging from simple monomers up to hexametallic systems, involving Mn(II/III), Co(II/III), Ni(II), Cu(II) and Ln(III) ions. The obtained monomers however have been utilised as building blocks in subsequent reactions to gain control over the assembly process of the polynuclear complexes. Those coordination complexes have been classified into five different families. The first one describes a series of "butterfly−like" systems ($[Mn_2Ni_2(OH)_2(H_3L)_2(H_2O)_2]Cl_2$ (**3**), $[Mn_2Cu_2(CH_3O)_2(H_3L)_2(CH_3COO)_2]$ (**4**), $[Mn^{III}_2Mn^{II}Cu_2O(HCOO)(H_4L)(H_2L)(CH_3COO)_3]$ (**5**)) where the magnetic properties of the final compounds can be easily tuned by changing the starting 3*d*−precursor. The second group focusses on the enhancement of the SMM properties of $\{Ln_2Cu_3(H_3L)_2X_n\}$ (X = CH_3COO^-, n = 6 for **6**−**7**; and X = NO_3^-, n = 7 or 8 for **8**−**12**), which is related to changes in the crystal field around the Ln(III) ions due to modifications in the synthetic strategy, such as the replacement of the co−ligands (CH_3COO^- *vs*. NO_3^-). Following on from this, the magneto−structural study performed on $[LnCu_4(H_4L)_4](Cl)_2(ClO_4)$ systems (**13**−**16**) attempts to shed light on the nature of the 3*d*−4*f* exchange interactions. The last two groups are based on the combination of Co(II) precursors with 4*f* ions (**17**−**21**). In both families the oxidation of the paramagnetic Co(II) centres to diamagnetic Co(III) centres was observed, thereby the overall magnetic properties were mainly defined by the lanthanide ions. One chapter discusses the single−ion magnet (SIM) features of $[Co^{III}_3Ln(H_2L)_2(H_3L)](ClO_4)$, while the other describes the magnetocaloric properties of the topologically novel $[Co^{III}_3Gd^{III}_3(H_2L)_3(acac)_2(CH_3COO)_4(H_2O)_2]$ ring. The last experimental chapter reviews the reactivity of the Schiff base derivative H_2L2. H_2L2 is a compartmental ligand capable of controlling the synthesis of Ni/Ln systems (**24**−**28** $[Ln_2Ni_2(L2)_2(CH_3COO)_6(H_2O)_2]$), with the Tb analogue displaying SMM features.

“Creéis que todo tiene un límite, así estáis todos limitados.

Cuidado, os avisamos, somos los mismos que cuando empezamos.”

Eskorbuto

Acknowledgements

At different times throughout the writing up of this thesis I remember having moments of lucidity, and thinking "I should put “this” and say “that” in my acknowledgments!". I also remember thinking "you should write this down in a post-it or something..." Well, those who know me know I do not remember now these brilliant and funny words. One day I will heed Mark's advice about buying a diary... So, my most sincere apologies in advance if I forget to thank something/someone in this last (chronologically speaking) section.

First of all I would like to thank Mark for giving me the opportunity to develop the PhD under his supervision. My current scientific skills and experimental background would not have been possible without your guidance and the trust you have placed in me at all times. I must also admit how brave you were offering a position to a Catalan/Spanish person, taking into account the emotional reputation which precedes us. Personally, I think I have managed to control my temper quite well (I am not joking). I want also to acknowledge my second supervisor Dr. Ross Forgan for the feedback and advice during these three years.

Sincere thanks to the people of the Coordination Chemistry Laboratory, and especially to Prof. Hiroki Oshio who kindly agreed my stay in Tsukuba. It must be stressed the generosity and kindness that all the group members showed me, making my experience in Tsukuba easy and pleasant. I want also to express my gratitude to the other collaborators that have contributed to this thesis, Prof. Wolfgang Wernsdorfer, Dr. Gunasekaran Velmurugan, Prof. Gopalan Rajaraman, Dr. Jordi Cirera, Prof. Eliseo Ruiz, Dr. Giulia Lorusso and Dr. Marco Evangelisti. Although it cannot be considered a collaborator, I am grateful to Dr. Nicholas F. Chilton for all the help with the fit of the magnetic data. The workshop organised in Glasgow was extremely helpful for understanding what was going on in most of the complexes presented in this thesis. Among them, Claire and Jim deserve especial thanks. Claire, I greatly appreciate your infinite patience in answering all my questions about crystallography; my interest in the exciting world of SXRD is largely due to the enthusiasm you show for it. Jim, thanks for always finding a last-minute gap in the EDX schedule when I had to do another “this is the last” experiment. I really enjoyed the long talks about football and history, always interesting.

I would also like to thank the people in the Murrie group who I was lucky to share short/medium/long periods of my PhD, particularly the original “crew” from when I started my Scottish adventure: Katie, Fraser, Laura and Vicki. They all have contributed in defining my criteria on how to work/proceed in a lab. They have also evidenced the stereotype about British/English/Scottish “chasing the sun like lizards” in our after-work drinks (ask me, Gavin or Isa for MJ-English translation). And of course, the current Murries: Alex, Angelos, Marsali and Moya. Thanks for the laughs, for the fun-facts, for the cakes and the snacks... For being there to have a drink when I was feeling a little bit down, and to be there to celebrate (drinking again) when there was something to be happy about. It may seem that we, the Murries, only interact by means of alcohol, but it is not true, we also have huge amounts of tea and coffee in the office. Moya, it is been a pleasure working with you. You are an example of utmost professionalism; please keep swimming. Alex, ευχαριστίες για τη Μεσόγειο ζεστασιά και ευγένεια (και επίσης για τις συνομιλίες μας για την παγκόσμια πολιτική). Fingers crossed google translator has translated properly what I wanted to say. I would also like to thank all the Forganisms. A special mention to Sarah (and Moya; I cannot imagine one without the other). I met you two when you were still undergrads full of joy and enthusiasm about academia... Hahaha! Anyway…I will be more than happy if I have been able to contribute to your lives a third of what you have contributed to me as a person. Priceless and invaluable the great moments we have spent together. Mini-Ross, I know Scottish are men of few words, so I will be brief. Cheers for the chats on the way home, I wish you the best in your future. To the rest of undergrads and post-grads of the department, thanks for always being up for “one” pint on Friday, you have created such a nice atmosphere in the chemistry department.

No puedo olvidarme de la gente de Barcelona. No sé cómo lo habéis hecho, pero os las habéis ingeniado para seguir mostrándome vuestro apoyo incluso en la distancia. En general, gràcies als integrants del GMMF (reserva 2011-2013), que van ser els culpables que decidís endinsar-me en la naïf aventura del món acadèmic. Me gustaría destacar a Guillem y Leo, quien siempre mostraron una confianza ciega en mi calidad científica, gracias de corazón. A Carolina, la jefa, que em va ensenyar el camí de com s’han de fer bé les coses, i en la importància de l’auto-motivació quan creus que les coses no van tan bé. La formació que vaig rebre i tota l’experiència que vaig guanyar durant la estancia al teu lab “va a misa”. Y Jorge... Sabes que la única razón por la que el pelirrojo (y yo, venga va) tenemos

pensado ir con el Imserso a Valencia eres tú. La paella, el solete, y el resto de cosas son secundarias, por supuesto.

Y ya vamos casi por la tercera página, así que vamos a ir cerrando el chiringuito. Irene y Marta, nuestra relación es especial, muchos no la entienden, y por eso aún la valoro más. Gracias por estar ahí, preocuparos por mis aventuras y desventuras en Glasgow, y por vuestra inteligencia emocional. Me considero afortunada de poder formar parte de vuestras vidas. Y paro ya que si no nos emocionamos.

No puedo más que agradecer a mi familia (Albert, también va por ti) todo el apoyo incondicional que me han mostrado, no sólo durante la tesis, durante toda mi vida. Me entendéis y respetáis, sin lugar a dudas soy lo que soy por vuestro ejemplo de perseverar en la vida. Gracias a mis padres en especial, que me enseñaron la importancia de ser coherente y honesto con uno mismo, a pesar que a veces eso me dé buenos quebraderos de cabeza. Gracias también por tanto, tantísimo esfuerzo invertido en nosotras. No lo decimos mucho, pero creernos que estamos profundamente agradecidas y orgullosas. Hermana, ahora que te has convertido en la sensible de la familia no me voy a poner tierna contigo, ya te pegare un “abrazo-lapa” cuando te vea. I would also like to show my gratitude to "my other family," the Clan Craig, and especially to Frances, thank you for making me feel at home while away from home, and for all your selflessly help.

Bueno, los que me conocen saben que dejo lo mejor para el final. Gavin mil cosas buenas podría decir sobre ti y me quedaría corta, cortísima. Así que intentare ser emocionalmente escueta. Eres un ejemplo a seguir, siempre. Tu capacidad motivadora es infinita, y me faltan palabras para agradecer todo el apoyo y ayuda mostrada durante mi tesis. Gracias por existir e incluirme en tu viaje por la vida. Ahora sí, ya puedes soltar algún comentario sarcástico.

Author’s Declaration

The work contained in this thesis, submitted for the degree of doctor of philosophy, is my own original work, except where due reference is made to others. No material within has been previously submitted for a degree at this or any other university.

Abbreviations and symbols

H_6L	Bis−tris propane, 2,2'−(propane−1,3-diyldiimino)bis[2-(hydroxymethyl)propane−1,3−diol].
BVS	Bond Valence Sum.
μ_B	Bohr magneton.
CSD	Cambridge Structural Database.
CShMs	Continuous shape measures.
$\Delta E/k_B$	Energy barrier; where k_B is the Boltzmann constant.
S	Entropy.
R	Gas constant.
c_p	Heat capacity.
H_2L2	*N,N′*−bis(2−Hydroxy−3−methoxyphenylmethylidene)−2,6-pyridinediamine.
IR	Infra−red.
z$\mathcal{J}$'	Intermolecular magnetic interaction.
JT	Jahn−Teller (distances or axes).
g_i	Landé *g*−factor.
$\mathcal{J}_i$	Magnetic exchange interaction.
MCE	Magnetocaloric effect.
χ_M	Molar magnetic susceptibility.
$NMe_4OH{\cdot}5H_2O$	Tetramethylammonium hydroxide pentahydrate.
Et_3N	Triethylamine.
SMM(s)	Single−molecule magnet(s).
τ_{Cu}	Geometrical parameter related to 5−coordinate Cu(II) ions.
τ_0	Pre−exponential factor.
QTM	Quantum tunnelling mechanism of the magnetisation.
τ	Relaxation rate.
SQUID	Superconducting Quantum Interference Device.
XRD	X−Ray Diffraction.
ZFS	Zero−Field Splitting.

Contents

Chapter 1

Contents

1. Introduction

The rapid development and social demand for ever smaller and multifunctional technological devices in recent years has attracted an increasing interest in the research of nanomaterials. Within this field of research of new materials with attractive properties on the nanoscale, molecular magnetism offers the possibility of controlled assembly through a *bottom−up* approach towards complexes with unique magnetic, optical and redox attributes on the molecular scale; which may allow their use as data storage media,[1] magnetic refrigerants[2] or quantum computing devices.[3] One type of compound that could feasibly be used for these applications is known as Single−Molecule Magnets (SMMs) or molecular nanomagnets. To understand more deeply why molecular nanomagnets have been the focus of attention over the last fifteen or so years, a brief introduction to their origins is necessary.

1.1. Fundamentals and general aspects of molecular magnetism[4–6]

Magnetochemistry is the branch of chemistry dedicated to the synthesis and study of substances with interesting magnetic properties, and more specifically molecular magnetism deals with molecules that possess unpaired electrons.[4, 7, 8] Electrons are negatively charged particles that possess some intrinsic properties, such as a total angular momentum or magnetic moment (J), which results from the combination of the spin magnetic (S) and the orbital magnetic momentum (L). Electrons are in fact responsible for the induced magnetic field (B) in a system and the temporary magnetisation (M, as magnetic moment per unit of volume) displayed by magnetic materials under the effect of an applied field (H). These quantities are related through:[8]

Eq. 1.1. $$B = H + 4\pi M$$

Therefore, molecular magnetism employs physical measurements to rationalise the magnetic properties of different systems, which depend on how these spins interact. A fundamental step in the understanding of magnetochemistry was taken by Paul Langevin who proposed the description of the different magnetic behaviours that can be displayed by a material.[9] This model proposed two principal phenomena in bulk materials, known as diamagnetism and paramagnetism, characterised by opposite responses to the application of an external magnetic field. Diamagnetic materials, *i.e*. those with no unpaired electrons (thus S = 0), are

repelled by an applied field as a consequence of its interaction with the paired electrons from the molecular or atomic orbitals. On the other hand, paramagnetic materials are attracted to an applied field as a result of its interaction with unpaired electrons, yielding a net spin in the bulk ($S \neq 0$). All molecular compounds have some diamagnetic contribution due to the paired electrons they contain, but only complexes with unpaired electrons display paramagnetic behaviour. To determine the magnetic properties of a material, magnetisation and magnetic susceptibility measurements under the application of a magnetic field are normally performed by Superconducting Quantum Interference Device (SQUID) magnetometry.[8]

Consider the most simplistic example of a coordination complex, that based on an isolated isotropic ion (*i.e.* $L = 0 \leftrightarrow J = S$), in the presence of a homogenous external magnetic field (*H*). The splitting of the S energy level into the constituent M_S sub−levels (see Fig 1.1) as a consequence of the interaction with the magnetic field is known as the Zeeman Effect. Note that g can differ from the free electron value (g_e = 2.0023) depending on many factors, such as the symmetry displayed around the metal ion. This will be covered in more detail in later sections.

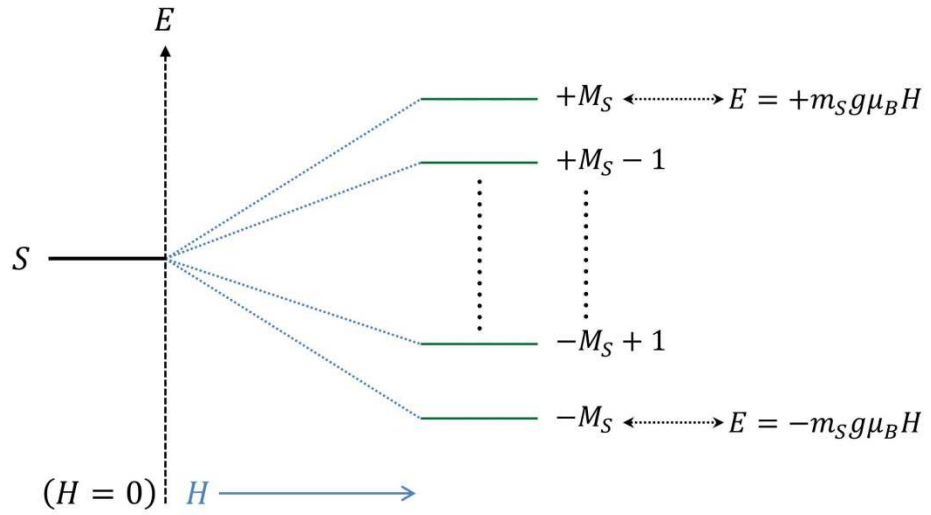

Fig 1.1 Zeeman Effect or splitting of the S levels into M_S sub−levels. E is the energy associated to a certain M_S, g is the Landé *g*−factor,μ_B is the Bohr magneton, and H is the magnetic field.

Given due consideration to the consequences of the Zeeman Effect on a system (*i.e.* each M_S possesses a quantified E_n), and that the magnetisation of a sample is related to the internal energy of the system $\left(M = \frac{-\delta E}{\delta H}\right)$, the microscopic magnetisation for a certain sub−level (μ_n) may be expressed as $\mu_n = \frac{-\delta E_n}{\delta H}$. Therefore, the total magnetisation resulting from the sum of each individual μ_n, after

performing a population analysis accounting for the Boltzmann distribution law, is expressed as:[5]

Eq. 1.2 $$M = N\sum \mu_n P_n = N\frac{\sum_n\left(\frac{\delta E_n}{\delta H}\right)exp\left(\frac{-E_n}{k_B T}\right)}{\sum_n exp\left(\frac{-E_n}{k_B T}\right)}$$

Where N is Avogadro's number, P_n is the population of a certain level (*n*), and k_B is the Boltzmann constant.

Thus, the total magnetisation of a certain magnetic ion mainly comes from the competition of S (as $E(S)$), *H* and *T*. The Brillouin function[5] is generally applied (see Eq. 1.3) to investigate the relation between those factors and the magnetic features exhibited by a material.

Eq. 1.3 $$\eta = g\mu_B\frac{H}{k_B T} \;\rightarrow\; M = Ng\mu_B S[B_S(\eta)]$$

Where $B_S(\eta)$ is the Brillouin function, $B_S(\eta) = \frac{S(S+1)}{2S}\coth\left\{\frac{(2S+1)}{2}\eta\right\} - \frac{1}{2S}\coth\left(\frac{\eta}{2}\right)$.

The limits of the Brillouin function reveal, in fact, a competition between the magnetic order and the thermal disorder:

a. <u>At high fields and low temperatures</u>, $\eta = g\mu_B\frac{H}{k_B T} \gg 1 \rightarrow B_S(\eta) = 1 \leftrightarrow M = N\mu_B gS$ ⇨ The most energetically stable state (*i.e*. ground state) tends to be populated, promoting the saturation of the magnetisation in the sample (M_{Sat}).
b. <u>At low fields and (relatively) high temperatures</u>, $\eta = g\mu_B\frac{H}{k_B T} \ll 1 \rightarrow B_S(\eta) = (S+1)\eta/3 \leftrightarrow M = \frac{N\mu_B^2}{3k_B T}Hg^2S(S+1)$ ⇨ As thermal energy increases, higher energy states are likely to be also populated.

The later situation, however, is normally investigated by the magnetic susceptibility. Magnetic susceptibility (χ) is the degree of magnetisation of a material in response to the applied magnetic field. Hence, at low fields and high temperatures, the magnetisation of a system is proportional to the applied field (See Eq. 1.4).

Eq. 1.4 $$\chi = \frac{\partial M}{\partial H} \xrightarrow{\downarrow H, \uparrow T} \chi = \frac{M}{H}$$

The experimental magnetic susceptibility is given by the sum of two magnetic contributions. The paired electrons present in the molecule provide a small, negative diamagnetic contribution (χ_D), while the unpaired electrons supply the main magnetic response through the paramagnetic molar susceptibility (χ_P). A normalisation of the observed magnetic susceptibility to the molecular weight of the studied compound is normally performed in order to relate the observed experimental properties with the electronic and geometric structure of the molecular systems, such as:

Eq. 1.5 $$\chi_g = \frac{\chi}{\rho}$$

Eq. 1.6 $$\chi_M = \chi_g \times \frac{MW}{m} + \left(\frac{MW}{2} \times 10^{-6}\right)$$

Where χ_g is the mass susceptibility, ρ is the density, MW and m are, respectively, the molecular weight and the mass of the studied complex.

Note also that here χ_M is referred to the molar magnetic susceptibility once the correction for the diamagnetic contribution related to the compound is applied (*i.e.* $-(MW/2) \times 10^{-6}$).[7] This paramagnetic susceptibility is temperature dependent according to the Curie Law under those ideal conditions, $\chi_M = C/T$. Consequently the value for $\chi_M T$ can be calculated by:

$$\chi_M = \frac{M}{H} = \frac{N\mu_B^2}{3k_B T} g^2 S(S+1) \;\leftrightarrow\; \chi_M T = \frac{N\mu_B^2}{3k_B} g^2 S(S+1)$$

So far, the magnetic properties have been analysed for the simplest example corresponding to an isotropic free ion, giving consideration only to the spin contribution. In the case of ions with a substantial spin−orbital coupling (SOC, $L \neq 0$) such as lanthanide elements or certain 3*d* ions (*e.g.* Octahedral Co^{2+}), the angular momentum is no longer equal to the spin momentum ($J = S \pm L$), and the orbital contribution must be taken into account. Therefore the *g*−Landé factor, the saturation magnetisation and the magnetic susceptibility (following Curie Law) are expressed as Eq. 1.7 and 1.8:

Eq. 1.7 $$g_J = \frac{3}{2} + \frac{S(S+1) - L(L+1)}{2J(J+1)}$$

Eq. 1.8 $$M = N\mu_B g_J J \leftrightarrow M/N\mu_B = g_J J; \quad \chi_M T = \frac{N\mu_B^2}{3k_B} {g_J}^2 J(J+1)$$

Nevertheless, most of the systems exhibit some deviations from the ideal behaviour, for example when the interactions between different paramagnetic ions are non−negligible. In that case, the magnetic susceptibility can be described by the Curie−Weiss law, $\chi_M = \frac{C}{T-\theta}$. The presence of these interactions leads to a sub−classification of paramagnetic materials. If neighbouring spins are arranged in a parallel fashion the magnetic interaction is described as ferromagnetic. In this situation, an increase in the $\chi_M T$ value is observed. On the other hand, an antiparallel arrangement is denominated an antiferromagnetic interaction, leading to a decrease in the $\chi_M T$ value. There is also a third possible situation, known as ferrimagnetism, when there are antiferromagnetic interactions between ions with different numbers of unpaired electrons, leading to a net spin (see Fig 1.2).

Fig 1.2 Spin orientation in a paramagnetic material at zero−applied field (in blue), and its different magnetic response under an external field (H).

The described magnetic behaviours exhibited by a bulk material can be extrapolated to the molecular scale, *i.e*. coordination complexes (CCs). Thus, the overlap between the atomic orbitals of metal centres and those of the bridging ligands leads to the parallel or antiparallel orientation of the spins associated with the metal ions analogous to the situation observed in the bulk. Ferromagnetic coupling leads to high ground state spin values due to the alignment of the spins, while antiferromagnetic coupling involves the cancellation of the spins that often generate a ground state spin equal to zero. In order to analyse the experimental magnetic behaviour observed for a certain CC by magnetic measurements (*i.e*. magnetisation and susceptibility), different models based on the Schrödinger equation are generally used. Therefore, the Hamiltonian equation is defined specifically for each complex considering the nature of the metal ions, the geometry, and the assembly of the different centres. In this way, certain key parameters for the promotion of SMM properties (such as the magnetic exchange between metal ions, $\mathcal{J}$) can be investigated.

1.2. Modelling magnetic properties using spin Hamiltonians[5, 6, 10]

The energy of an atom can be calculated from the Schrodinger equation ($\hat{\mathcal{H}}\Psi = E\Psi$). This equation can be decomposed into several operators related to the atom, the electrons and the nucleus depending on the type of interaction experienced by the metal ion and the particles that it is comprised of. Experimental measurements obtained by SQUID magnetometry give information about the following:[5]

$$\hat{\mathcal{H}} = \overbrace{\hat{H}_{ZE} + \hat{H}_{SS} + \hat{H}_{LS}}^{\hat{\boldsymbol{H}}} + \hat{H}_{Ex} + \hat{H}_{CF} \qquad \text{Eq. 1.7}$$

Where $\hat{H}_{ZE}$ corresponds to the Zeeman electronic term arising from the Zeeman Effect (*vide supra*); $\hat{H}_{SS}$ to the spin−spin interaction term; $\hat{H}_{LS}$ to the spin−orbit Hamiltonian (hence to the interaction between the spin of an electron and its orbital momentum); $\hat{H}_{Ex}$ is the exchange Hamiltonian corresponding to the interaction between (paramagnetic) metal ions; and $\hat{H}_{CF}$ the crystal field term related to the effect on the *d*/*f* orbitals resulting from the coordination of a ligand to the ion.[5]

The spin Hamiltonian formalism is generally applied in order to simplify the above total Hamiltonian.[5] In that, only the spin component, the spin−spin interactions and the interaction with an external field are considered, including the orbital component ($\lambda, \hat{L}$) into new parameters (g, D). Then, the spin Hamiltonian ($\hat{\boldsymbol{H}}$) can be expressed as:[5]

$$\hat{\boldsymbol{H}} = \lambda\hat{L}\cdot\hat{S} + \mu_B\left(\hat{L} + g_e\hat{S}\right)H \rightarrow \hat{\boldsymbol{H}} = \mu_B g H\hat{S} + D\hat{S}^2 \qquad \text{Eq. 1.8}$$

Where λ is a parameter derived from a first order SOC; $\hat{L}$, $\hat{S}$ are, respectively, the orbital and spin operators; and D is the axial parameter arising from the zero−field splitting. Hence, the g−Landé factor is now dependent on λ, and it can be calculated[5] as $g = g_e - \frac{n\lambda}{\Delta}$ (n being a constant related to the symmetry of the metal centre, and Δ the energy difference between the ground and the excited states). Note that *d*−elements displaying less than a half−filled shell (*i.e.* $n_{(d)} \leq 4$) have a positive λ, thus a $g < g_e = 2.0023$. On the other hand, elements displaying more than a half−filled shell (*i.e.* $n_{(d)} \geq 6$) have a negative λ, thus a $g > g_e$. The zero−field splitting (ZFS) that generates D stems from a weak interaction between the ground state and the excited states due to a second order SOC perturbation in polyelectronic systems.[11] If the CC is anisotropic due to geometric distortions, g is

orientation−dependent (*i.e*. g_x, g_y, g_z may display different values), and the spin Hamiltonian should account for both axial (D) and transverse (E) anisotropic components (Eq. 1.9).[5]

Eq. 1.9 $$\widehat{\boldsymbol{H}} = \mu_B g H \hat{S} + D\left[\hat{S}_z^2 - \frac{1}{3}S(S+1)\right] + E\left(\hat{S}_x^2 - \hat{S}_y^2\right)$$

Since a large number of the studied systems are polynuclear complexes, the properties no longer come from only the isolated metal ions. The $\widehat{H}_{Ex}$ term accounts for these interactions between spins of neighboring atoms given via superexchange mechanism. Assuming an isotropic interaction, $\widehat{H}_{Ex}$ can be described as:[5]

Eq. 1.10 $$\widehat{H}_{Ex} = -2\sum_{ij} \mathcal{J}_{ij} \hat{S}_i \hat{S}_j$$

Therefore, the magnetic exchange interaction between the spin operators $\hat{S}_i$ and $\hat{S}_j$ is quantified by the $\mathcal{J}_{ij}$ parameter. By convention, ferromagnetic coupling (*i.e*. spins are parallel aligned) involves a positive $\mathcal{J}$, whereas antiferromagnetic coupling (*i.e*. spins are antiparallel aligned) has a negative $\mathcal{J}$.

As shown in Eq. 1.7, magnetic measurements may also provide to some extent some information about the crystal field effect ($\widehat{H}_{CF}$). The term related to the crystal field is expressed as:[12]

Eq. 1.11 $$\widehat{H}_{CF} = \sum_{i=1}^{N} \sum_{k=2,4,6} \sum_{q=-k}^{k} \sigma_i^k B_{k_i}^q \theta_k \hat{O}_{k_i}^q$$

Where σ_i^k are the orbital reduction parameters, θ_k are the operator equivalent factors, $B_{k_i}^q$ are the crystal field parameters in Steven's notation, and $\hat{O}_{k_i}^q$ are the operator equivalents. The information extracted from $\widehat{H}_{CF}$, however, should not be taken as a quantification of the energy level splitting, but rather used to shed light on the magnetic properties exhibited by a system (especially important in Ln−complexes). This will be explained in more detail in Chapter 6.

It should be noted that parameters displayed as capital letters (*i.e*. S, D) are normally used to refer to the whole molecule, while lower case letters (*s*, *d*) are used for individual metal ions. For example, a dinuclear anisotropic Ni(II) system would have an associated total spin ground state of S resulting from the combination of s_1 and s_2, and a total magnetic anisotropy D arising from the combination of the individual d_1 and d_2.

Thus, it has been shown how spin Hamiltonians are great models for analysing the static magnetic properties of coordination compounds. To this end, new parameters have been introduced, such as magnetic exchange ($\mathcal{J}$) or anisotropy (D). Those are directly related to the dynamic magnetic features of the system, therefore to the SMM properties, which are explained in detail below.

1.3. Single−molecule magnets: features and characterisation[6, 8, 13]

Single−molecule magnets are coordination complexes that exhibit slow relaxation of their magnetisation and magnetic hysteresis of a purely molecular origin, thus leading to magnetic bistability. There are two main requirements for a molecule to be considered a classical SMM. First, the spin ground state of the molecule (S) should be high. Secondly, it should display a preferential direction for its spin, known as uni−axial anisotropy. This uni−axial anisotropy occurs by zero−field splitting (ZFS), as characterised by the axial parameter D, which should be ideally high and negative. The quantum mechanical description of the ZFS has been previously introduced in section 1.2, however, the consequences on the energy levels of an ion or a complex have not been yet thoroughly discussed.[11] ZFS is described as the splitting of the S energy levels of metal ions into their constituent M_s levels in the absence of an applied field. These properties can generate an appreciable energy barrier (ΔE_{cal}) between the two possible orientations of the spin ground state, which can lead to slow magnetic relaxation (*i.e*. reversal of the direction of the magnetisation). The energy barrier for a SMM with an integer and non−integer total spin S is given by:

$$\Delta E_{cal} = |D|S^2 \longrightarrow \text{Integer } S$$

$$\Delta E_{cal} = |D|\left(S^2 - {}^1/_4\right) \longrightarrow \text{Non−integer } S$$

Figure 1.3 shows a schematic representation of the double potential well associated with the slow relaxation process within a molecule that exhibits SMM behaviour (with D < 0) based on 3*d* transition metal ions where 2[nd] order SOC is present. At zero field (Fig 1.3, left), the lower energy and thus more stable M_s (+S, −S) are initially equally populated. When an external field is applied ($H \neq 0$), the sample is magnetised, thus breaking the energetic degeneracy of the M_s levels: negative M_s states become more stable (lower energy), while positive M_s states become more unstable (higher energy). This energetic difference leads to a preferential population of the M_s = −S level (Fig 1.3, centre), with a parallel

alignment of spins with respect to the direction of the external field (*z*−axis). On removing the external field the energetic degeneracy of the different M_S states is recovered (Fig 1.3, right), and the spins return slowly to their initial orientation, commonly via various relaxation processes.

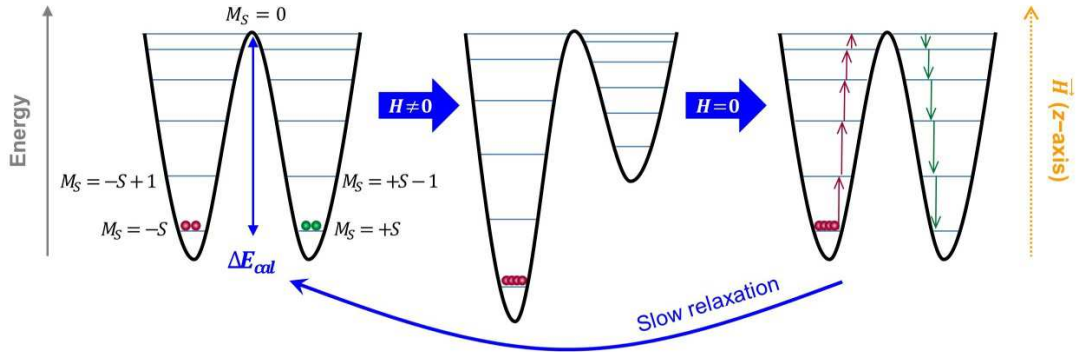

Fig 1.3 Diagram of the double−well generated by ZFS in a 3*d*−based SMM (with S ground state, and $D < 0$), showing the slow magnetic relaxation process related to the energy barrier ΔE_{cal}.

As introduced in previous sections, lanthanides behave magnetically different to transition metals, mainly due to dissimilarities related to their electronic structure. Unlike 3*d* metals, 4*f*−block elements (except Gd^{3+}) have much stronger spin−orbit coupling than the splitting caused by the ligand field effect (see Fig 1.4). Therefore the magnitude of the magnetic anisotropy in 4*f*−systems mainly arises from the crystal−field (CF) splitting caused by the metal−ligand interaction.[14]

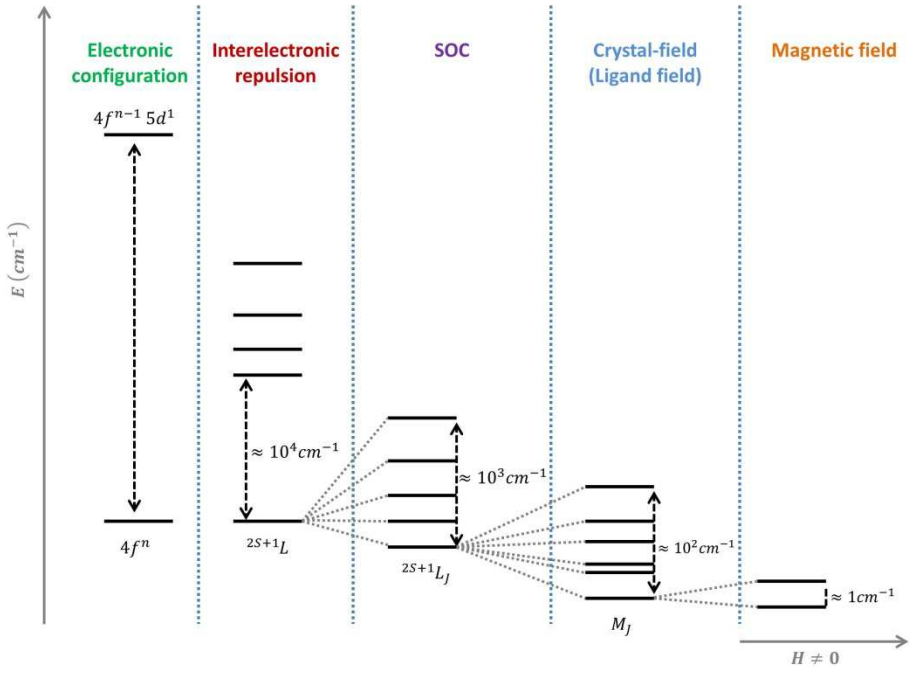

Fig 1.4 Electronic interactions in a Kramer's 4*f* ion and typical energy magnitudes related to the different perturbations (*i.e.* electron repulsion, SOC, CF and magnetic field).[13]

The resulting microstates, now referred to as M_J, are usually linear combinations of multiple m_J functions (apart from certain ideal symmetries). That also affects how the magnetic slow relaxation occurs.[14] While for transition metals the flip from the "spin−up" to the "spin−down" situation is ideally a consequence of several transitions between M_S microstates (Fig 1.3, right), for lanthanide complexes the relaxation usually occurs via one or two steps only. Hence, the investigation of the mechanism(s) involved in the relaxation process becomes of key importance for analysing the dynamic magnetic properties observed in Ln−SMMs (*vide infra*).

A suitable method to detect the slow relaxation in SMMs is through alternating current (ac) magnetic susceptibility measurements.[8, 12] In ac studies, the susceptibility of a sample is measured using a weak applied magnetic field (~ 1−5 G) that switches its direction at a fixed frequency (υ ~ 1−1500 Hz) over a range of temperatures (~ 1.8−50 K, however it could be higher for lanthanides).[15, 16] Under these conditions, the magnetic susceptibility of a compound (χ_{ac}, $cm^3 \cdot mol^{-1}$) depends on the angular frequency (ω) at which the magnetic field oscillates. Note that the higher the applied frequency ($\omega = 2\pi\upsilon$) the faster the ac field oscillates, thus the magnetisation becomes incapable of switch simultaneously with the oscillating field. Therefore, χ_{ac} can be described as the combination of two components (see Fig 1.5, left): a real contribution (also known as in−phase susceptibility, χ') and an imaginary contribution (out−of−phase susceptibility, χ''). Then, as the fixed frequency increases and starts to approach to the relaxation rate for the magnetisation (τ), the value of the real part of the susceptibility decreases.

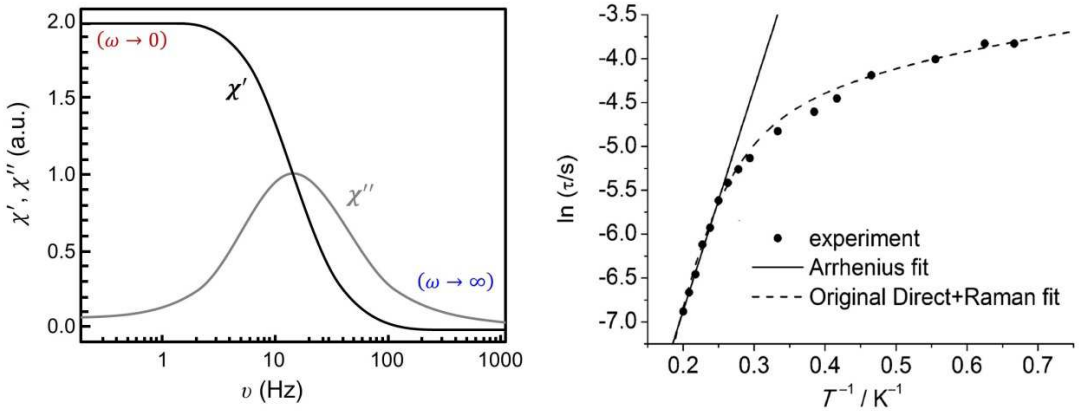

Fig 1.5 Left: Ac plot illustrating the dependent of the real (χ') and the imaginary (χ'') part of the susceptibility as a function of frequency. Right: Arrhenius plot from experimental ac data for 1% Tb^{3+} in $[Y(H_2O)_9](C_2H_5SO_3)_3$. Solid line represents the fit of the high−temperature regime to the Arrhenius law, whereas the dashed line is a fit to Direct and Raman processes simultaneously. Figure adapted from Ref. 14 (published by The Royal Society of Chemistry).

On the other hand, the magnitude of the imaginary part increases (since it cannot switch with the ac field) reaching a maximum before decreasing again with the highest frequencies (Fig 1.5, left). This maximum occurs at a given temperature where $\omega\tau = 1$, therefore the relaxation time for the magnetisation τ can be calculated by:[17]

Eq. 1.12 $$\omega\tau = 1 = 2\pi\upsilon\tau \leftrightarrow \tau = 1/2\pi\upsilon$$

The temperature dependence of the relaxation time (Fig 1.5, right) may be described by the Arrhenius law:

Eq. 1.13 $$\tau = \tau_0 \cdot exp(\Delta E/k_B T) \rightarrow \ln\tau = \ln\tau_0 + \Delta E/k_B T$$

Where ΔE is the value of the effective energy barrier of spin−reversal; and τ_0 (~10^{-5}–10^{-11} s) is the pre−exponential factor that provides a quantitative measure of the relaxation attempt time for reversal at $T \rightarrow \infty$. Note that the effective energy barrier ΔE extracted experimentally by ac experiments tends to be smaller than the calculated one (ΔE_{cal}) as a result of alternative routes for the magnetic relaxation (*e.g.* quantum tunnelling of the magnetisation, QTM). Note also that at relatively low temperatures the $\ln\tau \ vs. T^{-1}$ plot from Figure 1.5 (right) displays a deviation from the Arrhenius Law that could be related to the presence of several relaxation pathways in the molecule. These processes are phonon−assisted and temperature (T) and/or field (H) dependent, as discussed below.[16, 17]

The transition from “spin−up” to “spin−down” that involves the relaxation of the magnetisation occurs by means of interactions between the magnetic ion (spin) and the lattice, as a consequence of the principle of conservation of energy.[4] The exchange of energy between spin and lattice (*i.e.* the spin−lattice interaction) is assisted by the absorption and/or emission of at least one phonon, and can be described by three main thermal relaxation mechanisms: Direct, Orbach and Raman (see Fig 1.6).[14] In the **Direct mechanism**, the spin of the molecule flips to another energy level (from $-M_S$ to $+M_S$) under the absorption or emission of one phonon. In the **Orbach mechanism** the absorption of one phonon excites the spin system to a real state, followed by the emission of a second phonon, leading to the relaxation of the spin system. The above mentioned ideal pathway (ΔE_{cal}) can be thus described as an Orbach process. On the other hand, in the **Raman mechanism** the excitation (absorption of a phonon) and subsequent relaxation (emission of a phonon) of the spin occurs via a virtual intermediate state.

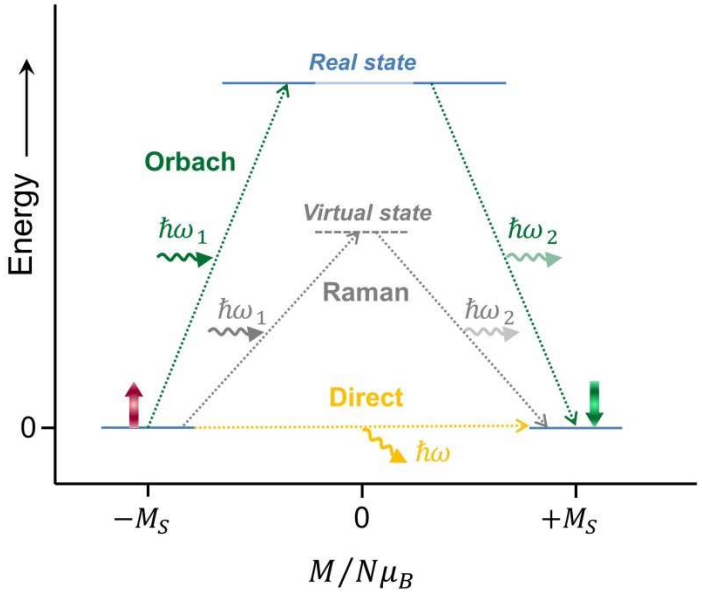

Fig 1.6 Schematic overview over the magnetisation relaxation process by different phonon−assisted ($\hbar\omega$), spin–lattice mechanisms. Blue solid lines represent real M_S states, while the grey dashed line a virtual state. Direct process is displayed as a yellow dotted arrow, Orbach as green arrows, and Raman as grey arrows.

In addition to these phonon−assisted spin−lattice processes, there is another possible pathway competing for the relaxation of the magnetisation, known as *quantum tunnelling of the magnetisation* (QTM). QTM occurs when there is a resonant alignment of some of the positive and negative M_S states of a molecule, therefore the spin flips through the anisotropy barrier instead of overcoming ΔE_{cal} (Fig 1.7). QTM arises by transverse perturbations on the pure axial symmetry of a certain system, such as low−symmetry components of the crystal field, any effective transverse magnetic field, or hyperfine interactions with nuclear spins.[14] The presence of transverse components leads to the mixing of microstates (*i.e*. $\pm M_S$), and to an energy or tunnel splitting equal to the rate at which the system can tunnel from one side of the barrier ($-M_S$) to the other (resonant $+M_S$). Note that the transverse field component resulting from the above mentioned perturbations allows tunnelling in the absence of field (purple arrow, Fig 1.7) or under the influence of an applied field (blue arrows, Fig 1.7).[18] The third possible tunnelling that a molecule could exhibit occurs by thermal population of excited $-M_S$ states (thermally−assisted tunnelling). Transitions between higher states (red arrows in Fig 1.7) result in much of the loss of magnetisation, since they are closer in energy to each other than the lower energy states. Note also that higher states (*i.e*. smaller $\pm M_S$) display more probability and a larger tunnelling than the lower states (*i.e*. greater $\pm M_S$).[19] These tunnelling mechanisms are indeed the origin of the different values observed between the calculated energy barrier (ΔE_{cal}) and the

experimental effective barrier extracted by the Arrhenius law (ΔE). In order to supress the tunnelling within a certain system, a dc static field is often applied during the ac experiments to break the degeneracy of the $\pm M_S$ states.

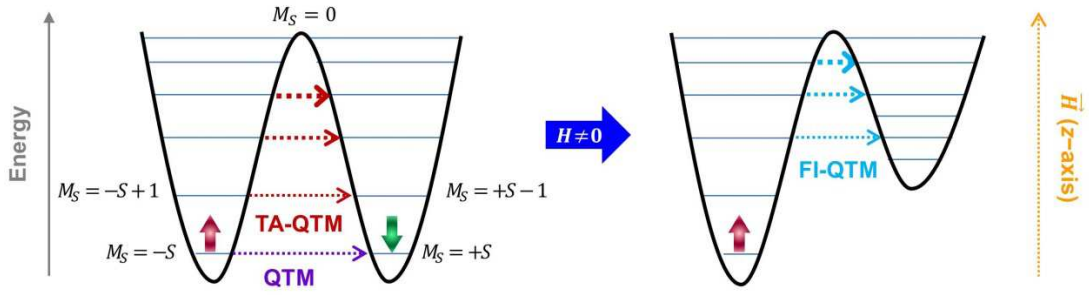

Fig 1.7 Diagram of the double−well generated by ZFS in a 3*d*−based SMM (with S ground state, and $D < 0$) at zero field (left) and in an applied field (right). The dotted arrows display the different quantum tunnelling mechanisms (QTM). Purple, zero−field ground state tunnelling (QTM); Red, thermally−assisted zero−field tunnelling (TA−QTM); Blue: field−induced tunnelling (FI−QTM).

Since the relaxation time of the spin−reversal is therefore dependent on the phonon−assisted and quantum tunnelling mechanisms, the fit of the ac susceptibility data may result from the combination of multiple mechanisms (see dashed line in Fig. 1.5). The equation for the calculation of the relaxation time τ and τ_0 including all the above mentioned processes is expressed as:[14]

Eq. 1.14 $$1/\tau(H,T) = 1/\tau_{Direct}(H,T) + 1/\tau_{Raman}(T) + 1/\tau_{Orbach}(T) + 1/\tau_{Tunnel}(H/T)$$

$$\downarrow$$

$$\tau^{-1} = \overbrace{AH^mT}^{Direct} + \overbrace{CT^n}^{Raman} + \overbrace{\tau_0^{-1}\cdot\exp(-\Delta E/k_BT)}^{Orbach} + \overbrace{\frac{B_1}{1+B_2H^2}}^{QTM}$$

or

$$\ln\tau = -\ln\left[AH^mT + CT^n + \tau_0^{-1}\cdot\exp(-\Delta E/k_BT) + \frac{B_1}{1+B_2H^2}\right]$$

Here, the parameters *A* and *C* are constant; n and m are variable parameters that depend on the type of the metal ion (*e.g.* 3*d*, 4*f*) and the symmetry of the system (*e.g.* Kramer's *vs*. non−Kramer's ion). Metal ions with an odd number of unpaired electrons have a half−integer total spin S, thus a half−integer angular momentum J (since $J = S \pm L$, and L is always integer). Consequently, the crystal field will split the $2J+1$ microstates into degenerate doublets. According to Kramer's theorem, the zero−field ground state of an ion with a half−integer angular momentum (*i.e.* Kramer's ion) will always be bistable, regardless of the ligand field symmetry.[15] On the other hand, non−Kramer's ions (those with an integer angular

momentum) only display a bistable ground state when the ligand field has axial symmetry. This is the reason why there are so many reported Dy−SMMs. For lanthanides, the common values for m and n for a non−Kramer's ion (*e.g*. Tb^{3+}, Ho^{3+}) are respectively 2 and 7, whereas for a Kramer's ion (*e.g*. Dy^{3+}, Er^{3+}) are 4 and 9.[14] Nevertheless, both parameters may differ from the expected ones depending on the presence of hyperfine interactions or very low−lying spin states. Note that the QTM τ term only refers to the non−thermally assisted tunnelling processes (*i.e*. QTM and low M_s levels of FI−QTM), as the thermally assisted (TA−QTM) would be accounted for in the Orbach term. QTM contribution leads to a deviation from linearity in the $\ln \tau \ vs. T^{-1}$ data at low temperatures, which eventually becomes temperature independent.[12, 16]

So far, only one single relaxation time related to the spin−reversal of the magnetisation within a system has been considered. Nevertheless, the observation of multiple processes with different relaxation times is common in polynuclear systems with more than one anisotropic paramagnetic centre (especially for Dy(III)).[20–22] In that case, two maxima in the $\chi'' \ vs. \upsilon$ plots are expected to be seen. This two−maximum feature, however, can also arise from quantum tunnelling effects. Therefore, the relaxation dynamics of a system can be further explored by Argand plots (commonly known as Cole−Cole).[12, 20] In Argand graphs the $\chi'' \ vs. \chi'$ data for each temperature is plotted (Fig 1.8). A system with a relaxation process with a single time constant τ (Debye process) will show perfectly symmetric, concentric semicircles.

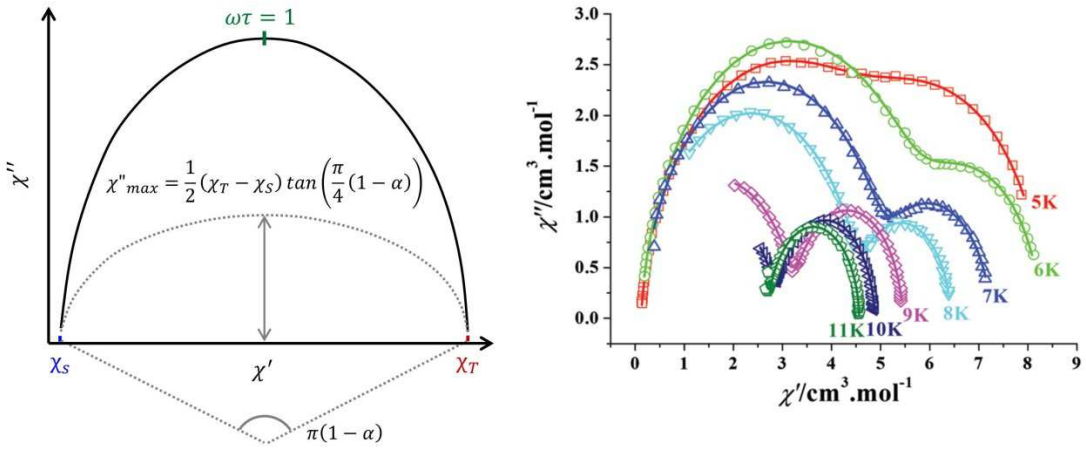

Fig 1.8 Left: Argand plots illustrating a relaxation process with a single time constant (τ, solid black line), and a distribution of relaxation time constants according to $\chi''_{max}(\alpha)$ (dotted grey line). Right: Cole−Cole plots characteristic for a system with two−time relaxation process (τ_1, τ_2). Coloured solid lines represent the fit of the experimental data. Reproduced from Ref. 23 with permission of The Royal Society of Chemistry.

The fit of the Cole−Cole plots based on the model developed by Jinkui and co−workers[12, 20] allows the calculation of the relaxation time for each temperature. The applied model also gives consideration to the distribution of relaxation times (α) in a system. The wider the distribution in relaxation times, the larger the value of α (given $0 \leq \alpha \leq 1$). Then, a system with a value of $\alpha \to 0$ is related to single time τ, whereas α becomes larger ($\alpha \to 1$) the flatter the distribution of the time constants around τ. That also may be related to the presence of multiple contributions to the slow relaxation of the magnetisation (*e.g.* QTM). SMMs with multiple relaxation processes and more than one relaxation time (*i.e.* τ_1, τ_2, and then α_1, α_2) display characteristically more than one semicircle (Fig 1.8, right), which vary with the temperature (see how those for *T* = 5 K are partially merged).

The slow relaxation of magnetisation leads to what is considered the fundamental characteristic of SMMs, the existence of magnetic hysteresis. Figure 1.9 shows an ideal hysteresis loop (left) compared to that experimental one from a reported SMM (right). As increasing the applied field (H), the spins tend to align with the field until reaching the magnetisation saturation value (M_{sat}). Upon removal of the external field, the sample has been magnetised as a consequence of the slow relaxation, since a remnant magnetisation (M_r) at zero field is observed (Fig 1.9, left). The same behaviour is observed by applying a negative field. Therefore, the cycle can be completed by reversing the process (*i.e.* increasing the field until reaching the positive saturation value).

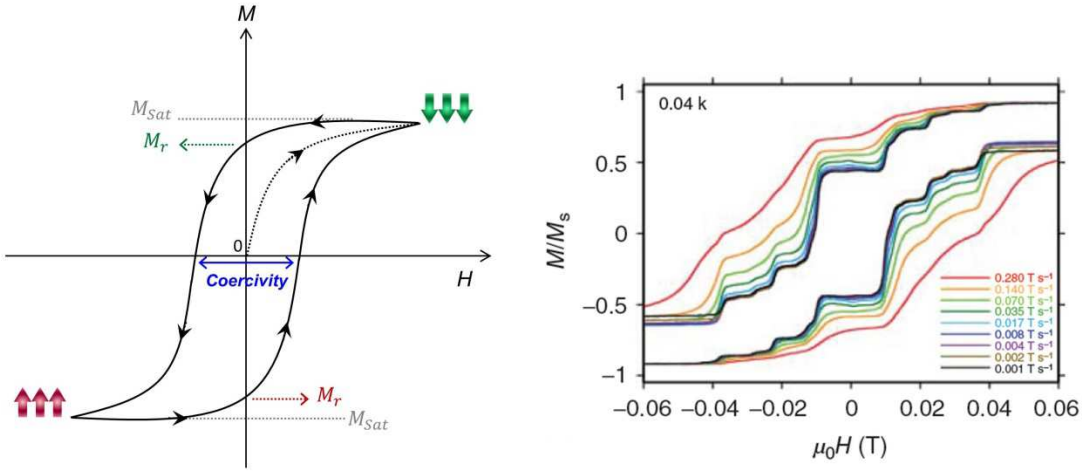

Fig 1.9 Left: Typical magnetic hysteresis loop. M_{sat} is the saturation of the magnetisation and M_r is the remnant magnetisation. Right: Single−crystal magnetisation versus field plot[13] performed at *T* = 0.04K and sweep rates between 0.001–0.280 T·s^{-1} on a sample of TBA[$(Pc)_2Tb^{III}_{0.02}Y^{III}_{0.98}$] (Pc=phthalocyaninato, TBA=tetrabutylammonium) (Copyright © 2015 by John Wiley Sons, Inc. Reprinted by permission of John Wiley & Sons, Inc.).

The width of the hysteresis cycle is the coercivity, and it gives information about the strength of a magnet: the wider the hysteresis loop, the stronger the magnet is considered. Consequently, the magnetic hysteresis cycle shows the characteristic bistability of SMMs: the magnetisation can be positive or negative at zero−field depending on the history of the sample. The experimental hysteresis curves, however, are not as smooth as the conventional ones, and usually present little "jumps" related to spin−reversal quantum tunnelling mechanisms (see Fig 1.9, right).[13] Note that hysteresis depends on the applied temperature and the magnetic field sweep rate. To avoid possible technical limitations that a conventional SQUID magnetometer may have, single−crystal experiments performed in a micro−SQUID are carried out when possible, since it can work with millikelvin temperatures and with large field−sweep rates.

1.4. Trends in the synthesis of molecular magnets

The first coordination complex identified as SMM (*i.e*. that possess slow relaxation of the magnetisation of a purely molecular origin) was $[Mn_{12}O_{12}(O_2CCH_3)_{16}(H_2O)_4]\cdot 4H_2O\cdot 2CH_3CO_2H$ ($Mn_{12}Ac$). $Mn_{12}Ac$ was characterised structurally in 1980 by Lis,[24] before being magnetically studied by Gatteschi and Christou in 1993.[25, 26] The structure of $Mn_{12}Ac$ (see Fig 1.10) is formed by a central $\{Mn^{IV}_4O_4\}$ unit arranged in a distorted cubane environment, surrounded by a ring of eight Mn^{III} ions. All of the $Mn^{III/IV}$ ions are linked by oxygen atoms provided by oxo− and acetate ligands.

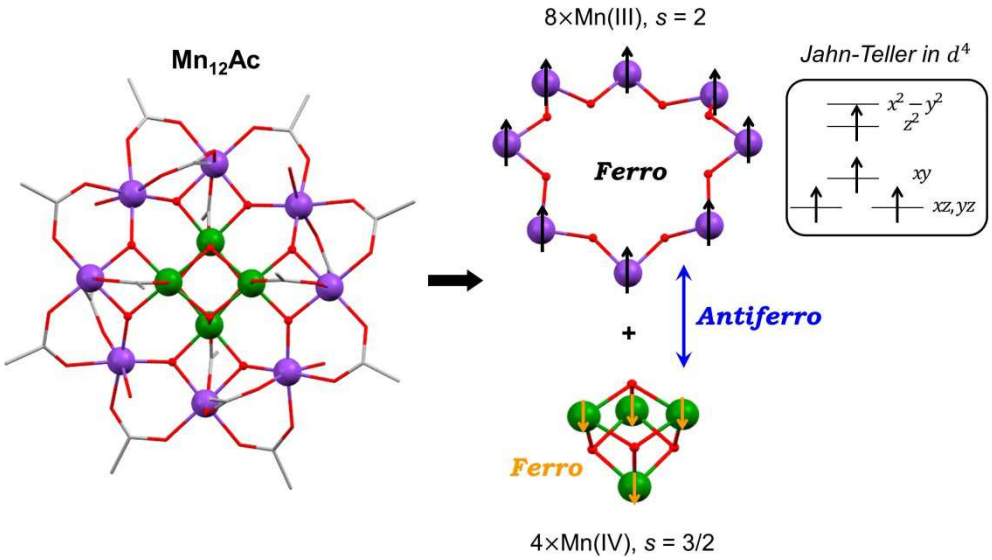

Fig 1.10 Crystal structure of $[Mn_{12}O_{12}(O_2CCH_3)_{16}(H_2O)_4]$ (left). Detail of $\{Mn^{IV}_4O_4\}$−cubane unit (right, bottom) and the Mn^{III}−ring unit (right, top). The *d*−orbital splitting of the electronic configuration of Mn^{III} ions is shown beside the Mn^{III}−ring.

The sixteen external acetate groups act as a shield, isolating the single molecule from neighbouring molecules. Manganese centres with the same oxidation state are coupled ferromagnetically, while ions with different oxidation states are antiferromagnetically coupled, leading to a net spin ground state in the molecule (S = 10). Due to the symmetry adopted and the magnetic interactions between metal ions, this molecule satisfies the requirements to be a SMM: a high total spin ground state of the molecule, and a high uni−axial anisotropy (due to the ZFS from the Mn^{III} ions). Since the discovery of the magnetic properties of $Mn_{12}Ac$, the synthesis of new coordination complexes displaying similar SMM features has been one of the main goals in molecular magnetism.[27] The major challenges in the design of molecular magnets are (i) the enhancement of the anisotropy barrier and hence, the blocking temperatures of the current nanomagnets; and (ii) quenching the tunnelling that suppresses the remnant magnetisation at zero applied field. Keeping in mind that the energy barrier (ΔE_{cal}) is related to the total spin of the system (S) and to the axial anisotropy parameter (D), one can think that large energy barriers can be obtained by increasing S and/or D. Consequently, early efforts focussed on the synthesis of high−nuclearity complexes with certain topologies prone to M···M ferromagnetic coupling.[28–31] Supramolecular coordination chemistry allows, to a certain extent, the synthesis of compounds that meet the requirements previously discussed. One of the most common and successful methodologies for the synthesis of new SMMs delineated by Winpenny is serendipitous self−assembly.[32] In this method, ligands containing multiple donor atoms capable of coordinating to one or more metal ions by different coordination modes are combined with metal salts or metallo−organic precursors. This strategy has been prolific, having generated many coordination complexes with interesting magnetic properties (*e.g*. $Mn_{12}Ac$), with Mn(III) being the most widely used metal ion due to its large number of unpaired electrons and magnetic anisotropy.[33–35] However, some of these large polynuclear complexes − with huge S values − did not display the desired SMM behaviour, due to a lack of magnetic anisotropy arising from the non−existent control over the topology of the final structure.[36–39]

Upon seeing that a large total spin did not necessarily imply a high energy barrier, other strategies were investigated based on the improvement of the total magnetic anisotropy of the system (D).[40-42] For that, a more deliberate design of the reaction conditions is required, *i.e*. careful choice of the ligand(s), the metal ion(s), and the solvent(s).[43] An alternative approach involving directed or rational design is then used rather than serendipitous self−assembly.[44, 45] The selected ligands and

metal precursors are more rigid and display lower flexibility when they are combined compared to those used in the former strategy. The ligand is also usually customised considering the preferred geometry of the metal precursor to be used in the synthesis, towards the control of certain magnetic properties in the final system. Schiff base ligands have been extensively used in the rational design of SMMs, since they can be easily tailored by varying the starting materials (*i.e*. amine and carbonyl groups).[43, 46] The use of Schiff bases in search of new nanomagnets will be further discussed in later sections. Regarding the choice of the metal precursor, *f*−block elements are an excellent option for the design of SMMs. This is due to their large single−ion anisotropy resulting from the strong spin−orbit coupling and CF splitting.[15, 16, 47] Despite the ideal qualities of lanthanide ions, some reported 4*f*−based single−molecule magnets show drawbacks, such as very efficient quantum tunnelling.[48, 49] The dynamic properties of 4*f*−complexes are really dependent on the symmetry displayed by the complex, as lanthanide ions are very sensitive to changes in the ligand environment (thus in the CF).[12, 13] The perturbations of the ideal symmetry provide a transverse component that, as previously commented, leads to the presence of QTM, and therefore greatly reduces the energy barrier for magnetisation reversal. Relatively recent studies proved that the combined use of 3*d*/4*f* ions can be a good strategy for the design of molecular magnets, since lanthanide ions provide the required magnetic anisotropy that is essential in SMMs and the 3*d*−4*f* exchange interaction can help to suppress QTM.[43, 50]

Apart from these routes, the development of new methodologies that allow the synthesis of high−nuclearity metal complexes with large intrinsic uniaxial magnetic anisotropy is currently a challenge in modern coordination chemistry. Lately, approaches that take advantage of both serendipitous self−assembly and rational design attributes have become the subject of study to control the synthesis of SMMs. One of those proposals is based on the use of metallo−organic precursors as potential "building−blocks" (BB) for the synthesis of polymetallic complexes.[51, 52] Over the last years the Murrie group has used different 3*d*−based building blocks in order to control, to some extent, the assembly of new heterometallic polynuclear compounds. For example, $[LnCu_3(H_2edte)_3(NO_3)](NO_3)_2$ (Ln = Tb, Dy; H_4edte = 2,2',2'',2'''−(ethane−1,2−diyldinitrilo)tetraethanol) are two new SMMs synthesised following a step−by−step approach involving the reaction of the pre−formed metallo−ligand $[Cu_2(H_3edte)_2](NO_3)_2$ with lanthanide salts (Fig 1.11).[50] Although the complexes did not exhibit large anisotropic barriers compared to other reported for

similar Cu−4*f* systems, the investigation of the exchange interactions by Inelastic Neutron Scattering shed light on the slow relaxation pathway within the molecule, and therefore about the origin of the SMM behaviour.

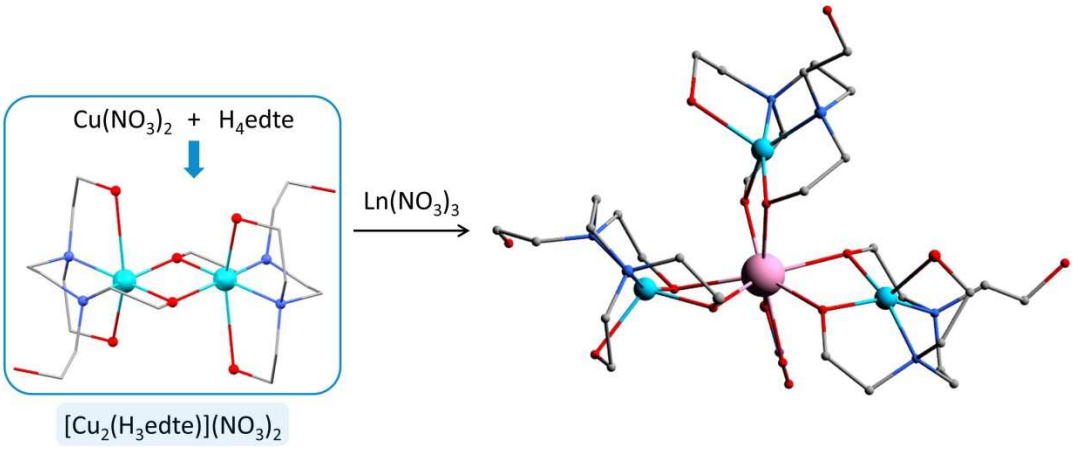

Fig 1.11 Synthetic approach and structure of $[Cu_2(H_3edte)_2](NO_3)_2$ (left) and $[LnCu_3(H_2edte)_3(NO_3)](NO_3)_2$ (right). C, grey; Cu, turquoise; Ln, pink; N, blue; O, red; Hydrogen atoms and solvent molecules are omitted for clarity.

Many other groups have followed a similar strategy based on the use of BB for directing the synthesis of new molecular materials to control to a certain extent the final magnetic properties. As discussed at the beginning of this thesis, the promising capability of some systems for acting as molecular refrigerants has been drawing the attention of a large number of researchers within the field of molecular magnetism. For instance, the group of Bendix has reported a family of heterometallic systems with the formula $[\{MF_3(Me_3tacn)\}_2Gd_3F_2(NO_3)_7(H_2O)(CH_3CN)]$ (M = Cr^{III}, Fe^{III}; Me_3tacn = *N*,*N*',*N*''−trimethyl−1,4,7-triazacyclononane), resulting from the reaction between *fac*−$[MF_3(Me_3tacn)]\cdot 4H_2O$ and $Gd(NO_3)_3\cdot 5H_2O$.[53] The replacement of the transition metal ion in the starting BB leads to a different M···Gd interaction, modifying the magnetocaloric properties of the final systems. That makes these systems interesting modules for low−temperature cooling applications (*i.e*. magnetic coolers). The requirements for considering a complex a potential molecular magnetic refrigerant will be explained in the following section.

1.5. Magnetic coolers[6, 54]

The magnetocaloric effect (MCE) is described as the reversible adiabatic temperature change (ΔT_{ad}) and magnetic entropy change (ΔS_m) of a material, following the application or removal of a magnetic field. The variable temperature

properties of a material associated with the magnetocaloric effect were first observed in a Fe−based material by Warburg in 1881.[55] But it was not until the late 1920s, when Debye and Giauque proposed adiabatic demagnetisation as an appropriate method for reaching sub−Kelvin temperatures.[56, 57] One of the many applications derived from the MCE is the use of magnetic materials as potential solid candidates for replacing the ^{3}He−based low−temperature refrigerant currently used. Figure 1.12 illustrates the operation of a magnetic refrigerant.[58] When an external magnetic field (H) is applied to a paramagnetic material, the spins align parallel to the field (Fig 1.12, a), thus the magnetic entropy of the system (S_m) decreases. The total entropy of a material (S) can be described as a summation of the magnetic (S_m), the lattice (S_{Lat}) and the electronic (S_{El}) contributions, *i.e.* $S(T,H) = S_m(T,H) + S_{Lat}(T,H) + S_{El}(T,H)$, and $S_m = Rln(2s+1)$.[6] Since this process is adiabatic, the decrease in S_m caused by the rearrangement of the spins is cancelled out by an increase of the lattice entropy (S_{Lat}) and of the temperature of the system. This first step is known as *adiabatic magnetisation*. Afterward, the generated heat in the system is removed by means of a fluid or a gas, thus restoring the initial temperature T_0 (Fig 1.12, b).

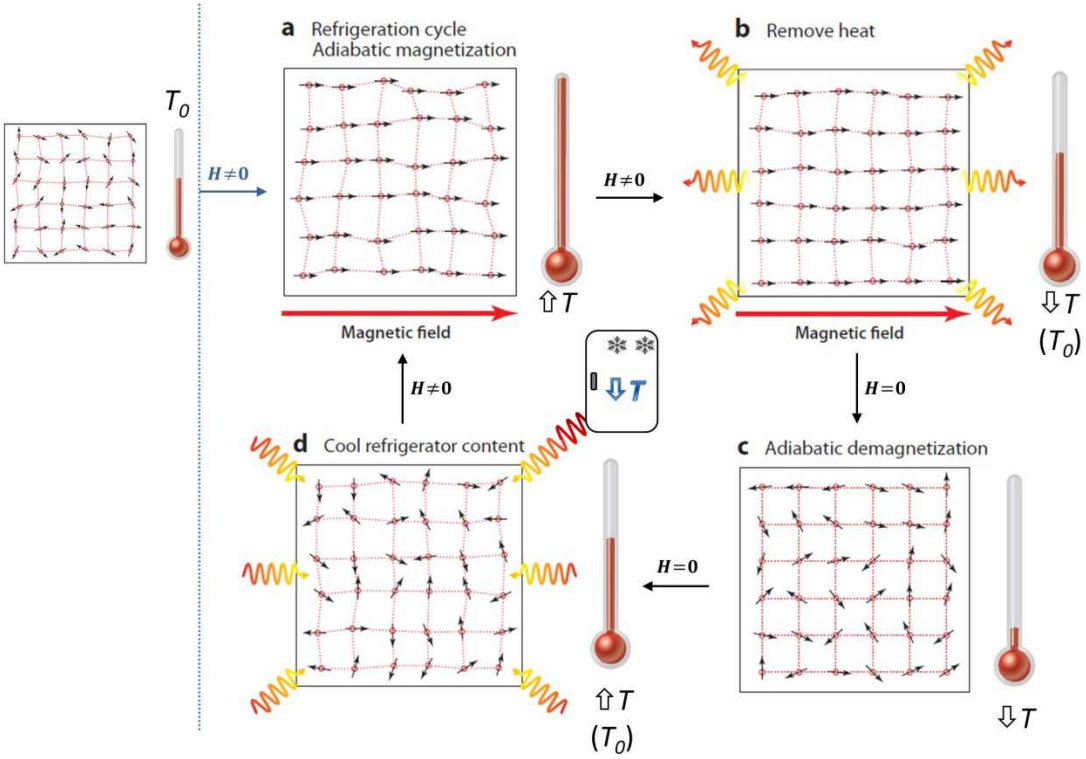

Fig 1.12 Scheme of the operation of a molecular cooler depicting the four stages of a magnetic refrigeration cycle: (a) adiabatic magnetisation, (b) remove heat, (c) adiabatic demagnetisation, and (d) cool refrigerator contents. Figure adapted from Ref. 58 (Published by Annual Reviews).

Upon the removal of the external field, the sample is demagnetised, resulting in an increase of S_m, and hence a decrease in S_{Lat} and the system temperature (*adiabatic demagnetisation*, Fig 1.12 c). The initial thermal conditions are re−established (Fig 1.12, d) when the magnetic system is connected to the instrument to be cooled (*e*.*g*. by a fluid/gas). At this point, the adiabatic cycle described by these four steps would be continuously repeated.

The development of new nanomagnets in search of optimum magnetocaloric properties (*i*.*e*. large MCE)[59-62] has become extremely important given that ^{3}He is rare and increasingly expensive. This is where coordination chemistry and molecular magnetism become powerful tools for optimising design towards the ideal magnetic refrigerant. Early examples of magnetic coolers focused on highly−anisotropic SMMs,[63] but subsequent studies revealed that a large MCE at low temperatures is more likely to be observed in polynuclear complexes with negligible magnetic anisotropy.[60, 64-75] Another common trend is to maximise the magnetic:non−magnetic ratio, so as to increase values of the refrigeration power and $-\Delta S_m$, when reported per unit mass or unit volume.[66, 76] The inherent drawback of this approach is that spin−spin correlations increase unavoidably, which ultimately limit the lower bound of ΔT_{ad} and the lowest temperature that can be attained in an adiabatic demagnetisation process.[69] Therefore, a compromise becomes necessary. Some recent studies explore the combined use of 3*d*/4*f* ions in search of the enhancement of magnetocaloric properties. As discussed in previous sections, the use of highly anisotropic lanthanides (*i*.*e*. Dy or Tb) is a commonly used strategy to provide a large anisotropy in the synthesis of SMMs. On the other hand, for magnetic cooling ΔS_m can be maximized by incorporating Gd(III) ions[66-75] into the 3*d*−4*f* system, as it provides the largest entropy per single−ion. Recently Winpenny and co−workers have reported very promising results on a new series of so−called $[n \times n]$ grids formed by multiple Co(II) and Gd(III) ions linked by several low molecular weight ligands (*e*.*g*. phosphonates) displaying huge low temperature MCE (with values of ΔS_m = 19.9–22.3 J·Kg^{-1}·K^{-1}).[77]

1.6. Use of polycompartmental ligands towards the design of heterometallic molecular magnets.

In this last section the aims of the project, along with some of the ligands used throughout the development of the experimental part of the PhD thesis are introduced. Both ligands herein presented have fairly different structural features,

but the same common goal, the controlled synthesis of heterometallic complexes. Firstly the commercial ligand 2,2'−(propane−1,3−diyldiimino)bis[2−(hydroxylmethyl)propane−1,3−diol] (related to Chapters 3−6) is described, and then secondly the Schiff base *N,N′*−bis(2−Hydroxy−3−methoxyphenylmethylidene)-2,6−pyridinediamine (related to Chapter 7).

1.6.1. Aminopolyol ligand 2,2'−(propane−1,3−diyldiimino)bis[2−(hydroxymethyl)-propane−1,3−diol] (Bis−tris propane, H_6L).

Based on a combination of different synthetic routes discussed in Section 1.4, the Murrie research group has synthesised a number of polymetallic coordination systems with the ligand bis−tris propane (2,2'−(propane−1,3−diyldiimino)-bis[2−(hydroxylmethyl)propane−1,3−diol]), named hereafter as H_6L (Scheme 1.1).[78-82] Bis−tris propane is a very flexible polydentate ligand, with well−defined coordination sites. Its skeleton has an internal $\{N_2O_2\}$ pocket ideal for the coordination of different transition metal ions, such as Mn(II), Fe(III), Co(III), Ni(II) or Cu(II) ions.[78-82] Other groups have also investigated lately the reactivity of H_6L in the presence of 3*d*, 4*f* ions.[23, 83] Note that, in spite of its potential as a ligand in coordination chemistry, H_6L had been mostly limited to be utilised as a biological buffer in fields such as biochemistry or molecular biology.[78]

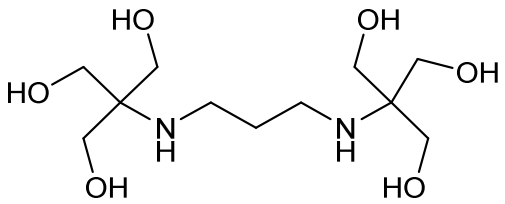

Scheme 1.1 Bis−tris propane, H_6L.

Some of the reported polynuclear complexes have been obtained by following a serendipitous process based on "one−pot" reactions,[79, 81, 82] whereas other ones were prepared from metallo−organic precursors.[78, 80] The synthesis of the two heterometallic Cu/Mn complexes is,[80] however, carried out by using a much more attractive approach to than those used for the rest, similar to that previously described for $[LnCu_3(H_2edte)_3(NO_3)](NO_3)_2$.[50] Figure 1.13 shows the preparative route for the synthesis of $[Mn_{18}Cu_6O_{14}(H_2L)_6Cl_2(H_2O)_6]Cl_6\cdot H_2O$. First, H_6L and $CuCl_2$ are combined to form the precursor $[Cu(H_6L)Cl]Cl$. As can be seen, the Cu(II) ion is chelated by the central $\{N_2O_2\}$ pocket in a octahedral geometry. The apical positions are occupied by one OH(R) and the more labile Cl^- group. That is quite an

important factor, since the mechanism in solution involving the coordination/discoordination of these labile groups increases the reactivity of the monomeric moiety, facilitating the next step. In addition, the three remaining uncoordinated hydroxyl groups from H_6L may potentially act as binding atoms with other metal centres. Secondly, the preformed metallo−ligand is reacted with $MnCl_2$ to give the final $\{Cu_6Mn^{II}_6Mn^{III}_{12}\}$ products, where hydroxyl groups from H_6L have been partially deprotonated under basic conditions. Both $\{Cu_6Mn^{II}_6Mn^{III}_{12}\}$ structures display a characteristic "core−shell" distribution of the metal atoms: after losing the chloride anion, the Cu(II) precursor surrounds the Mn(II/III) ions, encapsulating the Mn−oxide nanoclusters (Fig 1.13). But perhaps the most relevant conclusion extracted from the synthesis of these high−nuclearity compounds is the discriminatory tendency of H_6L with certain transition metal ions, and hence its capability for controlling and directing the final molecular assembly of heterometallic systems. In all the reported experimental procedures involving the combined use of H_6L and Cu(II) salts, the ligand shows a clear tendency to chelate Cu(II) ions in the internal $\{N_2O_2\}$ pocket to the detriment of other 3*d* ions present in the reaction media (*i.e*. Mn(II/III), Zn(II)).[80, 81] However, most of the attractive structures obtained with the ligand H_6L so far display antiferro− or very weak ferromagnetic coupling.

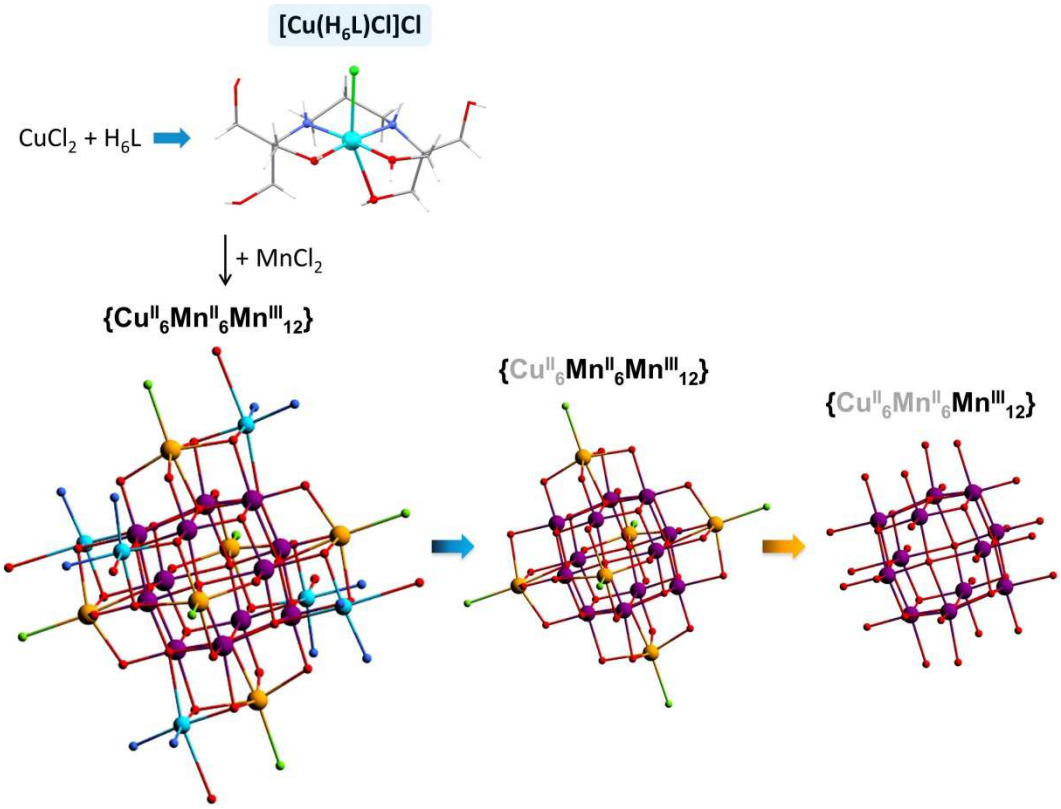

Fig 1.13 Synthetic approach and detail of the structure for $[Cu(H_6L)Cl]Cl$ (top) and for $\{Cu_6Mn_{18}\}$ (bottom). C, grey; Cl, green; Cu, turquoise; Mn^{III}, purple; Mn^{II}, orange; N, blue; O, red.

As previously discussed, the antiferromagnetic exchange interaction between different metal ions lowers the spin ground state, due to the antiparallel arrangement of the spins. To try to avoid some of these antiferromagnetic interactions, and therefore achieve the highest possible ground state value, we propose two different strategies that combine the advantages of serendipity and rational design. The first line of work focuses on the preparation of other metallo−organic precursors derived from H_6L. The replacement of the paramagnetic metal centre (Cu(II), Ni(II) and/or Co(II)) and the co−ligands (Cl^-, AcO^-) seeks to modify the nature of the magnetic interaction, and thus promote certain features related to SMM or MCE performance. The use of pre−formed building blocks helps to gain some degree of control over the assembly process of the final product. The second strategy takes advantage of the ability of H_6L to direct the synthesis of heterometallic compounds in one−pot reactions by following a (apparently) serendipitious approach. The coordination chemistry of lanthanide ions with H_6L in the presence of transition metal ions is likely to depend on two main factors: i) the steric limitations of the binding pocket defined by $\{N_2O_2\}$; ii) the great affinity of lanthanide ions for oxygen donors. Considering this, the 3*d* ions are expected to occupy the inner pocket, whereas 4*f* ions are expected to be coordinated to the remaining hydroxyl arms. In addition, the combined use of 3*d*, 4*f* ions has the purpose of promoting ferromagnetic interactions (especially for the heavier Ln ions).[84-87]

1.6.2. Schiff base ligand N,N'−bis(2−Hydroxy−3−methoxyphenylmethylidene)−2,6-pyridinediamine (H_2L2).

As explained in previous sections, the rational approach is based on the pre−design of relatively rigid multidentate ligands that are able to direct to some extent the assembly of the metal ions, and hence the magnetic properties of the final complexes. Schiff bases are great candidates to be used in the molecular design of heterometallic systems, due to their relatively simple ligand synthesis and the possibility to tailor structure by modifying the starting amines or carbonyls.[88-90] Several studies based on Schiff−base 3*d*−4*f* systems have provided invaluable information about the nature of the interactions between lanthanides and transition metals, as well as about the dynamic properties of SMMs (*i.e*. slow magnetic relaxation).[84, 91, 92] Many of the members of this family of ligands involve rigid aromatic aldehydes (*e.g*. salicyladehyde or *o*−vanillin) and flexible amines, possessing well−defined coordination pockets as well as outer donor atoms for

further linking. In the case of *o*−vanillin derivatives (also called valen−type), an inner binding pocket is defined by $\{N_2O_2\}$, and an external one defined by $\{O_2O_2'\}$ (see scheme 1.2).[46] Taking into account the nature of the atoms and the size of the different compartments, these ligands provide a synergetic coordination of 3*d* and 4*f* ions. Consequently, the transition metal ions are expected to occupy the less hindered inner pocket, whereas the oxophilic lanthanides would coordinate to the outer one.

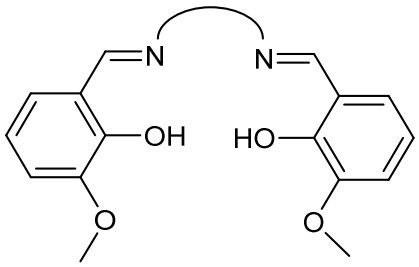

Scheme 1.2 Diagram for a general Schiff−base ligand derived from *o*−vanillin and a diamine.

N,N'−bis(2−Hydroxy−3−methoxyphenylmethylidene)−2,6−pyridinediamine is a member of the valen−Schiff base family, the structure of which was reported by Galić and co−workers a few years ago (see Fig 1.14).[93] *N,N'*−bis(2−Hydroxy−3-methoxyphenylmethylidene)−2,6−pyridinediamine (hereafter H_2L2) is formed by a central pyridyl ring and two *o*−vanillin groups occupying the iminic positions, to describe two different coordination pockets. The additional N−pyridyl opens the possibility to a third coordination pocket, in addition to those described above. The coordination chemistry of H_2L2 with 3*d* and/or 4*f* elements, however, has been barely explored.[94, 95] Hence, the exploration of H_2L2 as potential pro-ligand of heterometallic complexes is herein discussed.

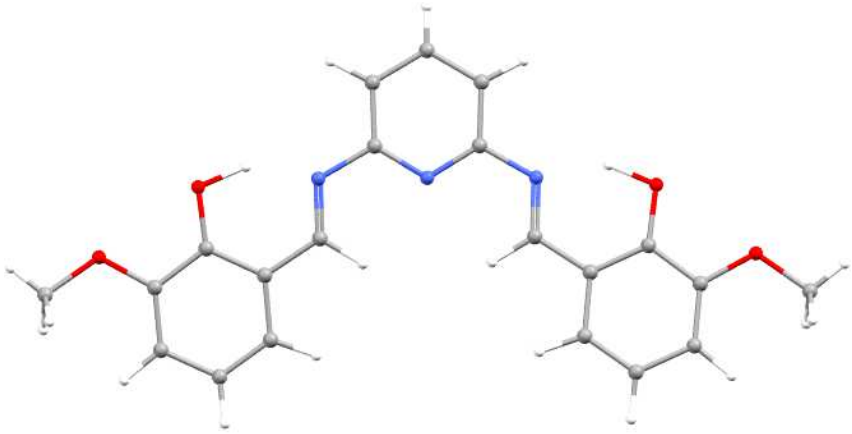

Fig 1.14 Structure of H_2L2. C, grey; H, white; N, blue; O, red.[93]

References

1. A. Ardavan, O. Rival, J. J. L. Morton, S. J. Blundell, A. M. Tyryshkin, G. A. Timco and R. E. P. Winpenny, *Phy. Rev. Lett.*, **2007**, *98*, 057201.
2. Y.−Z. Zheng, E. M. Pineda, M. Helliwell and R. E. P. Winpenny, *Chem. Eur. J.*, **2012**, *18*, 4161.
3. M. N. Leuenberger and D. Loss, *Nature*, **2001**, *410*, 789.
4. R. L. Carlin, *Magnetochemistry*, Springer−Verlag, Berlin, Heidelberg, **1986**.
5. J. Ribas Gispert, *Coordination Chemistry*, Wiley−VCH Verlag GmbH & Co. KGaA, Weinheim, **2008**.
6. C. Benelli and D. Gatteschi, *Introduction to Molecular Magnetism. From transition metals to lanthanides*, Wiley−VCH Verlag GmbH & Co. KGaA, Weinheim, **2015**.
7. O. Khan, *Molecular Magnetism*, VCH Publishers, New York, **1993**.
8. D. Gatteschi, Roberta Sessoli, and Jacques Villain, *Molecular Nanomagnets*, Oxford University Press Inc., New York, **2006**.
9. I. Langmuir, *J. Am. Chem. Soc.*, **1919**, *41*, 868.
10. T. Gupta and G. Rajaraman, *Chem. Commun.*, **2016**, *52*, 8972.
11. R. Boča, *Coord. Chem. Rev.*, **2004**, *248*, 757.
12. J. Tang and P. Zhang, *Lanthanide Single Molecule Magnets*, Springer−Verlag, Berlin, Heidelberg, **2015**.
13. R. A. Layfield and M. Murugesu, *Lanthanides and Actinides in Molecular Magnetism*, Wiley−VCH Verlag GmbH & Co. KGaA, Weinheim, **2015**.
14. S. T. Liddle and J. van Slageren, *Chem. Soc. Rev.*, **2015**, *44*, 6655.
15. D. N. Woodruff, R. E. P. Winpenny and R. A. Layfield, *Chem. Rev.*, **2013**, *113*, 5110.
16. L. Rosado Piquer and E. C. Sañudo, *Dalton Trans.*, **2015**, *44*, 8771.
17. G. A. Craig and M. Murrie, *Chem. Soc. Rev.*, **2015**, *44*, 2135.
18. T. Glaser, V. Hoeke, K. Gieb, J. Schnack, C. Schröder and P. Müller, *Coord. Chem. Rev.*, **2015**, *289–290*, 261.
19. J. Bartolomé, F. Luis and J. F. Fernández, *Molecular Magnetism: Physics and Applications*, Springer−Verlag, Berlin, Heidelberg, **2014**.
20. Y.−N. Guo, G.−F. Xu, Y. Guo and J. Tang, *Dalton Trans.*, **2011**, *40*, 9953.
21. S.−Y. Lin, W. Wernsdorfer, L. Ungur, A. K. Powell, Y.−N. Guo, J. Tang, L. Zhao, L. F. Chibotaru and H.−J. Zhang, *Angew. Chem. Int. Ed.*, **2012**, *51*, 12767.
22. L. Zhang , J. Jung, P. Zhang, M. Guo, L. Zhao, J. Tang and B. LeGuennic, *Chem. Eur. J.*, **2016**, *22*, 1392.
23. C.−M. Liu, D.−Q. Zhang and D.−B. Zhu, *Dalton Trans.*, **2013**, *42*, 14813.
24. T. Lis, *Acta Crystallog. Sect. B*, **1980**, *36*, 2042.
25. R. Sessoli, D. Gatteschi, A. Caneschi and M. A. Novak, *Nature*, **1993**, *365*, 141.
26. R. Sessoli, H. L. Tsai, A. R. Schake, S. Wang, J. B. Vincent, K. Folting, D. Gatteschi, G. Christou and D. N. Hendrickson, *J. Am. Chem. Soc.*, **1993**, *115*, 1804.
27. G. Aromí and E. K. Brechin, in *Struct. Bond.*, **2006**, *122*:*1*, Springer−Verlag, Berlin, Heidelberg, **2006**.
28. A. K. Powell, S. L. Heath, D. Gatteschi, L. Pardi, R. Sessoli, G. Spina, F. Del Giallo and F. Pieralli, *J. Am. Chem. Soc.*, **1995**, *117*, 2491.
29. J. C. Goodwin, R. Sessoli, D. Gatteschi, W. Wernsdorfer, A. K. Powell and S. L. Heath, *J. Chem. Soc., Dalton Trans.*, **2000**, 1835.
30. J. Larionova, M. Gross, M. Pilkington, H. Andres, H. Stoeckli−Evans, H. U. Güdel and S. Decurtins, *Angew. Chem. Int. Ed.*, **2000**, *39*, 1605.
31. D. M. Low, L. F. Jones, A. Bell, E. K. Brechin, T. Mallah, E. Rivière, S. J. Teat and E. J. L. McInnes, *Angew. Chem. Int. Ed.*, **2003**, *42*, 3781.
32. R. E. P. Winpenny, *J. Chem. Soc., Dalton Trans.*, **2002**, *1*.

33. D. N. Hendrickson, G. Christou, H. Ishimoto, J. Yoo, E. K. Brechin, A. Yamaguchi, E. M. Rumberger, S. M. J. Aubin, Z. Sun and G. Aromi, *Molecular Crystals and Liquid Crystals*, **2002**, *376*, 301.
34. R. Bagai and G. Christou, *Chem. Soc. Rev.*, **2009**, *38*, 1011.
35. T. C. Stamatatos and G. Christou, *Inorg. Chem.*, **2009**, 48, 3308.
36. E. K. Brechin, S. G. Harris, A. Harrison, S. Parsons, A. Gavin Whittaker and R. E. P. Winpenny, *Chem. Commun.*, **1997**, *653*.
37. A. J. Tasiopoulos, A. Vinslava, W. Wernsdorfer, K. A. Abboud and G. Christou, *Angew. Chem. Int. Ed.*, **2004**, *43*, 2117.
38. A. M. Ako, I. J. Hewitt, V. Mereacre, R. Clérac, W. Wernsdorfer, C. E. Anson and A. K. Powell, *Angew. Chem. Int. Ed.*, **2006**, *45*, 4926.
39. T. C. Stamatatos and G. Christou, *Phil. Trans. R. Soc. A*, **2008**, *366*, 113.
40. O. Waldmann, *Inorg. Chem.*, **2007**, *46*, 10035.
41. E. Ruiz, J. Cirera, J. Cano, S. Alvarez, C. Loose and J. Kortus, *Chem. Commun.*, **2008**, *52*.
42. S. Gomez−Coca, E. Cremades, N. Aliaga−Alcalde and E. Ruiz, *J. Am. Chem. Soc.*, **2013**, *135*, 7010.
43. K. Liu, W. Shi and P. Cheng, *Coord. Chem. Rev.*, **2015**, *289–290*, 74.
44. R. W. Saalfrank, H. Maid and A. Scheurer, *Angew. Chem. Int. Ed.*, **2008**, *47*, 8794.
45. T. Glaser, *Chem. Commun.*, **2011**, *47*, 116.
46. M. Andruh, *Dalton Trans.*, **2015**, *44*, 16633.
47. J. Luzon and R. Sessoli, *Dalton Trans.*, **2012**, *41*, 13556.
48. N. Ishikawa, M. Sugita, T. Okubo, N. Tanaka, T. Iino and Y. Kaizu, *Inorg. Chem.*, **2003**, *42*, 2440.
49. L. Zhang, P. Zhang, L. Zhao, S.−Y. Lin, S. Xue, J. Tang and Z. Liu, *Eur. J. Inorg. Chem.*, **2013**, *8*, 1351.
50. F. J. Kettles, V. A. Milway, F. Tuna, R. Valiente, L. H. Thomas, W. Wernsdorfer, S. T. Ochsenbein and M. Murrie, *Inorg. Chem.*, **2014**, *53*, 8970.
51. K. S. Pedersen, J. Bendix and R. Clerac, *Chem. Commun.*, **2014**, *50*, 4396.
52. F. Reichel, J. K. Clegg, K. Gloe, K. Gloe, J. J. Weigand, J. K. Reynolds, C.−G. Li, J. R. Aldrich−Wright, C. J. Kepert, L. F. Lindoy, H.−C. Yao and F. Li, *Inorg. Chem.*, **2014**, *53*, 688.
53. K. S. Pedersen, G. Lorusso, J. J. Morales, T. Weyhermüller, S. Piligkos, S. K. Singh, D. Larsen, M. Schau−Magnussen, G. Rajaraman, M. Evangelisti and J. Bendix, *Angew. Chem. Int. Ed.*, **2014**, *53*, 2394.
54. M. Evangelisti, in *Molecular Magnets: Physics and Applications*, Springer−Verlag, Berlin, Heidelberg, **2014**, pp. 365.
55. E. Warburg, *Ann.Phys.*, **1881**, *249*, 141.
56. P. Debye, *Ann. Phys.*, **1926**, *386*, 1154.
57. W. F. Giauque, *J. Am. Chem. Soc.*, **1927**, *49*, 1864.
58. V. B. Franco, J.S.; Ingale, B.; Conde, A., *Annu. Rev. Mater. Res.*, **2012**, *42*, 305.
59. M. Evangelisti, F. Luis, L. J. de Jongh and M. Affronte, *Journal of Materials Chemistry*, **2006**, *16*, 2534.
60. M. Evangelisti and E. K. Brechin, *Dalton Trans.*, **2010**, *39*, 4672.
61. J. W. Sharples and D. Collison, *Polyhedron*, **2013**, *54*, 91.
62. Y.−Z. Zheng, G.−J. Zhou, Z. Zheng and R. E. P. Winpenny, *Chem. Soc. Rev.*, **2014**, *43*, 1462.
63. F. Torres, X. Bohigas, J. M. Hernández and J. Tejada, *J. Phys.: Condens. Matter*, **2003**, *15*, L119.
64. G. Karotsis, M. Evangelisti, S. J. Dalgarno and E. K. Brechin, *Angew. Chem. Int. Ed.*, **2009**, *48*, 9928.

65. F. Luis and M. Evangelisti, in *Molecular Nanomagnets and Related Phenomena*, Springer−Verlag, Berlin, Heidelberg, **2015**, pp. 431.
66. M. Evangelisti, O. Roubeau, E. Palacios, A. Camón, T. N. Hooper, E. K. Brechin and J. J. Alonso, *Angew. Chem. Int. Ed.*, **2011**, *50*, 6606.
67. J. W. Sharples, Y.−Z. Zheng, F. Tuna, E. J. L. McInnes and D. Collison, *Chem. Commun.*, **2011**, *47*, 7650.
68. F.−S. Guo, J.−D. Leng, J.−L. Liu, Z.−S. Meng and M.−L. Tong, *Inorg. Chem.*, **2012**, *51*, 405.
69. M.−J. Martínez−Pérez, O. Montero, M. Evangelisti, F. Luis, J. Sesé, S. Cardona−Serra and E. Coronado, *Adv. Mat.*, **2012**, *24*, 4301.
70. T. N. Hooper, J. Schnack, S. Piligkos, M. Evangelisti and E. K. Brechin, *Angew. Chem. Int. Ed.*, **2012**, *51*, 4633.
71. P.−F. Shi, Y.−Z. Zheng, X.−Q. Zhao, G. Xiong, B. Zhao, F.−F. Wan and P. Cheng, *Chem. Eur. J.*, **2012**, *18*, 15086.
72. G. Lorusso, M. A. Palacios, G. S. Nichol, E. K. Brechin, O. Roubeau and M. Evangelisti, *Chem. Commun.*, **2012**, *48*, 7592.
73. R. Sibille, T. Mazet, B. Malaman and M. François, *Chem. Eur. J.*, **2012**, *18*, 12970.
74. L.−X. Chang, G. Xiong, L. Wang, P. Cheng and B. Zhao, *Chem. Commun.*, **2013**, *49*, 1055.
75. J. W. Sharples, D. Collison, E. J. L. McInnes, J. Schnack, E. Palacios and M. Evangelisti, *Nature Commun.*, **2014**, *5*, 5321.
76. G. Lorusso, J. W. Sharples, E. Palacios, O. Roubeau, E. K. Brechin, R. Sessoli, A. Rossin, F. Tuna, E. J. L. McInnes, D. Collison and M. Evangelisti, *Adv. Mat.*, **2013**, *25*, 4653.
77. Y.−Z. Zheng, M. Evangelisti and R. E. P. Winpenny, *Chem. Sci.*, **2011**, *2*, 99.
78. A. Ferguson, A. Darwish, K. Graham, M. Schmidtmann, A. Parkin and M. Murrie, *Inorg. Chem.*, **2008**, *47*, 9742.
79. A. Ferguson, M. Schmidtmann, E. K. Brechin and M. Murrie, *Dalton Trans.*, **2011**, *40*, 334.
80. V. A. Milway, F. Tuna, A. R. Farrell, L. E. Sharp, S. Parsons and M. Murrie, *Angew. Chem. Int. Ed.*, **2013**, *52*, 1949.
81. M. Heras Ojea, C. Wilson, S. J. Coles, F. Tuna and M. Murrie, *Dalton Trans.*, **2015**, *44*, 19275.
82. M. Heras Ojea, V. A. Milway, G. Velmurugan, L. H. Thomas, S. J. Coles, C. Wilson, W. Wernsdorfer, G. Rajaraman and M. Murrie, *Chem. Eur. J.*, **2016**, *22*, 12839.
83. S.−D. Han, S.−J. Liu, Q.−L. Wang, X.−H. Miao, T.−L. Hu and X.−H. Bu, *Cryst. Growth Des.*, **2015**, *15*, 2253.
84. J.−P. Costes, F. Dahan and A. Dupuis, *Inorg. Chem.*, **2000**, *39*, 5994.
85. C. Benelli and D. Gatteschi, *Chem. Rev.*, **2002**, *102*, 2369.
86. J. Cirera and E. Ruiz, *C. R. Chim.*, **2008**, *11*, 1227.
87. T. Shimada, A. Okazawa, N. Kojima, S. Yoshii, H. Nojiri and T. Ishida, *Inorg. Chem.*, **2011**, *50*, 10555.
88. T. Glaser, *Chem. Commun.*, **2011**, *47*, 116.
89. E. Colacio, J. Ruiz−Sanchez, F. J. White and E. K. Brechin, *Inorg. Chem.*, **2011**, *50*, 7268.
90. S. G. Dogaheh, M. Heras Ojea, L. R. Piquer, L. Artús Suàrez, H. Khanmohammadi, G. Aromí and E. C. Sañudo, *Eur. J. Inorg. Chem.*, **2016**, *20*, 3314.
91. J.−P. Costes, F. Dahan, A. Dupuis and J.−P. Laurent, *Inorg. Chem.*, **1996**, *35*, 2400.
92. J.−P. Costes, F. Dahan, A. Dupuis and J.−P. Laurent, *Inorg. Chem.*, **1997**, *36*, 3429.
93. N. Galić, D. Matković−Čalogović and Z. Cimerman, *Struct. Chem.*, **2000**, *11*, 361.
94. H.−J. Bai, F.−G. Xing, Z.−L. Wang, *J. Shaanxi Normal Univ. (Nat. Sci. Ed.)*, **2008**, *6*, 47.

95. L. Lei, G.−X. Xiong; Y.−Z. Wang, *Fine Chemicals*, **2012**, *2*, 155.

Chapter 2

Contents

Chapter 2. Physical Techniques

Chapter 2. Physical Techniques

2.1. Infrared spectroscopy

The IR spectra were measured using a FTIR−8400S SHIMADZU IR spectrophotometer.

2.2. Elemental analysis

The microanalyses were performed by the analytical services of the School of Chemistry at the University of Glasgow. Most of the complexes show a slight hygroscopic tendency similar to that observed in previously published complexes obtained using H_6L as a ligand.[1] Some of them displayed also a tendency to lose the more volatile lattice solvent (*e.g*. CH_3OH, $(CH_3CH_2)_2O$).

2.3. Energy−dispersive X−ray spectroscopy

EDX experiments for **3**−**5**, **13** and **19** were carried out by using Philips XL 30 Environmental Scanning Electron Microscope (ESEM) at different magnifications. In order to remove complications due to charging, samples were gold−coated using vacuum electric sputter coater (POLARON SC 7640) prior to analysis. The images were taken using a W−K*α* (57981.77 eV) radiation with a Secondary Electron detector and Oxford Instruments INCA 250Xact10 EDX detector.

2.4. Nuclear Magnetic Resonance Spectroscopy

The ^{1}H−NMR spectrum of *N,N′*−bis(2−Hydroxy−3−methoxyphenylmethylidene)-2,6−pyridinediamine (H_2L2) was obtained using a Bruker AVI 400M MHz.

2.5. Single−crystal X−Ray diffraction

Crystallographic data were collected at 100 K using Mo−K*α* radiation (λ = 0.71073 Å). For **16**, a Cu−K*α* radiation was used (λ = 1.54184 Å).

For **1**, **3**, **4**, **13**, and **18** a Bruker APEXII CCD diffractometer with an Oxford Cryosystems cryostream low−temperature device mounted on a sealed tube generator was used.

For **5**−**7**, **10**, **17**, **19**−**21** and **28** a Rigaku AFC12 goniometer equipped with an (HG) Saturn724+ detector mounted on an FR−E+ SuperBright rotating anode generator with HF Varimax optics (100µm focus)[2] was used.

For **8**, **9**, **11**, **12**, **14**, **15**, and **23**−**26** a Bruker−Nonius Kappa CCD diffractometer with an Oxford Cryosystems cryostream device mounted on a sealed tube generator was used.

For **16** a Rigaku Oxford Diffraction SuperNova equipped with an AtlasS2 CCD detector and an Oxford Cryosystems Cryostream cooling device was used. Data collection and processing were carried out using CrysAlisPro 1.171.38.42t (Rigaku OD, 2015).

For **27** a Bruker D8 VENTURE diffractometer equipped with a Photon II CMOS detector with an Oxford Cryosystems *n*−Helix device mounted on a IµS 3.0 (dual Cu and Mo) microfocus sealed tube generator was used.

All the structures were solved using SUPERFLIP[3] and refined using full−matrix least squares refinement on F^2 using SHELX2014[4, 5] within OLEX2.[6] Hydrogen atoms were placed in geometrically calculated positions and refined as part of a riding model (see exceptions in *Single crystal X−ray data collection and refinement details* in the corresponding appendix).

Note that no data were collected for **2** ($[Cu_2(H_5L)_2(CH_3COO)_2]$) and **22** ($[Co(H_6L)(CH_3COO)_2]$), since both were isolated as non-crystalline products.

2.6. SQUID magnetometry

Magnetic measurements were performed on polycrystalline samples constrained in eicosane (except **23**), using a Quantum Design MPMS−XL or MPMS−5S (only **15**) SQUID magnetometer.

Data were corrected for the diamagnetic contribution of the sample holder and eicosane (except **23**) by measurements, and for the diamagnetism of the compounds by using the approximation that χ_{diam} ~ −0.5 × *MW* × 10^{-6} $cm^3 \cdot mol^{-1}$ (*MW* = molecular weight).[7] The Temperature Independent Paramagnetism (TIP) contribution was taken into account for the dc magnetic measurements of some of the complexes (**2** and **16**). The TIP contribution arises from mixing the ground state with not thermally populated excited states.[8]

The magnetic dc data were fitted by using the program PHI and by applying the Spin Hamiltonians specified for the different complexes throughout the text.[9]

Ac susceptibility data were collected on cooling with an ac drive field of 3 Gauss oscillating at frequencies between 1 and 1500 Hz. The magnetic ac data were fitted by using the program CC−Fit and by applying the single− or two−step relaxation process model specified for the different complexes throughout the text.[10]

Ultra−low temperature (<1.8 K) hysteresis studies were performed on a single crystal sample of **9** using an array of micro−SQUIDS (the field is oriented along the easy axis, which is found in situ by changing the field orientation with three coils).[11]

Heat capacity measurements of **23** were carried out for temperatures down to *ca*. 0.3 K by using a Quantum Design 9T−PPMS, equipped with a ^{3}He cryostat. The experiments were performed on thin pressed pellets (*ca*. 1 mg) of a polycrystalline sample, thermalised by *ca*. 0.2 mg of Apiezon N grease, whose contribution was subtracted by using a phenomenological expression.[12]

2.8. Electrospray Ionisation mass spectroscopy

The mass spectrometry analyses of complexes **2** and **22** were performed by the analytical services of the School of Chemistry at the University of Glasgow.

2.9. Electronic spectroscopy

UV−Vis absorption spectrum of **22** was recorded on a Shimadzu UV−1800 spectrophotometer at the University of Glasgow.

References

1. M. Heras Ojea, V. A. Milway, G. Velmurugan, L. H. Thomas, S. J. Coles, C. Wilson, W. Wernsdorfer, G. Rajaraman and M. Murrie, *Chem. Eur. J.*, **2016**, *22*, 12839.
2. S. J. Coles and P. A. Gale, *Chem. Sci.*, **2012**, *3*, 683.
3. L. Palatinus and G. Chapuis, *J. Appl. Cryst.*, **2007**, *40*, 786.
4. G. Sheldrick, *Acta Crystallog. Sect. A*, **2008**, *64*, 112.
5. G. Sheldrick, *Acta Crystallog. Sect. C*, **2015**, *71*, 3.
6. O. V. Dolomanov, L. J. Bourhis, R. J. Gildea, J. A. K. Howard and H. Puschmann, *J. Appl. Cryst.*, **2009**, *42*, 339.
7. O. Kahn, in *Molecular Magnetism*, VCH Publishers, New York, **1993**.
8. R. L. Carlin, *Magnetochemistry*, Springer−Verlag, Berlin, Heidelberg, **1986**.
9. N. F. Chilton, R. P. Anderson, L. D. Turner, A. Soncini and K. S. Murray, *J. Comput. Chem.*, **2013**, *34*, 1164.
10. Y.-N. Guo, G.-F. Xu, Y. Guo and J. Tang, *Dalton Trans.*, **2011**, *40*, 9953.
11. W. Wernsdorfer, *Adv. Chem. Phys.*, **2001**, *118*, 99.
12. M. Heras Ojea, G. Lorusso, G. A. Craig, C. Wilson, M. Evangelisti and M. Murrie, *Chem. Commun.*, **2017**, *53*, 4799.

Chapter 3

Contents

3. Promoting single−molecule magnet properties in a 3*d*/3*d*' butterfly family

As discussed in previous sections, the use of building blocks (BB) as a tool for the rational design of heterometallic complexes directs and promotes to some extent certain magnetic properties (*e*. *g*. SMM behaviour).[1, 2] The most common synthetic approach towards heterometallic SMMs based on the use of BB could be described as the combination of two processes: 1) predesign of the metallo−ligand, and 2) subsequent assembly of a secondary metal ion (different to that used for the metallo-ligand).

However, this strategy is not so simple, and several factors must be considered to truly control the assembly process. For example, the ligand should preferably provide the precursor a moderately high robustness in order to maintain the structure in solution when being combined with another metal ion. Another important factor to consider is which geometry the ligand can promote around the metal ion. The use of multinucleating ligands with two or more unequivalent coordination environments as potential SMM precursors have been extensively investigated due to the capability to act as metallo−ligand acceptors of various metal centers.[2-6] The tendency of bis−tris propane ligand (H_6L) for chelating metals in the inner $\{N_2O_2\}$ pocket displayed in previous reported examples makes it a very attractive candidate for the synthesis of “ligand complexes”.[7, 8] The choice of the metal involved in this type of pseudo−rational approach also plays a key role, as it mainly defines the magnetic properties of the BB. Within the first row of the transition metals, Mn(III), Co(II) and Ni(II) ions have been widely used in the preparation of metallo−organic precursors due to their relatively high magnetic anisotropy derived from zero−field splitting or SOC effects.[9-15] Regarding the step related to the association of the BB with secondary metal ions, the experimental conditions should be carefully defined to get topological control of the polynuclear systems. The choice of solvent is, for example, important, since some of them can act as additional bridging ligands (*e.g*. CH_3OH).

In terms of polynuclear topology, the butterfly−like arrangement has been commonly observed in transition metal complexes.[16-20] Butterfly complexes, sometimes described as incomplete double−cubanes, take the name from the disposition of the metal ions and the bridging ligands that form the metal core. Schemes depicting the butterfly assembly in $\{M1_2M2_2(OR)_2\}$ and $\{M1_2M2_2(OR)_6\}$

tetranuclear systems are shown in Fig 3.1. The bridging groups defined as OR are usually oxo or hydroxide groups, but there are some reported examples with different bridging atoms.[21, 22] The positions occupied by the metal ions defined as M1 (shown in blue) have been defined as the "wing site" of the metal core, and the ones occupied by M2 (in green) as the "body site".[19, 23] In the case of heterometallic compounds, pairs of different metal ions are located in these wing/body positions.

As there are numerous reported examples in the literature, butterfly systems have been the subject of several magneto−structural studies looking for a better understanding of some key parameters in magnetism, such as the nature of the magnetic exchange between different metals atoms.[18, 20] A search based on the structures reported in the Cambridge Structural Database (CSD 5.37, April 2017) reveals that there are 257 structures with a comparable $\{M_4(OR)_6\}$ core to that one displayed in Fig 3.1 (M = 1st row transition metal ion), with Mn being one of the most popular elements (92 hits). However, it must be noted that this butterfly arrangement is not so common for heteronuclear complexes, as only 26 of the 257 structures contain at least two different transition metal ions, most of them showing a $\{M1_2M2_2(OR)_6\}$ assembly (see Fig 3.1, right).[24-28]

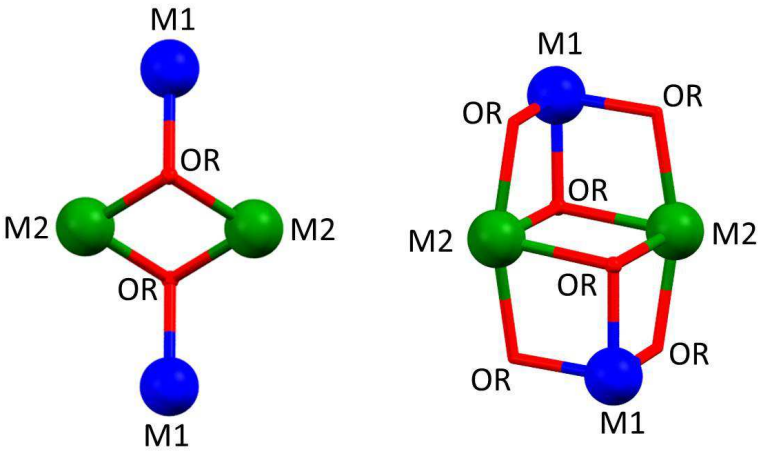

Fig 3.1 Schemes illustrating the "butterfly" topology for systems with formula $\{M1_2M2_2(OR)_2\}$ and $\{M1_2M2_2(OR)_6\}$.

Herein the synthesis and magneto−structural analysis of a family of $\{Mn_nM_2\}$ butterfly−like complexes are discussed. A rational bottom−up approach based on the combination of two novel 3*d*−building blocks ($[Ni(H_6L)]Cl_2$ (**1**) and $[Cu_2(H_5L)_2(CH_3COO)_2]$ (**2**)) with different manganese salts successfully leads to the synthesis of a new family of heterometallic complexes: $[Mn_2Ni_2(OH)_2(H_3L)_2(H_2O)_2]Cl_2\cdot 6H_2O$ (**3**), $[Mn_2Cu_2(CH_3O)_2(H_3L)_2(CH_3COO)_2]\cdot 2CH_3OH$ (**4**), and

$[Mn_2^{III}Mn^{II}Cu_2O(HCOO)(H_4L)(H_2L)(CH_3COO)_3]\cdot 4.5CH_3OH\cdot 3.5H_2O$ (**5**). Static and dynamic magnetic measurements performed on **3** and **4** reveal that the metallo−organic precursor plays a key role in tailoring the magnetic properties of the different complexes. Therefore by replacing the Ni(II) ions by Cu(II) ions we were able to control the M···M interactions, going from antiferromagnetic coupling in $\{Mn_2Ni_2\}$ to induce a $\{Mn_2Cu_2\}$ SMM. It has also been observed that the use of co−ligands (such as $HCOO^-$) causes topological alterations, and therefore modifies the magnetic properties seen for the Mn/Cu system.

3.1. Synthesis

Note: Complex **1** was synthesised and characterised by SXRD by Dr. Victoria A. Milway. Interpretation and data analysis, however, was performed as part of this PhD thesis.

$[Ni(H_6L)]Cl_2$ (**1**): $NiCl_2 \cdot 4H_2O$ (5.72 g, 24 mmol) and H_6L (5.80 g, 21 mmol) were combined in EtOH (100 mL) and heated to ~70°C for 6 h, then cooled slowly and stirred at ambient temperature overnight. The resulting mixture was filtered, yielding **7** as a pale purple precipitate. Yield (precipitate) 79% (7.88 g). Crystals grow by slow evaporation of a methanolic solution of the precipitate over several days. Elemental analysis of the precipitate ($[Ni(H_6L)]Cl_2$) [%], found: C, 32.10; H, 6.39; N, 6.73; calc: C, 32.07; H, 6.36; N, 6.80. IR: $\bar{\upsilon}$ (cm^{-1}) = 3374, 3070, 1458, 1298, 1064, 999, 945, 706, 662.

$[Cu_2(H_5L)_2(CH_3COO)_2]$ (**2**): $[Cu_2(CH_3COO)_4(H_2O)_2]$ (3.66 g, 9.17 mmol) was added to a white suspension of H_6L (2.32 g, 8.20 mmol) in EtOH (60 mL), and immediately dissolved, resulting in a dark blue solution. The solution became a suspension after stirring overnight at room temperature. The precipitate was filtered, washed with EtOH and dried with Et_2O. Yield 92% (4.48 g). IR: $\bar{\upsilon}$ (cm^{-1}) = 3111, 2880, 1570, 1400, 1330, 1049, 1020, 881, 656. Elemental analysis ($[Cu_2(H_5L)_2(CH_3COO)_2]$) [%], found: C 38.84, H 7.07, N 6.87; calc: C 38.66, H 6.99, N 6.94. MS (ESI^+, *m*/*z*): 345 $[Cu(H_5L)]^+$, 366 $[Cu(H_4L)Na]^+$, 687 $[Cu_2(H_5L)(H_4L)]^+$ (see Fig 3.2).

$[Mn_2Ni_2(OH)_2(H_3L)_2(H_2O)_2]Cl_2 \cdot 6H_2O$ (**3**): Et_3N (0.14 ml, 1.00 mmol) and $Mn(ClO_4)_2 \cdot H_2O$ (0.14 g, 0.57 mmol) were consecutively added to a pale blue solution of $[Ni(H_6L)]Cl_2$ (0.21 g, 0.51 mmol) in MeOH (30 mL), and immediately dissolved, resulting in a brown solution. The solution was stirred and heated to 60°C for 3 h. Brown block−like single crystals suitable for X−ray diffraction were obtained by slow evaporation of the reaction solution over one week. Yield 71% (166 mg). IR: $\bar{\upsilon}$ (cm^{-1}) = 3242, 2943, 1653, 1427, 1084, 1028, 739, 691. Elemental analysis ($[Mn_2Ni_2(OH)_2(H_3L)_2(H_2O)_2]Cl_2 \cdot 4.5H_2O$) [%], found: C 26.05, H 5.92, N 5.40; calc: C 26.22, H 6.10, N 5.56.

$[Mn_2Cu_2(CH_3O)_2(H_3L)_2(CH_3COO)_2] \cdot 2CH_3OH$ (**4**): Et_3N (0.10 ml, 0.70 mmol) and $Mn(CH_3COO)_2 \cdot 4H_2O$ (0.09 g, 0.38 mmol) were consecutively added to a blue suspension of $[Cu_2(H_5L)_2(CH_3COO)_2]$ (0.17 g, 0.21 mmol) in MeOH (30 mL), and immediately dissolved, resulting in a dark brown solution. The solution was stirred

overnight at room temperature. Brown block−like single crystals suitable for X−ray diffraction were obtained by vapour diffusion of Et_2O into the reaction solution over ten days. Yield 68% (121 mg). IR: $\bar{\upsilon}$ (cm^{-1}) = 3241, 2843, 1570, 1417, 1333, 1040, 1022, 780, 695. Elemental analysis ($[Mn_2Cu_2(CH_3O)_2(H_3L)_2$-$(CH_3COO)_2]\cdot 0.25CH_3OH$) [%], found: C 34.05, H 6.35, N 5.27; calc: C 34.49, H 6.04, N 5.70.

$[Mn_2^{III}Mn^{II}Cu_2O(HCOO)(H_4L)(H_2L)(CH_3COO)_3]\cdot 4.5CH_3OH\cdot 3.5H_2O$ (**5**): The same synthetic procedure described for **4** was followed, but using $Mn(HCOO)_2\cdot H_2O$ instead of $Mn(CH_3COO)_2\cdot 4H_2O$. Brown plate−like single crystals suitable for X−ray diffraction were obtained by vapour diffusion of Et_2O into the reaction solution over one week. Yield 31% (57 mg). IR: $\bar{\upsilon}$ (cm^{-1}) = 3215, 2874, 1587, 1416, 1331, 1040, 1022, 766, 700. Elemental analysis ($[Mn_2^{III}Mn^{II}Cu_2O(HCOO)(H_4L)$-$(H_2L)(CH_3COO)_3]\cdot 0.5CH_3OH\cdot 0.25H_2O$) [%], found: C 32.04, H 5.71, N 5.45; calc: C 31.94, H 5.32, N 5.05.

3.2. Results and discussion

The reaction between the polydentate ligand H_6L and different MX_2 salts (M = Ni(II), Cu(II); X = Cl^-, CH_3COO^-) allowed the synthesis of the complexes $[Ni(H_6L)]Cl_2$ (**1**) and $[Cu_2(H_5L)_2(CH_3COO)_2]$ (**2**). Both compounds are isolated in good yield as precipitates (79% and 92% respectively). Thin purple plate−like crystals of **1** were obtained by slow evaporation from a methanolic solution. Several experiments were performed in order to obtain crystals of **2**. Unfortunately, none of the attempts gave crystals suitable for the structural determination of **2** by single−crystal X−ray diffraction. Characteristic bands related to acetate anions were observed in the IR spectrum of **2** (υ(C=O) = 1570 cm^{-1}, υ(C−O) = 1400 cm^{-1}) in addition to those ones associated to the H_6L ligand, proving that compound **2** contains acetates.[29] To investigate if the acetates are in the ionic form (acting as counterions), or if they are coordinated to the Cu(II) ions, an analysis of the coordination modes of acetates based on the studies developed by Deacon and Philips were performed.[29, 30] These studies classify the different modes of the acetate anions by calculating the *Δ* value, which is defined as the difference between υ(C=O) and υ(C−O) stretching frequencies. The *Δ* value for **2** is equal to 170 cm^{-1}, which means that acetate anions are acting as bridges between the Cu(II) ions (see scheme depicted in Fig 3.2, left). Therefore the conclusions extracted from the IR are consistent with the molecular formula proposed from the elemental analysis results (*i.e*. $[Cu_2(H_5L)_2(CH_3COO)_2]$). Additional Electrospray Ionisation mass spectroscopy (ESI−MS) of **2** was performed to check the composition of the complex in solution (MeOH). Most of the peaks displayed in the ESI^+ spectrum (see Fig 3.2, right) were assigned considering the molecular weight and the charge of the potential cations which could be present in solution after some fragmentation processes. The tendency of H_6L for encapsulating Cu(II) ion in [4] to [4+2] coordination environments was also take into account.[7, 8] The spectrum presents a major molecular peak consistent with the cationic species $[Cu_2(H_5L)(H_4L)]^+$ at *m*/*z* = 687, which has a different assembly from the formula previously proposed due to the lack of the bridging acetate anions. The fragmentation of the Cu−acetate bonds in solution could promote the rearrangement of the $\{Cu(H_5L)\}$ units, and then the formation of the $[Cu_2(H_5L)(H_4L)]^+$ cation (see assignment in Fig 3.2). The spectrum also present peaks related to a metallo−organic monomeric species previously observed in copper complexes of H_6L (*e.g*. $[Cu(H_5L)]^+$ at *m*/*z* = 345).[7, 8] It is worth noting that the fact that the base peak seen in the spectrum does not correspond to the molecular ion highlights the fragility of the complex in solution, even with such a

soft ionisation technique as ESI−MS. Additional variable−temperature magnetic susceptibility experiments performed on **2** also support the formation of a copper dimer in accordance with previous characterisation techniques (see Fig A3.1 of the Appendix for details). Therefore, $[Cu_2(H_5L)_2(CH_3COO)_2]$ is assumed as the molecular formula of **2**, as it is consistent with the results of the different characterisation techniques.

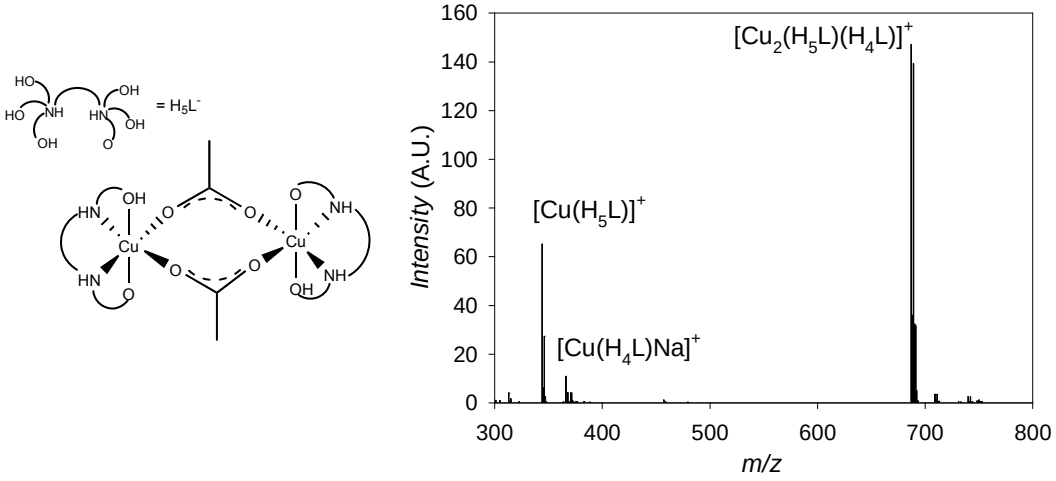

Fig 3.2 Proposed representation of the structure (left)[31, 32] and ESI^+ spectrum (right) of **2**.

The preparation of **1** and **2** is actually the first step of a strategy to direct the synthesis of heterometallic complexes by using a similar bottom−up approach to that one previously reported for other $3d$−$3d'$ polynuclear systems with H_6L.[8] The choice of Ni(II) and Cu(II) for synthesising the starting building blocks has been determined by structural and/or magnetic factors. The Cu(II) ion offers a wide variety of coordination environments (from [4] to [4+2]). Meanwhile the hexacoordinated Ni(II) ion provides magnetic anisotropy due to the ZFS parameter D, and could influence the resultant magnetic properties (since $\Delta E_{cal} = |D|S^2$). The combination of the Cu(II)/Ni(II) metallo−ligand precursors with different Mn(II)−metal salts under mild reaction conditions leads to the assembly of a family of new $\{Mn_nM_2\}$ "butterfly−like" systems (n = 2, 3; M = Ni, Cu). It was found that the final structure depends on the co−ligands present in the reaction media. Therefore the use of chloride, perchlorate and acetate salts promotes isostructural $\{Mn_2M_2\}$ alkoxide metal cores (M = Ni for **3**, and M = Cu for **4**), meanwhile the formate salt allows the formation of higher−nuclearity complexes (**5**). Nevertheless, the most interesting result related to these structural modifications is the dramatic difference in the final magnetic properties exhibited by the complexes. A complete

magneto−structural analysis is presented in the following sections to clarify the origins of the different magnetic behaviour.

X−ray crystallographic analysis

Selected crystallographic experimental details for complexes **1**, and **3** − **5** are shown in Table 3.2. Compound **1** crystallises in the triclinic space group *P*−1. The asymmetric unit of **1** contains one $[Ni(H_6L)]^{2+}$ cation and two Cl^- anions. The structure of **1** consists of a neutral H_6L ligand coordinated to one Ni(II) ion by four hydroxyl and two amine groups, giving a distorted octahedral environment (see Fig 3.3). The metal centre occupies the inner $\{N_2O_2\}$ pocket defining the equatorial plane of the octahedron, and two additional hydroxyl groups fill the axial positions. Two uncoordinated chloride anions balance the charge of the $[Ni(H_6L)]^{2+}$ cation. The average intramolecular Ni−N, Ni−O bond lengths are, respectively, $d_{(Ni-N)}$ = 2.056(1) Å, and $d_{(Ni-O)}$ = 2.071(9) Å.

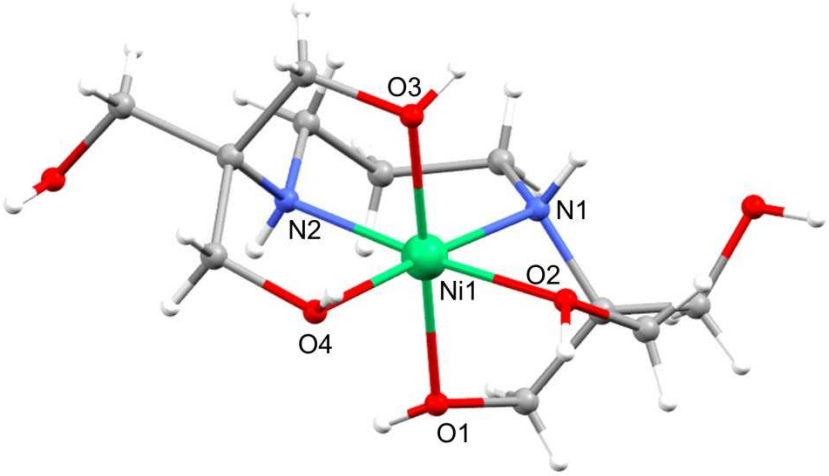

Fig 3.3 Structure of the cation of **1**. C, grey; H, white; N, blue; Ni, green; O, red. Only Ni and coordinating N, O atoms are labelled

Complex **3** crystallises in the monoclinic space group $P2_1/c$, meanwhile **4** crystallises in the triclinic space group *P*−1. The asymmetric unit of **3** contains a half cation of $[Mn_2Ni_2(OH)_2(H_3L)_2(H_2O)_2]^{2+}$, one chloride anion, and three molecules of water. On the other hand, the asymmetric unit of **4** contains a half molecule of $[Mn_2Cu_2(CH_3O)_2(H_3L)_2(CH_3COO)_2]$, and two half molecules of methanol. In order to further confirm the metal ratios obtained from the single−crystal X−ray crystallographic analysis, energy dispersive X−ray spectroscopy analysis (EDX) in bulk crystalline samples of complexes **3**−**5** were performed. The EDX spectra of **3**−**5** are shown in Figure 3.4. The Mn:M ratio found for **3** (M = Ni) and **4** (M = Cu) is

2:2 (with Avg. Atomic% being 2.88(30):2.86(31) for **3**, and 8.58(26):8.66(36) for **4**). The results are consistent with the Mn/M ratio established by single−crystal XRD for both complexes.

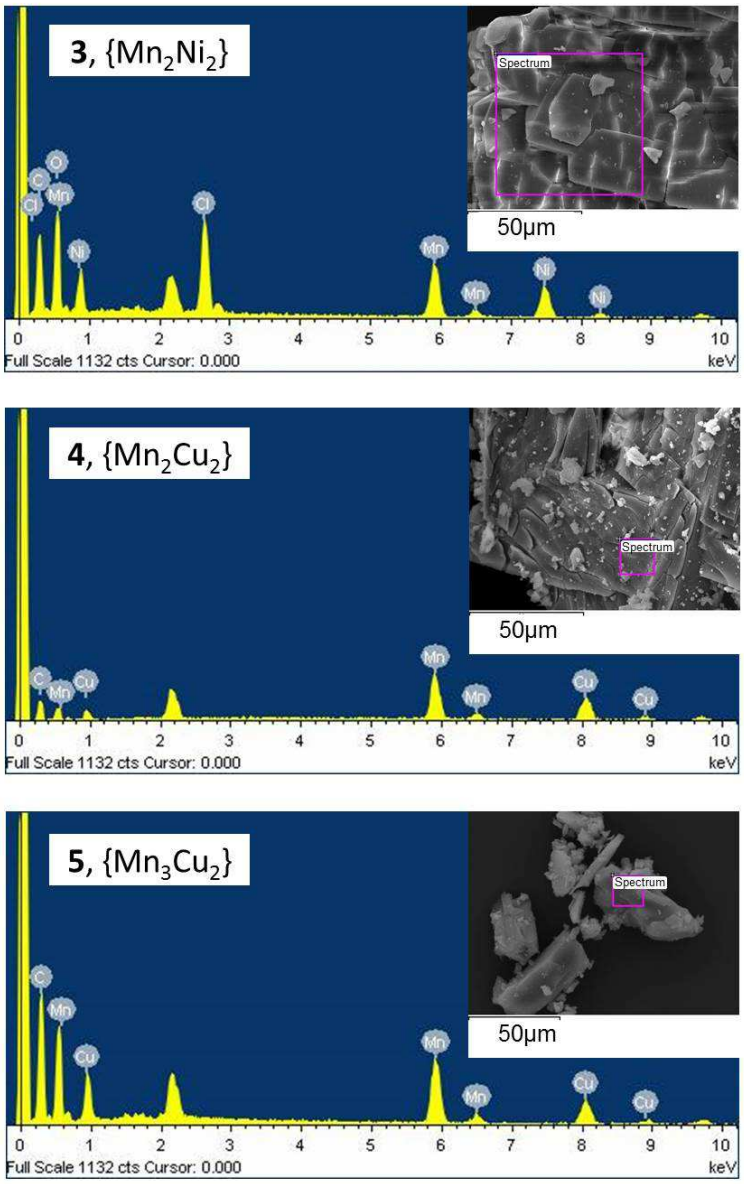

Fig 3.4 EDX spectra of **3**−**5**. The inset displays the area of the sample used for the analysis.

As previously commented, the topology displayed by **3** and **4** can be described as butterfly−like, with an heterometallic core comprised by two Mn(III) ions occupying the “body sites” and two Ni(II) or Cu(II) ions occupying the “wing sites”. Since **3** and **4** present an isostructural $\{Mn_2M_2O_6\}$ core, the following description of **3** is applicable to both structures. The main structural differences between **3** and **4** will be highlighted throughout the section. The structure of **3** contains two $\{Ni(H_3L)\}$ units and two Mn(III) ions (see Fig 3.5). Note that the octahedral Ni(II) ion still

occupies the central $\{N_2O_2\}$ pocket of the H_3L^{3-} ligand. However the apical OH−H_6L groups from the Ni(II) ion in **1** (Fig 3.3) have been replaced by a terminal water molecule and a bridging hydroxy group (μ_3−OH) in **3**. Each {Ni(H_3L)} unit is coordinated to two Mn(III) ions through one OH^- group and four oxygen atoms from the H_3L^{3-} ligand unit (only O110, highlighted in yellow in Fig 3.5, remaining protonated). In addition, the hexacoordinate Mn(III) ions are connected by two μ_3−OH groups.

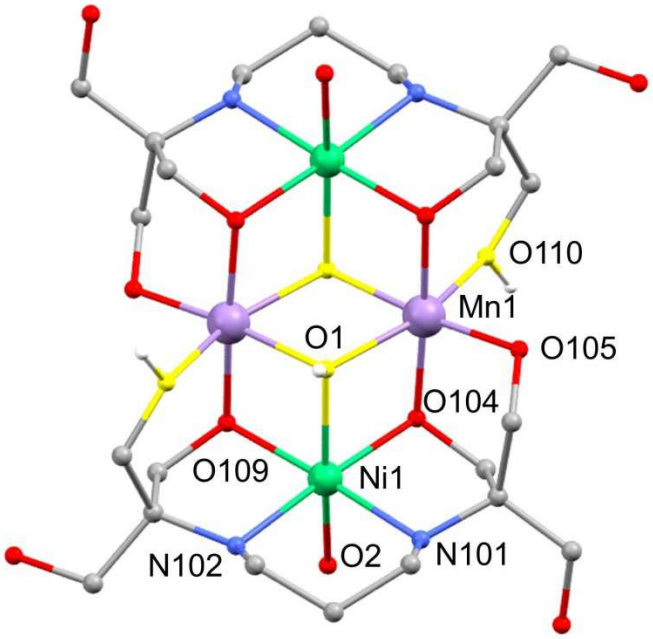

Fig 3.5 Structure of the cation of **3**. C, grey; Mn, lilac; N, blue; Ni, green; O, red; Hydrogen atoms (except those for O1, O110) and solvent molecules are omitted for clarity. Only crystallographically unique N, Ni and O atoms are labelled. O1, O110 atoms are highlighted in yellow.

The oxidation state of the manganese centre (Mn1) has been confirmed by bond length and charge balance considerations, and also by bond valence sum calculations (BVS).[33] The oxidation of the Mn(II) centres to Mn(III) could be due to the presence of an oxidising agent such as perchlorate, an excess of base, or even due to the aerobic conditions used during the synthesis. The characteristic Jahn−Teller effect related to some hexacoordinated 3*d* metals, such as high−spin d^4 Mn(III) ions, explains the distortion in the geometry of Mn1 and Mn1' in **3**. The metal alkoxide core of **3** is shown in Figure 3.6. The manganese centre Mn1 displays an elongated D_{4h} geometry, considering that two larger distances are observed (average $d^{eq}_{(Mn-O)}$ = 1.933(2) Å; $d^{ax}_{(Mn-O)}$ = 2.199(2) Å, 2.206(2) Å; see Table 3.1). These elongated JT axes exhibit a parallel orientation within the bridging plane defined by Mn1−O1···O1'−Mn1' (see Fig 3.6).

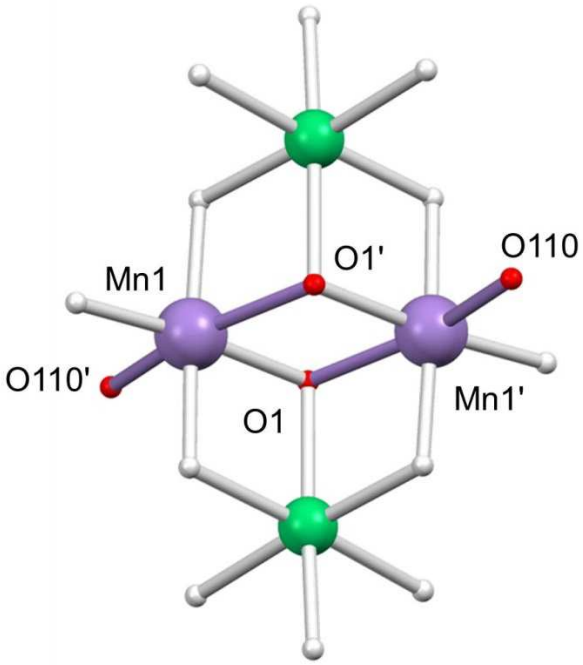

Fig 3.6 The metal alkoxide core of **3**. Only O, N, and Mn ions involved in the JT axes are labelled. JT axes are highlighted in lilac.

Table 3.1 Table with the corresponding Jahn−Teller axes (JT) for **3** and **4**.

JT axes/Complexes	**3**, $\{Mn_2Ni_2\}$	**4**, $\{Mn_2Cu_2\}$*
$d_{(Mn1-O1')}$	2.206(2) Å	−
$d_{(Mn1-O110')}$	2.199(2) Å	−
$d_{(Cu1-O1A)}$	−	2.377(4) Å
$d_{(Cu1-O1M')}$	−	2.425(4) Å

Note: see below explanation about the absence of Mn−O JT distances for **4.*

Regarding the $\{Mn_2Ni_2O_6\}$ core, all the Mn(III) and Ni(II) ions are in the same plane (see Fig 3.7) linked together by six oxygen atoms of two OH^- (O1, O1') and two H_3L^{3-} ligands (O104, O109, and their symmetry equivalents O104', O109'). The intramolecular distances between the different metal ions within this complex are $d_{(Ni\cdots Ni')}$ = 5.284(2) Å, $d_{(Mn\cdots Mn')}$ = 3.260(1) Å and $d^{Avg}_{(Mn\cdots Ni)}$ = 3.104(1) Å. The Mn−Ô−Mn angle is 101.8(9)°. On the other hand, two different Mn−Ô−Ni angles could be distinguished considering the nature of the oxygen bridge, displaying average values of $\alpha_{(Mn-\mu O-Ni)}$ = 102.2(4)° and $\alpha_{(Mn-\mu_3 O-Ni)}$ = 94.7(6)°. The average torsion angles defined by MnOONi and MnOOMn' are nearly 180° ($\theta_{(MnOONi)}$ = 179.9(1)° and $\theta_{(MnOOMn')}$ = 180.0(1)°), in good agreement with the co−planarity of the metal ions previously mentioned.

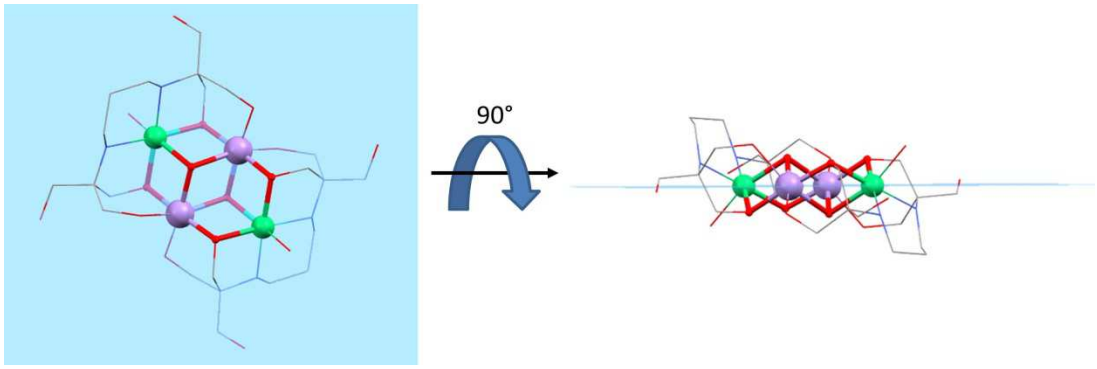

Fig 3.7 Structure of **3**. The blue plane shows the co−planarity of the metal ions within **3**. C, grey; Mn, lilac; N, blue; Ni, green; O, red.

In the case of $[Mn_2Cu_2(CH_3O)_2(H_3L)_2(CH_3COO)_2]\cdot 2CH_3OH$ (**4**), the replacement of the Ni(II) ions by two Cu(II) ions, and the substitution of the OH^- bridging ligands for CH_3O^- are the most notable structural differences, as the main $\{Mn_2Cu_2(H_3L)_2\}$ metal alkoxide core remains roughly identical to that described for **3** (see Fig 3.8). Consequently each H_3L^{3-} chelates one Cu(II) ion by the coordination of two N, and two O donor atoms. In addition, one terminal CH_3COO^- ligand and one CH_3O^- group fill the axial positions of each Cu(II) centre, leading to a Jahn−Teller distorted octahedral geometry. Since these two apical distances ($d^{ax}_{(Cu-O)}$ = 2.377(4) Å, 2.425(4) Å, see Table 3.1) are larger than the equatorial ones (average $d^{eq}_{(Cu-O/N)}$ = 2.000(1) Å), the octahedron is tetragonally distorted.

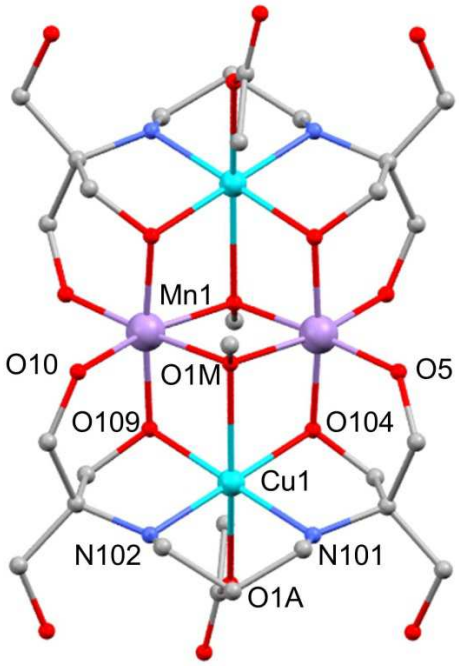

Fig 3.8 Structure of complex **4**. C, grey; Cu, turquoise; Mn, lilac; N, blue; O, red; Hydrogen atoms and solvent molecules are omitted for clarity. Only crystallographically unique Cu, Mn, N and O atoms are labelled.

It must be noted that the crystal structure of **4** presents a considerable disorder related to some of the alkoxo and hydroxo groups from the H_3L^{3-} ligands coordinated to the Mn(III) ions. For two of the arms of the H_3L^{3-} ligand there were clear signs of disorder of the oxygen sites (O5 and O10), each suggesting one oxygen position with a shorter Mn−O bond distance ($d_{(Mn-O5A)}$ = 1.898(7) Å, $d_{(Mn-O10A)}$ = 1.973(8) Å), and one position with a longer Mn−O bond distance ($d_{(Mn-O5B)}$ = 2.238(1) Å, $d_{(Mn-O10B)}$ = 2.264(10) Å). That is consistent with a deprotonated oxygen atom for the shorter Mn−O bonds (*i.e*. O-H_3L^{3-}) and a protonated oxygen atom for the longer Mn−O bonds (*i.e*. OH-H_3L^{3-}) in each case. Charge considerations mean that each of these need to be 50% occupied at each of the sites. Modelling of this disorder, in particular the deprotonated oxygen atoms, proved problematic with the Mn−O distance tending to unreasonably short values for a Mn(III) ion ($d_{(Mn-O)}$ < 1.81 Å). A distance restraint to the C−O bonds was applied resulting in more reasonable values but which limits the discussion of the detail of the Mn−O bonds, and thus the Jahn−Teller effect.

The intramolecular distances between the different metal ions in **4** are $d_{(Cu\cdots Cu)}$ = 5.442(9) Å, $d_{(Mn\cdots Mn')}$ = 3.146(1) Å and $d^{Avg}_{(Mn\cdots Cu)}$ = 3.143(4) Å. The angle between the manganese ions described by the methoxy group (Mn1−Ô1M−Mn1') is 100.2(2), whereas the rest of average Mn1−Ô−Cu angles are $\alpha_{(\mathrm{Mn-\mu O-Cu})}$ = 106.5(2)° and $\alpha_{(\mathrm{Mn-\mu_3 O-Cu})}$ = 88.9(2)°. The torsion angles defined by MnOOMn' and MnOOCu are again ~180° ($\theta_{(MnOOMn')}$ = 180.0(2)°, and average $\theta_{(MnOOCu)}$ = 178.6(2)°). The structural comparison of the {$Mn_2M_2O_6$} cores of **3** and **4** reveals that the substitution of Ni(II) ions for Cu(II) ions brings the Mn(III) ions closer together due to the elongation of the molecule along the axes in which Ni/Cu atoms are located (see Fig 3.9). That could be related to the elongation due to Jahn-Teller effect of the Cu(II) ions in **4**. Structural parameters that prove the elongation of the molecule from **3** to **4** are the average intramolecular Mn···M distances (*e.g*. $d_{(Mn\cdots Mn')}$ (**3**) = 3.260(1) Å > 3.146(1) Å = **4**; $d_{(Ni\cdots Ni)}$ = 5.284(2) Å < 5.442(9) Å = $d_{(Cu\cdots Cu)}$) and angles defined by the different metal ions (Mn−Ô−Mn (**3**) = 101.8(9)° > 100.2(2)° = **4**). Note that the structural changes caused by the use of a different metal precursor may modify the exchange interactions ($\mathcal{J}$) between M···Mn ions, since $\mathcal{J}$ is generally related to distances and angles. Therefore, the static and dynamic magnetic properties of the {Mn_2M_2} complexes can be also be affected by the distortions above discussed.

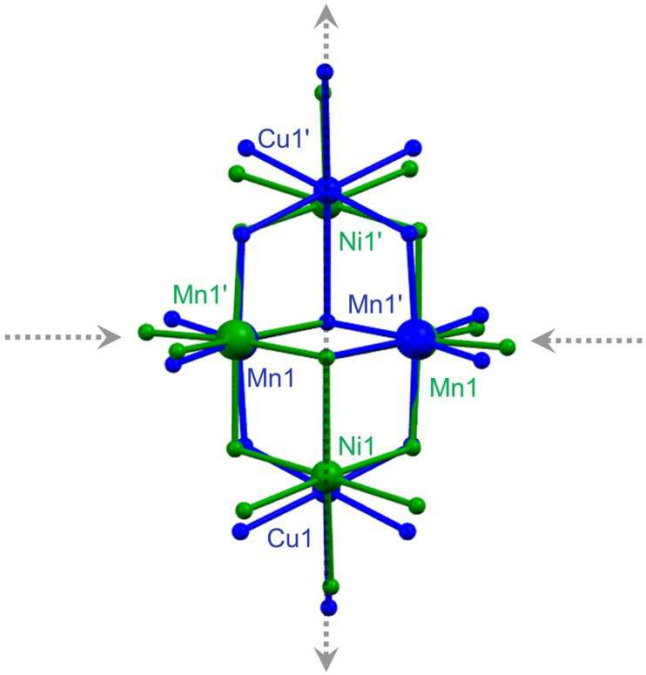

Fig 3.9 Overlay of the $\{Mn_2M_2O_6\}$ metal alkoxide core of **3** (M = Ni, green) and **4** (M = Cu, blue). Only metal ions are labelled.

The butterfly−like topology displayed in **3** and **4** is modified when additional potential coordinating co−ligands are present in the reaction media. Therefore, the use of formate salts leads to the formation of the higher nuclearity complex $[Mn_2^{III}Mn^{II}Cu_2O(HCOO)(H_4L)(H_2L)(CH_3COO)_3]\cdot 4.5CH_3OH\cdot 3.5H_2O$ (**5**), which could best be described as a $\{Mn_2^{III}Mn^{II}Cu\}$ cubane with an apical Cu atom (see structure in Fig 3.10). Although formate ions seem to play an important role in the synthesis of **5**, the presence of acetate ions is needed as they help to complete the coordination sphere of the Cu/Mn ions, bridge the different metal ions, and also balance the charge. Complex **5** crystallises in the triclinic space group *P*−1, with an asymmetric unit that consists of one molecule of $[Mn_2^{III}Mn^{II}Cu_2O(HCOO)(H_4L)$-$(H_2L)(CH_3COO)_3]$, 4.5 molecules of methanol, and 3.5 molecules of water. The Mn:Cu metal ratio found from the EDX analysis of **5** (3:2) is consistent with that established by single−crystal XRD (Avg. Atomic% Mn:Cu of 5.69(71):4.09(42); see Fig 3.4). The oxidation state of the manganese centres and the oxo group (O1) has been confirmed by bond length and charge balance considerations, and also by BVS.[33] The partial oxidation of the Mn(II) centres to Mn(III) could be due to an excess of base, or due to the aerobic conditions used during the synthesis. The structure contains two $\{Cu(H_xL)\}$ units (x = 2, 4) coordinated in two different environments (see Fig 3.10, 3.11). As a result, Cu1 is chelated by two O and two N donor atoms from one doubly deprotonated H_4L^{2-} unit, and one O atom from a

$HCOO^-$ ligand in a pentacoordinate geometry. In order to investigate the geometry of Cu1, the parameter τ has been calculated. The τ parameter specifies the degree of distortion of the square−pyramidal geometry in five−coordinate structures considering their basal angles (see Fig A3.2 of the Appendix).[34] Therefore, a τ value near zero is associated with a square−pyramidal environment, whereas τ close to unity is related to a trigonal−bipyramidal environment. As the τ parameter is τ_{Cu1} = 0.09, the geometry of Cu1 is described as square−pyramidal. In contrast, Cu2 is coordinated by two O and two N atoms from one tetradeprotonated H_2L^{4-} unit, one $HCOO^-$ and one CH_3COO^- in an elongated octahedral arrangement (average $d^{eq}_{(Cu-O/N)}$ = 1.980(2) Å; $d^{ax}_{(Cu-O)}$ = 2.529(5) Å, 2.455 (4) Å). Note that the bidentate formate ligand also acts as a link between the different Mn(III)/Cu(II) ions (see Fig 3.10, Fig 3.11). It is worth noting that the binding mode displayed by the bridging formate it has been previously observed between *s*-block and 3d ions, however, there is no reported structures showing such coordination mode between 3d/3d' ions (CSD 5.37, April 2017).

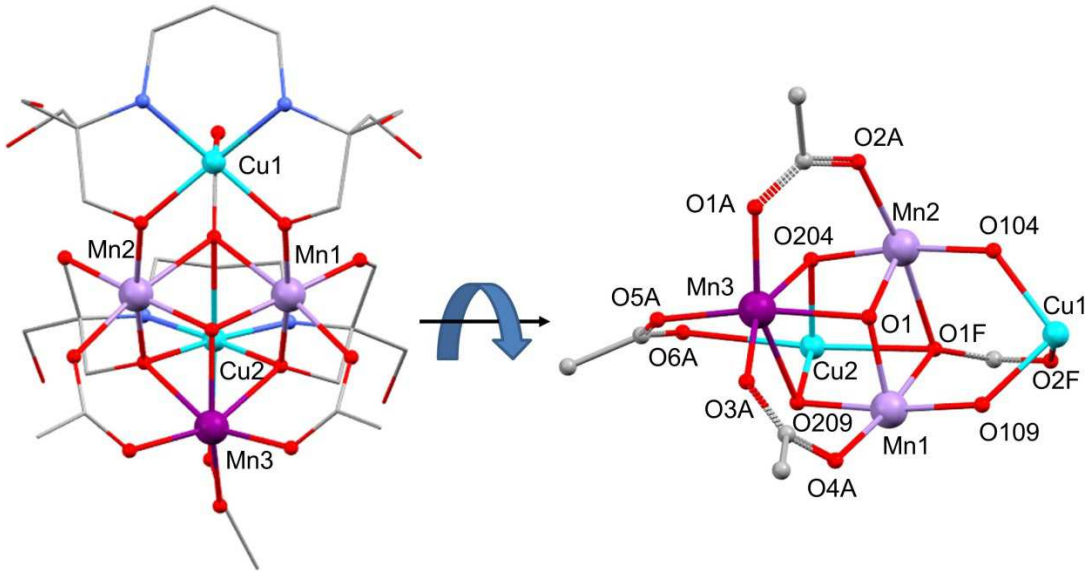

Fig 3.10 Structure (left) and detail (right) of **5**. C, grey; Cu, turquoise; Mn(II), purple; Mn(III), lilac; N, blue; O, red. Hydrogen atoms and solvent molecules are omitted for clarity.

The coordination of these {Cu(H_xL)} units to the Mn(III/II) ions, along with three acetates, one formate and one oxo group, provides an octahedral geometry around the Mn centres (see Fig 3.10, 3.11). Therefore, the {Cu1(H_4L)} unit is linked to the Mn(III) ions by two μ_3−O(H_4L^{2-}) atoms. On the other hand, the {Cu2(H_2L)} unit is linked to two Mn(III) ions and one Mn(II) ion by two μ_3−O(H_2L^{4-}). The Mn(II) ion (Mn3) is also bonded to three bidentate μ−CH_3COO^- anions (that linked to Mn1 and Mn2), and one μ_3−O^{2-} atom (which bridge the three Mn(II/III) ions). The Mn(III)

centres are also linked each other by the formate anion (O1F). Both Mn(III) ions displays a tetragonally elongated geometry as was seen in **3** (average $d^{eq}_{(Mn1-O)}$ = 1.920(3) Å, $d^{ax}_{(Mn1-O)}$ = 2.219(5) Å, 2.371 (5) Å for Mn1; average $d^{eq}_{(Mn2-O)}$ = 1.920(3) Å, $d^{ax}_{(Mn2-O)}$ = 2.161(5) Å, 2.417(5) Å for Mn2). However, the JT axes exhibit an anti−parallel alignment within **5** (81.8(1)°; see Fig 3.11).

As commented above, **5** can be defined as an heterometallic $\{Mn_2^{III}Mn^{II}Cu\}$ cubane (Mn1, Mn2, Mn3, Cu2) with an apical Cu atom (Cu1). Consequently the analysis of certain structural parameters, such as distances, angles and/or torsions between metal ions is made by distinguishing both units. Firstly the cubane unit parameters will be described, and later on those related to Cu1. The average intramolecular distances between the different metal ions within the $\{Mn_2^{III}Mn^{II}Cu\}$ cubane (see Fig 3.11) are $d_{(Mn\cdots Mn')}$ = 3.147(1) Å and $d_{(Mn\cdots Cu2)}$ = 3.219(1) Å. The range of the M−Ô−M' angle values within the cubane is relatively wide (from 81.8(1)° to 112.9(2)°). The Mn−Ô−Mn' angles where the bridging atom is the oxo group O1 display the largest values ($\alpha_{MnO1Mn'}$ = 104.2(2)–112.9(2)°), while the other ones are smaller and tend to be close to 90° ($\alpha_{MnOMn'}$ = 81.8(1)–93.2(2)°). Furthermore, the angles defined by Mn−Ô−Cu2 (see β_{MnOCu2} in Fig 3.11) range from 82.2(1)° to 109.7(2)°. In contrast, the torsion angles do not display any particular tendency that must be highlighted (θ_{MnOOM} = 177.0(2)–151.6(2)°, M = Mn', Cu2).

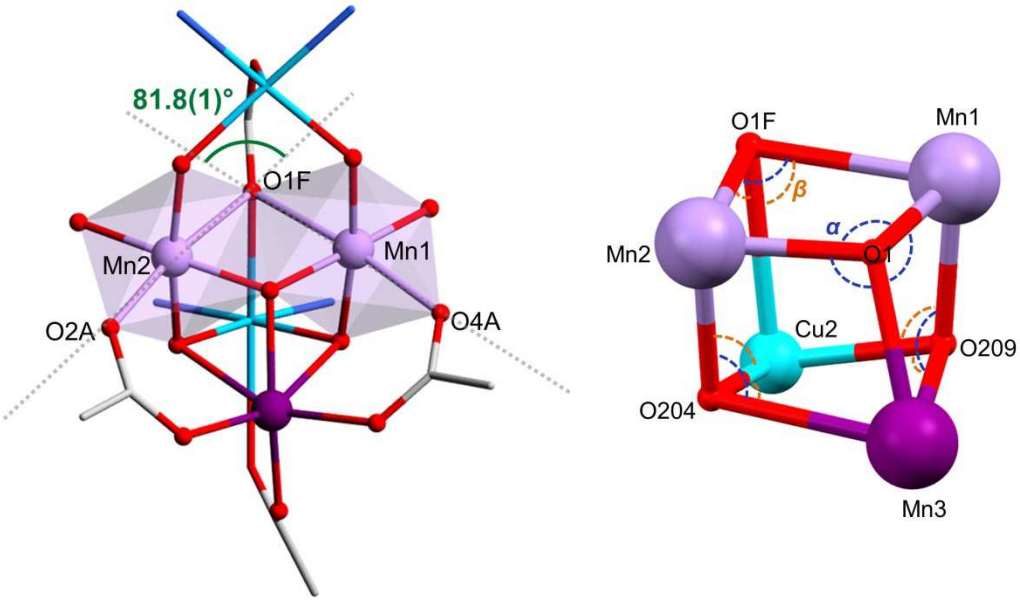

Fig 3.11 Detail of the metal alkoxide core (left) and the $\{Mn_2^{III}Mn^{II}Cu\}$ cubane unit (right) of **5**. C, grey; Cu, turquoise; Mn(II), purple; Mn(III), lilac; N, blue; O, red. JT axes and polyhedra around Mn(III) ions are highlighted in lilac.

Regarding the apical Cu1, the average intramolecular distance between Cu1 and the Mn(III) ions is $d_{(Mn\cdots Cu1)}$ = 3.484(1) Å, whereas the distance between Cu1 and Mn(II) is $d_{(Mn3\cdots Cu1)}$ = 5.637(1) Å. Moreover, the two copper ions Cu1, Cu2 linked by the formate anion are 5.511(1) Å apart. The average angle defined by Mn−Ô−Cu1 equal to 126.8(2)° (where Mn = Mn1, Mn2) is larger than those displayed within the cubane ($\alpha_{MnOMn'}$, β_{MnOCu2}).

In order to study the relationship between the structural alterations of the $\{Mn_nM_2\}$ metal core (M = Ni, Cu; n = 2, 3) caused by the use of different transition metals and co−ligands and the magnetic properties of the different systems, static and dynamic magnetic studies were carried out (see next section).

Table 3.2 Crystal Data and Structure Refinement Parameters of Complexes **1**−**5**.*

Complex	**1**	**3**	**4**	**5**
T/K	100(2)	100(2)	100(2)	100(2)
Crystal system	triclinic	monoclinic	triclinic	triclinic
Space group	*P*−1	$P2_1/c$	*P*−1	*P*−1
a/Å, *b*/Å, *c*/Å	6.7554(4), 7.2610(4), 17.5835(11)	11.693(5), 7.703(4), 21.581(9)	9.5928(6), 10.0314(6), 12.5120(7)	9.7076(7), 15.4508(11), 20.1377(14)
α/°, *β*/°, *γ*/°	97.250(3), 94.537(3), 96.841(3)	90, 95.474(12), 90	91.763(3), 106.974(3), 114.480(3)	105.743(7), 100.833(6), 93.978(6)
V/Å^3	845.61(9)	1935.0(15)	1032.00(11)	2832.1(4)
Z	2	2	1	2
ρ_{calc}/mg/m^3	1.618	1.776	1.673	1.518
μ/mm^{-1}	1.491	1.821	1.697	1.474
F(000)	432.0	1080.0	542.0	1347.0
2*θ* range for data collection	2.346 to 64.92°	3.5 to 50.222°	4.53 to 50.04°	5.138 to 54.992°
Index ranges	$-10 \le h \le 10$, $-10 \le k \le 10$, $-25 \le l \le 26$	$-13 \le h \le 13$, $-9 \le k \le 9$, $-18 \le l \le 25$	$-11 \le h \le 11$, $-11 \le k \le 11$, $-14 \le l \le 14$	$-12 \le h \le 12$, $-19 \le k \le 20$, $-26 \le l \le 17$
Reflections collected	31814	33391	32560	34515
Data/restraints/parameters	5637/4/217	3432/14/291	3624/242/286	12783/747/657
GOF on F^2	1.041	1.115	1.051	1.100
Final *R* indexes [$I \ge 2\sigma(I)$]	R_1 = 0.0277, wR_2 = 0.0709	R_1 = 0.0369, wR_2 = 0.0912	R_1 = 0.0634, wR_2 = 0.1448	R_1 = 0.0839, wR_2 = 0.2214
Final *R* indexes [all data]	R_1 = 0.0312, wR_2 = 0.0727	R_1 = 0.0451, wR_2 = 0.0967	R_1 = 0.0827, wR_2 = 0.1595	R_1 = 0.1120, wR_2 = 0.2419
Largest diff. peak/hole/e Å^{-3}	0.55/−0.47	0.46/−0.41	2.40/−1.43	1.80/−1.29

*__1__: $[Ni(H_6L)]Cl_2$; __3__ : $[Mn_2Ni_2(OH)_2(H_3L)_2(H_2O)_2]Cl_2 \cdot 6H_2O$; __4__: $[Mn_2Cu_2(CH_3O)_2(H_3L)_2(CH_3COO)_2] \cdot 2CH_3OH$; __5__: $[Mn_2^{III}Mn^{II}Cu_2O(HCOO)(H_4L)(H_2L)(CH_3COO)_3]$

Magnetic properties

The variable−temperature magnetic properties of **3**−**5** were investigated in an applied field of 1000 Oe. The variable−field magnetisation of **3**−**5** were also studied in the applied field range of H = 0–5 T at constant temperature (T = 2, 4, 5 and/or 6 K). The experimental value of $\chi_M T$ at 290 K for **3** of 7.59 $cm^3 \cdot mol^{-1} \cdot K$ (see Fig 3.12, left) is slightly lower than the spin−only value expected for two isolated Mn(III) and two Ni(II) ions (8.00 $cm^3 \cdot mol^{-1} \cdot K$; S_{Mn} = 2, S_{Ni} = 1, g_{Mn} = g_{Ni} = 2), suggesting the presence of antiferromagnetic interactions. Below 290 K, the $\chi_M T$ value tends to decrease reaching a minimum of 0.45 $cm^3 \cdot mol^{-1} \cdot K$ at 2 K, consistent with an S = 0 ground state. The small experimental magnetisation values are due to the population of excited states near to the spin ground state (S = 0) as a consequence of the application of the external field. A simultaneous fit of the susceptibility and magnetisation data was performed using the program PHI,[35] considering the magnetic model displayed in Fig 3.12 (right) and by applying the spin Hamiltonian shown in Eq. 3.1. A term related to intermolecular interactions was also included, given consideration to the short intermolecular distances between Ni(II) ions (5.345(2) Å; see Fig 3.13). The g_{Mn}, g_{Ni} parameters were fixed at 1.97 and 2.15, respectively, during the fit. Note that g_{Mn} was fixed as 1.97 given consideration to the results obtained from the fit of the magnetic data for **4** (*vide infra*).

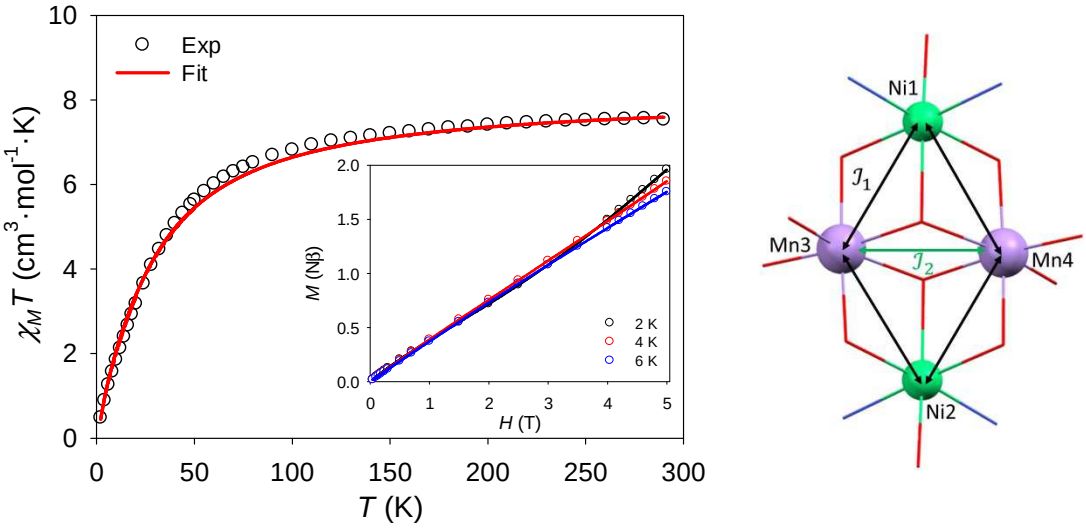

Fig 3.12 Left: Temperature dependence of $\chi_M T$ (in an applied field of 1000 Oe) and magnetisation *vs.* field at 2, 4 and 6 K (inset) for **3**. Solid lines correspond to the fit (see text for details). Right: Magnetic model used for the fit of **3**.

The best results (shown as solid lines in Fig 3.12) confirm the antiferromagnetic exchange coupling between Mn···Ni ($\mathcal{J}_1$ = −2.62 cm^{-1}) and Mn···Mn' ($\mathcal{J}_2$ = −2.08 cm^{-1}; *R* = 99.9%), and also the presence of ferromagnetic intermolecular interactions in the crystal structure (z$\mathcal{J}$' = 0.15 cm^{-1}).

Eq. 3.1 $$\hat{\mathcal{H}} = -2\mathcal{J}_1\left(\hat{S}_{Ni1}\cdot\hat{S}_{Mn3} + \hat{S}_{Ni1}\cdot\hat{S}_{Mn4} + \hat{S}_{Ni2}\cdot\hat{S}_{Mn3} + \hat{S}_{Ni2}\cdot\hat{S}_{Mn4}\right) - 2\mathcal{J}_2\left(\hat{S}_{Mn3}\cdot\hat{S}_{Mn4}\right) + g_{Ni}\mu_B\vec{B}\sum_{i=1}^{2}\vec{s_i} + g_{Mn}\mu_B\vec{B}\sum_{j=3}^{4}\vec{s_j}$$

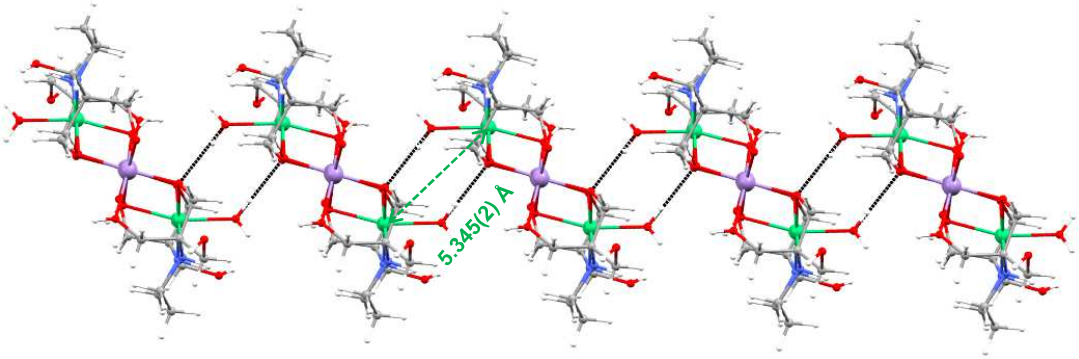

Fig 3.13 Intermolecular hydrogen bonding interactions (dashed black lines) in complex **3**. C, grey; H, white; Mn, lilac; N, blue; Ni, green; O, red. All the interactions involve $H_2O\cdots O(H_3L^{3-})$ hydrogen bonds. The displayed intermolecular Ni···Ni distance is 5.345(2) Å.

Studies based on Mn(III) dimers suggest that one of the determining factors of the nature of the magnetic interaction between metal ions is the alignment of their Jahn−Teller axes.[36, 37] The studies were undertaken by firstly classifying the Mn(III)−dimers in three types (I, II, or III) considering the alignment of the JT−axes with respect to one another, and also their orientation with the plane defined by {MnOOMn} (see Fig 3.14). The comparison of the coupling constant ($\mathcal{J}$) of the three families shows that complexes described as Type I, in which the JT axes are parallel to each other and aligned perpendicularly to the plane, show a clear antiferromagnetic tendency. On the other hand, Type II systems, in which the JT axes are aligned parallel within the plane, display a relatively wider range of values for the magnetic exchange (from ferro− to antiferromagnetic). It should be noted that although the alignment of the Jahn−Teller axes is an important factor, additional magneto−structural factors could also influence the nature of the magnetic interaction (*e.g*. coordination environment of the metal ions, angles and torsions, etc.). Although the complexes presented in this chapter are tetranuclear, the central $\{Mn_2(OR)_2\}$ unit is comparable to the manganese dimers and therefore, to some extent, the observed magneto−structural correlation between $\mathcal{J}$ and Jahn−Teller axes is applied. Hence, the value for the Mn···Mn' coupling suggested

by the fit ($\mathcal{J}_2$ = −2.08 cm^{-1}) is reasonable since complex **3** could be classified as Type II (*i.e*. the Jahn-Teller axes of the Mn(III) ions are parallel to each other within the plane). The proposed value is also consistent with that displayed for other similar reported structures (*i.e*. Mn−OH−Mn').[28, 38, 39] No additional alternating current (ac) magnetic susceptibility measurements were performed considering the *S* = 0 ground state of the complex.

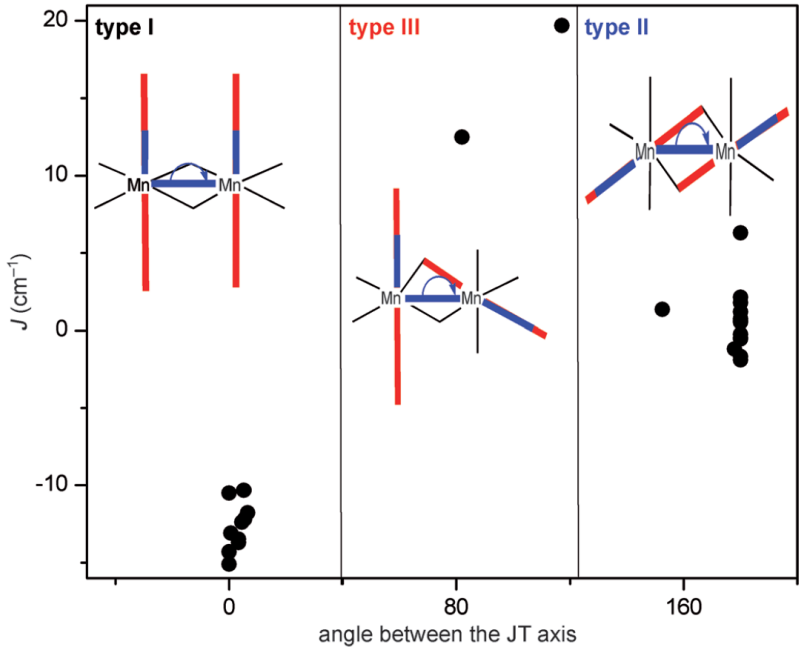

Fig 3.14 Scheme of the different types of Mn(III)−dimers (I, III and II) and plot of the exchange values ($\mathcal{J}$) *vs*. the angle between the Jahn−Teller axes within the dinuclear complexes. Figure taken from Ref. 36 (Copyright © 2012 by John Wiley Sons, Inc. Reprinted by permission of John Wiley & Sons, Inc.).

The replacement of the metallo-organic precursor in the synthesis of complex **4** (*i.e*. $[Cu_2(H_5L)_2(CH_3COO)_2]$ instead of $[Ni(H_6L)]Cl_2$) drastically changes the overall magnetic properties of the system (see Fig 3.15). The experimental value of $\chi_M T$ at 290 K for **4** (5.89 cm^3·mol^{-1}·K) is lower than the calculated spin−only value for two Mn(III) and two Cu(II) non−interacting ions (6.75 cm^3·mol^{-1}·K; S_{Mn} = 2, S_{Cu} = 1/2, g_{Mn} = g_{Cu} = 2). The low−temperature susceptibility product, however, display a different tendency compared to that previously shown by complex **3**. Therefore, the experimental $\chi_M T$ value slightly decreases with temperature from 5.89 cm^3·mol^{-1}·K to 5.02 cm^3·mol^{-1}·K at 75 K, then a gradual increase takes place until 18 K where the $\chi_M T$ value reaches 5.48 cm^3·mol^{-1}·K. Below 18 K the $\chi_M T$ product decreases to a minimum of 4.47 cm^3·mol^{-1}·K at 1.8 K. The displayed behaviour is characteristic of ferrimagnetically coupled complexes. The steady decrease of the experimental $\chi_M T$ values until 75 K is due to antiferromagnetic interactions within **4**, whereas that

observed below 18 K could be related to ZFS of the Mn(III) ions, or due to antiferromagnetic intermolecular interactions. It is worth noting that the replacement of the terminal H_2O molecules coordinated to the Ni(II) ions by CH_3COO^- groups set apart the molecules within the crystal lattice (thus increasing the Mn−M intermolecular distances) due to changes in the crystal packing (see Fig A3.3 in the Appendix). Therefore, the decrease of the susceptibility value at low temperatures is likely to be related to ZFS effects. Magnetisation *vs.* field plots show that the sample does not reach saturation at 2 K or 5 K (see inset Fig 3.15), which could be due to the magnetic anisotropy provided by the Mn(III) ions.

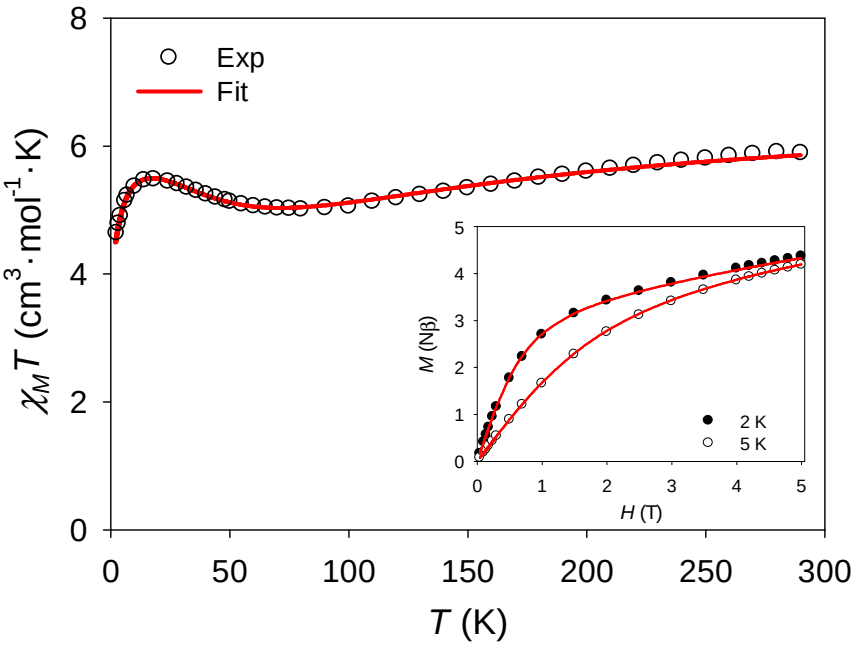

Fig 3.15 Temperature dependence of $\chi_M T$ (in an applied field of 1000 Oe) and magnetisation *vs.* field at 2 and 5 K (inset) for **4**. Solid lines correspond to the fit (see text for details).

The susceptibility and magnetisation data of **4** were simultaneously fit considering a similar magnetic model to that used in the fit of **3** (Fig 3.12, left). However, an additional term for the magnetic anisotropy of the Mn(III) ions was included in the spin Hamiltonian (see Eq 3.2) considering the changes observed in the static magnetic properties. The use of a rhombic contribution to the ZFS (E_{Mn}) is excluded to avoid overparameterisation. Different attempts to fit the magnetic data were performed in order to optimise the calculation. The variable term related to intermolecular interactions included in the fit of **3** was discarded, since the results propose an insignificant value (~10^{-5} cm^{-1}) and a null effect on the other parameters to be fitted (*i.e.* $\mathcal{J}$, d_{Mn}). The value for g_{Mn} was firstly included as a

variable parameter, giving 1.97. That g_{Mn} = 1.97 value was then included as a fixed term to simplify the model used in the final fit of the magnetic data. The best fit yields $\mathcal{J}_1$ = −17.6 cm^{-1} and $\mathcal{J}_2$ = 1.3 cm^{-1}, and the single−ion axial zero−field splitting (ZFS) parameter d_{Mn} = −3.04 cm^{-1} (99.9%). Note that the g_{Cu} = 2.11 parameter was fixed during the fit taking into account that one used in previous reported complexes presenting similar {Cu(H_6L)} environments.[7, 40] The results obtained from the fit are in good agreement with the ferrimagnetic tendency observed in the temperature dependence of $\chi_M T$ plot for **4**. The weak ferromagnetic coupling between Mn(III) ions is also comparable to that displayed for other similar {$Mn_2(OMe)_2$} structures.[41, 42] It is worth noting that the fit from **4** proposes a change in the nature of the Mn···Mn interaction, switching from weak antiferromagnetic coupling in **3** ($\mathcal{J}_2$ = −2.08 cm^{-1}) to weak ferromagnetic in **4** ($\mathcal{J}_2$ = 1.3 cm^{-1}). Also, the antiferromagnetic interaction described between Mn···M (M = Ni for **3**, Cu for **4**) becomes stronger. These different $\mathcal{J}$ values may be related to the structural changes discussed before (*i.e*. distances, angles). The replacement of Ni by Cu in the complexes promotes the elongation of the {$Mn_2M_2O_6$} core (*vide supra*) that may affect the different exchange interactions, and therefore the overall magnetic properties of the complexes.

Eq. 3.2 $$\hat{\mathcal{H}} = -2\mathcal{J}_1\left(\hat{S}_{Cu1}\cdot\hat{S}_{Mn3} + \hat{S}_{Cu1}\cdot\hat{S}_{Mn4} + \hat{S}_{Cu2}\cdot\hat{S}_{Mn3} + \hat{S}_{Cu2}\cdot\hat{S}_{Mn4}\right) - 2\mathcal{J}_2\left(\hat{S}_{Mn3}\cdot\hat{S}_{Mn4}\right) + g_{Cu}\mu_B\vec{B}\sum_{i=1}^{2}\vec{s_i} + g_{Mn}\mu_B\vec{B}\sum_{j=3}^{4}\vec{s_j} + d_{Mn}\sum_{i=1}^{2}\left(\hat{S}_{iz}^2 - \frac{1}{3}S_i(S_i+1)\right)$$

Given consideration to the ferrimagnetic tendency shown by **4**, the dynamic magnetic properties of **4** were investigated by ac susceptibility measurements as a function of the temperature (T = 2–10 K) in the absence and presence of an external field (H_{dc} = 2000 Oe) (see Fig A3.4 in the Appendix). The zero−field ac studies reveal the onset of a frequency−dependent out−of−phase component (χ''), suggesting the presence of quantum tunnelling (QTM). That is further confirmed by the appearance of peaks for the χ'' signal under the application of a 2000 Oe field. The effect of various field strengths on the dynamics was investigated in order to suppress the possible QTM (Fig A3.5 in the appendix). The out−of−phase susceptibility maxima were shifted to lower frequencies by applying an external dc field. However, no optimum field was found, suggesting the competition of multiple spin−reversal mechanisms (see Fig A3.5, right in the Appendix). Therefore ac susceptibility measurements were performed on **4** as a function of the frequency over the temperature range 1.8−7 K under selected external dc fields (500, 1000,

3000 Oe; see Fig 3.16) considering the local maximum observed around 2000 Oe (Fig A3.5 in the Appendix). Complex **4** displays frequency dependence of the out−of−phase signal related to slow relaxation of the magnetisation at temperatures below 5 K under the influence of an external field (Fig 3.16).

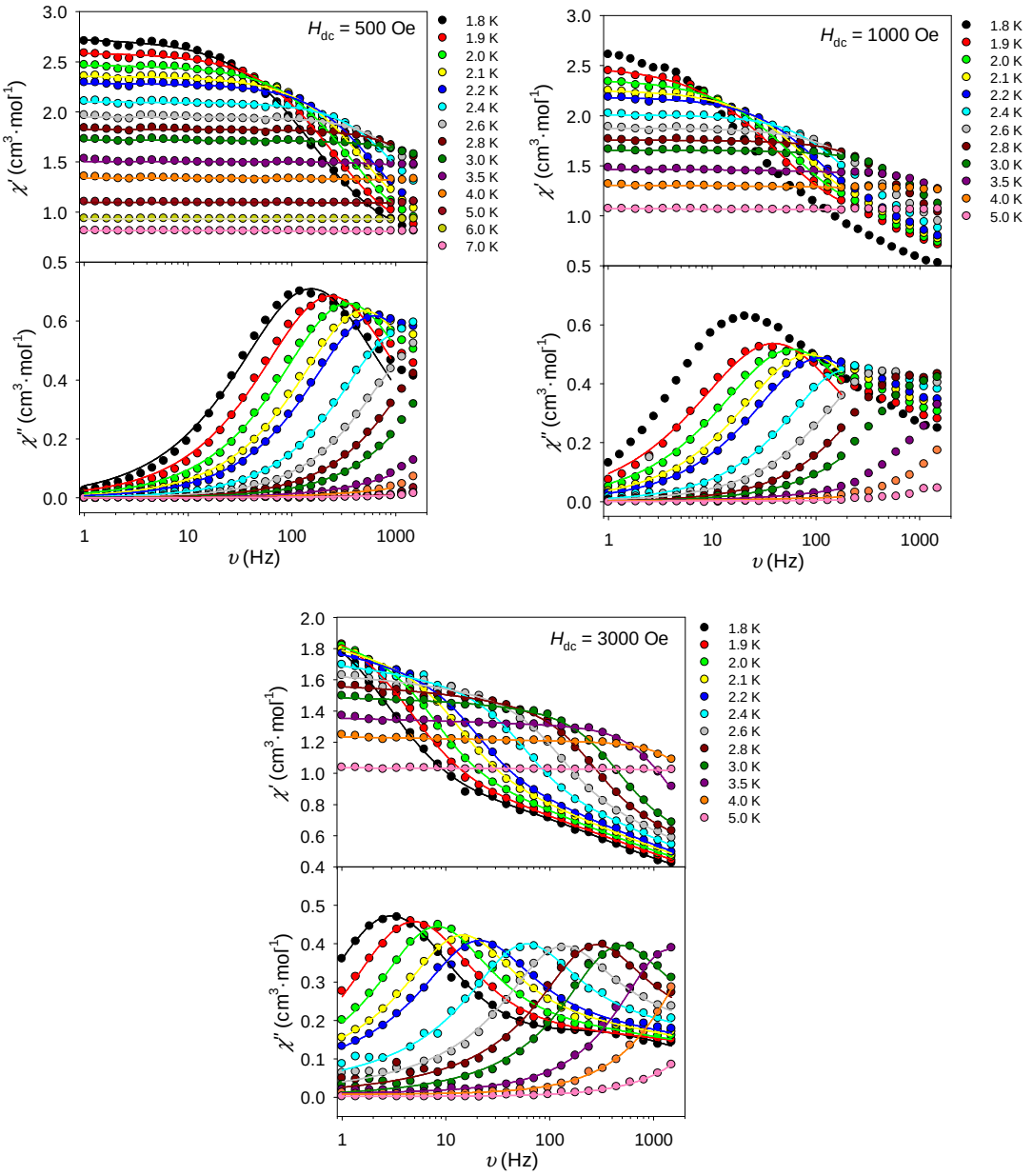

Fig 3.16 Ac magnetic susceptibility data of **4** at different frequencies in an applied field of 500 (top, left), 1000 (top, right) and 3000 Oe (bottom). The solid lines correspond to the fit (see text for details).

The Cole−Cole plots display dissimilar shapes at higher frequencies depending on the dc field applied, confirming that the relaxation occurs through more than one process (see Fig 3.17). Given that the Cole−Cole plots from the 500 and 1000 Oe data display a nearly symmetrical semi−circular shape, the ac susceptibility data

was fit to just one dominant relaxation process. Selected susceptibility data at high frequencies was also discarded due to the deviation from the semi−circular shape observed in the Argand plot, which could be related to secondary relaxation pathways (see Fig 3.17). The moderately wide distribution of the α parameters suggested by the fit of the experimental data ($0.26 < \alpha < 0.40$ for 500 Oe, and $0.26 < \alpha < 0.63$ for 1000 Oe) is consistent with multiple relaxation processes. The different relaxation times (τ) were treated using the Arrhenius law $\tau = \tau_0 \exp(\Delta E/k_B T)$, to extract the pre−exponential factor τ_0 and the energy barrier $\Delta E/k_B$ for 500 and 1000 Oe, yielding $\tau_0 = 1.6 \cdot 10^{-7}$ s (500 Oe), $3.6 \cdot 10^{-7}$ s (1000 Oe), and $\Delta E/k_B$ = 16.0 ± 0.3 K (500 Oe), 17.2 ± 0.2 K (1000 Oe) (see Fig 3.17). On the other hand, Cole−Cole plots from the 3000 Oe data clearly display the presence of two relaxation processes (see Fig 3.17): a single relaxation pathway dominant at higher temperatures, and a secondary pathway which becomes significant at low temperatures (and high frequencies). The Argand plots were then modelled considering a relaxation process with two time constants, τ_1 and τ_2. The extracted τ_2 values, however, do not look quite reliable, since they do certainly deviate from the Arrhenius behaviour. That may be a consequence of the lack of maxima in the experimental χ'' $vs.$ χ' plots related to this secondary process.

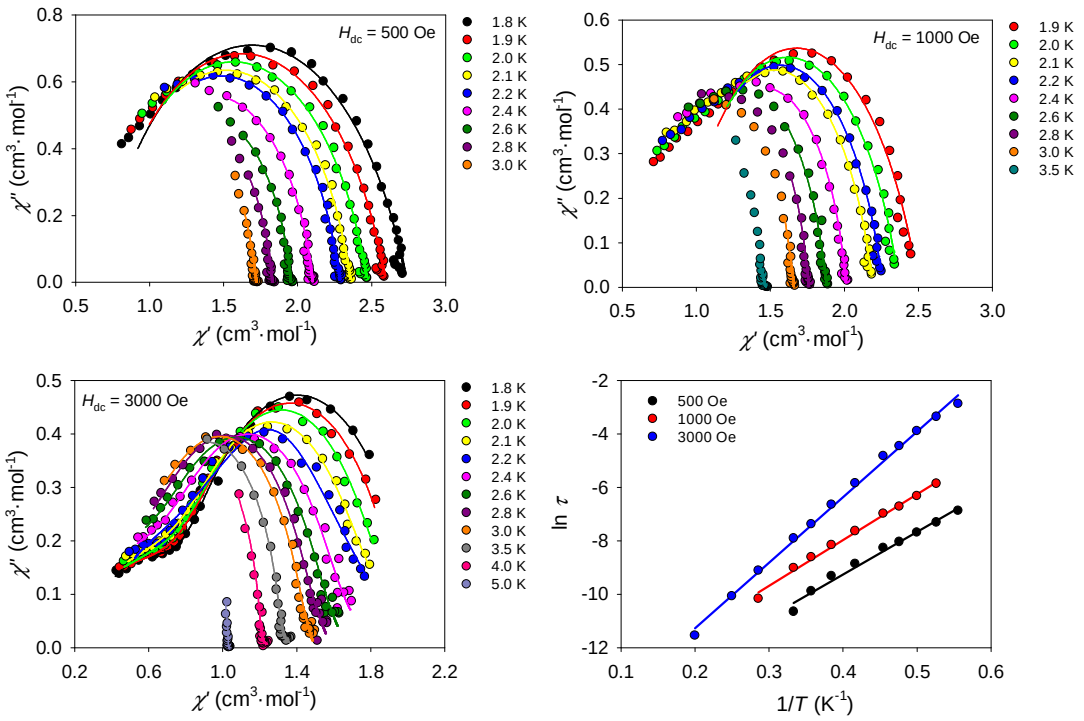

Fig 3.17 Cole–Cole plots and Arrhenius plot (bottom right) from the ac susceptibility data (different dc fields) of **4**. The solid lines correspond to the fit (see text for details).

Consequently only the pre−exponential factor and energy barrier parameters were calculated for the high−temperature dominant mechanism (0<*α*<0.18), yielding τ_0 = 9.4·10^{-8} s and $\Delta E/k_B$ = 24.5 ± 0.2 K. It must be stressed that the single relaxation time equation did not reproduce the experimental Cole-Cole plots, and thus was discarded as a possible model. Note that, to the best of our knowledge, there is only one reported complex containing Mn(III) and Cu(II) ions that displays SMMs features (CSD 5.37, April 2017).[43] In fact, the great majority of the reported complexes tend to be antiferromagnetically coupled, resulting in a small spin ground state and the absence of slow relaxation of magnetisation.

As previously discussed, the use of formate anions promotes the assembly of an additional Mn(II) metal ion to the {Mn_2Cu_2} metal core to form the pentanuclear compound **5**. Variable−temperature magnetic studies of **5** show that the structural alteration of the {$Mn_2M_2O_6$} moiety modifies the magnetic properties of the system again, by promoting the antiferromagnetic coupling within the system (see Fig 3.18). The room temperature $\chi_M T$ product (8.75 cm^3·mol^{-1}·K) is much lower than the expected spin−only value of 11.13 cm^3·mol^{-1}·K for two uncoupled Mn(III) ions, one Mn(II) and two Cu(II) (given $S_{Mn(III)}$ = 2, $S_{Mn(II)}$ = 5/2, S_{Cu} = 1/2, $g_{Mn(III)}$ = $g_{Mn(II)}$ = g_{Cu} = 2), suggesting the presence of relatively strong antiferromagnetic interactions within the compound. As the temperature drops, the $\chi_M T$ product decreases gradually reaching a minimum value of 2.40 cm^3·mol^{-1}·K at 1.8 K (see Fig 3.18).

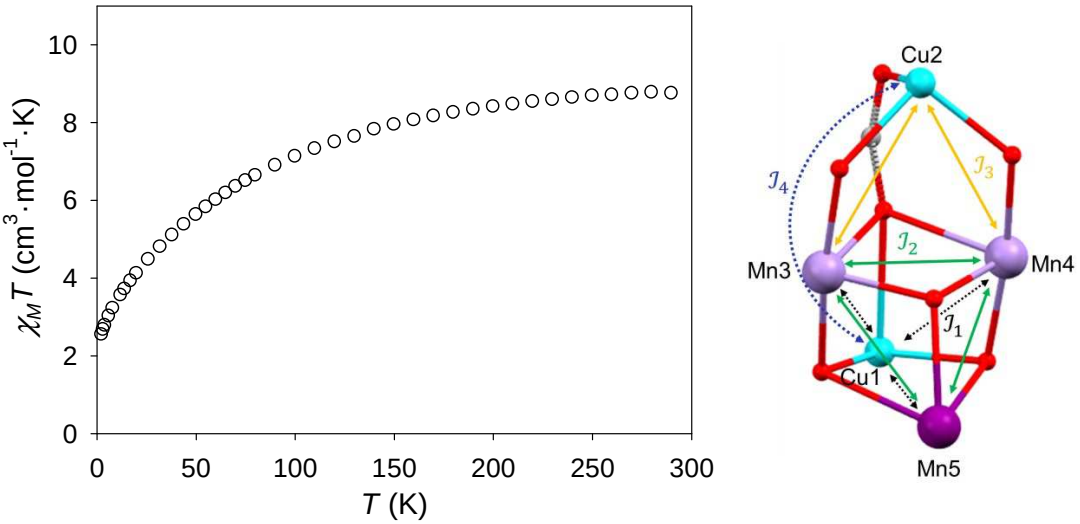

Fig 3.18 Temperature dependence of $\chi_M T$ (in an applied field of 1000 Oe) (left) and magnetic model proposed for the fit of the magnetic data for **5** (see text for details).

The variable−field magnetisation experiments (Fig A3.6 in the Appendix) confirm the main antiferromagnetic exchange between the different Cu/Mn centres seen in the susceptibility measurements, as the maximum experimental values at 2 and 5 K (2.98 and 2.76, respectively) are considerably smaller than the saturation of 15.24 (in a theoretical situation where S_{max} is achieved, considering g_{Avg} =2.032). Several attempts to model the magnetic data failed, either by not reproducing the tendency displayed by the experimental data, or by giving unreasonable results (*e*.*g*. $\mathcal{J} > 80$ cm^{-1}). Different magnetic models based on three or four exchange interactions (see model in Fig 3.18) were used, taking into account the structural differences formerly discussed. The different parameters to be adjusted (g, $\mathcal{J}$) were included as variable or as fixed terms, given consideration to the results obtained from previous fits (*i*.*e*. **3** and **4**). The addition of terms related to the single−ion ZFS of Mn(III) ions, intermolecular interactions, or to temperature-independent paramagnetism (TIP) to the model did not show any improvement in the fit. A more elaborate calculation strategy (*e*.*g*. DFT) is therefore needed in order to get a suitable analysis of the static magnetic data for **5**, since the system $\{Mn_2^{III}Mn^{II}Cu_2\}$ appears to be too complicated to be able to perform a fit by using a more simplistic software such as PHI. Hence, none of the fits for **5** were included in this report. Nevertheless, the fall in the $\chi_M T$ values with temperature, the small non−zero spin ground state at 1.8 K, and the maximum values of magnetisation at 5 T indicate a ferri− or antiferromagnetic tendency with a ZFS contribution of from the Mn(III) ions within the molecule.

Additional ac susceptibility experiments were performed on complex **5** to investigate whether the changes in the static properties compared to those shown by $\{Mn^{II}Mn_2^{III}Cu_2\}$ (**4**) have an effect on the dynamics of $\{Mn_2^{III}Mn^{II}Cu_2\}$ (**5**). The ac studies reveals a similar behaviour to that displayed for **4**, since a (weak) frequency dependent out−of−phase signal appears at zero-applied field and in H_{dc} = 2000 Oe, suggesting slow relaxation of the magnetisation in **5**, along with fast relaxation due to tunnelling (Fig 3.19). However, subsequent field−sweep ac experiments did not have the same effect on the χ'' signal seen for **4**, since the application of an external field causes an insignificant improvement of the SMM properties in **5** (see Fig A3.7 in the Appendix). Therefore, no further magnetic experiments were performed.

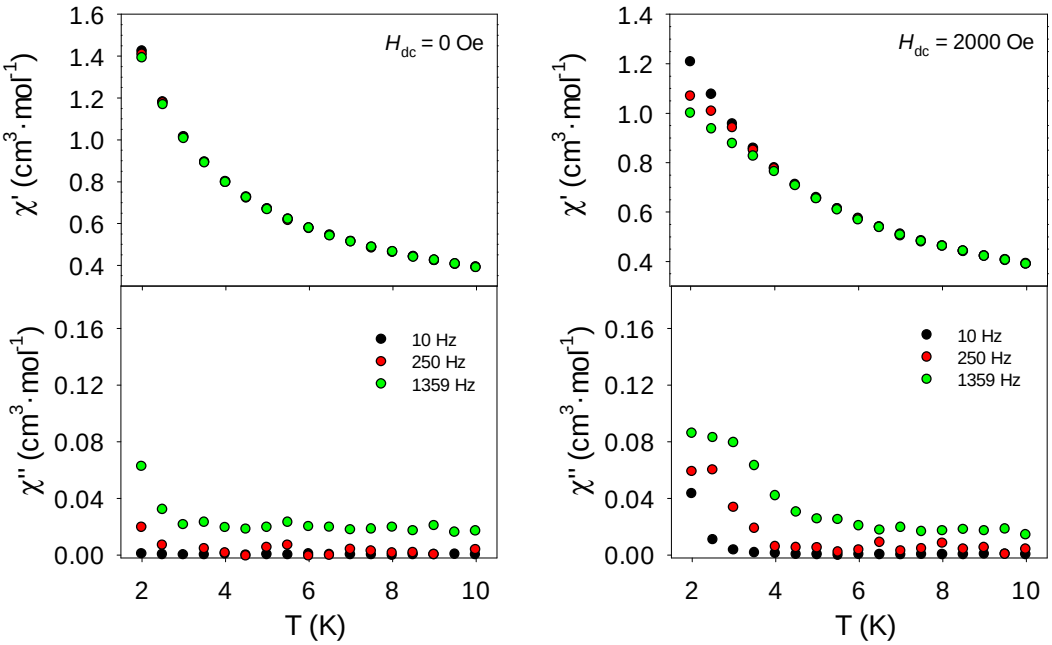

Fig 3.19 Ac magnetic susceptibility of **5** in the absence of an applied dc field (left) and in an external field of H_{dc} = 2000 Oe (right), over the range of 2−10 K at υ = 10, 250, 1359 Hz.

3.3. Concluding remarks

In conclusion, it has been shown that the strategy proposed for the synthesis of $3d$−$3d'$ heterometallic complexes by using metallo−organic precursors with bis−tris propane works. The combination of $[Ni(H_6L)]Cl_2$ (**1**) or $[Cu_2(H_5L)_2(CH_3COO)_2]$ (**2**) with metal salts of Mn(II) leads to the assembly of three new coordination systems, $[Mn_2Ni_2(OH)_2(H_3L)_2(H_2O)_2]Cl_2\cdot 6H_2O$ (**3**), $[Mn_2Cu_2(CH_3O)_2(H_3L)_2(CH_3COO)_2]\cdot 2CH_3OH$ (**4**) and $[Mn_2^{III}Mn^{II}Cu_2O(HCOO)(H_4L)(H_2L)(CH_3COO)_3]\cdot 4.5CH_3OH\cdot 3.5H_2O$ (**5**). Complexes **3** and **4** show an identical "butterfly−like" disposition of the $\{Mn_2M_2O_6\}$ core (M = Ni, Cu). On the other hand, **5** displays a distortion of the $\{Mn_2M_2O_6\}$ topology, due to the coordination of an additional Mn(II) atom related to the presence of new auxiliary ligands such as $HCOO^-$. Note that even though the butterfly topology is well−known for polynuclear compounds, only four structures show a similar disposition and oxidation state of the manganese atoms to that one displayed by **3** (Mn^{3+} occupying the "body sites"), based on the CSD search for heteronuclear $\{M1_2M2_2(OR)_6\}$ systems discussed in the introduction.[24, 25, 44] The structural differences between **3**−**5** arise from the precursor used in the synthesis, but also from the auxiliary ligands present in the reaction media. The magnetic studies reveal that these structural alterations in $\{Mn_2M_2O_6\}$ modify the exchange interactions between metal ions, affecting the overall static and dynamic magnetic properties. The fit of the dc data suggests that the substitution of Ni(II) by Cu(II) ions induces SMM behaviour as a consequence of a change in the nature and/or magnitude of the Mn···Mn' (−2.08 cm^{-1} in **3**, 1.3 cm^{-1} in **4**) and Mn···M (−2.62 cm^{-1} in **3**, −17.6 cm^{-1} in **4**) interactions. It must be stressed that to the extent of our knowledge, **4** is the second Mn/Cu-based complex displaying SMMs properties. The dc and ac experiments performed on **5** reveals that the structural changes caused by presence of the additional Mn(II) ion and the $HCOO^-$ group in **5** leads to the suppression of the slow magnetic relaxation displayed by **4**.

References

1. K. S. Pedersen, J. Bendix and R. Clerac, *Chem. Commun.*, **2014**, *50*, 4396.
2. T. Glaser, *Chem. Commun.*, **2011**, *47*, 116.
3. L. Zhang, P. Zhang, L. Zhao, J. Wu, M. Guo and J. Tang, *Dalton Trans.*, **2016**, *45*, 10556.
4. F. J. Kettles, V. A. Milway, F. Tuna, R. Valiente, L. H. Thomas, W. Wernsdorfer, S. T. Ochsenbein and M. Murrie, *Inorg. Chem.*, **2014**, *53*, 8970.
5. G. Wu, R. Clérac, W. Wernsdorfer, S. Qiu, C. E. Anson, I. J. Hewitt and A. K. Powell, *Eur. J. Inorg. Chem.*, **2006**, *10*, 1927.
6. P. Zhang, L. Zhang, S.−Y. Lin and J. Tang, *Inorg. Chem.*, **2013**, *52*, 6595.
7. M. Heras Ojea, C. Wilson, S. J. Coles, F. Tuna and M. Murrie, *Dalton Trans.*, **2015**, *44*, 19275.
8. V. A. Milway, F. Tuna, A. R. Farrell, L. E. Sharp, S. Parsons and M. Murrie, *Angew. Chem. Int. Ed.*, **2013**, *52*, 1949.
9. D. Gatteschi, R. Sessoli and J. Villain, *Molecular nanomagnets*, Oxford University Press Inc., New York, **2006**.
10. V. M. Mereacre, A. M. Ako, R. Clérac, W. Wernsdorfer, G. Filoti, J. Bartolomé, C. E. Anson and A. K. Powell, *J. Am. Chem. Soc.*, **2007**, *129*, 9248.
11. H. Miyasaka, A. Saitoh and S. Abe, *Coord. Chem. Rev.*, **2007**, *251*, 2622.
12. H. Miyasaka, T. Madanbashi, A. Saitoh, N. Motokawa, R. Ishikawa, M. Yamashita, S. Bahr, W. Wernsdorfer and R. Clérac, *Chem. Eur. J.*, **2012**, *18*, 3942.
13. D. M. Piñero Cruz, D. N. Woodruff, I.−R. Jeon, I. Bhowmick, M. Secu, E. A. Hillard, P. Dechambenoit and R. Clerac, *New J. Chem.*, **2014**, *38*, 3443.
14. R. Clérac, H. Miyasaka, M. Yamashita and C. Coulon, *J. Am. Chem. Soc.*, **2002**, *124*, 12837.
15. I. Nemec, R. Herchel, R. Boča, I. Svoboda, Z. Trávníček, Ľ. Dlháň, K. Matelková and H. Fuess, *Inorg. Chim. Acta*, **2011**, *366*, 366.
16. E. Moreno Pineda, N. F. Chilton, F. Tuna, R. E. P. Winpenny and E. J. L. McInnes, *Inorg. Chem.*, **2015**, *54*, 5930.
17. S. K. Langley, L. Ungur, N. F. Chilton, B. Moubaraki, L. F. Chibotaru and K. S. Murray, *Inorg. Chem.*, **2014**, *53*, 4303.
18. R. McLellan, M. A. Palacios, E. K. Brechin and S. J. Dalgarno, *Chem. Plus. Chem*, **2014**, *79*, 667.
19. A. S. R. Chesman, D. R. Turner, K. J. Berry, N. F. Chilton, B. Moubaraki, K. S. Murray, G. B. Deacon and S. R. Batten, *Dalton Trans.*, **2012**, *41*, 11402.
20. S. Gomez−Coca, T. Cauchy and E. Ruiz, *Dalton Trans.*, **2010**, *39*, 4832.
21. Q. Liu, Y. Yang, L. Huang, D. Wu, B. Kang, C. Chen, Y. Deng and J. Lu, *Inorg. Chem.*, **1995**, *34*, 1884.
22. J. A. Hriljac, S. Harris and D. F. Shriver, *Inorg. Chem.*, **1988**, *27*, 816.
23. J. K. McCusker, J. B. Vincent, E. A. Schmitt, M. L. Mino, K. Shin, D. K. Coggin, P. M. Hagen, J. C. Huffman, G. Christou and D. N. Hendrickson, *J. Am. Chem. Soc.*, **1991**, *113*, 3012.
24. P. Malpaharia, K. Pramanik, J.−P. Costes, J.−P. Tuchagues, B. Moulton, M. J. Zaworotko, B. Das and S. K. Chandra, *Eur. J. Inorg. Chem.*, **2014**, *22*, 3527.
25. G. P. Guedes, S. Soriano, L. A. Mercante, N. L. Speziali, M. A. Novak, M. Andruh and M. G. F. Vaz, *Inorg. Chem.*, **2013**, *52*, 8309.
26. H. Oshio, M. Nihei, S. Koizumi, T. Shiga, H. Nojiri, M. Nakano, N. Shirakawa and M. Akatsu, *J. Am. Chem. Soc.*, **2005**, *127*, 4568.
27. G. A. Seisenbaeva, S. Gohil and V. G. Kessler, *Inorg. Chem. Commun.*, **2004**, *7*, 18.
28. Y. Sunatsuki, H. Shimada, T. Matsuo, M. Nakamura, F. Kai, N. Matsumoto and N. Re, *Inorg. Chem.*, **1998**, *37*, 5566.

29. K. Nakamoto, *Applications in Inorganic Chemistry, in Infrared and Raman Spectra of Inorganic and Coordination Compounds: Part A: Theory and Applications in Inorganic Chemistry*, John Wiley & Sons, Inc., Hoboken, NJ, USA, **1986**.
30. G. B. Deacon and R. J. Phillips, *Coord. Chem. Rev.*, **1980**, *33*, 227.
31. M. Perec and R. Baggio, *Acta Crystallog. Sect. E*, **2010**, *66*, m275.
32. J. A. Kitchen, P. N. Martinho, G. G. Morgan and T. Gunnlaugsson, *Dalton Trans.*, **2014**, *43*, 6468.
33. I. D. Brown and K. K. Wu, *Acta Crystallogr. Sect. B*, **1976**, *32*, 1957.
34. A. W. Addison, T. N. Rao, J. Reedijk, J. van Rijn and G. C. Verschoor, *J. Chem. Soc., Dalton Trans.*, **1984**, *7*, 1349.
35. N. F. Chilton, R. P. Anderson, L. D. Turner, A. Soncini and K. S. Murray, *J. Comput. Chem.*, **2013**, *34*, 1164.
36. N. Berg, T. Rajeshkumar, S. M. Taylor, E. K. Brechin, G. Rajaraman and L. F. Jones, *Chem. Eur. J.*, **2012**, *18*, 5906.
37. P. Comar, T. Rajeshkumar, G. S. Nichol, M. B. Pitak, S. J. Coles, G. Rajaraman and E. K. Brechin, *Dalton Trans.*, **2015**, *44*, 19805.
38. S. K. Langley, N. F. Chilton, B. Moubaraki and K. S. Murray, *Dalton Trans.*, **2012**, *41*, 1033.
39. T. C. Stamatatos, R. Adam, C. P. Raptopoulou, V. Psycharis, R. Ballesteros, B. Abarca, S. P. Perlepes and A. K. Boudalis, *Inorg. Chem. Commun.*, **2012**, *15*, 73.
40 P. de Hoog, P. Gamez, O. Roubeau, M. Lutz, W. L. Driessen, A. L. Spek and J. Reedijk, *New J. Chem.*, **2003**, *27*, 18.
41. L. B. Jerzykiewicz, J. Utko, M. Duczmal, P. Starynowicz and P. Sobota, *Eur. J. Inorg. Chem.*, **2010**, *28*, 4492.
42. F. Habib, C. Cook, I. Korobkov and M. Murugesu, *Inorg. Chim. Acta*, **2012**, 380, 378.
43. H. Oshio, M. Nihei, A. Yoshida, H. Nojiri, M. Nakano, A. Yamaguchi, Y. Karaki and H. Ishimoto, *Chem. Eur. J.*, **2005**, *11*, 843.
44. T. Nakajima, K. Seto, A. Scheurer, B. Kure, T. Kajiwara, T. Tanase, M. Mikuriya and H. Sakiyama, *Eur. J. Inorg. Chem.*, **2014**, *29*, 5021.

Chapter 4

The content of this chapter has been published in Chem. Eur. J., 2016, 22, 12839.

Contents

4. Enhancement of Tb^{III}–Cu^{II} SMM performance through structural modification

4. Enhancement of Tb^{III}–Cu^{II} SMM performance through structural modification

Chapter 3 has shown the capability of bis−tris propane (H_6L) to control the synthesis of Mn/3*d* polynuclear compounds (3*d* = Ni or Cu). The aforementioned structures display a preference for encapsulating Ni or Cu in the internal pocket of the ligand to the detriment of Mn. In addition, Cu has been revealed as the most successful candidate for the synthesis of these heterometallic complexes since it is the one with the larger number of reported 3*d*/3*d*' complexes to date (*e.g.* {$Mn_{18}Cu_6$}).[1, 2] That may be due to the greater flexibility of Cu(II) ions for displaying different coordination environments compared to the rest of the candidates. However the assembly of metal ions within these structures promotes, mostly, antiferromagnetic exchange, hindering therefore any SMM property. To try to promote ferromagnetic interactions, and then achieve the highest possible spin value, we propose exploring the reactivity of the {$Cu(H_6L)$} units with rare earth elements, as it is known they lean towards ferromagnetic exchange for the heavier Ln ions.[3–6] As previously stated, the Cu···4*f* interaction can also help to suppress the QTM related to lanthanide ions.[7, 8] In addition, lanthanide ions provide the required magnetic anisotropy that is essential in SMMs.[9–11] Since the magnetic study of the first Cu/4*f* SMMs, several theoretical and experimental studies have investigated the factors that mainly influence the resultant magnetic properties.[7, 9] Recent studies suggest that perturbations in the ligand environment of the Ln(III) ions can cause changes in the crystal field (CF) that modify the overall magnetic behaviour of the complexes.[12, 13]

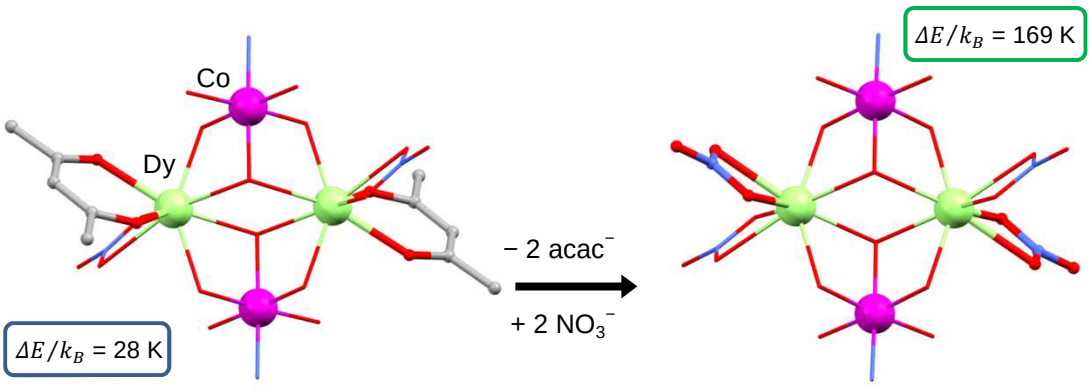

Fig 4.1 Detail of structure of $[Co^{III}_2Dy^{III}_2(OH)_2(teaH)_2(acac)_4(NO_3)_2]$ (left) and $[Co^{III}_2Dy^{III}_2(OH)_2(bdea)_2(acac)_2(NO_3)_4]$ (right). $teaH_3$ = triethanolamine, $bdeaH_2$ = *n*−butyldiethanolamine.[12, 14]

For example, the dynamic magnetic properties of a $\{Co^{III}_2Dy^{III}_2\}$ complex have been considerably improved by a strategy based on the replacement of two chelating $acac^-$ groups by two bidentate NO_3^- groups on the coordination sphere of the Dy ions (see Fig 4.1).[12, 14] The structural modifications related to that replacement results in a significant increase of the energy barrier and a reduction of the QTM.

Considering that, we have investigated the chemistry of $\{Cu(H_6L)\}$ with different Ln salts, by using a synthetic strategy based on the substitution of the lanthanide ion (Ln = Gd, Tb, Dy, Ho, Er), and the replacement of the auxiliary ligands (X = CH_3COO^-, NO_3^-). As a result we have successfully obtained a new family of Cu−4*f* heterometallic complexes with general formula $\{Ln_2Cu_3(H_3L)_2X_n\}$.[15] Slow magnetic relaxation is observed for all them, except for the isotropic Gd(III) analogues. The SMM properties of the final complexes have been tuned by the substitution of the auxiliary ligands, leading to the synthesis of $(NMe_4)_2[Tb_2Cu_3(H_3L)_2(NO_3)_7(CH_3OH)_2](NO_3)$, the Tb/Cu−based single−molecule magnet with the highest anisotropy barrier in zero applied dc field ($\Delta E/k_B$ = 36.0 ± 0.2 K). In this chapter we discuss the structure, magnetic properties and *ab initio* calculations of the $\{Ln_2Cu_3(H_3L)_2X_n\}$ family.

4.1. Synthesis

Note: complexes **8**−**12** were synthesised and characterised by Dr. Victoria A. Milway. Interpretation and data analysis, however, was performed as part of this PhD thesis.

$[Gd_2Cu_3(H_3L)_2(CH_3COO)_6]\cdot THF\cdot 3H_2O$ (**6**): Et_3N (0.13 mL, 0.9 mmol) was added to a white suspension of H_6L (0.09 g, 0.30 mmol) in MeOH (20 mL). $[Cu_2(CH_3COO)_4(H_2O)_2]$ (0.09 g, 0.23 mmol) was added, and immediately dissolved, resulting in a turquoise solution. $Gd(CH_3COO)_3\cdot H_2O$ (0.11 g, 0.33 mmol) was subsequently added, turning the turquoise solution blue. The final solution was stirred and heated to 60°C for 3 h. The initial blue solution turned violet. Violet plate−like single crystals suitable for X−ray diffraction were obtained by vapour diffusion of tetrahydrofuran (THF) into the solution overnight. Yield 71% (166 mg). IR: $\bar{\upsilon}$ (cm^{-1}) = 3200, 1549, 1445, 1265, 1101, 1045, 1020, 937, 671. Elemental analysis ($[Gd_2Cu_3(H_3L)_2(CH_3COO)_6]\cdot 2.25H_2O$) [%], found: C 28.29, H 4.72, N 3.56; calc: C 28.00, H 4.73, N 3.84.

$[Tb_2Cu_3(H_3L)_2(CH_3COO)_6]\cdot CH_3OH\cdot 2H_2O$ (**7**): The same synthetic procedure described for **6** was followed, but using $Tb(CH_3COO)_3\cdot H_2O$ instead of $Gd(CH_3COO)_3\cdot H_2O$. Violet plate−like single crystals suitable for X−ray diffraction were obtained by vapour diffusion of THF into the solution over 2 days. Yield 44% (110 mg). IR: $\bar{\upsilon}$ (cm^{-1}) = 3196, 1543, 1445, 1327, 1099, 1040, 1011, 934, 667. Elemental analysis ($[Tb_2Cu_3(H_3L)_2(CH_3COO)_6]\cdot CH_3OH\cdot 2H_2O$) [%], found: C 28.29, H 4.72, N 3.56; calc: C 28.22, H 4.87, N 3.76.

$(NMe_4)_2[Gd_2Cu_3(H_3L)_2(NO_3)_8(CH_3CH_2OH)_2]\cdot 2H_2O$ (**8**): H_6L (0.28 g, 1 mmol) and tetramethylammonium hydroxide pentahydrate ($NMe_4OH\cdot 5H_2O$) (0.38 g, 2 mmol) were combined in EtOH (40 mL), and heated to 60˚C for 20 min. $Cu(NO_3)_2\cdot 3H_2O$ (0.51 g, 2 mmol) was added, giving a green suspension, which was then heated at 60˚C for 40 min. $Gd(NO_3)_3\cdot 6H_2O$ (0.99 g, 2 mmol) was added and immediately dissolved, giving a dark blue solution. The resulting solution was heated for three hours, and then filtered. Blue block−like single crystals suitable for X−ray diffraction were obtained by slow evaporation of the filtrate over 2 weeks. Yield 7% (74 mg). IR: $\bar{\upsilon}$ (cm^{-1}) = 3393, 1651, 1493, 1333, 1296, 1072, 1017, 949, 679. Elemental analysis ($(NMe_4)_2[Gd_2Cu_3(H_3L)_2(NO_3)_8(CH_3CH_2OH)_2]\cdot 3.25H_2O$) [%], found: C, 21.62; H, 4.44; N, 10.93; calc: C, 21.97; H, 4.80; N, 10.55.

$(NMe_4)_2[Tb_2Cu_3(H_3L)_2(NO_3)_7(CH_3OH)_2](NO_3)$ (**9**): The same synthetic procedure described for **8** was followed, but using $Tb(NO_3)_3 \cdot 5H_2O$ instead of $Gd(NO_3)_3 \cdot 6H_2O$, and MeOH instead of EtOH as solvent. Blue block−like single crystals suitable for X−ray diffraction were obtained by slow evaporation of the filtrate over several weeks. Yield 16% (84 mg). IR: $\bar{\upsilon}$ (cm^{-1}) = 3200, 1655, 1493, 1333, 1296, 1044, 1017, 949, 679. Elemental analysis ($(NMe_4)_2[Tb_2Cu_3(H_3L)_2(NO_3)_7-(CH_3OH)_2](NO_3) \cdot 2.5CH_3OH$) [%], found: C, 22.62; H, 4.51; N, 10.56; calc: C, 22.33; H, 4.78; N, 10.57.

$(NMe_4)_2[Dy_2Cu_3(H_3L)_2(NO_3)_7(CH_3OH)_2](NO_3)$ (**10**): The same synthetic procedure described for **9** was followed, but using $Dy(NO_3)_3 \cdot 6H_2O$ instead of $Tb(NO_3)_3 \cdot 5H_2O$. Blue block−like single crystals suitable for X−ray diffraction were obtained by slow evaporation of the filtrate over a few days. Yield (crystals) 5% (60 mg). IR: $\bar{\upsilon}$ (cm^{-1}) = 3206, 1655, 1493, 1333, 1296, 1015, 949, 814, 633. Elemental analysis ($(NMe_4)_2[Dy_2Cu_3(H_3L)_2(NO_3)_7(CH_3OH)_2](NO_3) \cdot 3.25H_2O$) [%], found: C, 20.40; H, 4.11; N, 10.77; calc: C, 20.87; H, 4.63; N, 10.65.

$(NMe_4)_2[Ho_2Cu_3(H_3L)_2(NO_3)_7(CH_3OH)_2](NO_3)$ (**11**): The same synthetic procedure described for **9** was followed, but using $Ho(NO_3)_3 \cdot 5H_2O$ instead of $Tb(NO_3)_3 \cdot 5H_2O$. Blue block−like single crystals suitable for X−ray diffraction were obtained by slow evaporation of the filtrate over a few days. Yield (crystals) 26% (237 mg). IR: $\bar{\upsilon}$ (cm^{-1}) = 3242, 1649, 1474, 1385, 1310, 1074, 1007, 750, 679. Elemental analysis ($(NMe_4)_2[Ho_2Cu_3(H_3L)_2(NO_3)_7(CH_3OH)_2](NO_3) \cdot 6H_2O$) [%], found: C, 19.76; H, 4.26; N, 10.47; calc: C, 20.28; H, 4.79; N, 10.34.

$(NMe_4)_2[Er_2Cu_3(H_3L)_2(NO_3)_7(CH_3OH)_2](NO_3)$ (**12**): The same synthetic procedure described for **9** was followed, but using $Er(NO_3)_3 \cdot 5H_2O$ instead of $Tb(NO_3)_3 \cdot 5H_2O$. Blue block−like single crystals suitable for X−ray diffraction were obtained by slow evaporation of the filtrate over a few days. Yield (crystals) 19% (170 mg). IR: $\bar{\upsilon}$ (cm^{-1}) = 3401, 1657, 1491, 1333, 1072, 1017, 949, 679, 602. Elemental analysis ($(NMe_4)_2[Er_2Cu_3(H_3L)_2(NO_3)_7(CH_3OH)_2](NO_3) \cdot 1.25H_2O$) [%], found: C, 21.19; H, 4.29; N, 10.61; calc: C, 21.18; H, 4.47; N, 10.81.

4.2. Results and discussion

Several experiments involving different copper and lanthanide salts have been performed in order to study the reactivity of H_6L in the presence of Ln(III) ions. Moreover, the use of two different coordinating counterions such as acetates and nitrates is proposed as even a small alteration of the 4*f* environment could cause large changes in the magnetic properties of the complexes. The reaction between H_6L, $[Cu_2(CH_3COO)_4(H_2O)_2]$ and $Ln(CH_3COO)_3 \cdot H_2O$ (Ln = Gd^{3+}, Tb^{3+}) in the presence of Et_3N allowed the synthesis of the complexes $[Gd_2Cu_3(H_3L)_2(CH_3COO)_6] \cdot THF \cdot 3H_2O$ (**6**) and $[Tb_2Cu_3(H_3L)_2-(CH_3COO)_6] \cdot CH_3OH \cdot 2H_2O$ (**7**). Violet plate−like crystals of **6** and **7** were obtained by vapour diffusion of THF into the reaction solution in good yields. When nitrate salts are used in combination with NMe_4OH a different series of Cu/4*f* complexes with formula $(NMe_4)_2[Gd_2Cu_3(H_3L)_2(NO_3)_8(CH_3CH_2OH)_2] \cdot 2H_2O$ (**8**), or $(NMe_4)_2[Ln_2Cu_3(H_3L)_2(NO_3)_7(CH_3OH)_2](NO_3)$ (**9**−**12**) (Tb^{3+}, Dy^{3+}, Ho^{3+}, Er^{3+}) were successfully synthesised. Blue block−like crystals were obtained by slow evaporation of the reaction solution. The main structural difference between these two families of complexes ($\{Ln_2Cu_3(H_3L)_2(CH_3COO)_6\}$ and $\{Ln_2Cu_3(H_3L)_2(NO_3)_n\}$, n = 7 or 8) lies in the coordination environment around the metal centres, due partly to the solvent used and to the nature of the counterions present in the reaction media.

X−ray crystallographic analysis

Selected crystallographic experimental details for **6**−**12** are shown in Table 4.3. Complexes crystallise in the monoclinic space group No. 14; **9** and **10** are reported in setting $P2_1/n$, and **8**–**12** as $P2_1/c$. Complexes **6** and **7** are isostructural, as are **9** – **12**. Although all structures are in the same space group, in structures **8**–**12** the anionic unit has lower symmetry and the unit cell volume has doubled. The asymmetric unit of **6** and **7** contains a half molecule of $[Ln_2Cu_3(H_3L)_2(CH_3COO)_6]$, molecules of water (one and a half molecules for **6**, one for **7**), and a half THF for **6** or a half MeOH for **7**. For the members of the $\{Ln_2Cu_3(H_3L)_2(NO_3)_n\}$ family, the asymmetric unit contains one $[Ln_2Cu_3(H_3L)_2(NO_3)_7(CH_3OH)_2]^-$ anion, two NMe_4^+ cations, and one NO_3^- anion, with the exception of **8**. The asymmetric unit of **8** contains a half anion of $[Gd_2Cu_3(H_3L)_2(NO_3)_8(CH_3CH_2OH)_2]^{2-}$, one NMe_4^+ cation, and one water molecule. As the complexes are isostructural within the two 3*d*/4*f* families, the following descriptions of **6** and **9** are applicable to **7** and **10**−**12** respectively.

The structure of **6** contains two Gd(III) ions coordinated to a {$Cu_3(H_3L)_2$} linear unit through four μ−O and two μ_3−O bridging atoms from two triply deprotonated H_3L^{3-} ligands (see Fig 4.2). Three chelating acetate anions help to complete the coordination sphere of each lanthanide ion. The two external Cu(II) ions of the linear unit are encapsulated by two H_3L^{3-} ligands through O, N−donor atoms in a [4+1] distorted environment. As the τ parameters calculated for the external Cu(II) ions in **6** and **7** are, respectively, τ_{Cu} (**6**) = 0.21 and τ_{Cu} (**7**) = 0.22, the Cu(II) ions are both in a distorted square−pyramidal geometry.[16] The central Cu(II) ion presents a distorted octahedral geometry due to the coordination of six O(H_3L^{3-}) donor atoms, which act as bridges between the different metal centres. The two remaining hydroxyl arms on each ligand which do not bridge metal ions are uncoordinated. Since two longer distances can be observed (see values in Table 4.1), the central ion Cu2 presents an elongation Jahn−Teller distortion.

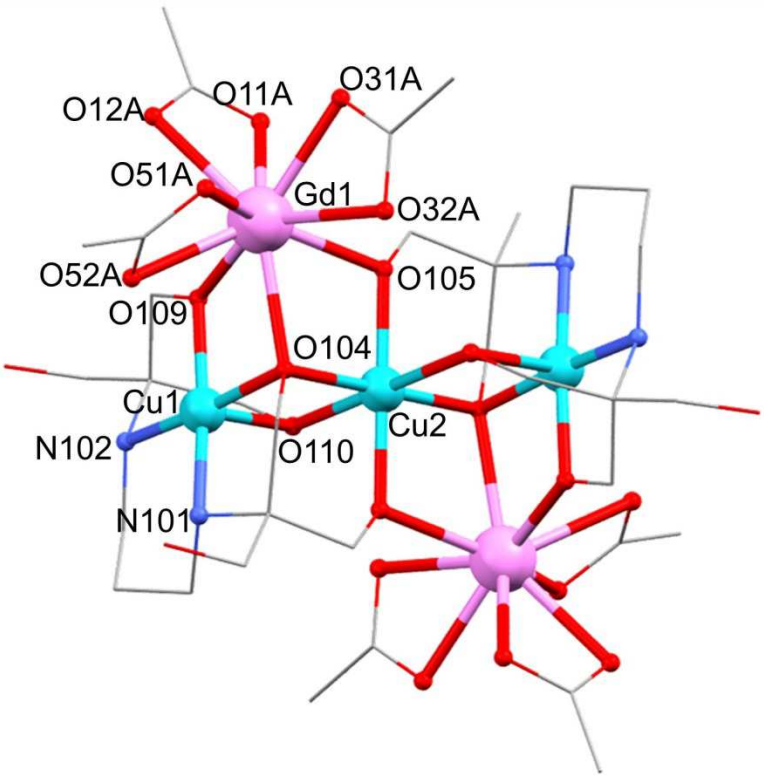

Fig 4.2 Structure of complex **6**. C, grey; Cu, turquoise; Gd, pink; N, blue; O, red; Hydrogen atoms and solvent molecules are omitted for clarity. Only crystallographically unique Cu, Gd, N and O atoms are labelled.

The symmetry analyses around the Ln(III) ion (Ln = Gd^{3+}, Tb^{3+}) have been performed using the program SHAPE.[17−19] SHAPE calculates continuous shape measures (CShMs) of a set of points (*e.g*. atomic positions) relative to the vertices of ideal polyhedra. For **6**−**12**, the assembly of the ligands, co−ligands and/or solvent

molecules with the lanthanide atom define a Ln−centred polyhedron with nine oxygen atoms occupying the vertices. Consequently the studies of **6** and **7** show the degree of the deviation of {LnO_9} from all the possible ideal 9−vertex polyhedra, being the closest shape that one with the smallest CShMs value (ideally zero). The results propose spherical capped square antiprism (C_{4v}) as the closest ideal geometry for both complexes (see Table A4.1 of the Appendix).

The average intramolecular Cu···M distances (M = Cu, Ln) are $d_{(Cu\cdots Cu')}$ = 2.875(5) Å, and $d_{(Cu\cdots Ln)}$ = 3.371(5) Å. Two clear CuÔCu' angles could be distinguished considering the nature of the oxygen bridge, displaying average values equal to $\alpha_{Cu-\mu O-Cu'}$ = 68.47(1)° and $\alpha_{Cu-\mu_3 O-Cu'}$ = 93.30(2)°. In the same way there are two different CuÔLn angles, with average values equal to $\beta_{Cu-\mu O-Ln}$ = 104.93(5)°, and $\beta_{Cu-\mu_3 O-Ln}$ = 99.19(5)°. Regarding the torsion angles, there is no remarkable structural difference between them as μ and μ_3−oxygen atoms are involved in all the angles. Considering that, the average torsion angles defined for CuOOCu' (*e.g.* Cu1−O104−O110−Cu2) and CuOOLn are $\theta_{CuOOCu'}$ = 168.1(1)°, and γ_{CuOOLn} = 166.8(1)° respectively (see Tables 4.1 and 4.2 for additional information).

Table 4.1 Summary of the Jahn−Teller axes related to the hexacoordinated Cu(II) ions ($d_{(Cu2-O)}$, $d_{(Cu-O)}$), and the average intramolecular distances between metal ions for **6**−**12**. Note that Cu2 is the central ion, while Cu is the peripheral one.

	$d_{(Cu2-O)}$/Å	$d_{(Cu-O)}$/Å	$d_{(Cu\cdots Cu')}$/Å	$d_{(Cu\cdots Ln)}$/Å
6 (Gd)	2.643(0) 2.643(0)	− −	2.878(3)	3.378(5)
7 (Tb)	2.620(0) 2.620(0)	− −	2.871(9)	3.364(9)
8 (Gd)	2.759(0) 2.759(0)	2.617(3) 2.542(3)	2.950(6)	3.420(6)
9 (Tb)	2.562(2) 2.555(2)	2.512(2) 2.439(2)	2.943(6)	3.409(7)
10 (Dy)	2.561(2) 2.555(2)	2.515(3) 2.440(2)	2.944(6)	3.400(7)
11 (Ho)	2.558(2) 2.551(2)	2.512(3) 2.437(2)	2.940(6)	3.390(7)
12 (Er)	2.552(2) 2.548(2)	2.509(3) 2.437(2)	2.944(6)	3.376(7)

Table 4.2 Summary of the average angles (*α*, *β*), and torsion angles (*θ*, *γ*) defined by the different metal ions for complexes **6**−**12**.

	$\alpha_{Cu-\mu O-Cu'}$/°	$\alpha_{Cu-\mu_3 O-Cu'}$/°	$\beta_{Cu-\mu O-Ln}$/°	$\beta_{Cu-\mu_3 O-Ln}$/°	$\theta_{CuOOCu'}$/°	γ_{CuOOLn}/°
6	68.43(1)	93.60(4)	104.90(9)	99.47(9)	167.9(1)	166.8(1)
7	68.50(2)	93.00(2)	104.95(2)	98.90(2)	168.3(1)	166.7(1)
8	67.48(5)	96.80(1)	108.35(1)	98.90(9)	163.6(1)	170.0(1)
9	72.01(5)	96.05(8)	107.95(8)	98.42(7)	166.5(1)	169.0(9)
10	72.01(7)	96.15(1)	107.95(1)	98.35(9)	167.6(1)	169.0(1)
11	72.06(5)	96.24(7)	107.88(8)	98.52(7)	167.1(1)	169.2(8)
12	72.18(9)	96.30(1)	107.76(1)	98.50(1)	167.1(2)	169.2(1)

The replacement of acetate for nitrate anions decreases the symmetry within the molecule, as there is one whole molecule in the asymmetric unit, and promotes different coordination environments around the metal ions present in the structure (see Fig 4.3). Consequently, the structure of $(NMe_4)_2[Ln_2Cu_3(H_3L)_2(NO_3)_7(CH_3OH)_2](NO_3)$ (**9** Ln = Tb^{3+}) contains a $\{Cu_3(H_3L)_2\}$ linear unit linked to two Tb(III) ions as seen in **7**, but this time the H_3L^{3-} ligands are coordinated to external Cu(II) centres which have two different geometries. As shown in Fig 4.3, Cu1 is in a [4+1] distorted square−based pyramidal geometry (τ_{Cu} (**9**) = τ_{Cu} (**10**) = 0.24, τ_{Cu} (**11**) = τ_{Cu} (**12**) = 0.25), and Cu3 is in an elongated octahedral geometry due to the coordination of an additional monodentate NO_3^- ligand (see JT axes in Table 4.1). The central Cu(II) ion displays the elongation Jahn−Teller distortion seen in **6**. Two bidentate and one monodentate NO_3^- ligands, plus one MeOH ligand complete the coordination environment of each nona−coordinated Tb(III) centre. The symmetry analyses around the Ln(III) ion for **9**–**12** (Ln = Tb^{3+}, Dy^{3+}, Ho^{3+}, Er^{3+}) propose two different environments around the lanthanide centres (see Table A4.1, A4.2 of the Appendix), which could be related to the dissimilar coordination sphere around the neighbouring Cu(II) atoms. The closest Ln centre to the outer hexacoordinated Cu(II) ion (Ln2, highlighted in pink in Fig 4.3, right) is in a spherical capped square antiprism environment (C_{4v}), whereas the one linked to the pentacoordinated Cu(II) ion (Ln1, highlighted in green in Fig 4.3, right) displays a muffin geometry (C_s).

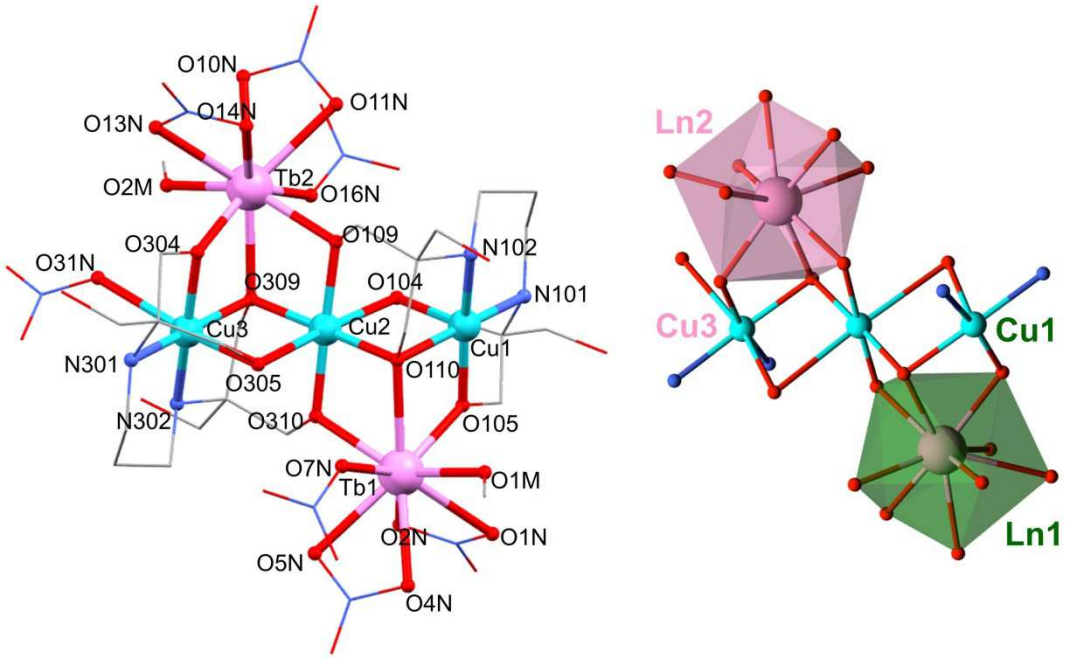

Fig 4.3 Structure of the anion (left) and detail of the metal alkoxide core (right) of **9**. C, grey; Cu, turquoise; N, blue; O, red; Tb, pink. Hydrogen atoms and counterions are omitted for clarity. Polyhedra around Ln are highlighted in pink and green.

It should be noted that the coordination sphere around the metal atoms is slightly different in the case of $(NMe_4)_2[Gd_2Cu_3(H_3L)_2(NO_3)_8(CH_3CH_2OH)_2]\cdot 2H_2O$ (**8**): as both outer Cu(II) ions are equivalent by symmetry, the three Cu(II) centres are in a distorted octahedral geometry (Fig 4.4), and an EtOH solvent molecule is coordinated to each Gd(III) centre instead of MeOH. Shape studies performed on complex **8** reveals again structural differences with the rest of the {$Ln_2Cu_3(H_3L)_2(NO_3)_n$} complexes, as there is only one crystallographically unique Gd(III) centre in the low−symmetry muffin geometry (C_s). The average intramolecular distances between the different metal ions range from $d_{(Cu\cdots Cu')}$ = 2.943(6)−2.950(6) Å, and $d_{(Cu\cdots Ln)}$ = 3.376(7)−3.420(6) Å. As a consequence of the lanthanide contraction $d_{(Cu\cdots Ln)}$ decrease along the series, $d_{(Cu\cdots Gd)}$ being the largest distance (3.420(6) Å) and hence $d_{(Cu\cdots Er)}$ the smallest one (3.376(7) Å). Moreover, the intramolecular distances between Cu···Cu′ and Cu···Ln are slightly shorter in compounds **6**−**7** than in **8**−**12** (see Table 4.1). The different CuÔCu' angles show $\alpha_{Cu-\mu O-Cu'}$ values between 67.48(5)–72.18(9)°, and $\alpha_{Cu-\mu_3 O-Cu'}$ between 96.05(8) – 96.80(1)°. The average CuÔLn angles values are $\beta_{Cu-\mu O-Ln}$ = 107.98(1)°, and $\beta_{Cu-\mu_3 O-Ln}$ = 98.55(9)°. Finally, the average torsion angles defined for CuOOCu' and CuOOLn are respectively $\theta_{CuOOCu'}$ = 166.3(2)°, and γ_{CuOOLn} = 169.3(1)° (see Table 4.2 for additional information).

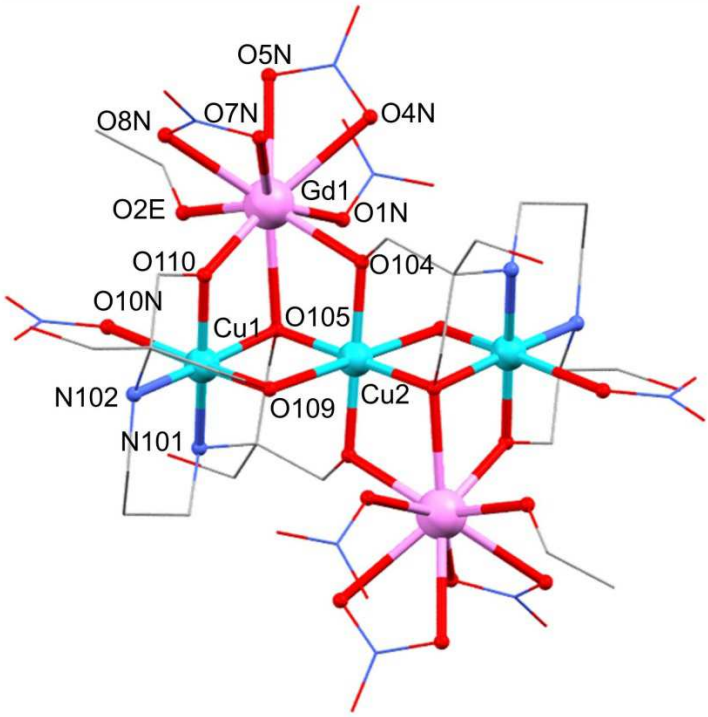

Fig 4.4 Structure of the anion of **8**. C, grey; Cu, turquoise; N, blue; O, red; Tb, pink; Hydrogen atoms, counterions and solvent molecules are omitted for clarity.

A search based on the complexes reported in the Cambridge Structural Database (CSD 5.36, February 2016) reveals that there are no pentanuclear structures comparable to {$Ln_2Cu_3(H_3L)_2$}. Moreover, the angles between Cu(II) ions defined as $\alpha_{Cu-\mu O-Cu'}$ for all the complexes display unusually small values (67.48(5)–72.18(9)°), with only a few examples reported in the CSD. This rare acute Cu−O−Cu' angle could influence some magnetic parameters such as the coupling between the metal ions, and therefore the overall magnetic behaviour of the complexes that will be discussed later. Besides the rarity of the {Ln_2Cu_3} structure, analysis of the evolution of the magnetic properties along the 4*f* series makes the magnetic study of these complexes interesting. Moreover, recent research points to the close relationship between the magnetic anisotropy of lanthanide ions and their local symmetry. Consequently, a comparative magneto−structural analysis of complexes **6**−**12**, and between both {$Ln_2Cu_3(H_3L)_2(CH_3COO)_6$} and {$Ln_2Cu_3(H_3L)_2(NO_3)_n$} families is discussed in the following section.

Table 4.3 Crystal Data and Structure Refinement Parameters of Complexes **6**−**12**.*

Complex	**6**	**7**	**8**	**9**	**10**	**11**	**12**
T/K	100(2)	100(2)	100(2)	100(2)	100(2)	100(2)	100(2)
Crystal system	monoclinic	monoclinic	monoclinic	monoclinic	monoclinic	monoclinic	monoclinic
Space group	$P2_1/n$	$P2_1/n$	$P2_1/c$	$P2_1/c$	$P2_1/c$	$P2_1/c$	$P2_1/c$
a/Å, *b*/Å, *c*/Å	11.9478(8), 18.8874(13), 13.1236(9)	11.8081(8), 18.9453(13), 12.5980(9)	9.7807(2), 19.9923(4), 16.3177(3)	15.8081(2), 16.1451(2), 23.7104(2)	15.8081(2), 16.1620(2), 23.7208(16)	15.7834(2), 16.12290(10), 23.6867(3)	15.78770(10), 16.0957(2), 23.6668(2)
β/°	108.0790(15)	106.663(2)	101.7210(10)	101.0060(10)	100.932(7)	100.7980(10)	100.8170(10)
V/Å^3	2815.3(3)	2699.9(3)	3124.21(11)	5940.14(12)	5948.2(4)	5920.93(11)	5907.21(10)
Z	2	2	2	4	4	4	4
ρ_{calc}/mg/m^3	1.822	1.832	1.952	1.985	1.991	2.005	2.015
μ/mm^{-1}	3.525	3.833	3.211	3.520	3.649	3.815	3.986
F(000)	1546.0	1486.0	1846.0	3556.0	3564.0	3572.0	3580.0
Reflections collected	47169	21410	11181	21261	39420	20490	11152
Data/restraints/ parameters	6441/534/366	6152/526/342	5707/5/435	10887/61/845	13420/10/827	10516/12/829	10733/34/825
GOF on F^2	1.066	1.045	1.108	1.070	1.030	1.032	1.050
Final *R* indexes [$I \geq 2\sigma(I)$]	R_1 = 0.0305, wR_2 = 0.0795	R_1 = 0.0663, wR_2 = 0.1737	R_1 = 0.0282, wR_2 = 0.0658	R_1 = 0.0207, wR_2 = 0.0521	R_1 = 0.0320, wR_2 = 0.0696	R_1 = 0.0206, wR_2 = 0.0486	R_1 = 0.0198, wR_2 = 0.0471
Final *R* indexes [all data]	R_1 = 0.0372, wR_2 = 0.0838	R_1 = 0.0798, wR_2 = 0.1845	R_1 = 0.0348, wR_2 = 0.0691	R_1 = 0.0251, wR_2 = 0.0544	R_1 = 0.0406, wR_2 = 0.0744	R_1 = 0.0247, wR_2 = 0.0502	R_1 = 0.0236, wR_2 = 0.0480
Largest diff. peak/hole/e Å^{-3}	1.62/−0.73	6.34/−0.80	0.80/−0.54	1.22/−0.74	0.84/−0.72	0.81/−0.55	1.18/−0.63

*__6__: $\{Gd_2Cu_3(H_3L)_2(AcO)_6\}$; __7__: $\{Tb_2Cu_3(H_3L)_2(AcO)_6\}$; __8__: $\{Gd_2Cu_3(H_3L)_2(NO_3)_8\}$; __9__: $\{Tb_2Cu_3(H_3L)_2(NO_3)_7\}$; __10__: $\{Dy_2Cu_3(H_3L)_2(NO_3)_7\}$; __11__: $\{Ho_2Cu_3(H_3L)_2(NO_3)_7\}$; __12__: $\{Er_2Cu_3(H_3L)_2(NO_3)_7\}$. *Note that these are abbreviations from the corresponding full formulae*.

Magnetic properties

The variable−temperature magnetic properties of complexes **6** and **7** were investigated in an applied field of 1000 Oe (Fig 4.5). The experimental values of $\chi_M T$ at 290 K for **6** and **7** are consistent with those expected for three uncoupled Cu(II) ions (S_{Cu} = 1/2, g_{Cu} = 2.11) and two Gd(III) ($^8S_{7/2}$, S = 7/2, g = 2) or two Tb(III) ions ($^7F_6$, L = 3, S = 3, g_J = 3/2) respectively (see Table 4.4 for further information). The g_{Cu} = 2.11 value used to calculate the expected $\chi_M T$ value is consistent with that used in previous reported complexes presenting similar {$Cu(H_6L)$} environments.[2, 20] Both complexes display ferromagnetic coupling, as their experimental $\chi_M T$ values tend to increase with temperature, reaching maximum values of 35.43 $cm^3 \cdot mol^{-1} \cdot K$ at 3.4 K for **6**, and of 50.58 $cm^3 \cdot mol^{-1} \cdot K$ at 4.0 K for **7**. Below these temperatures, the $\chi_M T$ products for **6** and **7** decrease to 33.13 $cm^3 \cdot mol^{-1} \cdot K$ and to 47.78 $cm^3 \cdot mol^{-1} \cdot K$ respectively. The decrease in the experimental susceptibility values at low temperature could be due to a weak antiferromagnetic intermolecular interaction. Field−dependent magnetisation measurements were also performed for **6** and **7** at 2 and 5 K (Fig 4.5 and A4.1). The magnetisation reaches the saturation at the highest measured field (5 T) for **6** (M_{sat} = 17.17; M_{exp} = 17.30), whereas for **7** the observed maximum value (11.56) differs significantly from the expected one (21.17). That could be related to the large magnetic anisotropy arising from the Tb(III) ions.

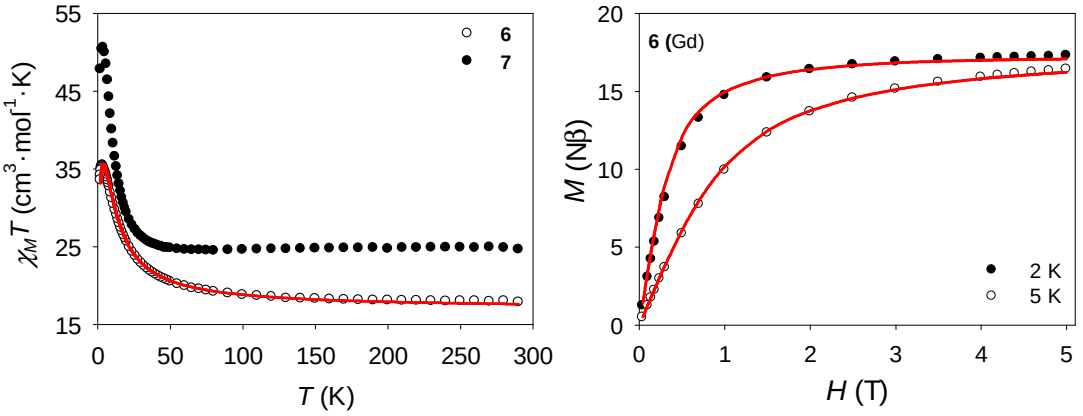

Fig 4.5 Temperature dependence of $\chi_M T$ (left) for complexes **6** (Gd) and **7** (Tb) in an applied field of 1000 Oe, and magnetisation *vs*. field (right) at 2 K, 5 K for **6**. Red lines correspond to the fit for **6** (see text for details).

As Gd(III) is an isotropic ion, we were able to simultaneously fit the susceptibility and magnetisation data of complex **6**. The fit was performed considering the magnetic model displayed in Figure 4.6, and by applying the spin Hamiltonian shown in Eq. 4.1, to give $\mathcal{J}_1$ = 1.8 cm^{-1}, $\mathcal{J}_2$ = 69.7 cm^{-1} (R = 99.6%). The $g_{Cu,}$ g_{Gd} = g parameters were fixed at 2.11 and 2, respectively, during the fit and a small intermolecular interaction of z$\mathcal{J}$' = −1.5·10^{-3} cm^{-1} was included. The results from the fit are reasonable considering the characteristic ferromagnetic tendency of Ln(III)−Cu(II) interactions in heteronuclear Cu/Gd complexes and that the nature and magnitude of the coupling between Cu(II) ions ($\mathcal{J}_2$ = 69.7 cm^{-1}) is consistent with the small Cu−O−Cu' angles (see Table 4.1).

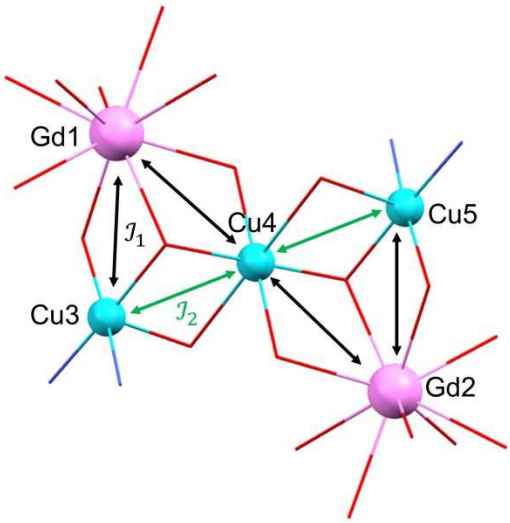

Fig 4.6 Magnetic model used for the fit of **6**.

Eq. 4.1 $$\widehat{\mathcal{H}} = -2\mathcal{J}_1\left(\hat{S}_{Gd1}\cdot\hat{S}_{Cu3}+\hat{S}_{Gd1}\cdot\hat{S}_{Cu4}+\hat{S}_{Gd2}\cdot\hat{S}_{Cu4}+\hat{S}_{Gd2}\cdot\hat{S}_{Cu5}\right) - 2\mathcal{J}_2\left(\hat{S}_{Cu3}\cdot\hat{S}_{Cu4}+\hat{S}_{Cu4}\cdot\hat{S}_{Cu5}\right) + g_{Gd}\mu_B\vec{B}\sum_{i=1}^{2}\overrightarrow{s_i} + g_{Cu}\mu_B\vec{B}\sum_{j=3}^{5}\overrightarrow{s_j}$$

In order to study the slow relaxation of the magnetisation in complex **7**, ac susceptibility measurements as a function of the frequency over the temperature range 1.9−5 K without an applied H_{dc} field were performed (see Fig 4.7). The ac studies show slow magnetic relaxation, associated with the presence of frequency−dependent out−of−phase maxima. Cole–Cole plots display a nearly symmetrical semi−circular shape, revealing that just one single relaxation process occurs in **7** (Fig 4.7). In light of this, the different relaxation times (τ) were treated using the Arrhenius law $\tau = \tau_0\exp(\Delta E/k_BT)$, to extract the pre−exponential factor τ_0 and the energy barrier $\Delta E/k_B$, yielding τ_0 = 1.3·10^{-7} s and $\Delta E/k_B$ = 21.4 ± 0.5 K

(see Fig 4.7). Moreover, the Cole–Cole fit displays a reasonably narrow distribution of α parameters in a temperature range of T = 1.9–3 K (0.09<α<0.12). The estimated τ_0 and $\Delta E/k_B$ values are comparable to those reported for other {LnCu} SMMs (see Table A4.3 of the Appendix).

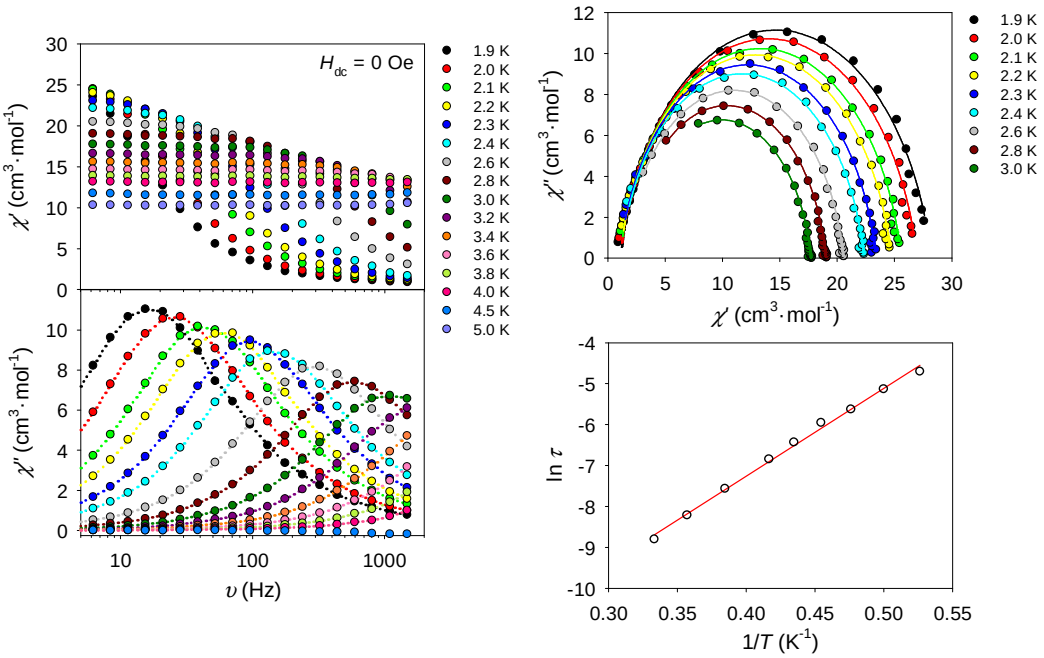

Fig 4.7 Dynamic magnetic properties for complex **7** (Tb). Left: ac magnetic susceptibility data at different frequencies in the absence of an external H_{dc} field. Right: Cole–Cole plots (top) and Arrhenius plot (bottom) from the ac susceptibility data. The solid lines correspond to the fit (see text for details).

Static and dynamic susceptibility measurements on complexes **8**–**12** were also performed to study whether the replacement of the auxiliary ligands has an effect on the magnetic properties of the {$Ln_2Cu_3(H_3L)_2$} family. The plots of $\chi_M T$ *vs.* T of **8**–**12** in an applied field of 1000 Oe are shown in Figure 4.8. The experimental values of $\chi_M T$ at 300 K for **8**–**12** are consistent with those expected for three uncoupled Cu(II) ions (S_{Cu} = 1/2, g_{Cu} = 2.11) and two Ln(III) ions (Gd^{3+} for **8**, Tb^{3+} for **9**, Dy^{3+} for **10**, Ho^{3+} for **11**, and Er^{3+} for **12**); see Table 4.4. The experimental $\chi_M T$ values slightly decrease along the temperature range from 300 to 60 K, excluding **8** (Gd) which increases. A sharp increase then takes place, until the $\chi_M T$ products reach maxima of 37.00 $cm^3 \cdot mol^{-1} \cdot K$ at 2.2 K (**11**), 42.78 $cm^3 \cdot mol^{-1} \cdot K$ at 6.5 K (**9**), 49.65 $cm^3 \cdot mol^{-1} \cdot K$ at 4.0 K (**10**), 41.16 $cm^3 \cdot mol^{-1} \cdot K$ at 3.4 K (**11**), and 38.33 $cm^3 \cdot mol^{-1} \cdot K$ (**12**) at 2.2 K. Below these temperatures the experimental $\chi_M T$ values drop to 36.70 $cm^3 \cdot mol^{-1} \cdot K$ (**8**), 35.73 $cm^3 \cdot mol^{-1} \cdot K$ (**9**), 46.43 $cm^3 \cdot mol^{-1} \cdot K$ (**10**), 39.21 $cm^3 \cdot mol^{-1} \cdot K$ (**11**), and 37.95 $cm^3 \cdot mol^{-1} \cdot K$ (**12**) at 2 K. Therefore, all the complexes show the ferromagnetic coupling previously displayed by **6** and **7**. The

field−dependent magnetisation measurements for **8**−**12** (Fig A4.1 of the Appendix) were not found to reach saturation for any of the complexes at 5 T. That could be caused again by the characteristic magnetic anisotropy from Tb (**9**), Dy (**10**), Ho (**11**) and Er (**12**) ions. The small deviation from the saturation value seen in **8** (M_{sat} = 17.17; M_{exp} = 16.29) may be a consequence of the change in the coordination environment of the Cu(II) ions compared to **6** (from square−based pyramidal to distorted octahedral geometry).

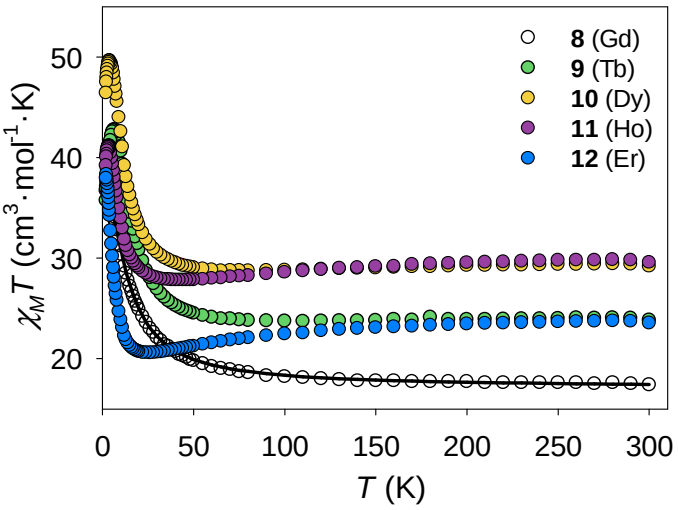

Fig 4.8 Temperature dependence of $\chi_M T$ for complexes **8**−**12** in an applied field of 1000 Oe. The black solid line corresponds to the fit for **8** (see text for details).

Table 4.4 Summary of the calculated ($\chi_M T_{cal}$) and experimental ($\chi_M T_{exp}$) susceptibility values for **6**–**12** (at room temperature). *L*, *S*, g_J and ground spin term symbol are related to each lanthanide ion.

Complex	***L***	***S***	g_J	**GS term symbol**	$\chi_M T_{cal}$ **{Ln_2Cu_3}** (cm^3·mol^{-1}·K)	$\chi_M T_{exp}$ **{Ln_2Cu_3}** (cm^3·mol^{-1}·K)
6 (Gd)	0	7/2	2	$^8S_{7/2}$	17.00	17.84
7 (Tb)	3	3	3/2	$^7F_6$	24.89	24.62
8 (Gd)	0	7/2	2	$^8S_{7/2}$	17.00	17.45
9 (Tb)	3	3	3/2	$^7F_6$	24.89	23.83
10 (Dy)	5	5/2	4/3	$^6H_{15/2}$	29.59	29.19
11 (Ho)	6	2	5/4	$^5I_8$	29.39	29.57
12 (Er)	6	3/2	6/5	$^4I_{15/2}$	24.21	23.54

As both {$Gd_2Cu_3(H_3L)_2$} complexes **6** and **8** display isostructural metal−alkoxide cores, the fit of the dc data for **8** was performed (see Fig 4.8) using Eq. 4.1, yielding

$\mathcal{J}_1$ = 1.9 cm^{-1}, $\mathcal{J}_2$ = 16.7 cm^{-1} (R = 99.7%). The $g_{Cu,}$ g_{Gd} = g parameters were fixed at 2.11 and 2, respectively, during the fit and a small intermolecular interaction of $z\mathcal{J}' = -1.1 \cdot 10^{-3}$ cm^{-1} was included. The parameters obtained from the fit are consistent with ferromagnetic exchange between both Cu···Cu centres, and Gd···Cu centres. The coupling constant $\mathcal{J}_1$ related to the interaction between Gd(III) and Cu(II) ions for complex **8** (1.9 cm^{-1}) is quite similar to that obtained for **6** (1.8 cm^{-1}). On the other hand, the $\mathcal{J}_2$ values corresponding to the Cu···Cu interaction are quite different (69.7 cm^{-1} for **6**, 16.7 cm^{-1} for **8**). An explanation for the weakening of the ferromagnetic Cu···Cu interaction may be related to structural differences between compounds **6** and **8** as a consequence of the replacement of CH_3COO^- for NO_3^- anions (Tables 4.1, 4.2). The Cu(II) centres are closer together in the case of **6**, and also the Cu−μ_3O−Cu' angles are slightly smaller.

The dynamic studies for **9**–**12** (over the temperature range 1.8−8 K at H_{dc} = 0) reveal a similar behaviour for all the compounds, where the appearance of a frequency dependent out−of−phase signal suggests SMM behaviour (see Fig 4.9, 4.10−4.12). In the Cole−Cole plots of complex **9** it can be seen that the relaxation of the magnetisation occurs again via a single relaxation process (α < 0.29, see Fig 4.9). The parameters extracted from the Arrhenius law for **9** are $\tau_0 = 1.0 \cdot 10^{-7}$ s and $\Delta E/k_B$ = 36.0 ± 0.2 K.

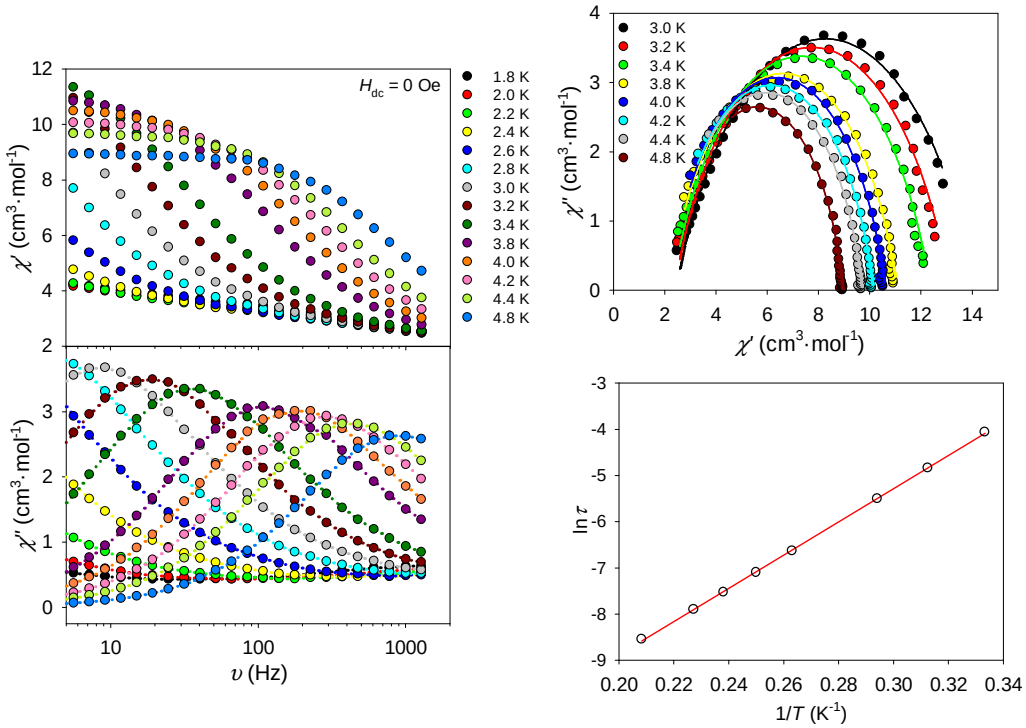

Fig 4.9 Dynamic magnetic properties for complex **9** (Tb). Left: ac magnetic susceptibility data at different frequencies in the absence of an external H_{dc} field. Right: Cole–Cole plots (top) and Arrhenius plot (bottom) from the ac susceptibility data. The solid lines correspond to the fit (see text for details).

The substitution of the three chelating acetate ligands for two chelating nitrates, one monodentate nitrate and one MeOH ligand leads to a ~70% improvement of the effective energy barrier (21.4 K for **7**, 36.0 K for **9**). It should be noted that the $\Delta E/k_B$ value for **9** is the largest reported value so far for Tb/Cu−based SMMs in the absence of an applied H_{dc} field (see Table A4.3 of the Appendix). The enhancement of the anisotropy barrier may be attributed to changes in the electronic structure of the lanthanide ions due to changes in the local symmetry or crystal field effects related to the replacement of the auxiliary ligands.[11–13, 21]

To probe the SMM behaviour of **9**, single−crystal measurements were carried out. The measurements were performed by Prof. Wolfgang Wernsdorfer. Low temperature magnetisation versus field hysteresis loops are shown in Figure 4.10. Complex **9** shows SMM−typical sweep−rate−dependent hysteresis curves with non−zero coercivity. The coercivity displayed in the hysteresis loops decreases as the temperature rises, however only at low enough sweep rates (below 0.001 T/s) and high enough temperatures (above 1.8 K) can it be suppressed. The large step at about zero magnetic field is induced by resonant spin ground state tunnelling, which is often very strong for lanthanide compounds. At larger fields the spin relaxes via a direct relaxation process. Steps related to quantum tunnelling of the magnetisation are smeared out, as often observed for relatively large SMMs such as **9**.[22–24]

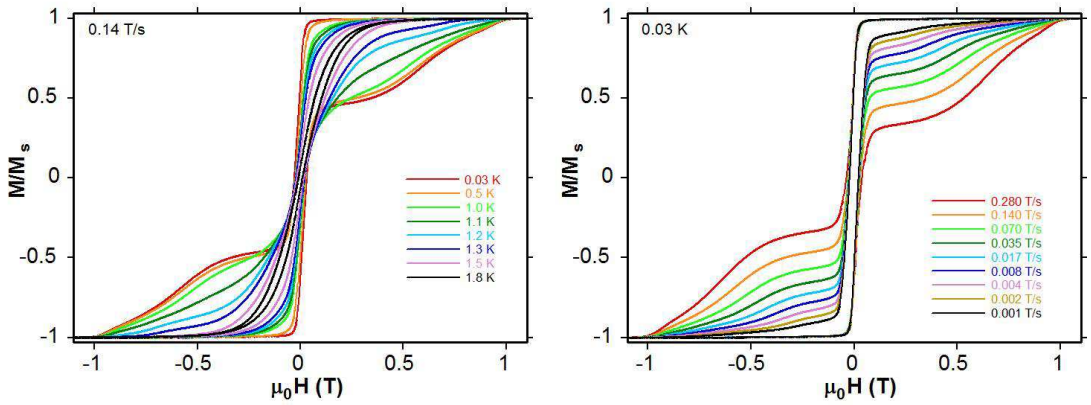

Fig 4.10 Single−crystal magnetisation *vs*. field hysteresis loops for **9**: with a constant field−sweep rate of 0.14 T/s at different temperatures between 0.03 and 1.8 K (left); at a constant temperature of 0.03 K with different sweep rates between 0.001 and 0.280 T/s (right).

Regarding the dynamic properties of **10**–**12**, the Kramer's−Kronig−derivate equation of the Arrhenius law $\ln(\chi''/\chi') = \ln(\omega\tau_0) + \Delta E/k_BT$ is applied,[25] either due to the lack of local χ'' maxima in the ac plots or the lack of a sufficient number of maxima to fit the Cole−Cole plots (see Fig 4.11–4.13), yielding the following pre−exponential factors and energy barriers: τ_0 = 7.5·10^{-8} s (**10**), 2.3·10^{-7} s (**11**), 1.2·10^{-7} s (**12**); and $\Delta E/k_B$ = 23.9 ± 0.1 K (**10**), 17.2 ± 0.2 K (**11**), 14.8 ± 0.1 K (**12**). Again, the estimated τ_0 and $\Delta E/k_B$ values are reasonable compared to those reported for similar {LnCu} SMMs (see Table A4.3 of the Appendix). There is a decrease of the effective barrier along the lanthanide series, with **9** showing the highest $\Delta E/k_B$ value, and **12** showing the lowest. This tendency is consistent with studies performed on 4*f*−based single−ion magnets that show the relationship between the atomic number of the lanthanide ions and the CF parameters (and thus SMM properties).[26]

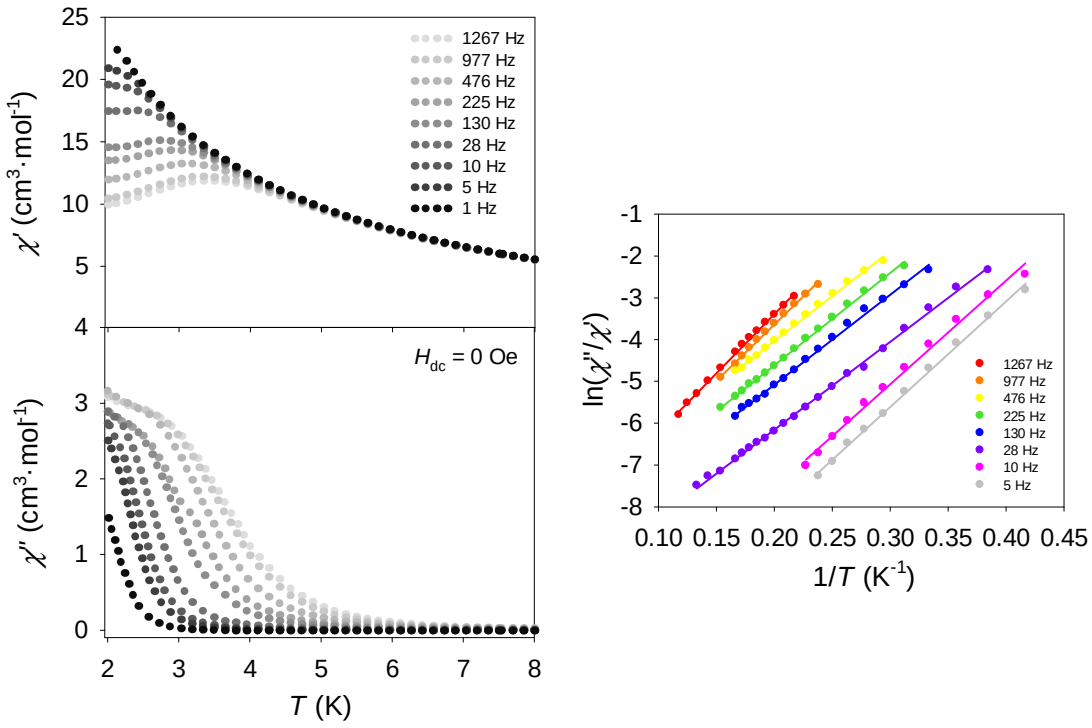

Fig 4.11 Ac magnetic susceptibility of **10** in the absence of an external dc field (left), and natural logarithm of χ'/χ'' vs 1/*T* at selected frequencies (right). Solid lines correspond to fits of the data. See text for details.[25]

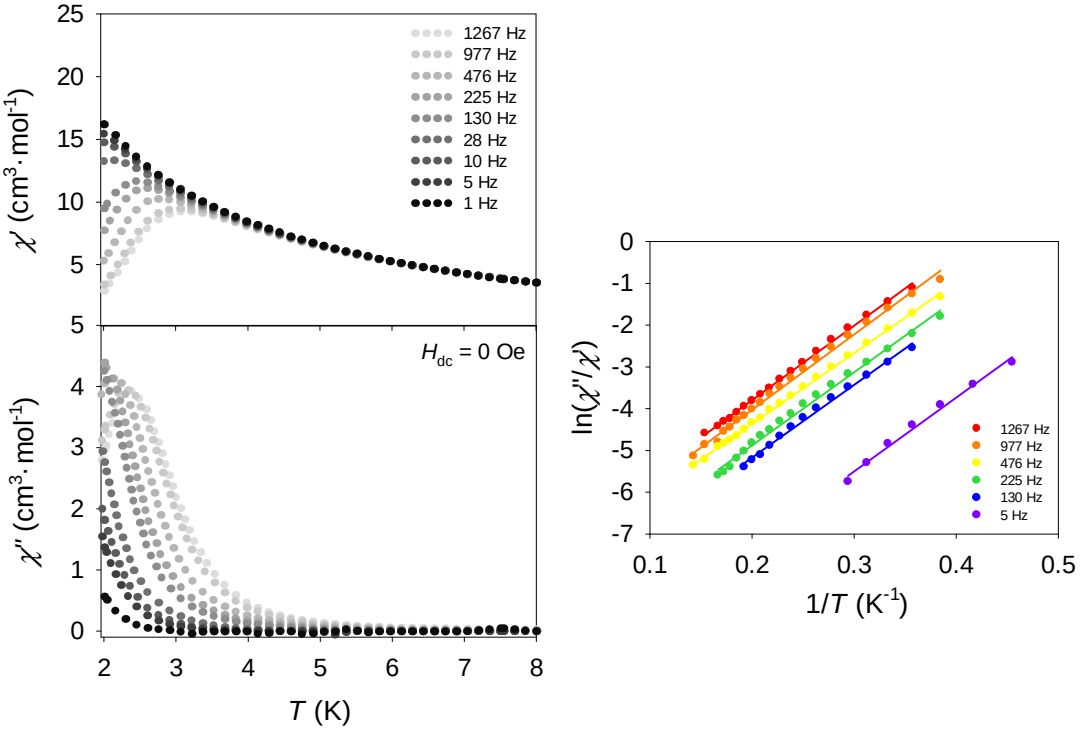

Fig 4.12 Ac magnetic susceptibility of **11** in the absence of an external dc field (left), and natural logarithm of χ'/χ'' vs 1/T at selected frequencies (right). Solid lines correspond to fits of the data. See text for details.[25]

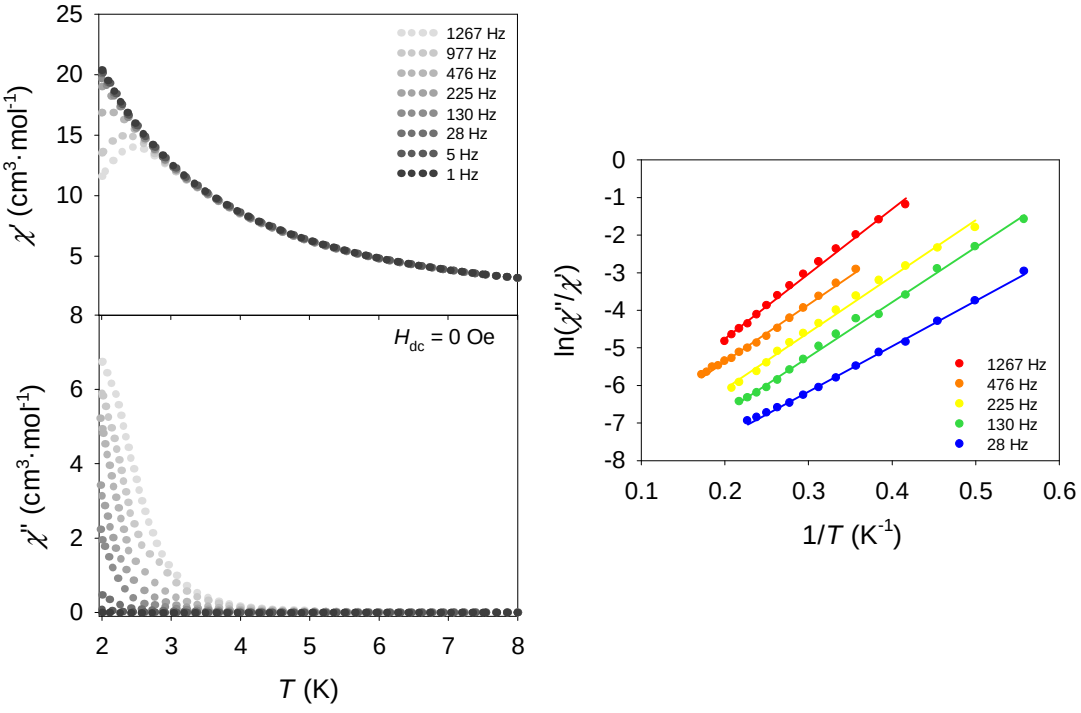

Fig 4.13 Ac magnetic susceptibility of **12** in the absence of an external dc field (left), and natural logarithm of χ'/χ'' vs 1/T at selected frequencies (right). Solid lines correspond to fits of the data. See text for details.[25]

Theoretical studies on model complexes of Tb analogues (**7** and **9**)

To understand the large barrier height observed for the Tb analogues and to probe the origin of the differences in the barrier height, mononuclear Tb(III) complexes derived from the X−ray structures of complexes **7** and **9** have been modelled. The theoretical studies were performed by Dr. Gunasekaran Velmurugan and Prof. Gopalan Rajaraman. The two Tb(III) ions in complex **7** are symmetry related and only one Tb(III) ion core (model−1) is considered. However, the Tb(III) ions present in complex **9** are different, hence two Tb(III) ions (model−2 and model−3) are considered for the calculations (see computational details and Fig A4.2 of the Appendix for further information). The energy spectrum *g* tensors, relative energies and angles (θ) of the principal anisotropy axes of the first excited states with respect to the ground state in all three model complexes are shown in Table 4.5. For complex **7**, as expected for the non−Kramer's ion, all the pseudo−doublets in model−1 are pure Ising−type. The ground pseudo−doublet possesses a g_z of 17.79 (see ground state g_z orientation in Fig 4.14), approaching that expected for a pure $m_J = \pm 6$ state of $g_z \sim 18$. A significant tunnel splitting (Δ_{tun}) is observed within the ground multiplet (0.45 cm^{-1}), suggesting that the magnetic bistability in **7** is not due to single−ion behaviour (see Table A4.4 of the Appendix).

Table 4.5 Calculated energy spectrum, *g* tensors, relative energies and angles (θ) of the principal anisotropy axes of the first excited states with respect to the ground state, for ground and excited state pseudo doublets (for model−1, model−2 and model−3).

Ground multiplet	**Complex 7 model−1**	**Complex 9 model−2**	**Complex 9 model−3**
g_x	0	0	0
g_y	0	0	0
g_z	17.79	17.80	17.72
Energy (cm^{-1})	0.00 and 0.45	0.00 and 0.08	0.0 and 0.32
1st excited multiplet	**Complex 7 model−1**	**Complex 9 model−2**	**Complex 9 model−3**
g_x	0	0	0
g_y	0	0	0
g_z	15.18	16.63	16.33
Energy (cm^{-1})	54.03 and 56.14	58.07 and 58.47	58.93 and 63.93
Angle (°)	153.62	56.48	86.29
U_{cal} (cm^{-1})	54.03	58.07	58.93

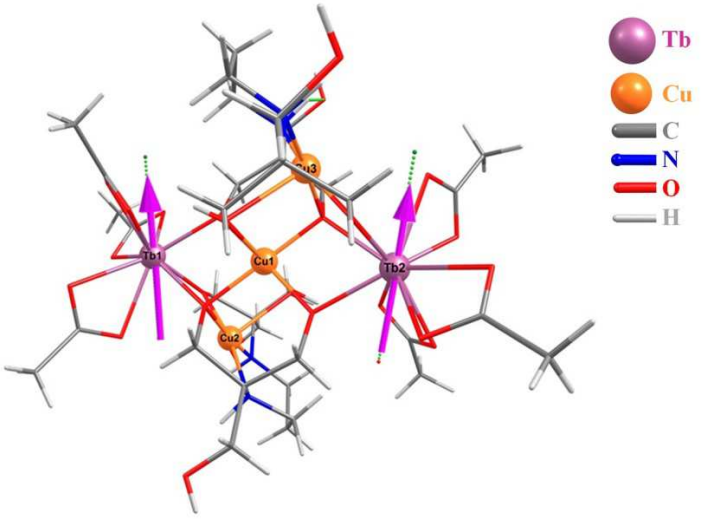

Figure 4.14 *Ab initio* computed orientation of the g_z tensor for the ground state Kramer's doublet in complex **7** shown with its crystal structure.

However the presence of both Cu···Cu and Cu···Tb interactions are likely to quench the tunnel splitting as they behave like an internal applied field, leading to the observation of zero−field SMM behavior.[27] If the tunnelling is quenched due to this effect, the relaxation is expected to occur via the first excited state of Tb(III) lying at 54 cm^{-1} (Table 4.5). This is due to the observation of a larger tunnel splitting for this level (Table A4.4 of the Appendix) and the g_z axis being tilted significantly compared to the ground state (see Table 4.5). Although this value is larger than the experimental estimate (14.9 cm^{-1}), the calculations performed do not take into account the effect of Cu···Tb exchange, intermolecular interactions and possible tunnelling between states. Therefore, it represents the maximum barrier if all the above−mentioned effects are eliminated. The orientation of the g_z tensor of the ground state pseudo−doublet intersects with the centre of the ligands in order to encounter the least electrostatic repulsion (see Fig 4.14). In contrast, for complex **9**, the tunnel splitting within the ground multiplet is small for model−2 (0.08 cm^{-1}) and significant for model−3 (0.32 cm^{-1}) (Tables A4.5 and A4.6 of the Appendix). This stems from the difference in the coordination geometry where model−2 has a muffin−like structure (C_s) while model−3 (and also model−1 of complex **7**) possess a capped square anti−prismatic geometry (C_{4v}) (see Table A4.1 of the Appendix). All the pseudo−doublets are computed to be pure Ising−type and the ground pseudo−doublet for this complex possesses g_z values of 17.80 and 17.72 (see ground state g_z orientation in Figure 4.15) respectively, approaching that expected for a pure $m_J = \pm 6$ state of $g_z \sim 18$. The tunnel splitting in the first excited pseudo−doublets are found to be 1.40 and 5.00 cm^{-1} for model−2 and model−3,

respectively (Tables A4.5, A4.6 of the Appendix). This gives the calculated energy barrier (U_{cal}) 58 and 59 cm^{-1} respectively to promote relaxation via this level. Our wave function analysis reveals the Tb(III) ground state as an admixture of 70% |±6> and small contributions from other m_J levels for all the complexes.

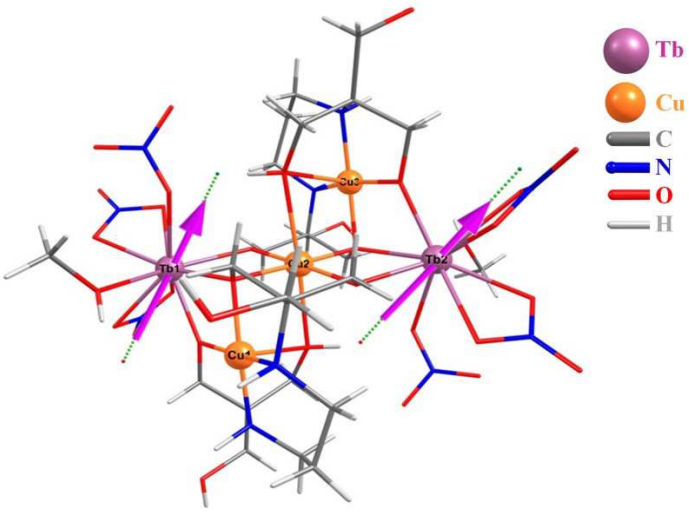

Figure 4.15 *Ab initio* computed orientation of g_z tensors for the ground state Kramer's doublets in complex **9** shown with its crystal structure.

The Cu···Tb exchange interaction is expected to quench the tunnelling behaviour as shown previously leading to the observation of zero−field SMM behaviour for complexes **7** and **9**.[28] The ground state axial (B_2^0 = 2.02, 1.88 and 1.99 for model−1, model−2 and model−3 respectively) and non−axial ($B_2^{-2,-1,+1,+2}$) crystal field parameters are competing with each other (see Table A4.7 of the Appendix) revealing the reasons for the relatively large tunnel splitting computed. Despite this, with the internal applied field from the Cu···Tb interactions we can observe SMM behaviour due to the Ising nature of the Tb ions. If the computed parameters for model−1 and model−3 are considered, it is apparent that the computed behaviour is very similar between these two models, despite the fact that model−1 has acetate ligands while model−3 has nitrate ligands. Although the chemical environments of the ligands are different, the geometry of both models are very close to each other (see Table A4.1 of the Appendix for shape analysis), leading to very similar computed behaviour. This suggests that the observed difference in the magnetic behaviour between complex **7** and complex **9** stems from one of the distorted Tb(III) ions in **9** possessing a muffin−like coordination geometry (C_s). A similar observation has been noted in previous works for Dy(III) SMMs.[29, 30] A similar environment, if created also for the second Tb(III) centre could improve further the SMM characteristics.

4.3. Concluding remarks

The potential of the ligand bis−tris propane has been shown to control and direct the assembly of the metal ions in the synthesis of Cu/4*f* complexes. The Cu(II) ions display a preference to occupy the inner {N_2O_2} pocket, leaving the hydroxyl arms to bind to further oxophilic−Ln(III) ions and Cu(II) ions. The synthesis of a new family of Cu/4*f* heterometallic complexes with general formula {$Ln_2Cu_3(H_3L)_2$}, and their structural and magnetic properties were discussed. All the complexes display ferromagnetic coupling in the static magnetic properties and the dynamic properties of each complex are dependent on two main factors: i) the choice of the lanthanide ion, and ii) the coordination environment of the 4*f* centres. Therefore, complexes with high−magnetic anisotropy Ln(III) ions, such as Tb^{3+} (present in **7**, **9**), Dy^{3+} (**10**), Ho^{3+} (**11**), and Er^{3+} (**12**) display the out−of−phase, frequency dependent ac signals characteristic of single−molecule magnets. Comparing the Tb−based complexes **7** and **9**, the ac studies show a considerable improvement (~70% increase) of the effective barrier. It should be also noted that complex **9** has the largest reported energy barrier for Tb/Cu−based SMMs, measured in the absence of a dc field. *Ab initio* CASSCF calculations performed on the mononuclear Tb(III) model complexes derived from complexes **7** and **9** suggest that the difference in the energy barrier arises from the structural variation around the Tb(III) ions (C_{4v} *vs.* C_s) and that the Cu···Tb exchange interactions help to quench the tunnelling leading to the observation of zero−field SMM behaviour.

References

1. V. A. Milway, F. Tuna, A. R. Farrell, L. E. Sharp, S. Parsons and M. Murrie, *Angew. Chem. Int. Ed.*, **2013**, *52*, 1949.
2. M. Heras Ojea, C. Wilson, S. J. Coles, F. Tuna and M. Murrie, *Dalton Trans.*, **2015**, *44*, 19275.
3. J.−P. Costes, F. Dahan and A. Dupuis, *Inorg. Chem.*, **2000**, *39*, 5994.
4. T. Shimada, A. Okazawa, N. Kojima, S. Yoshii, H. Nojiri and T. Ishida, *Inorg. Chem.*, **2011**, *50*, 10555.
5. J. Cirera and E. Ruiz, *C. R. Chim.*, **2008**, *11*, 1227.
6. C. Benelli and D. Gatteschi, *Chem. Rev.*, **2002**, *102*, 2369.
7. K. Liu, W. Shi and P. Cheng, *Coord. Chem. Rev.*, **2015**, *289–290*, 74.
8. F. J. Kettles, V. A. Milway, F. Tuna, R. Valiente, L. H. Thomas, W. Wernsdorfer, S. T. Ochsenbein and M. Murrie, *Inorg. Chem.*, **2014**, *53*, 8970.
9. L. Rosado Piquer and E. C. Sañudo, *Dalton Trans.*, **2015**, *44*, 8771.
10. D. N. Woodruff, R. E. P. Winpenny and R. A. Layfield, *Chem. Rev.*, **2013**, *113*, 5110.
11. J. Luzon and R. Sessoli, *Dalton Trans.*, **2012**, *41*, 13556.
12. S. K. Langley, N. F. Chilton, B. Moubaraki and K. S. Murray, *Chem. Commun.*, **2013**, *49*, 6965.
13. Y. Peng, V. Mereacre, A. Baniodeh, Y. Lan, M. Schlageter, G. E. Kostakis and A. K. Powell, *Inorg. Chem.*, **2016**, *55*, 68.
14. S. K. Langley, N. F. Chilton, B. Moubaraki and K. S. Murray, *Inorg. Chem.*, **2013**, *52*, 7183.
15. M. Heras Ojea, V. A. Milway, G. Velmurugan, L. H. Thomas, S. J. Coles, C. Wilson, W. Wernsdorfer, G. Rajaraman and M. Murrie, *Chem. Eur. J.*, **2016**, *22*, 12839.
16. A. W. Addison, T. Nageswara Rao, J. Reedijk, J. van Rijn and G. C. Verschoor, *J. Chem. Soc., Dalton Trans.*, **1984**, *7*, 1349.
17. M. Pinsky and D. Avnir, *Inorg. Chem.*, **1998**, *37*, 5575.
18. A. Ruiz−Martínez, D. Casanova and S. Alvarez, *Chem. Eur. J.*, **2008**, *14*, 1291.
19. A. Ruiz−Martinez, D. Casanova and S. Alvarez, *Dalton Trans.*, **2008**, *19*, 2583.
20. P. de Hoog, P. Gamez, O. Roubeau, M. Lutz, W. L. Driessen, A. L. Spek and J. Reedijk, *New J. Chem.*, **2003**, *27*, 18.
21. J. Zhu, C. Wang, F. Luan, T. Liu, P. Yan and G. Li, *Inorg. Chem.*, **2014**, *53*, 8895.
22. T. C Stamatatos, K. A. Abboud, W. Wernsdorfer and G. Christou, *Angew. Chem. Int. Ed.*, **2007**, *46*, 884.
23. V. Baskar, K. Gopal, M. Helliwell, F. Tuna, W. Wernsdorfer and R. E. P. Winpenny, *Dalton Trans.*, **2010**, *39*, 4747.
24. A. J. Tasiopoulos, A. Vinslava, W. Wernsdorfer, K. A. Abboud and G. Christou, *Angew. Chem. Int. Ed.*, **2004**, *43*, 2117.
25. J. Bartolomé, G. Filoti, V. Kuncser, G. Schinteie, V. Mereacre, C. E. Anson, A. K. Powell, D. Prodius and C. Turta, *Phys. Rev. B*, **2009**, *80*, 014430.
26. N. Ishikawa, M. Sugita, T. Okubo, N. Tanaka, T. Iino and Y. Kaizu, *Inorg. Chem.*, **2003**, *42*, 2440.
27. A. Bhunia, M. T. Gamer, L. Ungur, L. F. Chibotaru, A. K. Powell, Y. Lan, P. W. Roesky, F. Menges, C. Riehn and G. Niedner−Schatteburg, *Inorg. Chem.*, **2012**, *51*, 9589.
28. X.−C. Huang, V. Vieru, L. F. Chibotaru, W. Wernsdorfer, S.−D. Jiang and X.−Y. Wang, *Chem. Commun.*, **2015**, *51*, 10373.
29. K. R. Vignesh, S. K. Langley, B. Moubaraki, K. S. Murray and G. Rajaraman, *Chem. Eur. J.*, **2015**, *21*, 16364.
30. S. K. Gupta, T. Rajeshkumar, G. Rajaraman and R. Murugavel, *Chem. Sci.*, **2016**, *7*, 5181.

Chapter 5

Contents

5. Elucidating the nature of the spin interactions in a structurally exceptional Ln^{III}–Cu^{II} family

5. Elucidating the nature of the spin interactions in a structurally exceptional Ln^{III}–Cu^{II} family

The interesting properties displayed by the first 3*d*−4*f* SMM (*i.e*. $[Cu^{II}LTb^{III}(hfac)_2]_2$; H_3L = 1−(2−hydroxybenzamido)−2−(2−hydroxy−3−methoxybenzylideneamino)-ethane, Hhfac = hexafluoroacetylacetone) were a major breakthrough in molecular magnetism, establishing the advantages of the combined use of transition metal ions and rare earth ions in the design of SMMs.[1-3] As previously explained, the large single−ion anisotropy and number of unpaired electrons present in lanthanide ions, as well as the tendency for Cu···4*f* ions to couple ferromagnetically provides high−spin ground states and could lead to the slow relaxation of the magnetisation within the complex.[3-10] Regarding the understanding of the magnetic exchange between Cu(II) and 4*f* ions, Gd/Cu−based complexes have been probably the most widely investigated, since the analysis of their magnetic properties is much simplified compared to other lanthanides due to the non−orbital contribution of Gd(III) ions (L = 0).[6, 8, 11] However, the relationship between the spin interaction and overall magnetic properties in mixed 3*d*−4*f* high−nuclearity complexes remains a subject of intense study. Previous work based on new Cu/Ln SMMs using the bis−tris propane ligand (H_6L) showed the key influence of the co−ligands used in the synthetic route in the magneto−structural parameters that define the overall magnetic properties (see Chapter 4).[12] Consequently, we believe that exploring alternative auxiliary ligands to those previously used is an interesting idea. The use of different co−ligands (ClO_4^-, Cl^-) allows the synthesis of a new family of Cu/4*f* heterometallic complexes. The new systems display a genuinely original topology, which is almost unique, as there is only one similar structure published, making the study of the magnetic properties very attractive.

The synthesis of the new heterometallic systems $[LnCu_4(H_4L)_4](Cl)_2(ClO_4)$ (Ln = Gd, Tb, Dy, La), and a complete magneto−structural analysis is presented in this chapter. The understanding of the observed magnetic properties is developed by density functional calculations (DFT) on the exchange interaction between Cu···Gd, Cu···Cu and Cu···La ions.

5.1. Synthesis

$[GdCu_4(H_4L)_4](Cl)_2(ClO_4)\cdot 6CH_3OH$ (**13**): H_6L (1.41g, 5 mmol) and Et_3N (1.39 mL, 10 mmol) were consecutively added to a solution of $GdCl_3\cdot 6H_2O$ (0.38 g, 1 mmol) in MeOH (154 mL), resulting in a white suspension. $Cu(ClO_4)_2\cdot 6H_2O$ (1.86 g, 5 mmol) was then added, and immediately dissolved, giving a dark violet solution. The solution was stirred and heated up to 60°C for 3 h. The initial dark violet solution turned purple. Purple plate−like single crystals suitable for X−ray diffraction were obtained by vapour diffusion of Et_2O into the reaction solution over one week. Yield 74% (1.26 g). IR: $\bar{\upsilon}$ (cm^{-1}) = 3227, 2880, 1738, 1425, 1267, 1040, 1074, 878, 623. Elemental analysis ($[GdCu_4(H_4L)_4](Cl)_2(ClO_4)\cdot 3.5H_2O$) [%], found: C 29.79, H 5.72, N 6.24; calc: C 29.92, H 5.88, N 6.34.

$[TbCu_4(H_4L)_4](Cl)_2(ClO_4)\cdot 6CH_3OH$ (**14**): The same synthetic procedure described for **13** was followed, but using $TbCl_3\cdot 6H_2O$ instead of $GdCl_3\cdot 6H_2O$. Yield 71% (1.49 g). IR: $\bar{\upsilon}$ (cm^{-1}) = 3219, 2882, 1738, 1425, 1072, 1013, 880, 673, 623. Elemental analysis ($[TbCu_4(H_4L)_4](Cl)_2(ClO_4)\cdot 5.5H_2O$) [%],C 28.9, H 5.55, N 6.03; calc: C 29.3, H 5.98, N 6.21.

$[DyCu_4(H_4L)_4](Cl)_2(ClO_4)\cdot 6CH_3OH$ (**15**): The same synthetic procedure described for **13** was followed, but using $DyCl_3\cdot 6H_2O$ instead of $GdCl_3\cdot 6H_2O$. Yield 42% (0.91 g). IR: $\bar{\upsilon}$ (cm^{-1}) = 3219, 2882, 1738, 1425, 1072, 1013, 880, 673, 623. Elemental analysis ($[DyCu_4(H_4L)_4](Cl)_2(ClO_4)\cdot 3H_2O$) [%], found: C 29.7, H 5.85, N 6.17; calc: C 29.64, H 5.93, N 6.25.

$[LaCu_4(H_4L)_4](Cl)_2(ClO_4)\cdot 6CH_3OH$ (**16**): The same synthetic procedure described for **13** was followed, but using $LaCl_3\cdot H_2O$ instead of $GdCl_3\cdot 6H_2O$. Yield 86% (0.20 g). IR: $\bar{\upsilon}$ (cm^{-1}) = 3231, 2880, 1643, 1425, 1072, 1020, 880, 673, 623. Elemental analysis ($[LaCu_4(H_4L)_4](Cl)_2(ClO_4)\cdot 5.75H_2O$) [%], found: C 29.70, H 6.02, N 6.11; calc: C 29.55, H 6.06, N 6.27.

5.2. Results and discussion

As shown in Chapter 4, H_6L is a very useful tool for controlling the assembly of the metal ions towards the synthesis of Cu/Ln−SMMs.[12] A remarkable enhancement of the SMM properties was shown by subtle modifications of the coordination environment of the Ln ions in {Ln_2Cu_3} complexes, promoted by the replacement of the co−ligands (OAc^-, NO_3^-) used during the synthetic procedure. In this chapter the effect of using non−coordinating and/or monodentate co−ligands, such as perchlorates or chlorides is investigated. Applying a very similar synthetic route to those published for {$Ln_2Cu_3(H_3L)_2X_n$} (when X = OAc^-, Ln = Gd, Tb or when X = NO_3^-, Ln = Gd, Tb, Dy, Ho, Er) a new family of Cu/4*f* complexes has been successfully synthesised. However, the new $[LnCu_4(H_4L)_4](Cl)_2(ClO_4)$ systems (Ln being Gd (**13**), Tb (**14**), Dy (**15**) or La (**16**)) display an unusual and completely different topology to that observed when OAc^- and NO_3^- were used. The oxophilic nature of lanthanides may explain to some extent the new metal arrangement: the substitution of oxo−donor co−ligands (OAc^-, NO_3^-) by Cl^- and ClO_4^- could promote the coordination of the {$Cu(H_6L)$} units around the Ln ions at the expense of Cl^-.

X−ray crystallographic analysis

Selected crystallographic experimental details for complexes **13**−**16** are shown in Table 5.3. The complexes crystallise in the monoclinic space group *C*2/*c*. The asymmetric unit of all the compounds contents a half cation of $[LnCu_4(H_4L)_4]^{3+}$, a chloride anion, a half perchlorate anion, and three lattice molecules of methanol. As the cations $[LnCu_4(H_4L)_4]^{3+}$ of **13**−**16** are isostructural, the following description applies to all the complexes.

The crystal structure of $[LnCu_4(H_4L)_4]^{3+}$ displays four {$Cu(H_4L)$} units surrounding one central Ln(III) ion. Each {$Cu(H_4L)$} moiety binds to the Ln centre by the coordination of two *μ*−O from the doubly deprotonated H_4L^{2-} ligand (see Fig 5.1). The symmetry analyses of the octa−coordinated Ln(III) ions were performed by calculating Continuous Shape Measures (CShMs), proposing the square antiprism (D_{4d}) as the closest ideal geometry in the four complexes (see CShMs results in Table A5.1 of the Appendix).[13, 14] Each Cu(II) ion occupies the inner {N_2O_2} pocket of one H_4L^{2-} ligand, presenting two different coordination environments depending on the number of bonding O atoms (see Fig 5.1). Therefore two Cu(II) ions display a square−planar (Sp) geometry due to the coordination of two N from H_4L^{2-} and two *μ*−O from H_4L^{2-}, whereas the two others show a distorted square−based pyramidal

(Sbp) geometry (τ_{Cu} = 0.19 (**13**), 0.21 (**14**), 0.21 (**15**), 0.17 (**16**))[12, 15] due to the coordination of an additional H_4L^{2-} O atom. The intramolecular distances between the different metal centres vary from $d^{Avg}_{(Cu1\cdots Cu2)}$ = 4.761(5) Å−4.874 (6) Å; $d^{Avg}_{(Cu\cdots Cu)}$ = 6.309(6) Å−6.471(6) Å; $d_{(Cu1\cdots Ln1)}$ = 3.242(8) Å−3.313(9) Å; and $d_{(Cu2\cdots Ln1)}$ = 3.295(4) Å−3.383(9) Å (see Table 5.1). Two Cu−O−Ln average angles can be distinguished considering the geometry of the Cu(II) ion. Consequently the Cu1−O−Ln angles lie between 93.95(6)° and 94.75(7)°, while the values for Cu2−O−Ln are notably larger (100.75(6)°–101.45(10)°). The complexes show the same feature for the Cu−O···O−Ln average torsion angles (see Table 5.2): Cu1−O···O−Ln values are smaller (from 134.87(3)° to 136.68(1)°) compared to those displayed for Cu2−O···O−Ln (from 160.08(3)° to 161.06(1)°). The dependence of bridging angles and torsion angles related to the environment around the Cu centres is reasonable, as Cu2 is sterically more hindered than Cu1.

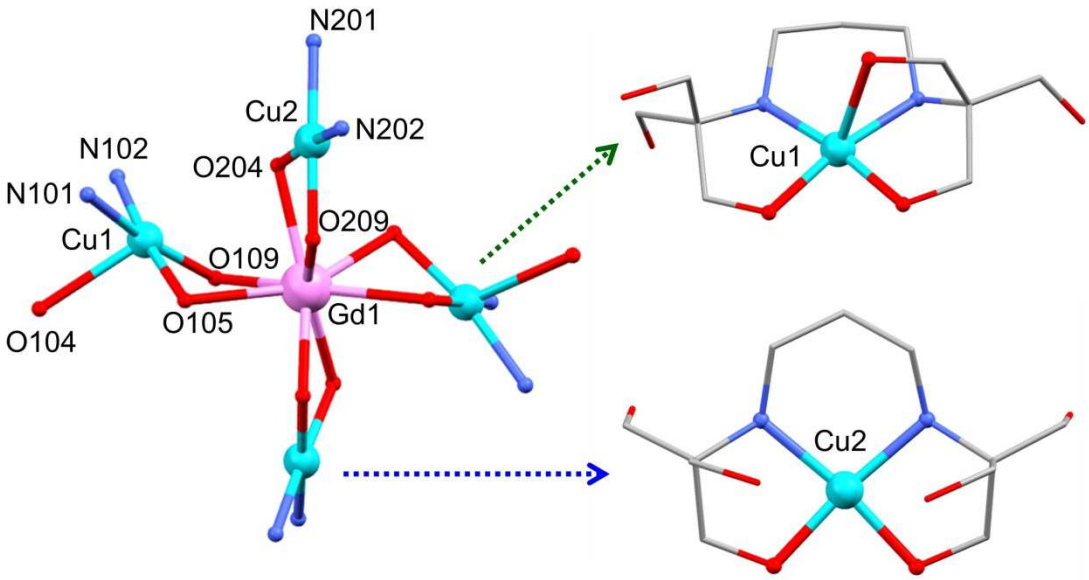

Fig 5.1 Structure of the cation (left) and detail (right) of **13**. C, grey; Cu, turquoise; Gd, pink; N, blue; O, red. Hydrogen atoms, solvent and counterion molecules are omitted for clarity. Only crystallographically unique Cu, Gd, N and O atoms are labelled.

These {LnCu$_4$} systems display an exceptional molecular assembly, as there is only one structure with a similar topology based on {LnCu$_4$O$_8$}−like reported structures, where the four Cu(II) ions enclose a central lanthanide (CSD 5.38, April 2017).[16] However, the compound previously mentioned[16] has all the Cu(II) centres in a square−planar environment, whereas **13**–**16** show alternating square−planar and square−based pyramidal geometries. That might be the cause of the differences displayed in angles, torsions, and symmetry of the Ln(III) ions between the two complexes. The dissimilar structural parameters could also involve changes

in the exchange interactions between Cu···Cu and/or Cu···Ln, and therefore in the magnetic behaviour of $[LnCu_4(H_4L)_4](Cl)_2(ClO_4)$. Finally, given that relatively minor modifications on the Ln symmetry can promote drastic changes in the overall magnetic properties of the complex,[12] an accurate magnetic study based on direct−(dc) and alternating−current (ac) experiments of the $[LnCu_4(H_4L)_4](Cl)_2(ClO_4)$ family, and DFT calculations of the Gd (**13**) and La (**16**) analogues has been performed.

Table 5.1 Summary of the average intramolecular distances between metal ions for complexes **13**–**16**.

Complex	$d^{Avg}_{(Cu1\cdots Cu2)}$/Å	$d^{Avg}_{(Cu\cdots Cu)}$/Å	$d_{(Cu1\cdots Ln1)}$/Å	$d_{(Cu2\cdots Ln1)}$/Å
13 (Gd)	4.777(6)	6.332(1)	3.250(2)	3.311(5)
14 (Tb)	4.766(7)	6.318(7)	3.242(8)	3.304(7)
15 (Dy)	4.761(5)	6.309(6)	3.242(3)	3.295(4)
16 (La)	4.874(6)	6.471(6)	3.313(9)	3.383(9)

Table 5.2 Summary of structural parameters of **13**−**16**: geometry around the Cu(II) centres (Cu1, Cu2), Cu−O−Ln angles, Cu−O···O−Ln torsion angles, and dihedral angles (*α*). Note Sbp means square−based pyramidal geometry, and Sp means square−planar geometry.

Complex	Atom	Coord. environment	Cu−O−Ln (°)	Cu−O···O−Ln (°)	*α* (°)
13 (Gd)	Cu1	Sbp	94.3(9)	135.83(20)	44.17
	Cu2	Sp	101.07(10)	160.61(21)	19.39
14 (Tb)	Cu1	Sbp	94.5(6)	136.18(13)	43.81
	Cu2	Sp	101.16(6)	160.74(14)	18.97
15 (Dy)	Cu1	Sbp	94.75(7)	136.68(1)	43.28
	Cu2	Sp	101.45(7)	161.06(1)	18.53
16 (La)	Cu1	Sbp	93.95(6)	134.87(3)	45.13
	Cu2	Sp	100.75(6)	160.08(3)	19.92

Table 5.3 Crystal Data and Structure Refinement Parameters of Complexes **13**−**16**.* Note that the data for **16** was collected by using a Cu−K*α* radiation source.

Complex	**13**	**14**	**15**	**16**
T/K	100(2)	100(2)	100(2)	100(2)
Crystal system	monoclinic	monoclinic	monoclinic	monoclinic
Space group	*C*2/*c*	*C*2/*c*	*C*2/*c*	*C*2/*c*
a/Å, *b*/Å, *c*/Å	32.405(2), 11.0450(6), 25.0948(17)	32.4050(7), 11.0378(2), 25.0517(5)	32.3685(8), 11.0392(2), 25.0804(6)	32.5448(19), 11.0401(3), 25.2051(15)
β/°	125.610(3)	125.632(1)	125.6170(10)	125.674(9)
V/Å^3	7302.0(8)	7282.9(3)	7285.3(3)	7356.7(9)
Z	4	4	4	4
ρ_{calc}/*g*/cm^3	1.724	1.7226	3.065	1.695
μ/mm^{-1}	2.150	2.216	4.463	7.460
F(000)	3916.0	3889.8	6912.0	3888.0
2*θ* range for data collection	3.092 to 50.322°	4 to 50.38°	3.338 to 48.596°	7.206 to 133.2°
Index ranges	−38 ≤ *h* ≤ 38, −13 ≤ *k* ≤ 13, −29 ≤ *l* ≤ 29	−38 ≤ *h* ≤ 38, −13 ≤ *k* ≤ 12, −29 ≤ *l* ≤ 29	−37 ≤ *h* ≤ 37, −12 ≤ *k* ≤ 12, −28 ≤ *l* ≤ 27	−38 ≤ *h* ≤ 34, −13 ≤ *k* ≤ 9, −21 ≤ *l* ≤ 30
Reflections collected	48082	12292	10957	11988
Data/restraints/ parameters	6489/484/499	6503/48/486	5647/46/499	6449/38/485
GOF on F^2	1.083	1.053	1.063	1.054
Final *R* indexes [$I \geq 2\sigma(I)$]	R_1 = 0.0492, wR_2 = 0.1003	R_1 = 0.0323, wR_2 = 0.0789	R_1 = 0.0358, wR_2 = 0.0793	R_1 = 0.0393, wR_2 = 0.1055
Final *R* indexes [all data]	R_1 = 0.0871, wR_2 = 0.1149	R_1 = 0.0458, wR_2 = 0.0842	R_1 = 0.0521, wR_2 = 0.0850	R_1 = 0.0410, wR_2 = 0.1073
Largest diff. peak/hole/e Å^{-3}	1.44/−0.98	1.06/−0.72	0.86/−0.72	1.29/−1.14

*: $[LnCu_4(H_4L)_4](Cl)_2(ClO_4)$ systems; Ln being Gd for **13**, Tb for **14**, Dy for **15** and La for **16**.

Magnetic properties

The magnetic susceptibility of **13**−**16** was explored by dc experiments in an applied field of 1000 Oe and a range of temperatures of *T* = 290–1.8 K (see Fig 5.2). The experimental values of $\chi_M T$ at room temperature for **13**−**16** are in accord with those expected for four isolated Cu(II) ions (S_{Cu} = 1/2, g_{Cu} = 2.11) and one Ln(III) ion (Gd^{3+} for **13**, Tb^{3+} for **14**, Dy^{3+} for **15**, La^{3+} for **16**); see Table 5.4 for additional information. The g_{Cu} = 2.11 value used to calculate the expected $\chi_M T$ products is consistent with that used in previous reported complexes presenting similar {$Cu(H_6L)$}

environments.[12, 17, 18] The dc measurements show that the magnetic behaviour of the complexes varies when the Ln centre is changed. Compound **13** (Gd) displays ferromagnetic coupling, as the experimental $\chi_M T$ product increases with temperature, reaching a maximum of 10.61 cm^3·mol^{-1}·K at 20 K. Below 20 K the $\chi_M T$ value drops to 8.47 cm^3·mol^{-1}·K at 1.8 K. EDX was performed on a bulk crystalline sample of **13** in order to investigate the homogeneity of the bulk sample, thus ruling out any Cu−monomeric impurity (Fig 5.3). The average Gd:Cu ratio found is 1:4 (Avg. Atomic% Gd:Cu is 19.2(3):80.8(3)), which is consistent with that established by single−crystal XRD. Further EDX map analysis by using different colour schemes for Cu (red) and Gd (green) was performed to establish the distribution of the metal ions in the sample (Fig 5.3 top, left). This reveals the even distribution of Gd/Cu in the crystalline bulk sample (Avg. Atomic% Gd:Cu is 1.01:4.06).

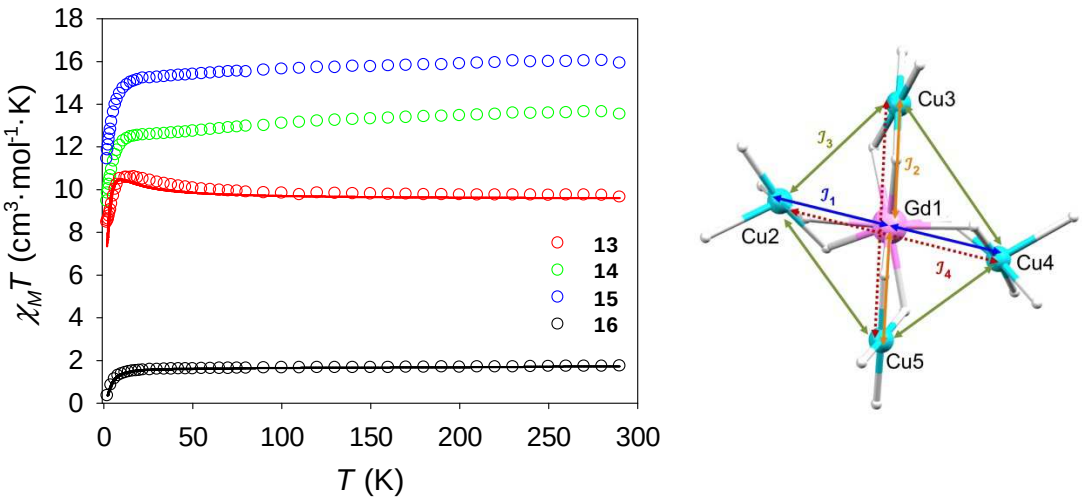

Fig 5.2 Temperature dependence of $\chi_M T$ for **13** (Gd), **14** (Tb), **15** (Dy) and **16** (La) in an applied field of 1000 Oe (left), and magnetic model used for the DFT calculation of **13** (right). The solid lines correspond to the fit for **13** and **16** (see next section in the text for details).

In contrast, **14** (Tb) and **15** (Dy) display a moderate decrease of the $\chi_M T$ values along the temperature range 290−15 K (from 13.53 cm^3·mol^{-1}·K to 12.47 cm^3·mol^{-1}·K for **14**, and 15.91 cm^3·mol^{-1}·K to 15.02 cm^3·mol^{-1}·K for **15**). That could be related to the temperature depopulation of the Stark sub−levels due to crystal field effects. A sharp decrease then takes place, until the $\chi_M T$ products reach minima of 9.46 cm^3·mol^{-1}·K (**14**) and 11.44 cm^3·mol^{-1}·K (**15**) at 1.8 K. On the other hand, **16** (La) was studied in order to investigate the possible interactions between the different Cu(II) ions, since La(III) is diamagnetic. $\chi_M T$ decreases at low temperatures (below 20 K), reaching a minimum of 0.35 cm^3·mol^{-1}·K at 2 K. This

decrease is consistent with a small antiferromagnetic intramolecular Cu···Cu exchange, although the presence of weak antiferromagnetic intermolecular interactions cannot be discounted.

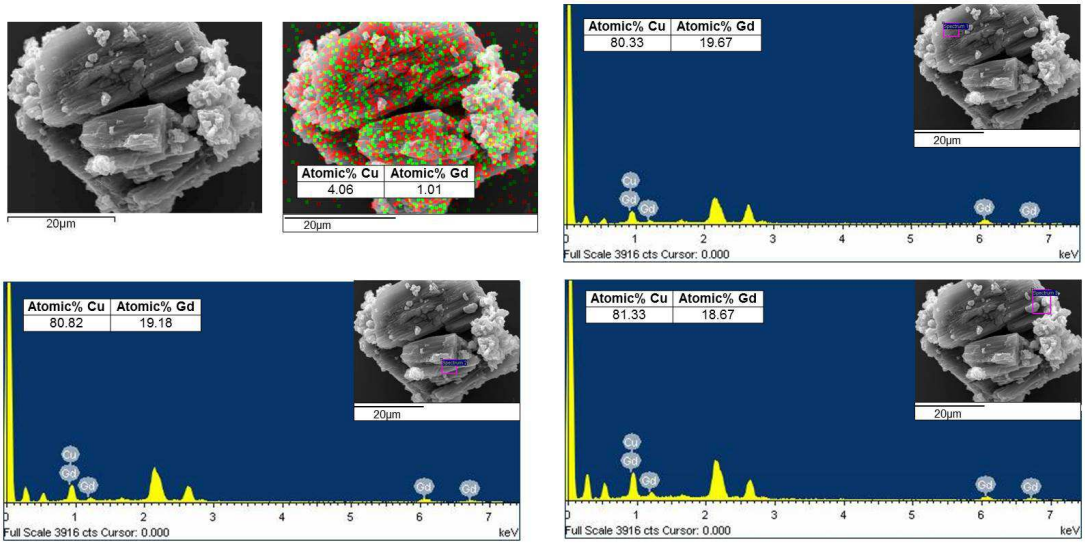

Fig 5.3 EDX spectra and elemental map (Cu, red; Gd, green) showing the distribution of Gd and Cu in a bulk sample of **13**. The inset displays the area of the sample used for the analysis; the Atomic% is shown for each area.

Table 5.4 Summary of the calculated ($\chi_M T_{cal}$) and experimental ($\chi_M T_{exp}$) susceptibility values for **13**–**16** (at room temperature). *L*, *S*, g_J and ground spin term symbol are related to each lanthanide ion.

Complex	***L***	***S***	g_J	**GS term symbol**	$\chi_M T_{cal}$ **{LnCu$_4$}** (cm^3·mol^{-1}·K)	$\chi_M T_{exp}$ **{LnCu$_4$}** (cm^3·mol^{-1}·K)
13 (Gd)	0	7/2	2	$^8S_{7/2}$	9.54	9.64
14 (Tb)	3	3	3/2	$^7F_6$	13.49	13.53
15 (Dy)	5	5/2	4/3	$^6H_{15/2}$	15.84	15.91
16 (La)*	–	–	–	–	1.67	1.73

*****Lanthanum does not have any 4*f* electrons. Therefore $\chi_M T_{cal}$ {LaCu$_4$} was calculated considering four isolated Cu(II) ions, S_{Cu} = 1/2 and g_{Cu} = 2.11.

Several experimental and theoretical studies based on Cu/Ln complexes prove the tendency of Cu···Gd for interacting ferromagnetically.[6-9] Previous work based on {Gd('O')$_2$Cu} complexes reveals the relationship between the nature of the Cu···Gd interaction ($\mathcal{J}$) and the dihedral angle, here described as *α*.[6] The dihedral angle is defined by the planes formed by the atoms involved in the magnetic exchange (see

Fig 5.4). The experiments show that the $\mathcal{J}$ value decreases when *α* becomes larger and may even display small negative values, *i.e*. weak antiferromagnetic exchange, when *α* ≥ 40°. For **13**−**16**, two non−equivalent Cu(II) atoms displaying different coordination environments could be distinguished, and thus two different magnetic pathways could be expected (see Fig 5.2 and Fig 5.4). Figure 5.4 shows geometrically equivalent Cu atoms (Sbp−Cu1 in green; Sp−Cu2 in blue) and their corresponding dihedral angles (*α*, in orange) defined within **13**. The *α* parameter from the planes defined by the square−based pyramidal Cu1 atom (green) and O105−Gd1−O109 (pink) display values close to 40° (see Table 5.2). In contrast, *α* values related to planes described by the square−based Cu2 atom (blue) and O204−Gd1−O209 (pink) are much smaller (range from 18.53 to 19.92°, see Table 5.2). Consequently we anticipate a stronger ferromagnetic Cu2···Gd1 exchange interaction ($\mathcal{J}_2$ in the magnetic model from Fig 5.2, right) compared to that displayed for Cu1···Gd1 ($\mathcal{J}_1$). These conclusions are in good agreement with the smaller values of the torsion angles for Cu1−O···O−Ln (~135°; see Table 5.2) compared to those displayed for Cu2−O···O−Ln (~160°).[8, 19, 20] A further interpretation of the different Cu···Cu and Cu···Gd magnetic interactions within **13** and **16** will be developed in the next section.

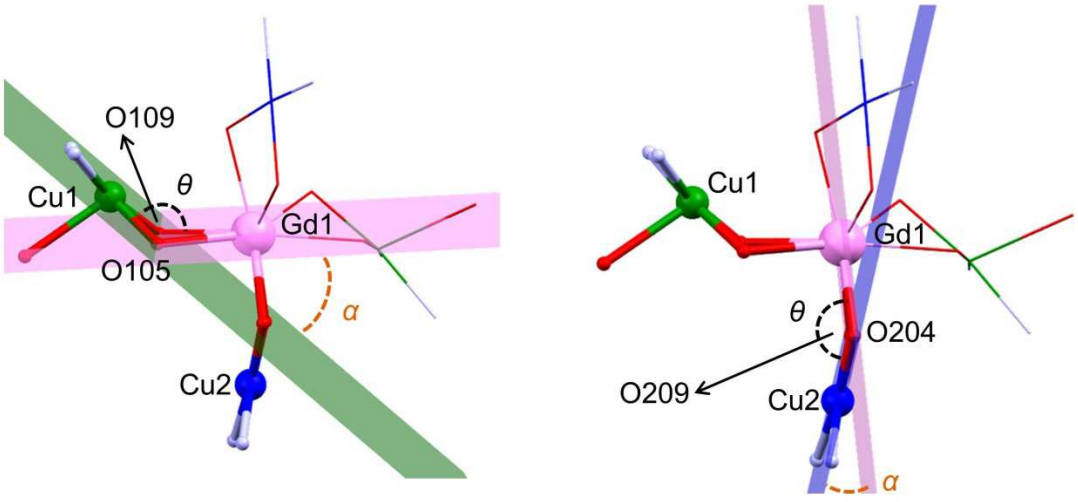

Fig 5.4 Detail of the crystal structure of **13**. Cu1, green; Cu2, blue; Gd, pale pink; N, lavender; O, red. The different planes are shown in green (O105−Cu1−O109), blue (O204−Cu2−O209), and pink (O105−Gd1−O109, O204−Gd1−O209).The dihedral (*α*) and the torsion (*θ*) angles are highlighted in orange and black respectively.

The dynamic properties of **14** and **15** were also investigated in order to see if the compounds with high−magnetic anisotropy Ln(III) ions, such as Tb^{3+} (**14**) and Dy^{3+} (**15**), would display any slow reversal of the magnetisation. Ac susceptibility studies were performed as a function of the frequency in the absence of dc field and under

different applied fields, at 2 K (for **14** and **15**) and over the temperature range of 1.8−5 K (**15**). Complex **14** displays the onset of an out−of−phase χ'' signal at zero dc field, however, the signal is very weak, and no enhancement was observed despite the application of an external field (see Fig A5.2, left in the Appendix). On the other hand, complex **15** shows a promising stronger χ'' signal at zero-field, which is improved under the influence of an external dc field (see Fig A5.2, right in the Appendix). That might result from the suppression of QTM within the {DyCu$_4$} molecule. The different dynamic properties between **14** and **15** arise due to the nature of the central Ln(III) ion. Dy(III) is a Kramer's ion, therefore its ground state is well described as a doublet. In contrast Tb(III) is a non−Kramer's ion, and thus its ground state depends on the axiality generated by crystal field effects.[4, 21-23] The effect of the dc field on **15** effectively improves the magnitude of the χ'' signal, however, it was not possible to shift the out−of−phase signal enough to see the maxima. The dynamics of **15** have been studied by the application of three different field strengths, H_{dc} = 1000 Oe shown in Figure 5.5, and 1500 Oe and 2000 Oe (in Fig A5.3 from the Appendix). All the experiments show slow relaxation of the magnetisation. Given the lack of local χ'' maxima in the ac plots, the relaxation rate (τ_0) and the energy barrier ($\Delta E/k_B$) parameters were calculated by using the Kramer's−Kronig−derivate equation of the Arrhenius law $\ln(\chi''/\chi') = \ln(\omega\tau_0) + \Delta E/k_B T$.[24]

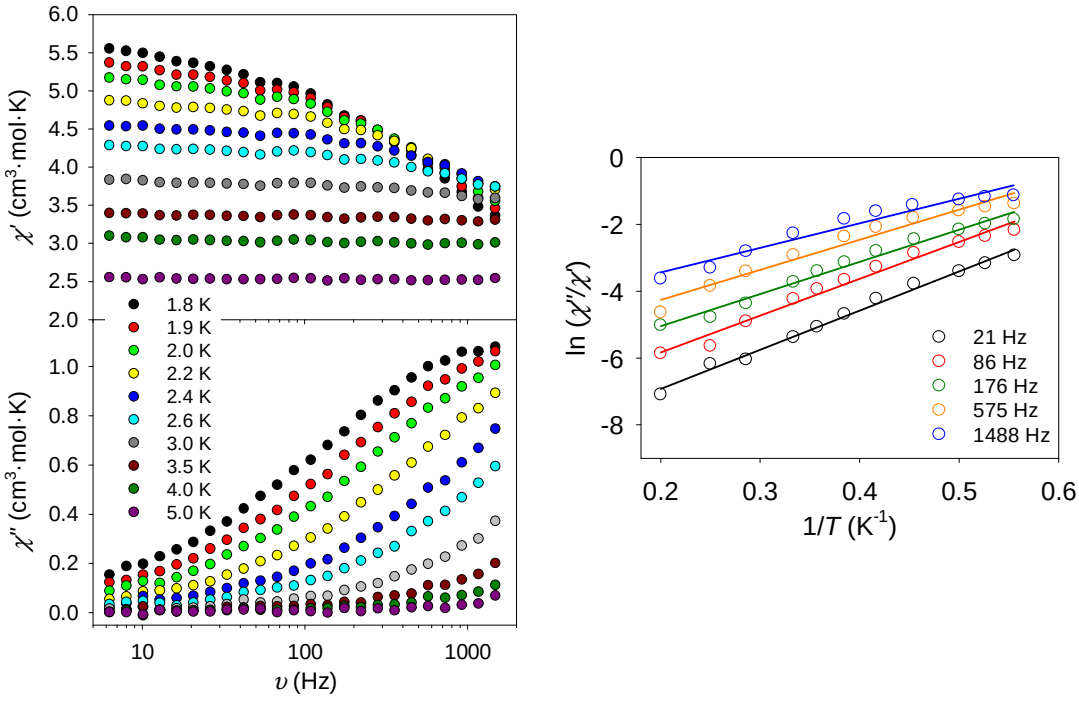

Fig 5.5 Ac magnetic susceptibility of **15** at H_{dc} = 1000 Oe (left), and natural logarithm of χ''/χ' $vs.$ $1/T$ (right) at selected frequencies (υ = 21, 86, 176, 575, 1488 Hz). Solid lines correspond to fits of the data.[24]

The fit of the experimental ac susceptibility gives the relaxation rates τ_0 = 7.2·10^{-7} s, 7.4·10^{-7} s and 8.8·10^{-7} s, and the energy barriers $\Delta E/k_B$ = 9.7 ± 0.2 K, 9.9 ± 0.3 K and 9.8 ± 0.3 K for fields of 1000, 1500 and 2000 Oe, respectively (see Fig A5.3 and Table A5.2 in the Appendix). The calculated τ_0 and $\Delta E/k_B$ values are reasonable compared to those reported for similar {LnCu} SMMs.[12]

Electronic structure calculations (preliminary results)

Electronic structure calculations have been carried out in order to analyse in detail the different exchange pathways between metal centres within {GdCu$_4$} (**13**) and {LaCu$_4$} (**16**). The calculations were performed by Dr. Jordi Cirera and Prof. Eliseo Ruiz from the Universitat de Barcelona. The Hamiltonian used to calculate the exchange interactions is $\hat{\mathcal{H}} = -\sum_{a<b}(J_{ab}\hat{S}_a\hat{S}_b)$ (see further computational details in the Appendix). As indicated in Figure 5.6 (left), compound **13** presents four different exchange pathways, $\mathcal{J}_1$ between Gd1−Cu2 and Gd1−Cu4, $\mathcal{J}_2$ between Gd1−Cu3 and Gd1−Cu5, $\mathcal{J}_3$ between Cu(II) in the *cis* configuration and $\mathcal{J}_4$ between those in the *trans* configuration. In compound **16** though, because La^{3+} has no *f* electrons, no exchange pathway is observed between La···Cu, and only $\mathcal{J}_3$ and $\mathcal{J}_4$ are considered (Fig 5.6, right). The computed values for the Gd···Cu coupling constants ($\mathcal{J}_1$ = −0.528 cm^{-1} and $\mathcal{J}_2$ = +2.549 cm^{-1}) are in good agreement with similar magnetic interactions previously reported for other Gd/Cu complexes.[6, 8, 25, 26]

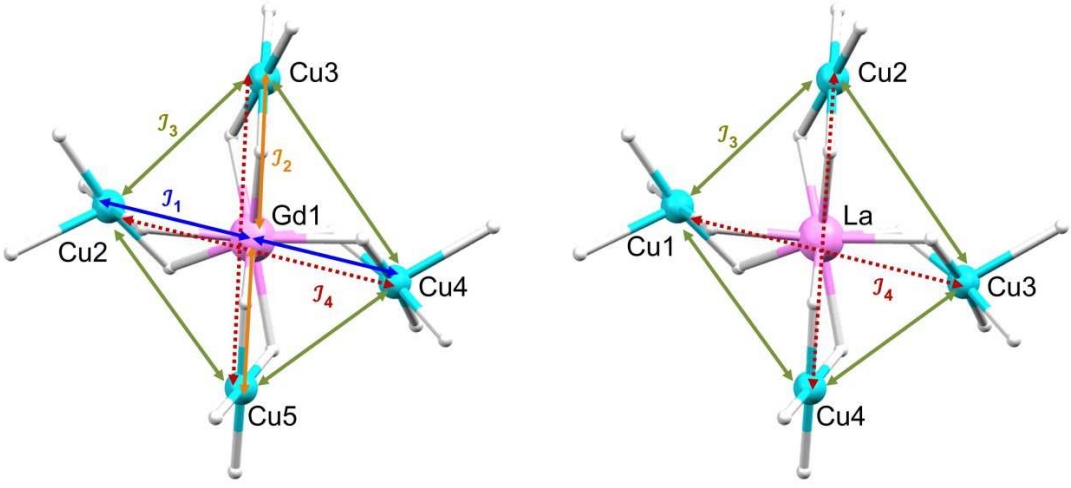

Fig 5.6 Magnetic model used for the DFT calculation of **13** (left) and **16** (right).

As mentioned before, the dihedral angle (*α*) is defined by the planes formed by the atoms involved in the magnetic exchange (see Fig 5.4). The computed $\mathcal{J}_1$, $\mathcal{J}_2$

values are also consistent with the structural features related to the Cu−Gd dihedral angles formerly discussed, *i.e*. the smaller dihedral angle, the stronger the tendency to be ferromagnetically coupled (*vide supra*). Therefore, the magnetic exchange between Cu(Sp)···Gd (Cu2, Cu4 in Fig 5.6, left) is ferromagnetic ($\mathcal{J}_2$ = +2.549 cm^{-1}), in good agreement with the relatively small *α* angle (19.39°) and large torsion (160.61(21)°). In contrast, the exchange interaction between Cu(Sbp)···Gd (Cu3, Cu5 in Fig 5.6, left) is weakly antiferromagnetic ($\mathcal{J}_2$ = −0.528 cm^{-1}), which is consistent with the large *α* value (44.17°) and the relatively smaller torsion (135.83(20)°).

Table 5.5 Summary of calculated Ln···Cu and Cu···Cu exchange interactions for {GdCu$_4$} (**13**) and {LaCu$_4$} (**16**) from DFT studies.

	13 (Gd)	Cu−O···O−Ln	Dihedral angle *α*	**16** (La)
$\mathcal{J}_1$ (Ln···Cu)	−0.528 cm^{-1}	135.83(20)°	44.17°	−
$\mathcal{J}_2$ (Ln···Cu)	+2.549 cm^{-1}	160.61(21)°	19.39°	−
$\mathcal{J}_3$ (Cu···Cu)	+1.741 cm^{-1}	−	−	−0.145 cm^{-1}
$\mathcal{J}_4$ (Cu···Cu)	−0.444 cm^{-1}	−	−	−0.093 cm^{-1}

The exchange interactions between Cu(II) ions ($\mathcal{J}_3$, $\mathcal{J}_4$) differ between **13** and **16**, resulting in a change of the nature of the coupling between *cis*−ions: from ferro− in **13** ($\mathcal{J}_3$ = +1.741 cm^{-1}) to antiferromagnetic in **16** (−0.093 cm^{-1}). The spin density plots for {GdCu$_4$} (**13**) and {LaCu$_4$} (**16**) show the different charge distribution within the molecule as a consequence of the replacement of the central Ln ion (Fig 5.7). The unpaired electrons of the Gd(III) ion in **13** seems to provide a greater spin delocalisation over the molecule. In contrast, the spin density for **16** is confined to the Cu(II) coordination environment due to the lack of *f* electrons in the La(III) ion. That is consistent with the stronger calculated values $\mathcal{J}_3$, $\mathcal{J}_4$ corresponding to the different intramolecular Cu···Cu interactions for **13** ($\mathcal{J}_3$ = +1.741 cm^{-1}, $\mathcal{J}_4$ = −0.444 cm^{-1}) compared to those for **16** ($\mathcal{J}_3$ = −0.145 cm^{-1}, $\mathcal{J}_4$ = −0.093 cm^{-1}). That might also explain the different coupling described by $\mathcal{J}_3$ in **13** and **16**. However, it is worth underlining that the interactions $\mathcal{J}_3$, $\mathcal{J}_4$ are very weak, hence the dissimilar values can arise from associated errors from the DFT calculations. In addition to these intramolecular interactions, the sharp drop in the $\chi_M T$ value at low temperatures for **13**−**16** suggests the presence of some intermolecular interactions.

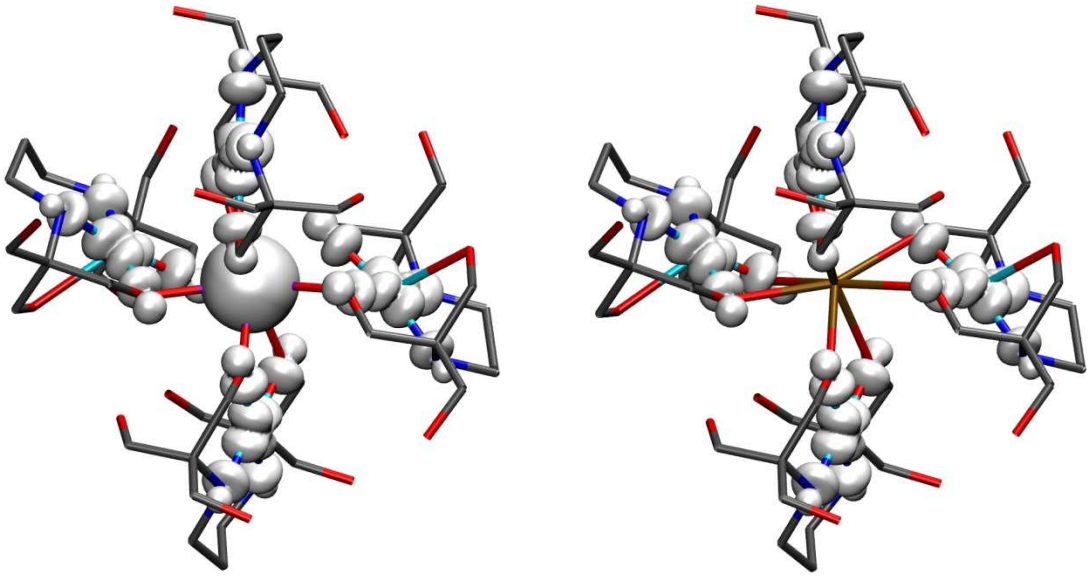

Fig 5.7 DFT computed spin density plots for {GdCu$_4$} (**13**, left) and {LaCu$_4$} (**16**, right).

These interactions, however, may differ slightly between both complexes, since they present dissimilar Van−der Waals interactions as a consequence of different crystal packing. Compound **16** displays H−bonds between OH(H_4L^{2-}) and NH(H_4L^{2-}) groups of different molecules, with a Cu···Cu distance of 7.436(1) Å (see Fig A5.5 in the Appendix). On the other hand, in complex **13** the interactions are *via* the Cl^- anion, OH(H_4L^{2-}) and NH(H_4L^{2-}) groups (see Fig A5.4 in the Appendix). That leads to an increase of the Cu···Cu distances (7.821(1) Å), and maybe to a weaker intermolecular interaction. A fit of the susceptibility experimental data of **13** and **16** is then performed to investigate the intermolecular interactions present in the crystal structures. Therefore, the value of the intermolecular interaction ($z\mathcal{J}'$) for **13** and **16** was extracted by using the program PHI,[27] giving consideration to the magnetic models displayed in Figure 5.6 and by applying the spin Hamiltonians shown in Equation 5.1 (**13**) and 5.2 (**16**). The computed $\mathcal{J}$ values from the DFT (see Table 5.5) were included as a fixed parameter during the fit. The best results give $z\mathcal{J}'$ = −0.027 cm^{-1} (R = 89.9%) for **13**, and −0.423 cm^{-1} (R = 92.3%) for **16**. As expected from the former analysis of the H−bonds in **13** and **16**, the fit suggests that the intermolecular interactions in the crystal structure of **16** are stronger to those in **13** (*i.e.* $z\mathcal{J}'$(La) > $z\mathcal{J}'$(Gd)).

Eq 5.1
$$\hat{\mathcal{H}} = -2\mathcal{J}_1\left(\hat{S}_{Gd1}\cdot\hat{S}_{Cu2}+\hat{S}_{Gd1}\cdot\hat{S}_{Cu4}\right)-2\mathcal{J}_2\left(\hat{S}_{Gd1}\cdot\hat{S}_{Cu3}+\hat{S}_{Gd1}\cdot\hat{S}_{Cu5}\right)-$$
$$2\mathcal{J}_3\left(\hat{S}_{Cu2}\cdot\hat{S}_{Cu3}+\hat{S}_{Cu3}\cdot\hat{S}_{Cu4}+\ \hat{S}_{Cu4}\cdot\hat{S}_{Cu5}+\hat{S}_{Cu5}\cdot\hat{S}_{Cu2}\right)-$$
$$2\mathcal{J}_4\left(\hat{S}_{Cu2}\cdot\hat{S}_{Cu4}+\hat{S}_{Cu3}\cdot\hat{S}_{Cu5}\right)+\ g_{Gd}\mu_B\vec{B}\vec{s}_{Gd}+g_{Cu}\mu_B\vec{B}\sum_{i=2}^{5}\vec{s}_i$$

Eq 5.2 $$\hat{\mathcal{H}} = -2\mathcal{J}_3\left(\hat{S}_{Cu1}\cdot\hat{S}_{Cu2} + \hat{S}_{Cu2}\cdot\hat{S}_{Cu3} + \hat{S}_{Cu3}\cdot\hat{S}_{Cu4} + \hat{S}_{Cu4}\cdot\hat{S}_{Cu1}\right) - 2\mathcal{J}_4\left(\hat{S}_{Cu1}\cdot\hat{S}_{Cu3} + \hat{S}_{Cu2}\cdot\hat{S}_{Cu4}\right) + g_{Cu}\mu_B\vec{B}\sum_{i=1}^{4}\vec{s}_i$$

The $g_{Cu,}$ g_{Gd} = g parameters were fixed at 2.11 and 2, respectively, during the fit and a temperature−independent paramagnetic term of TIP = $2\cdot10^{-4}$ cm$^3\cdot$mol^{-1} was also included for **16**. The results from the fit are consistent with the experimental $\chi_M T$ *vs*. *T* data as they correctly reproduce the observed magnetic tendency (see solid lines in Fig 5.2). Nevertheless, it should be stressed that these are preliminary results. Although the calculated values for the different Cu···Cu, Cu···Gd interactions are reasonable compared to those proposed for similar {CuGd} systems for previous experimental and computational works, they are not definitive. Supplementary calculations to get a better fit of both susceptibility and magnetisation experimental data are currently underway. In addition, inelastic neutron scattering (INS) spectroscopy experiments on [TbCu$_4$(H$_4$L)$_4$](Cl)$_2$(ClO$_4$) are also being performed to determine the magnetic interactions within the molecule by interpreting the observable transitions between exchange−split components of the ground state.

5.3. Concluding remarks

A thorough magneto−structural study has been performed on a family of new 3*d*−4*f* systems, $[LnCu_4(H_4L)_4](Cl)_2(ClO_4)$, displaying an uncommon topology. Auxiliary ligands play again a very important role over the assembly process of the {$Cu(H_4L)$} units and the lanthanide ions. The static magnetic studies performed on **13** (Gd) show that the Cu/Gd centres have a tendency to couple ferromagnetically. Furthermore, the measurements carried out on **16** (La) propose a weak antiferromagnetic coupling between the different Cu(II) ions and/or the presence of antiferromagnetic intermolecular interactions. The investigation of the dihedral angles (*α*) related to the Cu−Gd ions suggests different magnetic exchange pathways depending on the Cu(II) ion. According to that, a ferromagnetically interaction is expected between the Sp−Cu(II) ions and the Gd(III) ion (small *α*), whereas the Sbp−Cu(II) ions are likely to be weakly antiferromagnetically coupled to the Gd(III) ion (large *α*). Preliminary DFT calculations support both Cu−Gd interactions ($\mathcal{J}_1$ = −0.528 cm^{-1}, $\mathcal{J}_2$ = +2.549 cm^{-1}), as well as a weak interaction between the Cu(II) ions in **13** and **16**. The results from the theoretical calculations also indicate additional antiferromagnetic intermolecular interactions. The calculated spin density diagrams display a different charge delocalisation in **13** (Gd) and **16** (La) as a consequence of the substitution of the paramagnetic Gd(III) ion by the diamagnetic La(III) ion, which may explain the different magnitudes and signs in the Cu···Cu coupling constants calculated for **13** and **16**. The fit of the susceptibility experimental data of **13** and **16** proposes a stronger antiferromagnetic intermolecular interaction for **16** compared to that for **13**, in agreement with the different H−bonds seen in the crystal packing. The dynamic susceptibility measurements show that only **15** (Dy) displays slow magnetic relaxation. Future INS studies may help to shed light on the different dynamics observed between **14** (Tb) and **15** (Dy).

References

1. S. Osa, T. Kido, N. Matsumoto, N. Re, A. Pochaba and J. Mrozinski, *J. Am. Chem. Soc.*, **2004**, *126*, 420.
2. T. Hamamatsu, K. Yabe, M. Towatari, S. Osa, N. Matsumoto, N. Re, A. Pochaba, J. Mrozinski, J.-L. Gallani, A. Barla, P. Imperia, C. Paulsen and J.-P. Kappler, *Inorg. Chem.*, **2007**, *46*, 4458.
3. L. Rosado Piquer and E. C. Sañudo, *Dalton Trans.*, **2015**, *44*, 8771.
4. D. N. Woodruff, R. E. P. Winpenny and R. A. Layfield, *Chem. Rev.*, **2013**, *113*, 5110.
5. J. Luzon and R. Sessoli, *Dalton Trans.*, **2012**, *41*, 13556.
6. J.-P. Costes, F. Dahan and A. Dupuis, *Inorg. Chem.*, **2000**, 39, 5994.
7. T. Shimada, A. Okazawa, N. Kojima, S. Yoshii, H. Nojiri and T. Ishida, *Inorg. Chem.*, **2011**, *50*, 10555.
8. J. Cirera and E. Ruiz, *C. R. Chimie*, **2008**, *11*, 1227.
9. C. Benelli and D. Gatteschi, *Chem. Rev.*, **2002**, *102*, 2369.
10. R. E. P. Winpenny, *Chem. Soc. Rev.*, **1998**, *27*, 447.
11. A. Bencini, C. Benelli, A. Caneschi, R. L. Carlin, A. Dei and D. Gatteschi, *J. Am. Chem. Soc.*, **1985**, *107*, 8128.
12. M. Heras Ojea, V. A. Milway, G. Velmurugan, L. H. Thomas, S. J. Coles, C. Wilson, W. Wernsdorfer, G. Rajaraman and M. Murrie, *Chem. Eur. J.*, **2016**, *22*, 12839.
13. M. Pinsky and D. Avnir, *Inorg. Chem.*, **1998**, *37*, 5575.
14. D. Casanova, M. Llunell, P. Alemany and S. Alvarez, *Chem. Eur. J.*, **2005**, *11*, 1479.
15. A. W. Addison, T. Nageswara Rao, J. Reedijk, J. van Rijn and G. C. Verschoor, *J. Chem. Soc., Dalton Trans.*, **1984**, 1349.
16. P. Richardson, D. I. Alexandropoulos, L. Cunha-Silva, G. Lorusso, M. Evangelisti, J. Tang and T. C. Stamatatos, *Inorg. Chem. Front.*, **2015**, *2*, 945.
17. P. de Hoog, P. Gamez, O. Roubeau, M. Lutz, W. L. Driessen, A. L. Spek and J. Reedijk, *New J. Chem.*, **2003**, *27*, 18.
18. M. Heras Ojea, C. Wilson, S. J. Coles, F. Tuna and M. Murrie, *Dalton Trans.*, **2015**, *44*, 19275.
19. F. Yan and Z. Chen, *J. Phys. Chem. A*., **2000**, *104*, 6295.
20. J. Paulovič, F. Cimpoesu, M. Ferbinteanu and K. Hirao, *J. Am. Chem. Soc.*, **2004**, *126*, 3321.
21. J. D. Rinehart and J. R. Long, *Chem. Sci.*, **2011**, *2*, 2078.
22. D. Aravena and E. Ruiz, *Inorg. Chem.*, **2013**, *52*, 13770.
23. P. Zhang, L. Zhang and J. Tang, *Dalton Trans.*, **2015**, *44*, 3923.
24. J. Bartolomé, G. Filoti, V. Kuncser, G. Schinteie, V. Mereacre, C. E. Anson, A. K. Powell, D. Prodius and C. Turta, *Phys. Rev. B*, **2009**, *80*, 014430.
25. G. Rajaraman, F. Totti, A. Bencini, A. Caneschi, R. Sessoli and D. Gatteschi, *Dalton Trans.*, **2009**, 3153.
26. J.-P. Costes, F. Dahan, A. Dupuis and J.-P. Laurent, *Inorg. Chem.*, **2000**, *39*, 169.
27. N. F. Chilton, R. P. Anderson, L. D. Turner, A. Soncini and K. S. Murray, *J. Comput. Chem.*, **2013**, *34*, 1164.

Chapter 6

Contents

6. Towards the synthesis of pseudo−single−ion magnets

6. Towards the synthesis of pseudo−single−ion magnets

In view of the experimental results obtained so far, the study of the coordination chemistry of bis−tris propane (H_6L) with other 3*d*/4*f* combinations is proposed, in order to optimise our approach for the design of heterometallic SMMs. Since the discovery of the multiple benefits of the combined use of 3*d* metals and lanthanides in the synthesis of new magnetic materials, several complexes with chromium,[1–3] manganese,[4–6] iron,[7, 8] nickel[9, 10] or copper[11, 12] have been studied.[13, 14] The number of compounds derived from the combination of cobalt and 4*f* elements although is surprisingly much lower than the rest. That is a rather unexpected fact, since monometallic cobalt compounds have given a large variety of molecular magnets, due to the anisotropy resulting from crystal−field effects.[15] One may think that the reason for such a difference could be to avoid complicating the analysis of the final magnetic properties displayed by the Ln−complexes. Recent studies propose the investigation of 3*d*/4*f* compounds containing diamagnetic 3*d* ions (*i.e*. Zn(II), Co(III)) instead of the ordinary paramagnetic ones, and the study of its influence on the single−ion magnet dynamics.[16–18] For example, an outstanding improvement of the anisotropic barrier (from 16 to 83 cm^{-1}) of the complex [$Dy(HL)_2(NO_3)_3$] (where HL = 2−methoxy−6−[I−phenyliminomethyl]phenol) has been prompted by the structural incorporation of diamagnetic Zn(II) ([$ZnDy(NO_3)_2(L)_2(CH_3CO_2)$]; see Fig 6.1).[18]

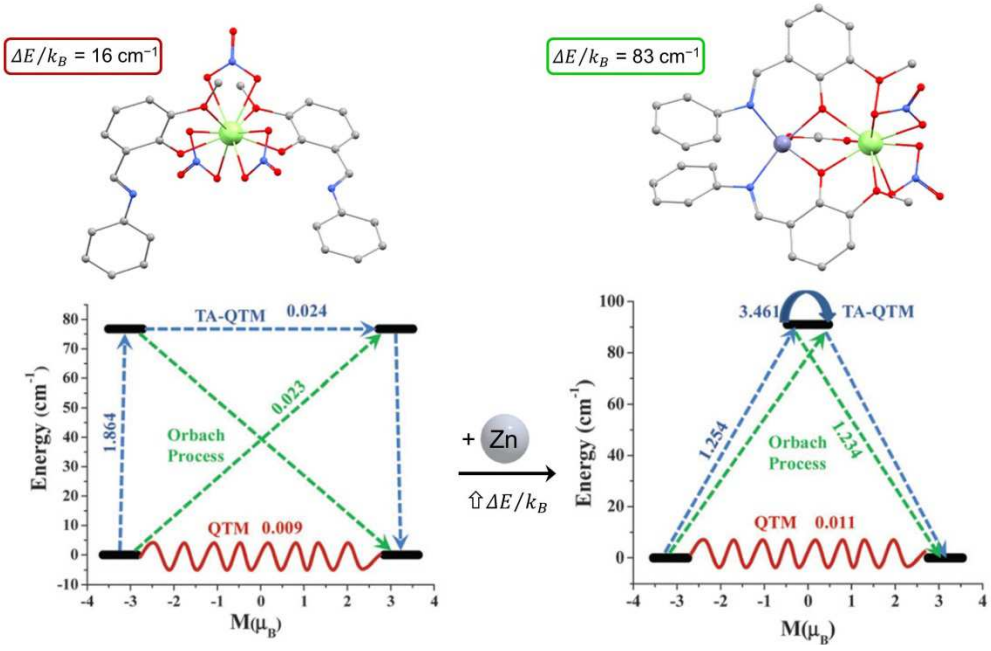

Fig 6.1 Detail of the structure and *Ab initio* results for [$Dy(HL)_2(NO_3)_3$] (left) and [$ZnDy(NO_3)_2(L)_2(CH_3CO_2)$] (right). Orbach processes are shown as dotted green lines, whereas QTM are shown in red and blue. Picture adapted from Ref. 18 with permission of The Royal Society of Chemistry.

Theoretical calculations in both complexes proved that the presence of Zn(II) near the phenoxo group forces the polarization of the charge towards the oxygen, magnifying the Ln−O(Phen) electrostatic interaction. As a consequence, there is an increase in the energy difference between the ground state and first excited state, resulting in an increase of the anisotropic barrier (Fig 6.1). Although Zn(II)/4*f* complexes have been broadly studied, the influence of octahedral strong−field Co(III) in Co/4*f* compounds has been barely investigated.[16] Since aminopolyol−type ligands similar to bis−tris propane seem to promote the oxidation of different Co(II) starting materials,[19−21] the exploration of H_6L with Co(II) ions with the prospect of obtaining Co(III)/4*f* systems is here proposed. Therefore, this chapter focuses on:

1. Does the replacement of Cu(II) ions by Co(II) ions in the synthesis of 3*d*/4*f* systems lead to any structural modifications on the assembly of the final products?
2. Does the electrostatic density of cobalt ions affect the Ln−SIM properties?

For this, copper perchlorate was substituted for cobalt perchlorate in the synthesis used to prepare the {$LnCu_4$} family. The magnetic and structural studies of a novel series of compounds with formula [$Co_3Ln(H_2L)_2(H_3L)$](ClO_4) (Ln = Tb, Dy, Ho, Er, Yb) revealed that the presence of Co(III) centres partially modifies the electrostatic potential of the ligand−field around the lanthanide ions. In addition, the effect of the electrostatic field on the dynamic properties of the compounds depends on the nature of Ln. In later sections the reason for the different properties observed throughout the {Co_3Ln} series is discussed.

6.1. Synthesis

Note: The number of solvents included in the formula for complexes **17**−**21** was proposed given consideration the results from the microanalyses and the number of electrons accounted by SQUEZE (in PLATON).

$[Co_3Tb(H_2L)_2(H_3L)](ClO_4)\cdot 5.5H_2O$ (**17**): H_6L (0.33 g, 1.17 mmol) and Et_3N (0.49 mL, 3.51 mmol) were consecutively added to a colourless solution of $TbCl_3\cdot 6H_2O$ (0.15 g, 0.39 mmol) in MeOH (30 mL), resulting in a pale pink suspension. $Co(ClO_4)_2\cdot 6H_2O$ (0.43 g, 1.17 mmol) was added and immediately dissolved, giving a brown solution. The resulting solution was heated to 60°C for three hours, and then filtered. Dark burgundy plate single crystals suitable for X−ray diffraction were obtained by vapour diffusion of Et_2O into the reaction solution in several days. Yield (crystals) 13% (62 mg). IR: $\bar{\upsilon}$ (cm^{-1}) = 3192, 2839, 1632, 1431, 1078, 1064, 1020, 800, 692. Elemental analysis ($[Co_3Tb(H_2L)_2(H_3L)](ClO_4)\cdot 5H_2O$) [%], found: C 28.77, H 5.39, N 6.18; calc: C 29.12, H 5.70, N 6.17.

$[Co_3Dy(H_2L)_2(H_3L)](ClO_4)\cdot 5.5CH_3OH\cdot 1.5H_2O$ (**18**): The same synthetic procedure described for **17** was followed, but using $DyCl_3\cdot 6H_2O$ instead of $TbCl_3\cdot 6H_2O$. Dark burgundy plate single crystals suitable for X−ray diffraction were obtained by layering Et_2O into the reaction solution in several days. Yield (crystals) 26% (87 mg). IR: $\bar{\upsilon}$ (cm^{-1}) = 3192, 2822, 1647, 1435, 1080, 1063, 1022, 800, 692. Elemental analysis ($[Co_3Dy(H_2L)_2(H_3L)](ClO_4)\cdot 5CH_3OH\cdot H_2O$) [%], found: C 31.49, H 5.71, N 5.33; calc: C 31.41, H 6.17, N 5.78.

$[Co_3Ho(H_2L)_2(H_3L)](ClO_4)\cdot 4.5CH_3OH\cdot 5.5H_2O$ (**19**): The same synthetic procedure described for **17** was followed, but using $HoCl_3\cdot 6H_2O$ instead of $TbCl_3\cdot 6H_2O$. Dark burgundy plate single crystals suitable for X−ray diffraction were obtained by vapour diffusion of Et_2O into the reaction solution in several days. Yield (crystals) 36% (177 mg). IR: $\bar{\upsilon}$ (cm^{-1}) = 3206, 2930, 1433, 1366, 1229, 1217, 1065, 1020, 692. Elemental analysis ($[Co_3Ho(H_2L)_2(H_3L)](ClO_4)\cdot 5.25H_2O$) [%], found: C 28.59, H 5.30, N 5.96; calc: C 28.90, H 5.69, N 6.13.

$[Co_3Er(H_2L)_2(H_3L)](ClO_4)\cdot 0.75CH_3OH\cdot 5H_2O$ (**20**): The same synthetic procedure described for **17** was followed, but using $ErCl_3\cdot 6H_2O$ instead of $TbCl_3\cdot 6H_2O$. Dark burgundy plate single crystals suitable for X−ray diffraction were obtained by vapour diffusion of Et_2O into the reaction solution in several days. Yield (crystals) 41% (202 mg). IR: $\bar{\upsilon}$ (cm^{-1}) = 3194, 2841, 1433, 1366, 1229, 1065, 1020, 800, 692.

Elemental analysis ($[Co_3Er(H_2L)_2(H_3L)](ClO_4)\cdot 5H_2O$) [%], found: C 28.28, H 5.24, N 5.92; calc: C 28.75, H 5.70, N 6.10.

$[Co_3Yb(H_2L)_2(H_3L)](ClO_4)\cdot 4CH_3OH\cdot 5H_2O\cdot 5(CH_3H_2)_2O$ (**21**): The same synthetic procedure described for **17** was followed, but using $YbCl_3\cdot 6H_2O$ instead of $TbCl_3\cdot 6H_2O$. Dark burgundy plate single crystals suitable for X−ray diffraction were obtained by vapour diffusion of Et_2O into the reaction solution in several days. Yield (crystals) 19% (67 mg). $\bar{\upsilon}$ (cm^{-1}) = 3198, 2970, 1435, 1366, 1217, 1067, 1020, 743, 696. Elemental analysis ($[Co_3Yb(H_2L)_2(H_3L)](ClO_4)\cdot 5.25H_2O$) [%], found: C 28.29, H 5.23, N 5.87; calc: C 28.73, H 5.66, N 6.09.

6.2. Results and discussion

This chapter focuses on exploring the reactivity of H_6L with cobalt in the presence of Ln ions, and the magnetic changes that the replacement of Cu(II) for Co(II) ions could cause in the final complexes compared to the Cu/4*f* systems. Therefore, following an analogous approach to that used for the preparation of {$LnCu_4$}, but using $Co(ClO_4)_2 \cdot 6H_2O$ instead of $Cu(ClO_4)_2 \cdot 6H_2O$, we have isolated a new family of complexes with general formula $[Co_3Ln(H_2L)_2(H_3L)](ClO_4)$ (Ln = Tb in **17**, Dy **18**, Ho **19**, Er **20**, Yb **21**). Although both families show multiple {$M(H_6L)$} moieties (M = Cu, Co) surrounding a central lanthanide, the number of these 3*d*/H_6L−units has changed, maybe due to the different coordination environment displayed by the cobalt atoms (further details will be given in next sections). The synthesis was subsequently optimised considering the stoichiometric ratio exhibited by the final products in their crystalline structures. Note also that considering all the paramagnetic Co(II) centres have been oxidised to diamagnetic Co(III) centres, the magnetic properties of the complexes are defined mainly by the Ln(III) ions. Hence the analysis of the magnetic properties is based on treating the {Co_3Ln} system as 4*f* mononuclear complexes.

X−ray crystallographic analysis

Selected crystallographic experimental details for **17**−**21** are shown in Table 6.1. The complexes crystallise in the monoclinic space group $P2_1/c$. Their asymmetric units content one $[Co_3Ln(H_2L)_2(H_3L)]^+$ cation and one perchlorate anion. For **17** the perchlorate anion is modelled over three partially occupied sites (see further information in the appendix). The compounds also contain several solvent molecules in the crystal lattice. However, given the poorly defined solvent region, SQUEEZE (in PLATON)[22, 23] was used to calculate and account for diffuse solvent in addition to those modelled as lattice molecules. The final number of solvent molecules for each complex (see appendix) was proposed considering the results from the microanalysis. The $[Co_3Ln(H_2L)_2(H_3L)]^+$ cations for **17**−**21** are isostructural, therefore the description of **17** can be applied to all of them.

The topology displayed for $[Co_3Ln(H_2L)_2(H_3L)]^+$ could be described as propeller−like, with the lanthanide occupying the central part and the cobalt centres as blades (Fig 6.2). As was observed in previous structures, each H_2L^{4-}/H_3L^{3-} ligand chelates one Co(III) ion by the coordination of four oxygen and two nitrogen atoms in a distorted octahedral geometry (see detail in Fig 6.2, right). However, two

different units can be distinguished depending on the deprotonation of the ligand, being two of them {$Co(H_2L)$} and one {$Co(H_3L)$}. These metallo−organic units surround a central Ln(III) ion with distinct coordination modes: the two {$Co(H_2L)$} are linked to the lanthanide by three μ−O atoms, meanwhile the {$Co(H_3L)$} is bound by two μ−O atoms (Fig 6.2, left). The valence of the cobalt centres have been confirmed by bond length, charge balance considerations, and bond valence sum calculations (BVS).[24−26] The oxidation of the Co(II) ions to Co(III) ions could have been caused by many reasons, such as the presence of the ClO_4^- oxidant agent, an excess of base, or the aerobic reaction conditions. Co(III) may be also favoured considering the size of the coordination pocket, as previously mixed−valence Co−based complexes obtained with H_6L show the same tendency.[27]

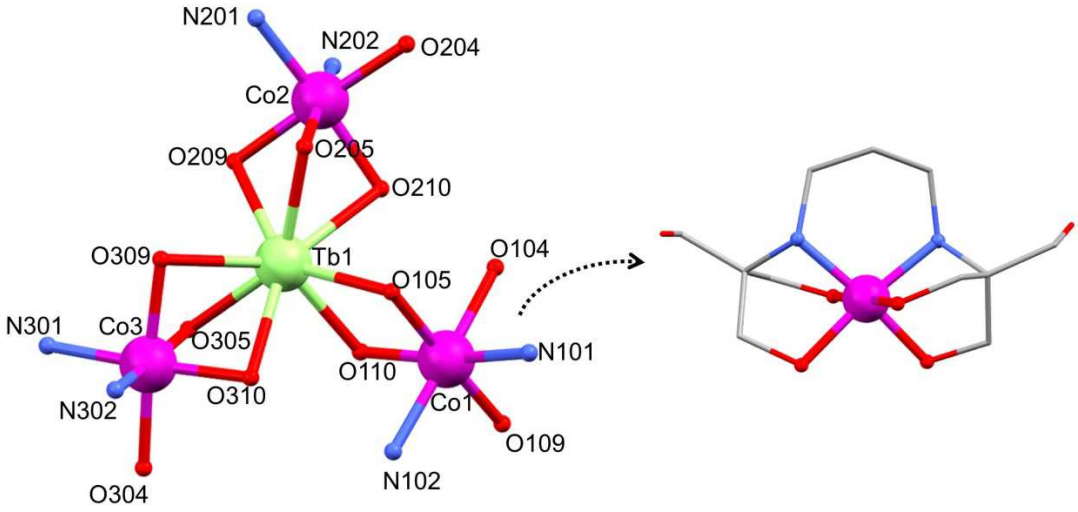

Fig 6.2 Detail of $[Co_3Tb(H_2L)_2(H_3L)]^+$ cation (left) and {$Co(H_2L)$} unit (right) of **17**. C, grey; Co, fuchsia; N, blue; O, red; Tb, green. Hydrogen atoms, counterions and lattice solvents are omitted for clarity.

The results from the symmetry analysis[28, 29] of the octacoordinated Ln(III) ion for **17**–**21** propose the square antiprism (D_{4d}) as the closest ideal geometry in all the compounds (see Table A6.1 of the Appendix). However, the deviation of the continuous measurements from zero (CShMs = 1.096−0.888) implies a distortion in the square antiprism (SAP) geometry compared to the ideal one. Square antiprism symmetry has also characteristic geometrical parameters that shed light on the type of distortion (see Fig 6.3), such as Ln−O distances, the angle between the diagonals of the squares (skew angle, Φ), the angle between the S_8 axis and the direction described by a Ln–O bond (α), the shortest intraplanar distance in a {O_4} square (d_{in}), and the shortest interplanar distance between oxygen donor atoms (d_{pp}).[30] For an ideal SAP polyhedron all the Ln−O are equal, however in the {Co_3Ln}

complexes the distances differ considerably between each other ($d_{(Ln-O)}$ = 2.211(6) – 2.519(7) Å, see Table A6.2 in the appendix), leading to non−planar, asymmetric {O_4} squares (Fig 6.3). The average skew angle Φ defined by the two {O_4} irregular squares within {Co_3Ln} for **17**−**21** (Table A6.3 in the appendix) displays expected values for an ideal D_{4d} symmetry (Φ = 45°).[31, 32] In addition, the α angle for **17**−**21** (~ 59°) indicates an axial elongation distortion of the polyhedron along the *z*−axis, as they are slightly larger than that reported for the ideal SAP (54.5°).[30] That is also consistent with the observed longer d_{pp} values compared to those displayed for d_{in}. The elongation of the SAP has been commonly observed in previously reported phthalocyanine Ln−complexes displaying a similar geometry.[32, 33] It is rather important to stress that the above introduced structural parameters are closely related to the magnetic relaxation properties of these lanthanide−based SIMs (*e.g.* quantum tunnelling).

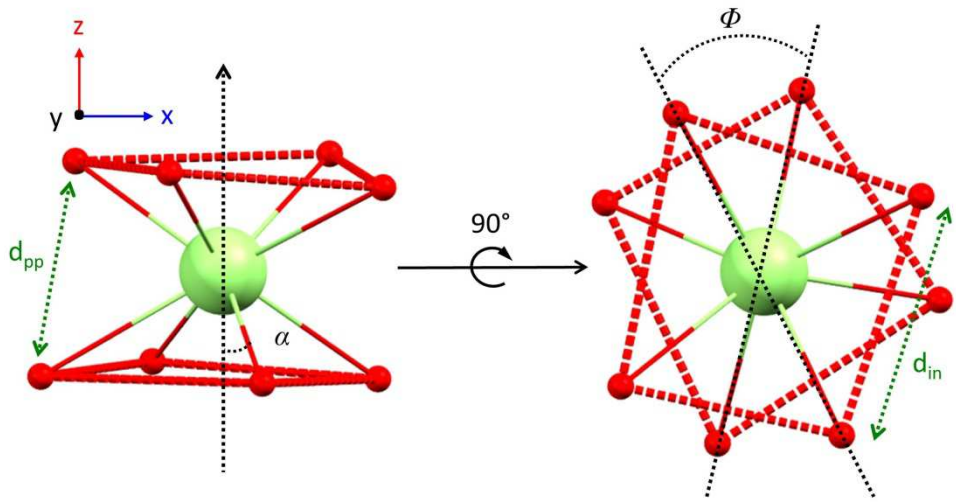

Fig 6.3 Detail of the coordination environment around the Ln centres showing the square antiprism geometry for {LnO_8}, and structural parameters relevant to the degree of distortion of the polyhedron (Φ, α, d_{in}, d_{pp}). See text for further details. O, red; Ln, green.

The assembly of the {Co_3Ln} family is quite unusual, based on similar 3*d*/4*f* published structures with 3*d* = Cr–Zn (CSD 5.36, August 2016). The vast majority of the structures from the search display 3*d* atoms linked to a central Ln ion through multiple μ−O bridges, although additional co−ligands are needed to complete the coordination sphere of the lanthanides.[16, 34, 35] The most comparable structures to those here introduced are probably the [$Fe_3Ln(tea)_2(dpm)_6$] complexes (Ln= Tb–Yb, H_3tea = triethanolamine, Hdpm = dipivaloylmethane) described by Sessoli and co−workers.[7, 8] Nevertheless, the unique encapsulation of the lanthanide centres by exclusively {$Co^{III}(H_nL)$} units seen in [$Co_3Ln(H_2L)_2(H_3L)$](ClO_4) could promote the isolation of the Ln(III) ions from possible long range intermolecular interactions

(Ln···Ln ions in **17**−**21** are more than 10 Å apart), making the study of their magnetic dynamic properties highly attractive.

Table 6.1 Crystal Data and Structure Refinement Parameters of Complexes **17**−**21**.

Complex	**17** {Co_3Tb}	**18** {Co_3Dy}	**19** {Co_3Ho}	**20** {Co_3Er}	**21** {Co_3Yb}
T/K	100(2)	100(2)	100(2)	100(2)	100(2)
Crystal system	monoclinic	monoclinic	monoclinic	monoclinic	monoclinic
Space group	$P2_1/c$	$P2_1/c$	$P2_1/c$	$P2_1/c$	$P2_1/c$
a/Å, b/Å, c/Å	20.6019(5), 13.9479(7), 20.5238(8)	20.587(3), 14.777(2), 19.983(3)	20.5558(14), 14.7075(10), 19.9898(14)	20.5330(3), 14.7979(2), 19.9222(3)	20.5034(4), 14.7558(3), 19.8562(4)
β/°	104.901(3)	104.410(3)	104.1250(7)	104.3435(17)	104.236(2)
V/Å^3	5699.3(4)	5887.9(13)	5860.7(7)	5864.58(17)	5822.9(2)
Z	4	4	4	4	4
ρ_{calc}/mg/m^3	1.481	1.466	1.447	1.476	1.466
μ/mm^{-1}	2.201	2.201	2.284	2.367	2.546
F(000)	2584.0	2644.0	2592.0	2650.0	2604.0
2θ range for data collection	4.09 to 54.968°	3.43 to 50.052°	3.476 to 55.078°	3.752 to 55.118°	3.764 to 54.972°
Index ranges	−26 ≤ h ≤ 26, −18 ≤ k ≤ 18, −23 ≤ l ≤ 26	−19 ≤ h ≤ 24, −17 ≤ k ≤ 17, −23 ≤ l ≤ 23	−26 ≤ h ≤ 26, −19 ≤ k ≤ 19, −25 ≤ l ≤ 25	−26 ≤ h ≤ 25, −19 ≤ k ≤ 18, −24 ≤ l ≤ 25	−25 ≤ h ≤ 25, −19 ≤ k ≤ 19, −26 ≤ l ≤ 26
Reflections collected	71351	82862	99916	72212	125850
Data/restraints/parameters	13001/64/628	10226/926/631	13450/1193/714	13533/1047/746	13347/1045/706
GOF on F^2	1.021	1.095	1.082	1.036	1.050
Final R indexes [I≥2σ (I)]	R_1 = 0.0875, wR_2 = 0.2264	R_1 = 0.0949, wR_2 = 0.1931	R_1 = 0.0613, wR_2 = 0.1679	R_1 = 0.0551, wR_2 = 0.1476	R_1 = 0.0664, wR_2 = 0.1892
Final R indexes [all data]	R_1 = 0.1339, wR_2 = 0.2551	R_1 = 0.1320, wR_2 = 0.2169	R_1 = 0.0669, wR_2 = 0.1730	R_1 = 0.0677, wR_2 = 0.1557	R_1 = 0.0736, wR_2 = 0.1971
Largest diff. peak/hole/e Å^{-3}	4.01/−1.40	3.13/−1.21	4.37/−1.65	3.43/−0.87	3.46/−1.15

Note the {Co_3Ln} *labels are abbreviations from the full formula* [$Co_3Ln(H_2L)_2(H_3L)$](ClO_4). *See further single crystal X−ray data collection and refinement details in the Appendix*

Magnetic properties

The dc magnetic susceptibilities of **17**−**21** were studied in an applied field of 1000 Oe in the temperature range of 290–1.8 K (see plots Fig 6.4). Considering that octahedral LS−Co(III) ions are diamagnetic, the experimental values of $\chi_M T$ at room temperature for **17**−**21** are consistent with those calculated for mononuclear Ln(III) systems (see Table 6.2 for additional information). All the complexes display a similar magnetic trend, as their $\chi_M T$ products decrease with temperature as a consequence of the depopulation of the Stark levels and the single−ion anisotropy characteristic of lanthanides. However, the product for **21** (Yb) decreases more gradually in the whole temperature region compared to those displayed for **17**−**20** (Tb, Dy, Ho, Er). Variable−field magnetisation experiments of **17**−**21** were also performed in the applied field range of *H* = 0–5 T at different constant temperatures (2, 4, 5 and/or 6 K). The magnetisation *vs*. field plots show that the samples do not reach the saturation (see Fig 6.5). The non−saturation of the samples at low temperatures and high fields proved the magnetic anisotropy suggested in the dc susceptibility data. A simultaneous fit[36] of the susceptibility and the magnetisation data is then proposed to investigate the magnetic anisotropy arising from the crystal field (CF) effects that lead to the splitting of the ground term of the Ln ions at zero field.

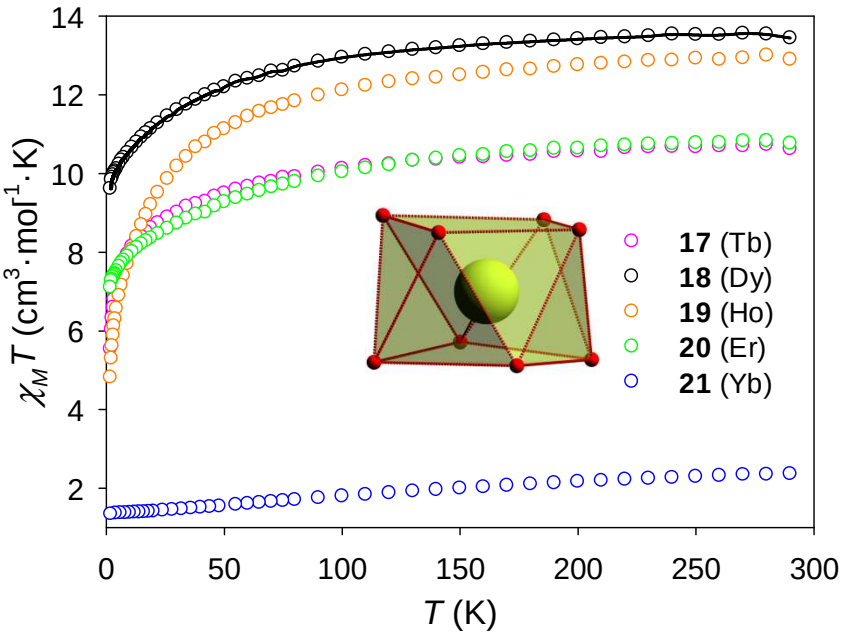

Fig 6.4 Temperature dependence of $\chi_M T$ for **17** (Tb), **18** (Dy), **19** (Ho), **20** (Er) and **21** (Yb) in an applied field of 1000 Oe. Black line correspond to the fit for **18** (see text for details)

Table 6.2 Summary of the calculated ($\chi_M T_{calc}$) and experimental ($\chi_M T_{exp}$) susceptibility values for **17**–**21** (at room temperature).

Complex	Ln ion	*L*	*S*	g_J	GS term symbol	$\chi_M T_{exp}$ ($cm^3 \cdot mol^{-1} \cdot K$)	$\chi_M T_{calc}$ ($cm^3 \cdot mol^{-1} \cdot K$)
17	Tb	3	3	3/2	$^7F_6$	10.73	11.82
18	Dy	5	5/2	4/3	$^6H_{15/2}$	13.54	14.17
19	Ho	6	2	5/4	$^5I_8$	13.00	14.07
20	Er	6	3/2	6/5	$^4S_{15/2}$	10.83	11.48
21	Yb	3	1/2	8/7	$^2F_{7/2}$	2.36	2.57

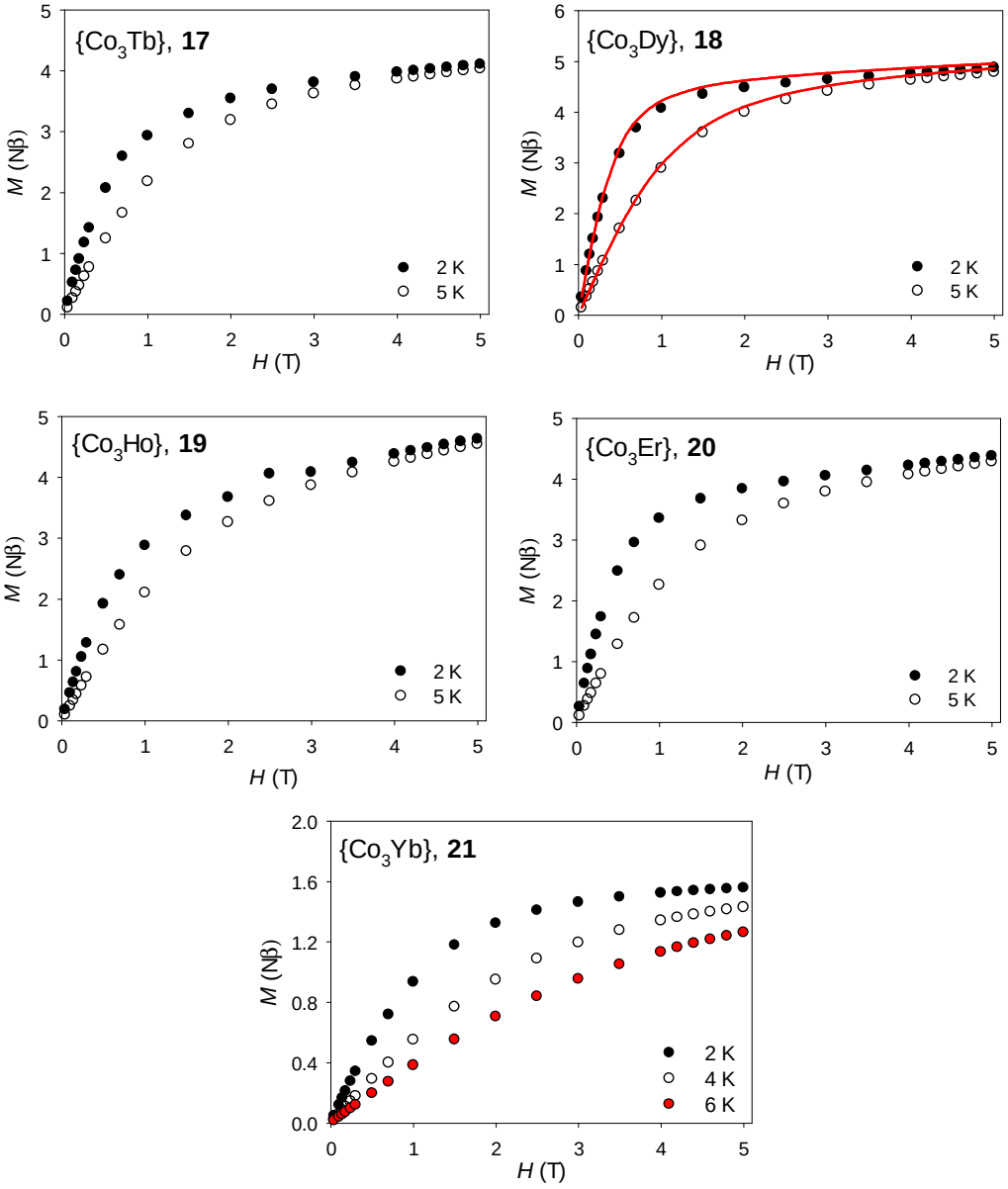

Fig 6.5 Magnetisation *vs*. field at different temperatures for **17**–**20** (2, 5 K) and **21** (2, 4, 6 K). Red lines correspond to the fit for **18** (see text for details)

Since Dy(III) is a Kramer's ion (*i.e*. displays doublet m_J states), the dc data analysis is performed for **18**. According to SHAPE results (*vide supra*), the distortion of the Ln−SAP geometry could cause mixing of the m_J states and non−negligible transverse anisotropy components.[30, 31] Hence the Hamiltonian used in the fit (see Eq. 6.1) is proposed considering the minimum number of crystal field parameters (CFP) related to the symmetry displayed for the Dy(III) ion to avoid overparameterisation (B_0^2, B_0^4, B_4^4).

Eq. 6.1 $$\hat{\mathcal{H}} = \hat{H}_{CF} = \sum_{i=1}^{N} \sum_{k=2,4,6} \sum_{q=-k}^{k} \sigma_i^k B_{k_i}^q \theta_k \hat{O}_{k_i}^q$$

Where σ_i^k are the orbital reduction parameters, θ_k are the operator equivalent factors, $B_{k_i}^q$ are the CFPs in Steven's notation, and $\hat{O}_{k_i}^q$ are the operator equivalents.

It must be noted that alternative models to that proposed above, based on the use of purely axial CFP (B_0^2, B_0^4, B_0^6) did not give satisfactory results. The best fit gives $B_0^2 = 181$, $B_0^4 = 290$, $B_4^4 = 2348$. These values are used in the subsequent survey towards the determination of any possible additional minimal CFP sets that could give also a good final fit. The results from the survey suggest that there is not a unique solution, as several CFP sets with local minimum residuals were found (Table A6.4 in the appendix shows those where Res ≤ 0.1). The CFP sets obtained from the survey (Res ≤ 0.1) were used to simulate the corresponding energy levels and to extract qualitative information about the ground state, the excited states, and the magnetic anisotropy of the molecule (*i.e*. g_J). The simulation of the energy levels leads to some common conclusions: I) the ground state for **18** is mixed, with m_J = ±15/2 (87%), ±1/2, ±7/2, and +9/2; II) the first excited state is relatively close in energy (E ~ 70 cm^{-1}); III) the ground state doublets are not pure Ising−type ($g_x = g_y$ ~ 1, g_z ~ 18). As expected for a Kramer's ion, the strong axiality is characterised by a large axial g_z component, and zero or really small transverse g_x, g_y components. The information extracted from the fit of **18** indicates that quantum−tunnelling could occur in the low−temperature region of the slow−relaxation dynamic studies, in accord with the conclusions from the geometric analysis of Ln−SAP.[31, 37]

The study of the dynamics of the {Co_3Ln} systems is therefore proposed in order to investigate possible SIM properties arising from the axial anisotropy. For that, magnetic ac susceptibility studies of complexes **17**−**21** were performed as a function of the temperature and/or frequency at zero field and in different dc fields. For **17** (Tb), no signal was observed in the out−of−phase susceptibility (χ"), and

neither was there frequency dependence in the in−phase plot (χ') in the absence of field (see Fig 6.6, left). However, when a dc field is applied, an onset of a very weak out−of−phase signal appears (Fig 6.6, right). Isothermal field sweep ac susceptibility experiments as a function of frequency were performed towards the enhancement of the χ" signal by cancelling QTM within the molecule – which may be responsible for the null signal at zero field (see Fig A6.1 in the appendix). Unfortunately, no significant improvement in the magnitude of the out−of−phase signal was observed.

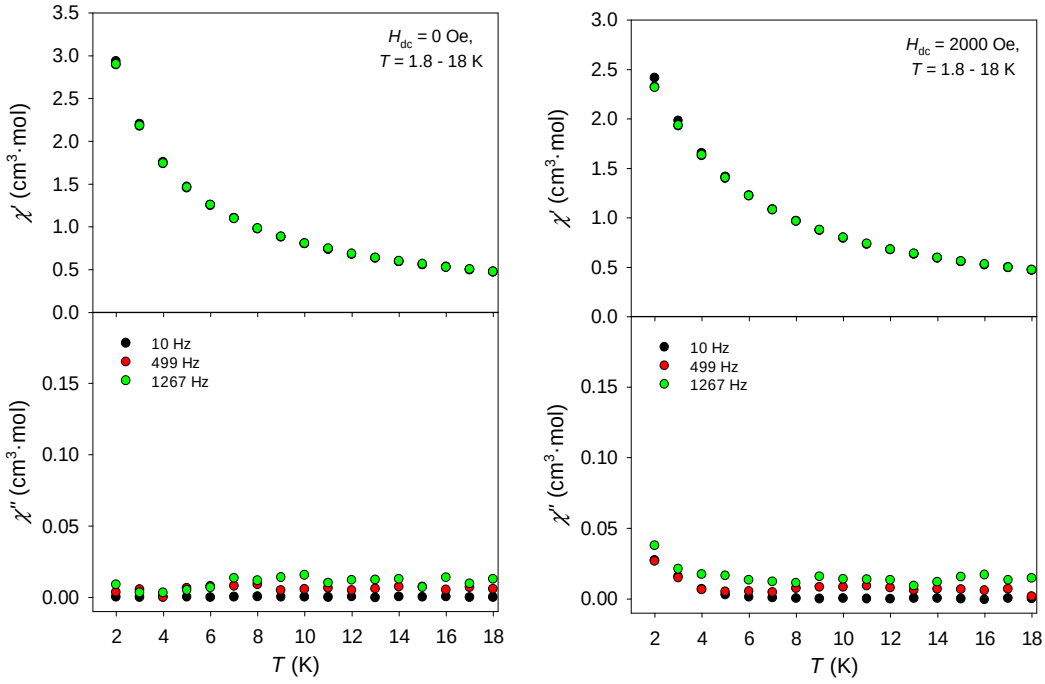

Fig 6.6 Magnetic ac susceptibility of **17** (Tb) as a function of the temperature (T = 1.8 – 18 K) at zero field (left), and in an external field of H_{dc} = 2000 Oe (right) at selected frequencies (υ = 10, 499, 1267 Hz).

For **18**, the considerable single−ion anisotropy typical of dysprosium (III) leads to the improvement of the SIM phenomena. At zero dc field, the χ" signal is again basically imperceptible, however the application of a relatively small dc field causes a remarkable enhancement of the dynamic magnetic properties (see Fig 6.7, left). That suggests the presence of quantum tunnelling as an alternative route to the ideal slow relaxation of the magnetisation. The spin reversal seems to be also related to additional field dependent processes though, as the Argand plots of the ac susceptibility components reveal an upcoming secondary pathway at higher fields (Fig 6.7 top, right). If we consider that the different contributions (Eq. 6.2) can be distinguished as temperature dependent (Orbach, Raman and direct) or temperature independent/field dependent (tunnelling), the first local maximum for τ

in the field dependence plot (Fig 6.7 bottom, right) could arise from the suppression of the tunnelling mechanism, and then the second one due to direct and/or Raman processes. Therefore the calculation of the optimum field for the different observed processes is not straight forward.

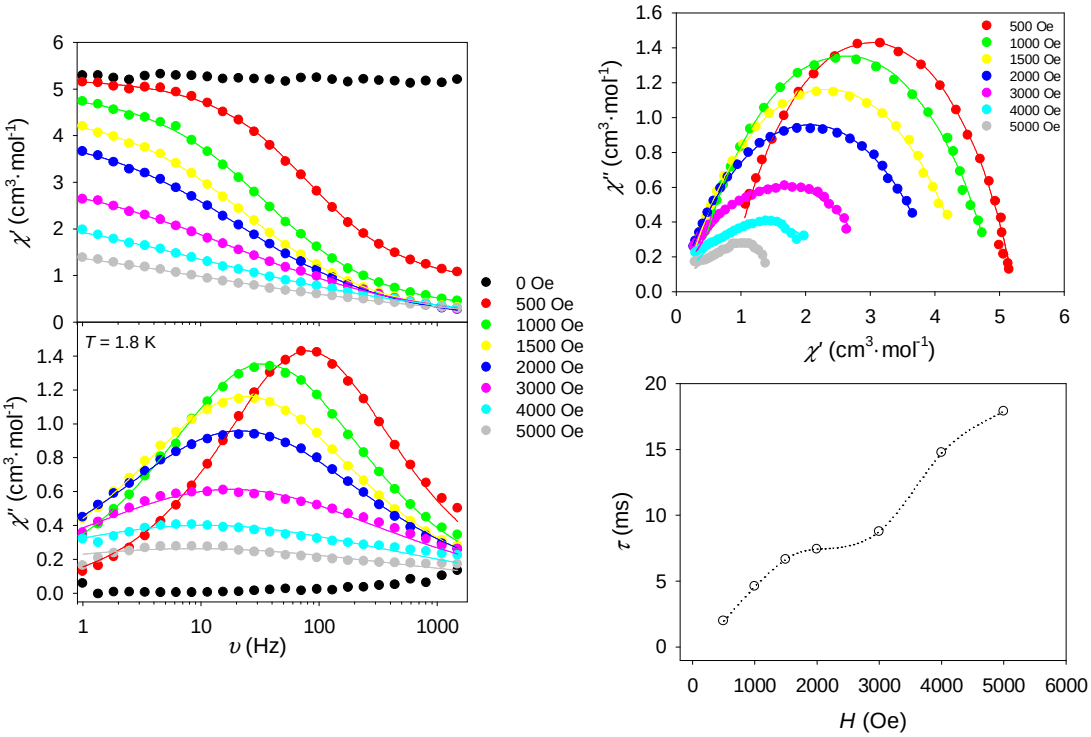

Fig 6.7 Ac magnetic susceptibility of **18** (Dy), at T = 1.8 K in applied fields over 0−5000 Oe (left); Argand plots from the susceptibility data (right, top), and field dependence of the magnetic relaxation time (right, bottom). The solid lines of the ac data correspond to the fit of the data (see text for details). The dotted line in τ vs H is a guide for the eye

Eq. 6.2[38]

$$\tau^{-1} = \overbrace{AH^mT}^{Direct} + \overbrace{CT^n}^{Raman} + \overbrace{\tau_0^{-1} \cdot \exp(-\Delta E/k_BT)}^{Orbach} + \overbrace{\frac{B_1}{1+B_2H^2}}^{QTM}$$

Given that the low−field major relaxation pathway displays a local maximum around 1500 Oe in the τ vs H graph, ac experiments applying dc fields of 500, 1000 and 1500 Oe over the range of 1.8−8 K were performed. The dynamic studies display a similar frequency dependent out−of−phase signal, suggesting field induced SIM properties (see Fig 6.8). The Cole−Cole plots of the ac data between 1.8 and 4 K show a fairly symmetrical shape for the three dc fields (Fig 6.9), and thus the Debye model for a single relaxation time was applied to fit the data. The analysis by CCFit program, however, reveals relatively high α parameters (see Table 6.3), which are clearly dependent on the applied field and the temperature. That tendency suggests that more than one thermally dependent relaxation process is occurring. Since α increases with field, one can think the high−field secondary

pathway is competing the low−field major process (Fig 6.7 bottom, right). Nevertheless, the proposed Debye model involving one relaxation time is valid as all the *α* values are *ca.* below 0.5.[38, 39] In addition, further alternative fits applying the two step relaxation model involving more than one relaxation time (*i.e.* τ_1, τ_2)[39] led to unreasonable results, and therefore they were discarded.

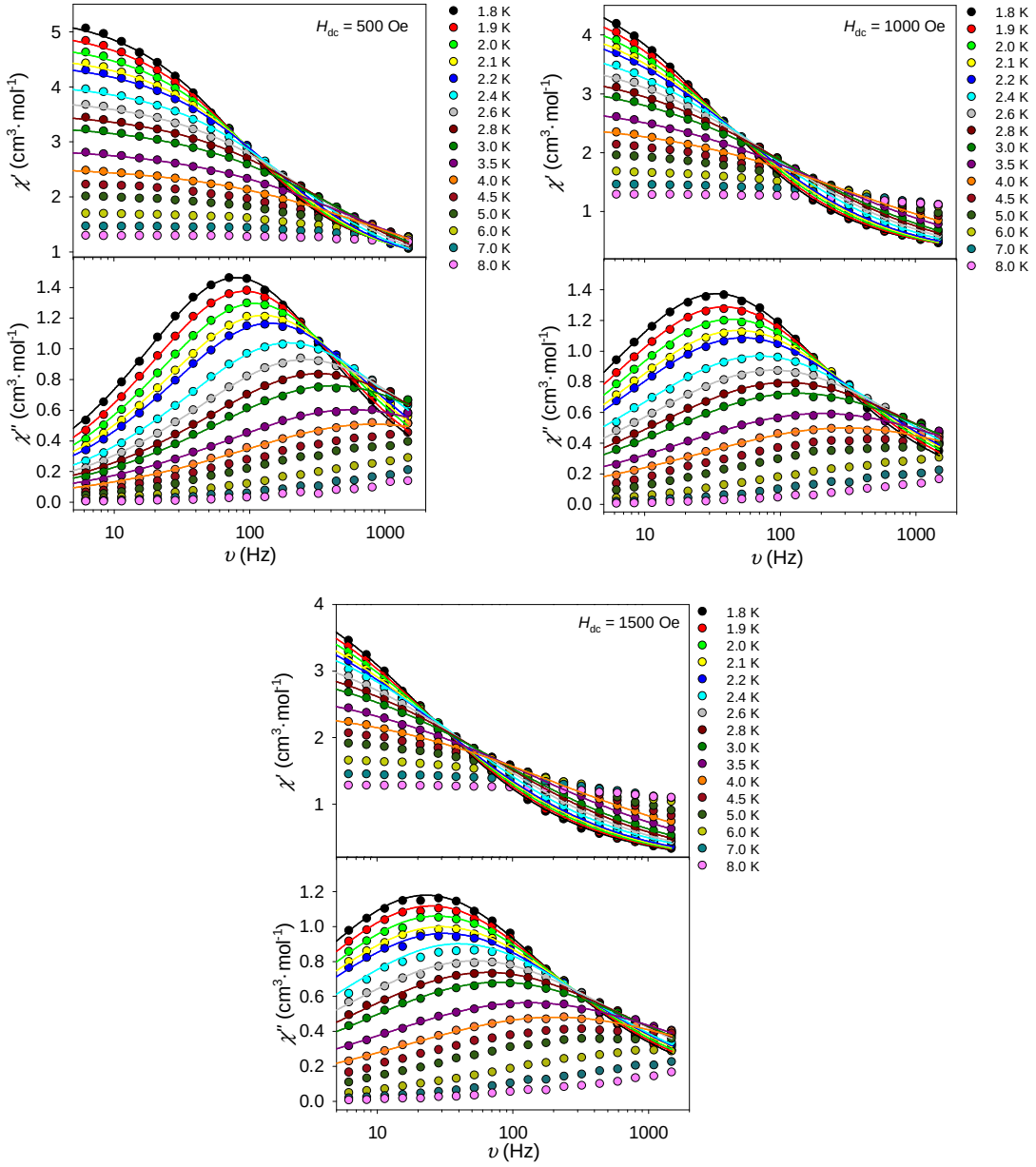

Fig 6.8 Ac magnetic susceptibility data for **18** (Dy), at different frequencies in a dc field of 500, 1000 (top), and 1500 Oe (bottom).

As can be observed in the ln τ vs 1/*T* plots (Fig 6.9 bottom, right), the data shows temperature dependence above ~2.4 K, which can be related to a thermally activated Orbach contribution. Below ~2.4 K, a change in the temperature dependency (therefore in the data trendline) happens which could be related to

additional magnetisation reversal processes. Consequently, an estimation of the pre−exponential factor (τ_0) and energy barrier ($\Delta E/k_B$) parameters was obtained from the fit of the high temperature range data by using a model based only on the Orbach contribution (see Fig A6.2 in the appendix). The best results are τ_0 = 2.4·10^{-5} s, 6.4·10^{-5} s, 7.3·10^{-5} s and $\Delta E/k_B$ = 8.5 ± 0.2 K, 8.6 ± 0.3 K, 9.7 ± 0.5 K for, respectively, 500, 1000 and 1500 Oe. The large resulting τ_0 values (typically around 10^{-6}–10^{-11} s for SMMs) indicate the presence of tunnelling.[40] That agrees with the distortion of the SAP geometry and the conclusions extracted from the analysis of the dc data (*vide supra*). Since tunnelling and direct relaxation processes are field dependent (see Eq. 6.2), the parameters *A*, B_1, B_2 can be calculated by fitting the field−dependent relaxation data (Fig 6.7).[41, 42] These calculated values can be then fixed in the fit of ln τ vs 1/*T* plots (500, 1000, 1500 Oe) to avoid overparameterisation. Unfortunately, all the attempts to fit the data failed (*i.e.* meaningless fit or unreasonable results). Additional models involving tunnelling, direct and/or Raman processes with fixed or variable *n*, *m* parameters were proposed to fit the ln τ vs 1/*T* data for 500, 1000, 1500 Oe. As an example, the use of Orbach and direct contributions with variable *m* gives a nice fit of the data, but proposes pointless τ_0 (*i.e.* negative) values for a Dy(III) SIM (see Fig A6.3 in the appendix). Those different fits were then discarded.

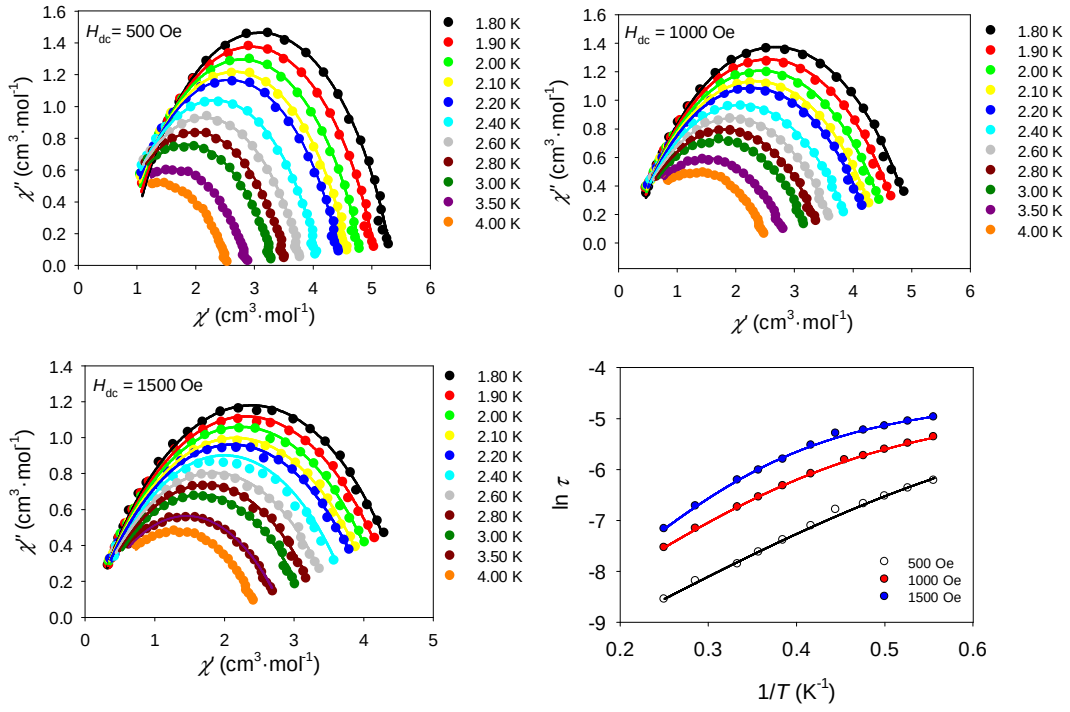

Fig 6.9 Cole–Cole plots and Arrhenius plot (bottom, right) of the ac data for **18** at 500, 1000, and 1500 Oe. The solid lines correspond to the fit (see text for details).

Nevertheless, some general features were extracted from these unsuccessful fits: i) Orbach contribution is needed; that is reasonable considering that the first excited state is relatively close in energy (ΔE ~ 70 cm^{-1}); ii) The direct contribution should be included, whereas the Raman contribution should be discarded; that is also reasonable, since direct processes are promoted by applying a H_{dc} field (see Eq. 6.2); iii) The QTM contribution (isolated or among other processes) did not reproduce the tendency of the experimental data; it was then discarded in spite of the relatively large τ_0 values. The most reasonable results (plotted in Fig 6.9) are given when Orbach and direct contributions (*m* fixed as 4) are included in the model, with final values of τ_0 = $2.0 \cdot 10^{-5}$ s, $3.5 \cdot 10^{-5}$ s, $2.1 \cdot 10^{-5}$ s, $\Delta E/k_B$ = 9.5 ± 0.5 K, 11.9 ± 0.3 K, 15.4 ± 0.4 K, and A = $2.0 \cdot 10^{-9}$ $s^{-1} \cdot K^{-1} \cdot Oe^{-4}$, $1.6 \cdot 10^{-9}$ $s^{-1} \cdot K^{-1} \cdot Oe^{-4}$, $1.2 \cdot 10^{-9}$ $s^{-1} \cdot K^{-1} \cdot Oe^{-4}$ for 500, 1000 and 1500 Oe respectively. The τ_0 parameters are again slightly larger than those expected for SIMs, in accord with the non−supressed tunnelling previously proposed. Nevertheless the values are acceptable as several reported Ln−based SMMs display similar τ_0.[40, 43–47]

Table 6.3 Summary of the *α* values extracted from the fit of the Cole−Cole plots of the ac data for **18** at 500, 1000, and 1500 Oe.

T (K)	*α* 500 Oe	*α* 1000 Oe	*α* 1500 Oe
1.80	0.27	0.34	0.40
1.90	0.28	0.36	0.41
2.00	0.29	0.37	0.42
2.10	0.30	0.38	0.44
2.25	0.31	0.39	0.44
2.40	0.33	0.41	0.44
2.60	0.35	0.43	0.46
2.80	0.37	0.44	0.47
3.00	0.40	0.46	0.48
3.50	0.43	0.49	0.52
4.00	0.45	0.50	0.52

To understand the results observed in the dynamic experiments for **18**, an estimation of the magnetic anisotropy of the Dy(III) ion is calculated by using Magellan.[48] Magellan is a program that predicts the orientation of the ground state magnetic anisotropy axis of Dy centres, based on the calculation of the electrostatic energy minimum from a model that takes into account the different atoms as formal charges. The model used for the calculation of the magnetic anisotropy axis for **18** is shown in Fig 6.10 (left). As can be seen, all the metal ions are in the same plane,

whereas all the alkoxide groups from the H_2L^{4-}/H_3L^{3-} ligands are above or below this plane. Therefore, two competitive crystal fields are expected in **18**: the field generated by the alkoxide groups *vs*. that related to the Co(III) ions (see Fig 6.10, right). Note that negatively charged oxygen atoms from the H_2L^{4-}/H_3L^{3-} ligands are closer to the Dy(III) ion than the Co(III) ions, and therefore they may have a greater effect on the orientation of the anisotropy axis.[48]

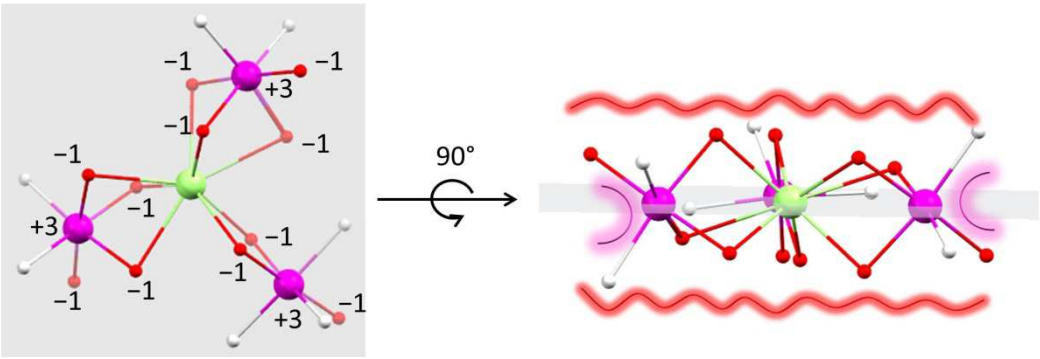

Fig 6.10 Model for the charge distribution on the ligands and the Co(III) ions around the Dy centre used for the calculation of the magnetic anisotropy axis for **18**. Co, fuchsia; Dy, green; O, red. Neutral coordinated O, N atoms are indicated in white. The plane defined by the metal ions is shown in grey. The electron density caused by the O(−1) atoms is highlighted in red, while that for the Co(+3) is in pink.

Long and co−workers have developed a qualitative model for predicting the crystal field suitable for a particular Ln(III) ion towards the promotion of magnetic anisotropy (see Fig 6.11).[49]

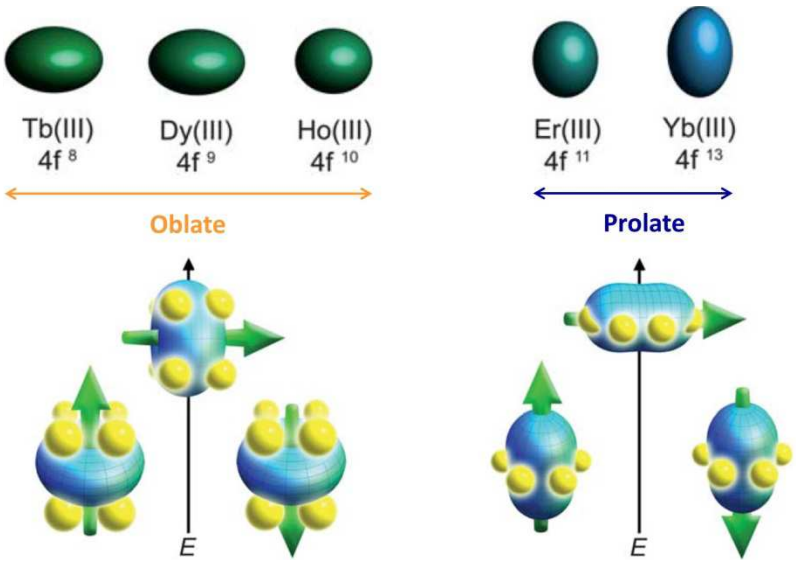

Fig 6.11 Top: Quadrupole approximations of the 4*f*−shell electron distribution for Tb(III), Dy(III), Ho(III) (Oblate) and Er(III), Yb(III) (Prolate) ions. Bottom: Depiction of the effect of an axially symmetric crystal field effect over an oblate ion (left) *vs.* an equatorially symmetric crystal field over a prolate ion. Figures adapted from Ref. 49 with permission of The Royal Society of Chemistry.

The model proposes that the anisotropy of an oblate−shaped ion (*e.g*. Tb(III), Dy(III), Ho(III)) can be enhanced by placing the Ln(III) ion in an axial crystal field (*i.e*. electron density concentrated above and below the *xy*−plane). In contrast, the anisotropy of a prolate−shaped ion (*e.g*. Er(III), Yb(III)) can be maximised by placing the Ln(III) ion in an equatorial crystal field. Therefore, the axial field caused by the alkoxide groups in **18** promote the single−ion anisotropy from the Dy(III) ion, while the equatorial field related the Co(III) ions may minimise it. That could justify the weak SMM properties proposed from the analysis of the dynamic studies in **18**. Figure 6.12 shows the orientation of the ground state anisotropy axis for **18** calculated by Magellan (green rod). As can be seen, the resulting anisotropy axis of Dy(IIII) slightly deviates from the pseudo−C_4 axis of the molecule, consistent with the distortion of the ideal SAP geometry previously described. That suggests that the axial−alkoxide field has a greater effect than the equatorial−Co one on the Dy ion, causing the magnetic anisotropy to be oriented towards the pseudo−C_4 axis, thus stabilising the oblate density in the Dy(III) ion to the detriment of the prolate−shape.

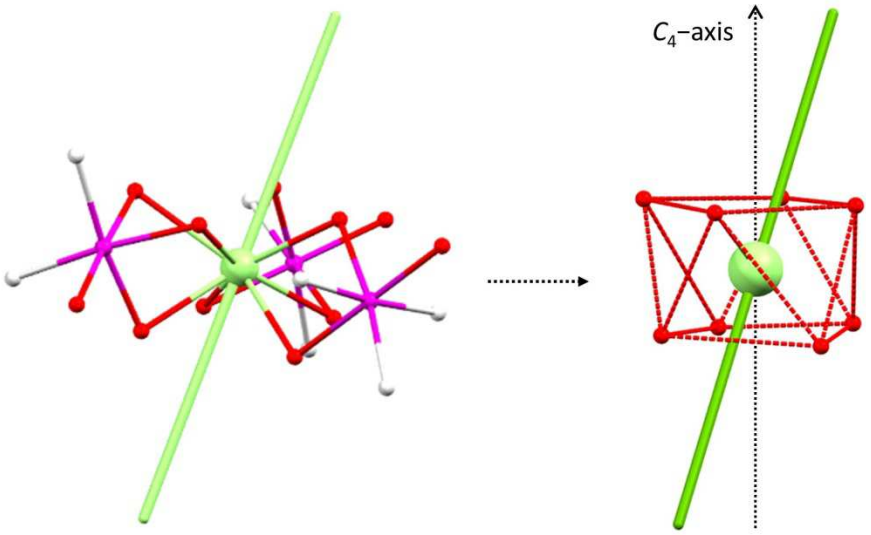

Fig 6.12 Orientation of the ground state anisotropy axis for **18** (green rod) calculated by Magellan. Co, fuchsia; Dy, green; O, red. Neutral coordinated O, N atoms are indicated in white.

The isothermal field sweep ac experiments for **19** (Ho) and **20** (Er) show a similar behaviour to those discussed respectively for **17** (Tb) and **18** (Dy). In consequence, no signal was observed in the out−of−phase susceptibility for **19**, and neither was there frequency dependence in the in−phase plot regardless of the application of an external field (Fig 6.13, left). For **20**, the application of a field leads to the enhancement of the dynamic properties, resulting in the appearance of a

frequency−dependent out−of−phase signal in the χ', χ" *vs.* υ plots (Fig 6.13, right). Considering the lack of local maxima, the ac properties were investigated over 1.8–5.0 K by applying the same field strength to that used in **18** (*i.e*. 500, 1000, 1500 Oe) at selected frequencies (see Fig 6.14 and 6.15). The ac magnetic susceptibility plots for **20** (Er) show an increase of the χ" value at high frequencies and low temperatures (see plots Fig 6.14, 6.15). The relaxation rate (τ_0) and the energy barrier ($\Delta E/k_B$) parameters were calculated, as proposed in previous chapters, by using the Kramer's−Kronig−derivate equation of the Arrhenius law $\ln(\chi''/\chi') = \ln(\omega\tau_0) + \Delta E/k_B T$.[50]

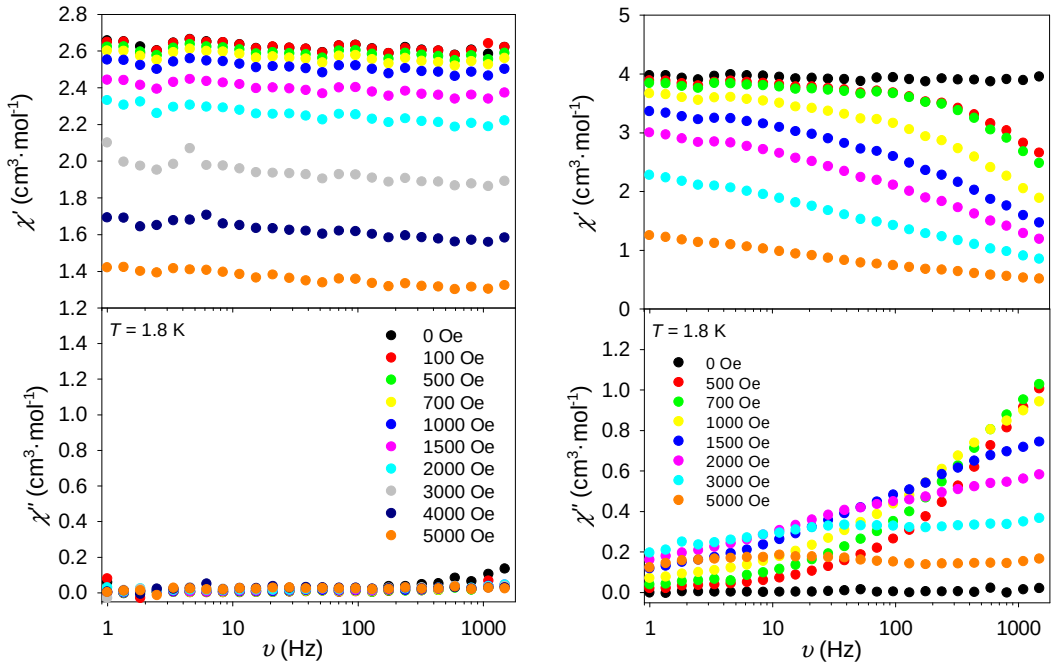

Fig 6.13 Ac magnetic susceptibility of **19** (Ho, left) and **20** (Er, right), at *T* = 1.8 K in applied fields over 0−5000 Oe.

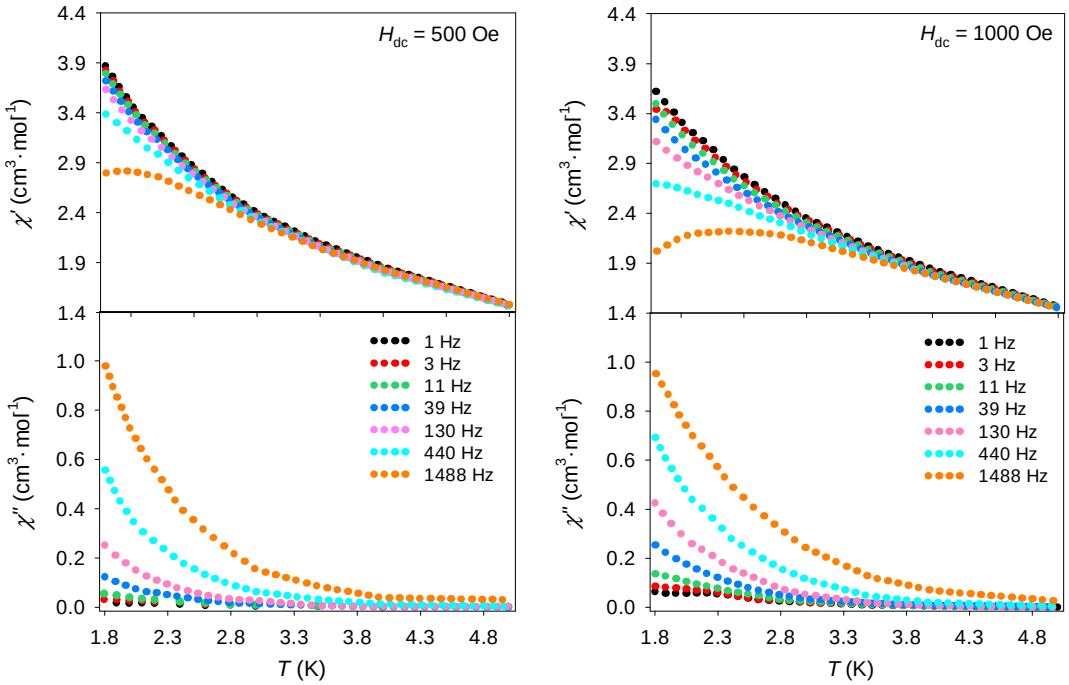

Fig 6.14 Ac magnetic susceptibility of **20** (Er) in a dc field of 500 (left) and 1000 Oe (right).

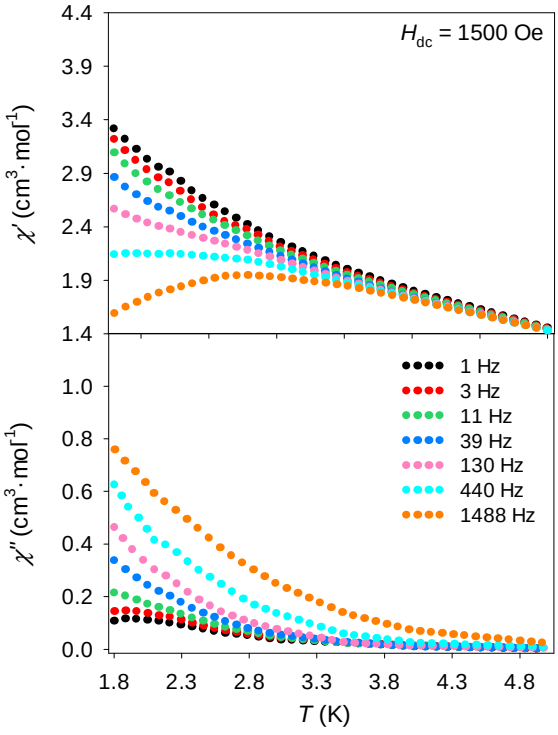

Fig 6.15 Ac magnetic susceptibility of **20** (Er) in a dc field of 1500 Oe.

The linear regression plots of the ac experiments are displayed in the Appendix (Fig A6.4) to better visualise the $\ln(\chi''/\chi')$ vs 1/*T* trend at different experimental conditions. As can be seen in Figure 6.16, the low field and/or low frequency data appears to be quite noisy, especially at high temperatures (*e.g.* 5 K). That is consistent with the decline of the weak out−of−phase signal seen at higher temperatures. Note also that the experimental values begin to describe more clearly a logarithmic trend by applying a stronger dc field (Fig 6.16). Therefore, a deviation of the linearity is observed at low temperatures, suggesting that the reversal of the magnetisation is related again to multiple H_{dc}, *T* dependent relaxation processes. The fit of the data was performed considering two different regions, the high temperature one (**HT**, $T \geq 3.5$ K) and the low temperature one (**LT**, $T \leq 3.0$ K). Accordingly, τ_0, $\Delta E/k_B$ were estimated for each range of temperatures. A summary of the best results for both ranges is displayed below in Table 6.4 (see all values in Table A6.5 of the appendix). The average values for the **HT** region are τ_0 = $1.5 \cdot 10^{-8}$ s, $1.7 \cdot 10^{-7}$ s, $2.5 \cdot 10^{-7}$ s and $\Delta E/k_B$ = 26.4 ± 3.7 K, 22.2 ± 3.6 K, 18.3 ± 1.1 K for, respectively, 500, 1000 and 1500 Oe.

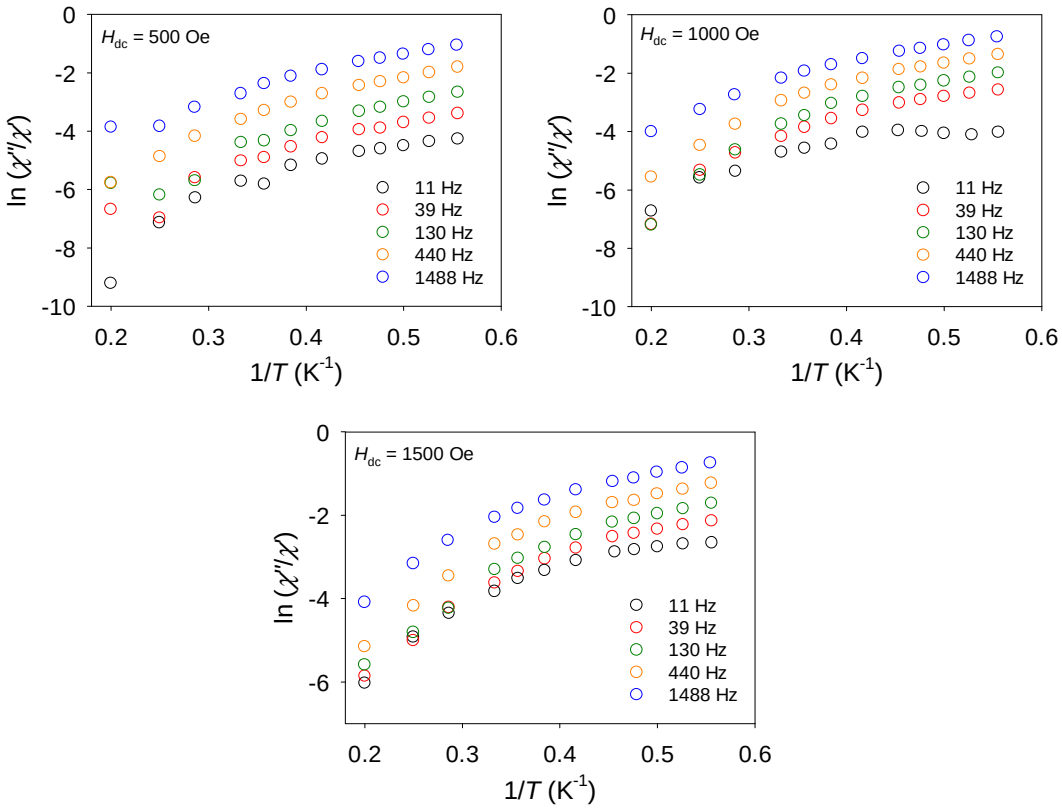

Fig 6.16 Natural logarithm of χ''/χ' *vs*. 1/*T* for H_{dc} = 500, 1000, 1500 Oe at selected frequencies.

Although the results are comparable to other reported SIMs, relatively large standard deviations were observed for the calculated energy barriers, questioning the reliability of these values. That could be a consequence of the lack of sufficient number data points, and also due to the poor quality data used for the analysis. Additional ac experiments below 5 K are required in order to make a more accurate estimation of τ_0 and $\Delta E/k_B$. On the other hand, the fit of the **LT** experimental data results in larger pre−exponential factors ($1.9\cdot10^{-6}$ s, $1.4\cdot10^{-5}$ s, $1.8\cdot10^{-5}$ s) and lower energy barriers (7.6 ± 0.5 K, 6.2 ± 0.6 K, 6.2 ± 0.5 K) to those calculated for the **HT** region. The relatively large τ_0 values suggest again that the slow relaxation has different contributions, *e.g*. quantum tunnelling. It must be stressed that the approach used for the analysis of τ_0 and $\Delta E/k_B$, based on a linear model of two different temperature ranges, has been carried out to throw light on the nature of the reversal of the magnetisation in **20** (Er), and at no time are the resulting values conclusive. In order to obtain more precise results, the fit of the ac experimental data should be carried out with an alternative model, for example, that incorporates the rest of the possible contributions to the relaxation process (*e.g*. direct, Raman, and/or tunnelling).

Table 6.4 Average calculated energy barrier ($\Delta E/k_B$) and pre−exponential factor (τ_0) parameters for **20** (Er) for different dc fields (500, 1000, 1500 Oe) and temperature regions ($T \geq 3.5$ K and $T \leq 3.0$ K).

		H_{dc} = 500 Oe	H_{dc} = 1000 Oe	H_{dc} = 1500 Oe
HT $T \geq 3.5$ K	$\Delta E/k_B$	26.4 ± 3.7 K	22.2 ± 3.6 K	18.3 ± 1.1 K
	τ_0	$1.5\cdot10^{-8}$ s	$1.7\cdot10^{-7}$ s	$2.5\cdot10^{-7}$ s
LT $T \leq 3.0$ K	$\Delta E/k_B$	7.6 ± 0.5 K	6.2 ± 0.6 K	6.2 ± 0.5 K
	τ_0	$1.9\cdot10^{-6}$ s	$1.4\cdot10^{-5}$ s	$1.8\cdot10^{-5}$ s

Finally, the dynamics of the Yb analogue (**21**) were investigated by ac susceptibility studies performed as a function of the temperature (2–10 K), in the absence of an external field and under the influence of an applied field (2000 Oe) at selected frequencies (υ = 10, 496, 997, 1267 Hz). Despite the presence of magnetic anisotropy suggested by both dc (Fig 6.4) and ac experiments in H_{dc} = 2000 Oe (see Fig 6.17, right), the in−phase and out−of−phase products of the susceptibility are too weak, and further magnetic relaxation studies were discarded.

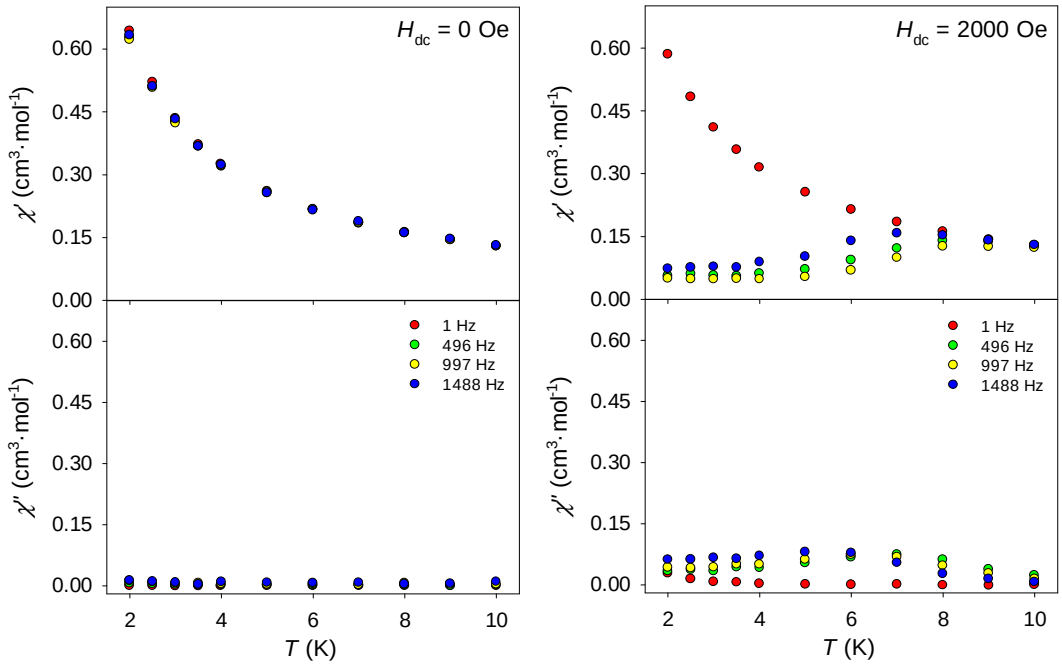

Fig 6.17 Magnetic ac susceptibility of **21** (Yb) as a function of the temperature in absence of applied field (left), and under an external field of H_{dc} = 2000 Oe (right) at selected frequencies.

In conclusion, the magnetic studies show distinct tendencies depending on the nature of the ground state of the lanthanide. Non−Kramer's ions such as Tb (**17**) or Ho (**19**) display a negligible out−of−phase susceptibility in the ac experiments. In contrast, Kramer's ions such as Dy (**18**) and Er (**20**) show relatively strong frequency−dependent ac signals induced by an applied dc field. The analysis of the ac studies of these Kramer's ions, however, display dissimilar results (*e.g*. different $\Delta E/k_B$ values). This may be due to the different electron distribution shape described for the Dy(III) ion (oblate) and the Er(III) ion (prolate), and also due to the presence of two competing crystal fields (axial−alkoxide *vs*. equatorial−Co, see Fig 6.10). However, no further comparative analysis between the SMM properties of Dy and Er is performed since no out−of−phase maximum was observed in the ac studies on **20** (Er), and that the estimated τ_0 and $\Delta E/k_B$ for **20** are preliminary results.

6.3. Concluding remarks

The reactivity of bis−tris propane (H_6L) with cobalt in the presence of lanthanide ions is similar to that shown by the copper ions, since the tendency of the ligand to encapsulate the transition metal ion to the detriment of the lanthanide is repeated. It must be highlighted that the {$Co_3Ln(H_2L)_2(H_3L)$} compounds introduced in this chapter are the first Co/H_6L complexes obtained to date. The synthetic reaction conditions used (*i.e*. presence of oxidising agent, excess of base and/or aerobic conditions) promote the oxidation of the Co(II) centres to Co(III) centres. As a consequence, the magnetic properties are defined essentially by the Ln(III) ions. The dynamics seem to be closely related to the electronic structure of the Ln ions due to ligand−field effects. Only complexes containing Kramer's ions (**18**, **20**) display field−induced slow magnetic relaxation, as they have a doubly−degenerate ground state independent of the symmetry of the lanthanide ion. In the case of **18**, the slow relaxation may arise from the fact that the anisotropic axis is closer to the pseudo−C_4 axis of the molecule than to the equatorial plane defined by {Co_3Dy}. The ac data for **18** and **20** also reveals the presence of multiple processes for the reversal of the magnetisation, such as tunnelling. The tunnelling could be triggered by crystal−field perturbations due to the distortion observed from ideal square antiprism geometry for Ln centres. That is consistent with non−zero transverse components of anisotropy, the mixture of different m_J states, and the presence of low energy excited states proposed by the fit of the dc data for **18**. However, additional optical and theoretical studies about the electronic properties of the complexes must be carried out in order prove the hypothesis herein proposed.

References

1. S. K. Langley, D. P. Wielechowski, V. Vieru, N. F. Chilton, B. Moubaraki, B. F. Abrahams, L. F. Chibotaru and K. S. Murray, *Angew. Chem. Int. Ed.*, **2013**, *52*, 12014.
2. S. K. Langley, D. P. Wielechowski, N. F. Chilton, B. Moubaraki and K. S. Murray, *Inorg. Chem.*, **2015**, *54*, 10497.
3. S. K. Langley, D. P. Wielechowski, B. Moubaraki and K. S. Murray, *Chem. Commun.*, **2016**, *52*, 10976.
4. C. M. Zaleski, E. C. Depperman, J. W. Kampf, M. L. Kirk and V. L. Pecoraro, *Angew. Chem. Int. Ed.*, **2004**, *43*, 3912.
5. G. Karotsis, M. Evangelisti, S. J. Dalgarno and E. K. Brechin, *Angew. Chem. Int. Ed.*, **2009**, *48*, 9928.
6. V. Mereacre, A. M. Ako, R. Clérac, W. Wernsdorfer, I. J. Hewitt, C. E. Anson and A. K. Powell, *Chem. Eur. J.*, **2008**, *14*, 3577.
7. L. Rigamonti, A. Cornia, A. Nava, M. Perfetti, M.−E. Boulon, A.−L. Barra, X. Zhong, K. Park and R. Sessoli, *Phys. Chem. Chem. Phys.*, **2014**, *16*, 17220.
8. L. Rigamonti, A. Nava, M.−E. Boulon, J. Luzon, R. Sessoli and A. Cornia, *Chem. Eur. J.*, **2015**, *21*, 12171.
9. K. C. Mondal, G. E. Kostakis, Y. Lan, W. Wernsdorfer, C. E. Anson and A. K. Powell, *Inorg. Chem.*, **2011**, *50*, 11604.
10. C. Meseguer, S. Titos−Padilla, M. M. Hänninen, R. Navarrete, A. J. Mota, M. Evangelisti, J. Ruiz and E. Colacio, *Inorg. Chem.*, **2014**, *53*, 12092.
11. A. Bencini, C. Benelli, A. Caneschi, R. L. Carlin, A. Dei and D. Gatteschi, *J. Am. Chem. Soc.*, **1985**, *107*, 8128.
12. F. J. Kettles, V. A. Milway, F. Tuna, R. Valiente, L. H. Thomas, W. Wernsdorfer, S. T. Ochsenbein and M. Murrie, *Inorg. Chem.*, **2014**, *53*, 8970.
13. L. Rosado Piquer and E. C. Sañudo, *Dalton Trans.*, **2015**, *44*, 8771.
14. K. Liu, W. Shi and P. Cheng, *Coord. Chem. Rev.*, **2015**, *289–290*, 74.
15. M. Murrie, *Chem. Soc. Rev.*, **2010**, *39*, 1986.
16. J. Goura, J. Brambleby, P. Goddard and V. Chandrasekhar, *Chem. Eur. J.*, **2015**, *21*, 4926.
17. J.−L. Liu, Y.−C. Chen, Y.−Z. Zheng, W.−Q. Lin, L. Ungur, W. Wernsdorfer, L. F. Chibotaru and M.−L. Tong, *Chem. Sci.*, **2013**, *4*, 3310.
18. A. Upadhyay, S. K. Singh, C. Das, R. Mondol, S. K. Langley, K. S. Murray, G. Rajaraman and M. Shanmugam, *Chem. Commun.*, **2014**, *50*, 8838.
19. S. K. Langley, N. F. Chilton, L. Ungur, B. Moubaraki, L. F. Chibotaru and K. S. Murray, *Inorg. Chem.*, **2012**, *51*, 11873.
20. J. A. Sheikh, S. Goswami and S. Konar, *Dalton Trans.*, **2014**, *43*, 14577.
21. J. A. Sheikh and A. Clearfield, *Inorg. Chem.*, **2016**, *55*, 8254.
22. P. van der Sluis and A. L. Spek, *Acta Crystallog. Sect. A*, **1990**, *46*, 194.
23. A. Spek, *J. Appl. Cryst.*, **2003**, *36*, 7.
24. I. D. Brown and D. Altermatt, *Acta Crystallog. Sect. B*, **1985**, *41*, 244.
25. N. E. Brese and M. O'Keeffe, *Acta Crystallog. Sect. B*, **1991**, *47*, 192.
26. R. M. Wood and G. J. Palenik, *Inorg. Chem.*, **1998**, *37*, 4149.
27. A. Ferguson, M. Schmidtmann, E. K. Brechin and M. Murrie, *Dalton Trans.*, **2011**, *40*, 334.
28. M. Pinsky and D. Avnir, *Inorg. Chem.*, **1998**, *37*, 5575.
29. D. Casanova, M. Llunell, P. Alemany and S. Alvarez, *Chem. Eur. J.*, **2005**, *11*, 1479.
30. C. Benelli and D. Gatteschi, *Introduction to Molecular Magnetism. From transition metals to lanthanides*, Wiley−VCH Verlag GmbH & Co. KGaA, Weinheim, **2015**.
31. J. Tang and P. Zhang, *Lanthanide Single Molecule Magnets*, Springer−Verlag, Berlin, Heidelberg, **2015**

32. M. A. AlDamen, S. Cardona−Serra, J. M. Clemente−Juan, E. Coronado, A. Gaita−Ariño, C. Martí−Gastaldo, F. Luis and O. Montero, *Inorg. Chem.*, **2009**, *48*, 3467.
33. N. Koike, H. Uekusa, Y. Ohashi, C. Harnoode, F. Kitamura, T. Ohsaka and K. Tokuda, *Inorg. Chem.*, **1996**, *35*, 5798.
34. C.−M. Liu, D.−Q. Zhang, X. Hao and D.−B. Zhu, *Chem. Asian J.*, **2014**, *9*, 1847.
35. K. S. Lim, J. J. Baldoví, W. R. Lee, J. H. Song, S. W. Yoon, B. J. Suh, E. Coronado, A. Gaita−Ariño and C. S. Hong, *Inorg. Chem.*, **2016**, 55, 5398.
36. N. F. Chilton, R. P. Anderson, L. D. Turner, A. Soncini and K. S. Murray, *J. Comput. Chem.*, **2013**, *34*, 1164.
37. L. Sorace, C. Benelli and D. Gatteschi, *Chem. Soc. Rev.*, **2011**, *40*, 3092.
38. Y.−N. Guo, G.−F. Xu, Y. Guo and J. Tang, *Dalton Trans.*, **2011**, *40*, 9953.
39. S. T. Liddle and J. van Slageren, *Chem. Soc. Rev.*, **2015**, *44*, 6655.
40. S.−Y. Lin, L. Zhao, Y.−N. Guo, P. Zhang, Y. Guo and J. Tang, *Inorg. Chem.*, **2012**, *51*, 10522.
41. J. M. Zadrozny, M. Atanasov, A. M. Bryan, C.−Y. Lin, B. D. Rekken, P. P. Power, F. Neese and J. R. Long, *Chem. Sci.*, **2013**, *4*, 125.
42. L.−F. Wang, J.−Z. Qiu, J.−L. Liu, Y.−C. Chen, J.−H. Jia, J. Jover, E. Ruiz and M.−L. Tong, *Chem. Commun.*, **2015**, *51*, 15358.
43. P.−H. Lin, T. J. Burchell, L. Ungur, L. F. Chibotaru, W. Wernsdorfer and M. Murugesu, *Angew. Chem. Int. Ed.*, **2009**, *48*, 9489.
44. S. K. Langley, N. F. Chilton, I. A. Gass, B. Moubaraki and K. S. Murray, *Dalton Trans.*, **2011**, *40*, 12656.
45. C. Ritchie, M. Speldrich, R. W. Gable, L. Sorace, P. Kögerler and C. Boskovic, *Inorg. Chem.*, **2011**, *50*, 7004.
46. J.−L. Liu, K. Yuan, J.−D. Leng, L. Ungur, W. Wernsdorfer, F.−S. Guo, L. F. Chibotaru and M.−L. Tong, *Inorg. Chem.*, **2012**, *51*, 8538.
47. M. Fang, H. Zhao, A. V. Prosvirin, D. Pinkowicz, B. Zhao, P. Cheng, W. Wernsdorfer, E. K. Brechin and K. R. Dunbar, *Dalton Trans.*, **2013**, *42*, 14693.
48. N. F. Chilton, D. Collison, E. J. L. McInnes, R. E. P. Winpenny and A. Soncini, *Nature Commun.*, **2013**, *4*, 2551.
49. J. D. Rinehart and J. R. Long, *Chem. Sci.*, **2011**, *2*, 2078.
50. J. Bartolomé, G. Filoti, V. Kuncser, G. Schinteie, V. Mereacre, C. E. Anson, A. K. Powell, D. Prodius and C. Turta, *Phys. Rev. B*, **2009**, *80*, 014430.

Chapter 7

The content of this chapter has been published in Chem. Commun. 2017, 53, 4799.

Contents

7. A topologically unique alternating $\{Co^{III}_3Gd^{III}_3\}$ magnetocaloric ring

7. A topologically unique alternating $\{Co^{III}_3Gd^{III}_3\}$ magnetocaloric ring

As previously introduced, a potential application of paramagnetic complexes is very-low-temperature magnetic refrigeration, arising from a large magnetocaloric effect (MCE). Some recent studies explore the combined use of 3*d*/4*f* ions in search of the enhancement of magnetocaloric properties, such as Co/Gd.[1-4] However, Co(II) ions appear to negatively influence the MCE, as a consequence of the characteristic large magnetic anisotropy. Herein, we explore an attractive solution to this problem, namely the tuning of the oxidation state, by changing anisotropic Co(II) to diamagnetic Co(III), concomitantly with an effective dilution of the Gd(III) ions, in order to favour ΔT_{ad}. Chapter 6 shows that the combination of bis−tris propane with Co(II) and Ln(III) salts in mild reaction conditions leads to the oxidation of the Co(II) centres to Co(III) centres. Using the reported $\{Mn_{18}Cu_6\}$ complexes obtained by means of the metallo-ligand $[Cu(H_6L)Cl]Cl$ (Fig 7.1, left) as a basis,[5] our approach is to use $\{Co^{II}(H_6L)\}$ precursors (Fig 7.1, right), that can undergo facile oxidation to diamagnetic Co(III), whilst encapsulating the cobalt centres and directing/separating the Ln(III) ions. Bearing in mind the oxophilic nature of lanthanides, $Co(CH_3COO)_2$ was used instead of $CoCl_2$ for the synthesis the $\{Co^{II}(H_6L)\}$ precursor. Therefore by using this strategy, herein we present the magnetocaloric properties of a new $\{Co^{III}_3Gd^{III}_3\}$ star-shaped ring, showing that the Co(III) ions have a significant impact on the adiabatic temperature change in this system, by separating the Gd(III) ions and weakening the Gd(III)···Gd(III) exchange. In terms of ΔT_{ad}, this complex is among the best gadolinium-based molecular refrigerants reported so far (*vide infra*).

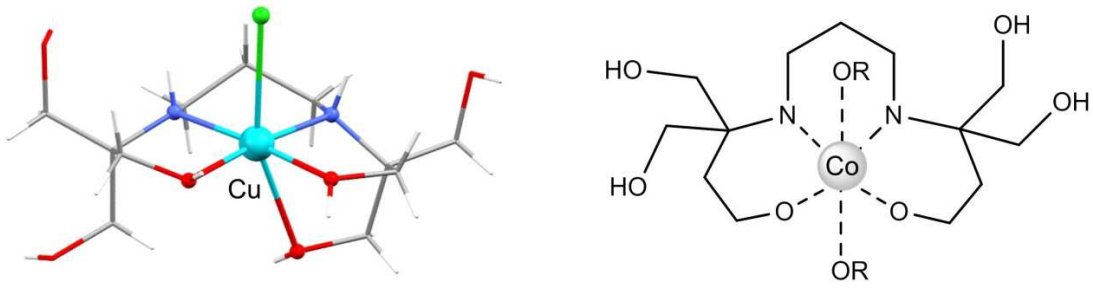

Fig 7.1 Structure of $[Cu(H_6L)Cl]Cl$ (left) and scheme for a $\{Co^{II}(H_6L)\}$ monomeric species (OR = CH_3COO^-). C, grey; Cu, turquoise; Cl, green; N, blue; O, red; H, white.

7.1. Synthesis

[$Co(H_6L)(CH_3COO)_2$] (**22**): $Co(CH_3COO)_2 \cdot 4H_2O$ (4.98 g, 20 mmol) was added to a white suspension of H_6L (5.64 g, 20 mmol) in isopropanol (100 mL), resulting in a pale pink suspension. The pink suspension was stirred overnight at room temperature. Yield 75% (6.90 g). IR: $\bar{\upsilon}$ (cm^{-1}) = 3198, 2874, 1560, 1406, 1269, 1034, 1013, 768, 660. Elemental analysis ([$Co(H_6L)(CH_3COO)_2$]) [%], found: C 39.25, H 7.08, N 6.06; calc: C 39.22, H 7.02, N 6.10. MS (ESI+, *m*/*z*): 362 $Na[Co(H_4L)]^+$, 340 $[Co(H_5L)]^+$.

[$Co^{III}_3Gd^{III}_3(H_2L)_3(acac)_2(CH_3COO)_4(H_2O)_2$] (**23**): $Gd(acac)_3 \cdot H_2O$ (0.10 g, 0.21 mmol) was added to a pink suspension of [$Co(H_6L)(CH_3COO)_2$] (0.10 g, 0.21 mmol) in a mixture of $4CH_3CN$:$1CH_3OH$ (20 mL), turning the pink suspension into a purple solution. The final solution was stirred and heated to 85°C for 45 min. Dark purple block-like single crystals suitable for X-ray diffraction were obtained by vapour diffusion of tetrahydrofuran into the solution over one week. Yield 20% (26 mg). IR: $\bar{\upsilon}$ (cm^{-1}) = 2971, 1576, 1520, 1449, 1366, 1217, 1036, 685. Elemental analysis ([$Co_3Gd_3(H_2L)_3(acac)_2(CH_3COO)_4(H_2O)_2$]$\cdot 0.5CH_3OH \cdot 4H_2O$) [%], found: C 30.24, H 5.04, N 3.92; calc: C 30.29, H 5.23, N 4.12.

7.2. Experimental results and discussion.

A new hexanuclear complex $[Co^{III}_3Gd^{III}_3(H_2L)_3(acac)_2(CH_3COO)_4(H_2O)_2]$ (**23**) with a unique alternating wheel-like structure was obtained by combining the metallo-ligand $[Co(H_6L)(CH_3COO)_2]$ (**22**) and $Gd(acac)_3 \cdot H_2O$ (see Fig 7.2). The pre-formation of a metallo-organic precursor seems to be essential for the assembly of **23**, as previously seen for the $\{Mn_{18}Cu_6\}$ complexes.

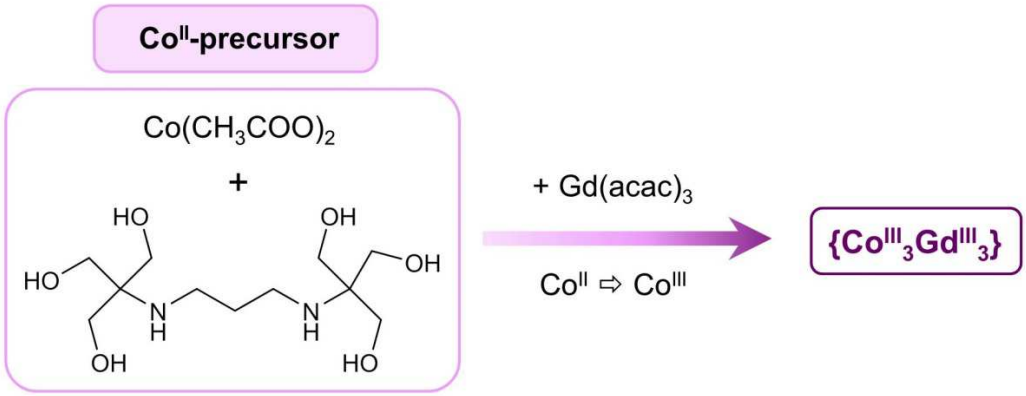

Fig 7.2 Synthetic approach for the preparation of **23**.

The characterisation of **22** was carried out by different spectroscopic techniques (IR, UV−Vis, ESI−MS) due to the impossibility of isolating crystals suitable for SXRD analysis. However, we were able to obtain the structure of a Ni(II)−monomer from an analogous reaction to that described for **22**, but using Ni(II) instead of Co(II) as starting material (see inset Fig 7.3). Therefore, a comparison of the IR spectra for both $[Ni(H_6L)(CH_3COO)_2]$ and **22** is shown in Fig 7.3. The position of the frequency bands related to the acetate groups for **22** ($\upsilon_{(C=O)}$ = 1561 cm^{-1}, $\upsilon_{(C-O)}$ = 1406 cm^{-1}) suggests that the counterions are coordinated to the Co(II) ion in a monodentate mode.[6, 7] The similarity between both spectra, the tendency of H_6L to encapsulate 3*d* metal ions in the central $\{N_2O_2\}$-pocket previously shown by other complexes,[5, 8, 9] and given that the crystal structure of $[Ni(H_6L)(CH_3COO)_2]$ is known,[10] we believe that the Co(II) ion in **22** presents an analogous coordination environment to that displayed for the nickel monomer.

UV-Vis studies were performed on methanolic solutions of **22** to investigate the geometry adopted by the Co(II) ion in solution, and to confirm the suggested oxidation state. For that, solutions of **22** in methanol at *c* = 1 mM, 5 mM, 50 mM were measured (Fig 7.4).

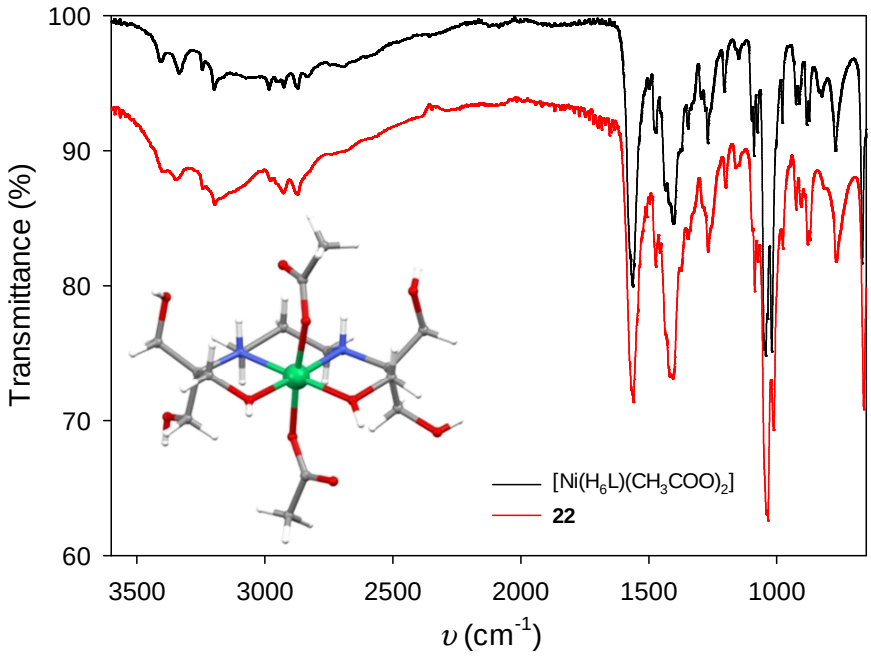

Fig 7.3 IR spectra for [Co(H_6L)($CH_3COO)_2$] (**22**) and [Ni(H_6L)($CH_3COO)_2$]. The inset shows the crystal structure of [Ni(H_6L)($CH_3COO)_2$].

The spectra corresponding to c_2 = 5 mM and c_3 = 50 mM display three broad absorption bands around λ = 495, 520, 565 nm. The most diluted solution c_1 = 1 mM shows only the band around 520 nm. The molar absorption coefficient (ε) of the displayed bands at different concentrations was calculated by applying the Beer-Lambert law ($A = \varepsilon \cdot l \cdot c$), giving ε_{495} = 17 (c_2), 20 (c_3) L·mol^{-1}·cm^{-1}, ε_{520} = 16 (c_2), 19 (c_3) L·mol^{-1}·cm^{-1}, ε_{565} = 23 (c_1), 15 (c_2), 17 (c_3) L·mol^{-1}·cm^{-1}. Considering that all the values are comprised in the range of 10–100 L·mol^{-1}·cm^{-1}, the bands are related to the spin-allowed *d-d* transitions for octahedral Co(II) complexes. The crystal field parameter Δ_0 = 9588 cm^{-1}, and the Racah parameter B = 827 cm^{-1}, have been calculated taking into account that:

- ⇨ λ ~ 565 nm: υ_1 = 17746 cm^{-1}, related to $^4A_{2g} \leftarrow {}^4T_{1g}$
- ⇨ λ ~ 520 nm: υ_2 = 19305 cm^{-1}, related to $^4T_{1g}(P) \leftarrow {}^4T_{1g}$
- ⇨ λ ~ 495 nm: υ_3 = 20177 cm^{-1}, related to spin-orbit coupling effects.

The observed absorption bands were assigned according to previous studies on octahedral $[Co^{II}(H_2O)_6]^{2+}$ complexes.[11] The extracted crystal-field splitting value ($\Delta_0/B \approx 12$), is consistent with high-spin Co(II) in **22**, in good agreement with the results of the dc magnetic experiments performed on **22** (*vide infra*). Therefore, the conclusions extracted from the UV-Vis spectroscopy are consistent with the ligand-

metal arrangement previously proposed, *i.e.* [$Co(H_6L)(CH_3COO)_2$] (see IR discussion), and with those from the rest of characterisation techniques.

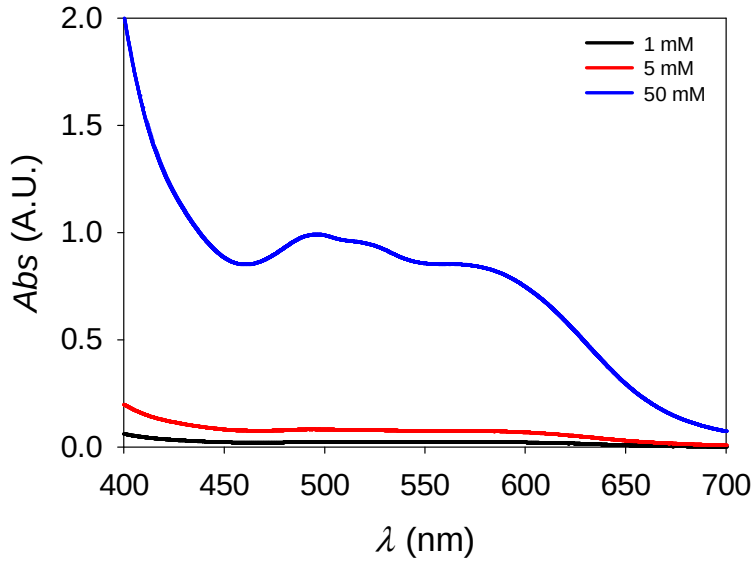

Fig 7.4 UV-Vis spectrum for methanolic solutions of **22** at *c* = 1 mM, 5 mM, 50 mM.

Additional Electrospray Ionisation Mass Spectroscopy (ESI−MS) experiment on **22** was performed to confirm the stability of the complex in solution (MeOH), and thus check the composition proposed by the UV-Vis and IR studies. The majority of the displayed peaks were assigned considering results from the IR, the molecular weight and the charge of the potential cations which could be present in solution after some fragmentation processes (Fig 7.5).

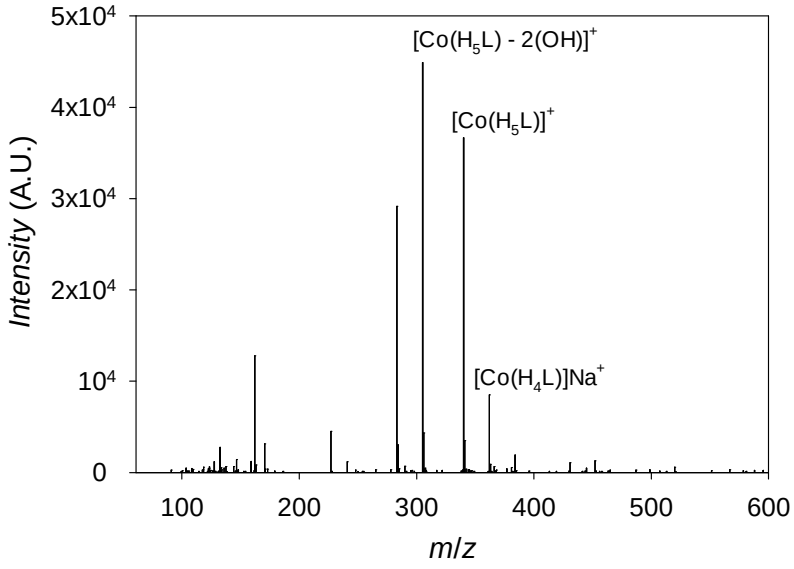

Fig 7.5 ESI^+ mass spectrum for **22**. The experiments were carried out in MeOH.

The spectrum for complex **22** shows peaks related to a monomeric species ($[Co(H_5L)]^+$, $[Co(H_4L)]Na^+$). The monodentate acetate anions could have been removed from the structure due to the relatively high lability of the Co-O(CH_3CO) bonds compared to the $\{N_2\text{-}O_2\}$ ones from the chelating ligand. Furthermore, the peaks observed in the region of 150-310 g/mol suggest a possible fragmentation of some hydroxyl groups from H_6L chelating ligand (*e.g.* $[Co(H_5L)-2(OH)]^+$).

As previously mentioned, although $[Co(H_6L)(CH_3COO)_2]$ was isolated as a precipitate in high yield, efforts to obtain the crystal structure for **22** were unsuccessful. Several attempts based on modifications on the synthetic route (changes in the reaction conditions, *e.g.* type of solvent or heat source) and crystallisation strategies (layering, slow evaporation, and/or vapour diffusion of different counter-solvents into the mother liquor solution or into a solution of the precipitate) were carried out, leading to very poor quality crystals (*i.e.* Diamond Light Source or NCS facilities needed). The SXRD analysis performed on some of those revealed high−nuclearity clusters that were incompatible with the results observed in the UV-Vis and magnetic experiments (*e.g.* $\{Co_8\}$ structure displayed in Fig A7.1 in the Appendix). That suggests that $[Co(H_6L)(CH_3COO)_2]$ tends to re-arrange in solution on attempted crystallisation. Nevertheless, the results proposed by all the other spectroscopic studies pointed consistently $[Co(H_6L)(CH_3COO)_2]$ as the chemical composition for **22**.

X-ray crystallographic analysis

Selected crystallographic experimental details for **23** are shown in Table 7.1. Complex **23** crystallises in the tetragonal space group *I*-42*d*. The asymmetric unit contains 1/2 molecule of $[Co^{III}_3Gd^{III}_3(H_2L)_3(acac)_2(CH_3COO)_4(H_2O)_2]$. The structure contains also significant solvent accessible voids. Difference Fourier maps of the solvent regions suggest the presence of several CH_3CN, CH_3OH, and H_2O molecules in the crystal lattice. However, they are poorly defined, and it was not possible to obtain a good model. Consequently, SQUEEZE (in PLATON)[12, 13] was used to identify the solvent voids and account for the electron density within them, calculated to contain 2124 e^- per unit cell, corresponding to approximately 265 e^- per complex. EDX experiments were performed on **23** in order to confirm the metal ratios proposed by the SXRD, and to investigate the homogeneity of the bulk crystalline sample (Fig 7.6). The average Co:Gd ratio found for **23** is 3:3 (Avg. Atomic% Co:Gd is 49.7(7):50.3(7)), which is consistent with that established by

single-crystal XRD. Further EDX map analyses by using different colour schemes for Co (red) and Gd (green) were performed to establish the distribution of the metal ions in the sample (Fig 7.6). These reveal the even distribution of Co/Gd in the crystalline bulk sample (Avg. Atomic% Co:Gd is 3.00:3.01).

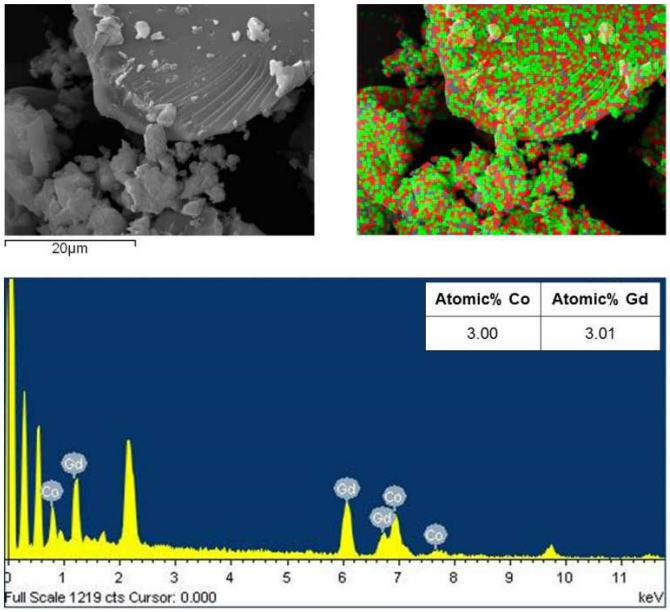

Fig 7.6 EDX spectrum and elemental map showing the distribution of Co and Gd in a bulk sample of **23**. Co is displayed in red, while Gd is in green. The inset displays the analysis of the Atomic% for the metal ions.

The structure of **23** contains three octahedral Co(III) ions, each one encapsulated by one tetra-deprotonated H_2L^{4-} ligand through four O and two N atoms (see Fig 7.7). The two remaining ligand arms are uncoordinated. Each {$Co(H_2L)$} unit is linked to two octa-coordinated Gd(III) ions through four *μ*-O bridging atoms forming a ring-like structure, in which Co(III) and Gd(III) centres alternately occupy the corners of a six-pointed star. Note that during the reaction, under aerobic conditions in the presence of bis-tris propane, Co(II) is oxidised to Co(III) and hence, the magnetic properties of **23** are defined exclusively by the paramagnetic Gd(III) ions (*vide infra*). The oxidation state of each cobalt centre has been confirmed by BVS calculations.[14-16] Two different Gd atoms can be distinguished based on the co-ligands that complete their coordination sphere: two bidentate acetates for Gd1, or one $acac^-$, one monodentate acetate and one water ligand for Gd2 and Gd2'. The symmetry analyses around the Gd(III) ion reveal a triangular dodecahedron (D_{2d}) as the closest ideal geometry for both Gd1, and Gd2 centres (see CShMs results in Table A7.1 in the Appendix).[17-19] The average intramolecular Gd···M distances (M = Co, Gd) are $d_{(Gd\cdots Co)}$ = 3.389(1) Å, and $d_{(Gd\cdots Gd)}$ = 5.802(9) Å.

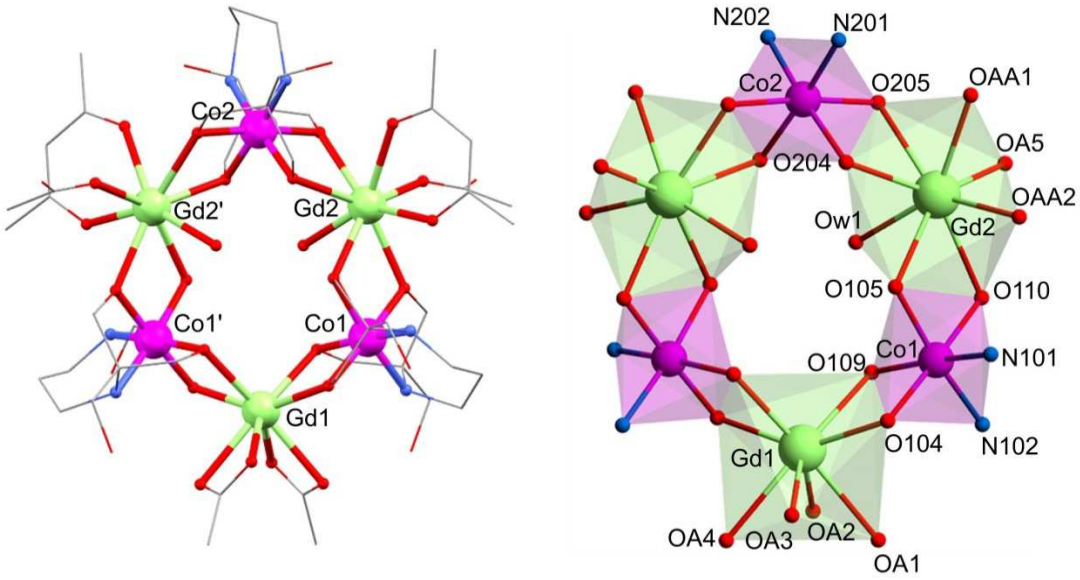

Fig 7.7 Structure of **23**. C, grey; Co, fuchsia; Gd, green; N, blue; O, red; Hydrogen atoms omitted for clarity.

Note that the {$Co^{III}_3Gd^{III}_3$} wheel is not perfectly planar: the Co(III) ions are co-planar (see Fig 7.8), while the Gd(III) ions are in a different plane, with a dihedral angle between the planes of 9°. Note that, to the best of our knowledge, the structure shown by {$Co^{III}_3Gd^{III}_3$} is unprecedented for Co/4*f* complexes (CSD 5.37, November 2016, where 3*d* = Sc → Zn, 4*f* = La → Lu) and remarkably only larger alternating 3*d*/4*f* rings (where 3*d* = Mn or Fe only), such as {Mn_4Ln_4}, {Mn_8Ln_8} or {$Fe_{10}Yb_{10}$} have been reported to date, where the structures are all more puckered than in {$Co^{III}_3Gd^{III}_3$}.[20-22]

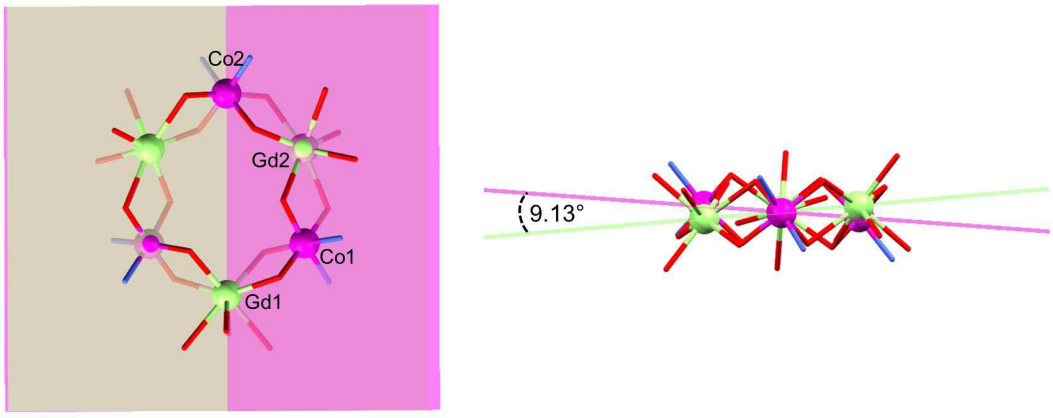

Fig 7.8 Detail of the metal alkoxide core of **23** Co, fuchsia; Gd, green; N, blue; O, red. Planes are highlighted in pink and green.

Table 7.1 Crystal Data and Structure Refinement Parameters of **23**.

Complex	**23**
T/K	100(2)
Crystal system	tetragonal
Space group	*I*-42*d*
a/Å, *c*/Å	26.644(3), 27.368(3)
V/Å^3	19428(4)
Z	8
ρ_{calc}/mg/m^3	1.337
μ/mm^{-1}	2.583
F(000)	7800.0
2θ range for data collection/°	3.674 to 50.064
Index ranges	-31 ≤ *h* ≤ 31, -31 ≤ *k* ≤ 31, -32 ≤ *l* ≤ 32
Reflections collected	246917
Data/restraints/ parameters	8610/588/432
GOF on F^2	1.172
Final *R* indexes [$I \geq 2\sigma(I)$]	R_1 = 0.0355, wR_2 = 0.0845
Final *R* indexes [all data]	R_1 = 0.0492, wR_2 = 0.0976
Largest diff. peak/hole/e Å^{-3}	0.92/-0.66
Flack parameter	-0.012(3)

Magnetic properties

The variable-temperature magnetic properties of complexes **22** and **23** were investigated in an applied field of 1000 Oe (Fig A7.2 and 7.9 respectively). The room temperature susceptibility value for **22** (2.86 cm^3·mol^{-1}·K) is in good agreement with that expected for an anisotropic Co(II) mononuclear complex (2.81 cm^3·mol^{-1}·K, considering S_{Co} = 3/2, g_{Co} = 2.45).[23] The experimental values (see Fig A7.2 in the Appendix) decrease gradually down to 150 K, before reaching a minimum of 1.50 cm^3·mol^{-1}·K at 2 K. This behaviour is consistent with a high-spin, octahedral Co(II) centre subject to 1st order spin-orbit coupling, in accord with the results observed in the UV-Vis studies (*vide supra*).

The experimental value of the static magnetic susceptibility temperature product $\chi_M T$ at 290 K (23.37 cm^3·mol^{-1}·K) for **23** is consistent with that estimated for three uncoupled Gd(III) centres (23.63 cm^3·mol^{-1}·K, $^8S_{7/2}$, s_{Gd} = 7/2, g_{Gd} = 2). $\chi_M T$

displays an almost imperceptible decrease between 290 and 26 K and then drops to 21.33 $cm^3 \cdot mol^{-1} \cdot K$ at 2 K (see Fig 7.9), consistent with very weak spin ordering promoted either by antiferromagnetic correlations or zero−field splitting (ZFS) of the ground multiplet. The magnetisation reaches the saturation at the highest measured field (5 T) for **23**, since the maximum experimental value (20.11) is in good agreement with that expected one (20.89, for g_{Gd} = 1.99).

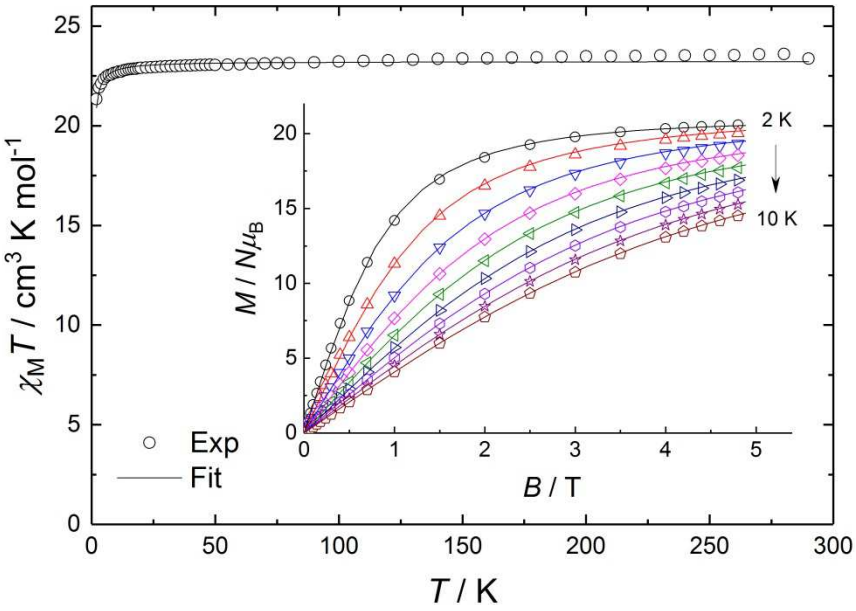

Fig 7.9 Temperature dependence of $\chi_M T$ for **23** in an applied field of 1000 Oe (inset shows magnetisation *vs*. field at 2 to 10 K, step 1 K. The solid lines correspond to the simultaneous fit (see text for details).

Exchange coupling through the diamagnetic Co(III) ions is a potential pathway for the very weak Gd···Gd′ intramolecular antiferromagnetic interaction, similar to previous Cu···Cu′ coupling through Zn(II) in heterometallic Cu/Zn bis-tris propane complexes.[8] The simultaneous fit of the susceptibility and magnetisation data at T = 2 to 10 K, step 1 K (see spin Hamiltonian and magnetic model in Fig 7.10) gives $\mathcal{J}$ = $-5 \cdot 10^{-3}$ cm^{-1}, and g_{Gd} = 1.99 (R = 88%).[24] In the mean-field approximation, $\mathcal{J}$ can interpreted as an effective interaction constant resulting from dipole-dipole magnetic interactions, which are well documented for molecular materials.[25-28] The g_{Gd} value obtained from the fit is reasonable for Gd(III) ions considering similar complexes.[29-31] The small deviation from the expected spin−only g value could be a consequence of a small ZFS, induced by crystal-field effects combined with spin-orbit coupling.[32, 33] Considering the relatively large average Gd···Gd′ distance (5.802(9) Å), one could argue that the exchange coupling likely is the relatively less effective than spin ordering. All sources, though, are extremely weak and we cannot discriminate between them, on basis of the experimental data.

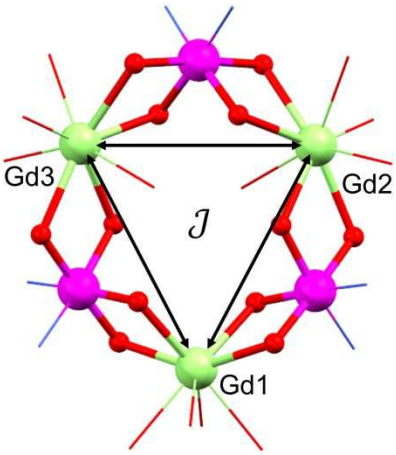

$$\hat{\mathcal{H}} = -2\mathcal{J}\left(\hat{S}_1 \cdot \hat{S}_2 + \hat{S}_1 \cdot \hat{S}_3 + \hat{S}_2 \cdot \hat{S}_3\right) + g_{Gd}\mu_B \vec{B} \sum_{i=1}^{3} \vec{s}_i$$

Fig 7.10 Magnetic model and spin Hamiltonian used for the fit of **23**. Co, fuchsia; Gd, green; N, blue; O, red.

Heat capacity studies

The dc experiments suggest, therefore, that **23** should display a relatively large MCE, arising from the weakly-interacting Gd(III) ions.[34-36] Heat capacity analysis was performed by Dr. Giulia Lorusso and Dr. Marco Evangelisti from the Instituto de Ciencia de Materiales de Aragón (ICMA), CSIC and Universidad de Zaragoza. The MCE is best evaluated from heat capacity c_p experiments (Fig 7.11, top panel). As is typical for molecular magnetic materials,[37] lattice vibrations contribute predominantly to c_p as a rapid increase above *ca*. 5−10 K. The non-magnetic lattice contribution can be described by the Debye model (dotted line in Fig 7.11), which simplifies to a $c_{latt}/R = aT^3$ dependence at the lowest temperatures, where a = $6.7 \cdot 10^{-3}$ K^{-3} for **23**. At such low temperatures, c_p is mainly determined by a Schottky-like anomaly, which is strongly dependent on B and can be well modelled by Hamiltonian (see Fig 7.9), using the same parameters obtained from fitting the susceptibility and magnetisation data. For B = 0, the system becomes sensitive to any perturbation, hence the need to add an effective internal field $B_{eff} \approx 0.3$ T to our model, in order to simulate the zero-applied-field c_p. For B > 1 T, such a correction is not necessary. We ascribe B_{eff} to the dipole-dipole magnetic interactions, although to a minor extent, it could also be associated with a small ZFS at the Gd(III) sites. From the experimental heat capacity data, we derive the entropy S of the system, according Eq. 7.1.

Eq. 7.1 $$S = \int \frac{c_p}{T} dT$$

Similarly, we derive the lattice entropy S_{latt} from c_{latt} and the magnetic entropy S_m from c_m, that is, the magnetic contribution to c_p, *viz*., the aforementioned Schottky-like anomaly, calculated on basis of Hamiltonian (see Fig 7.9). The bottom panel of Fig 7.11 shows the resulting temperature dependence of the experimental entropy S, which thus corresponds to the sum of S_{latt} (dotted line) and S_m (solid lines), for any applied magnetic field employed. Because of the very weak ZFS and interactions present, temperatures as low as *ca*. 3-4 K are already sufficient for fully decoupling the Gd(III) spins. Therefore, within the investigated temperature range, the zero-applied-field S reaches the maximum entropy value per mole involved, which corresponds to three non-interacting Gd(III) spins s = 7/2 and is calculated as $3 \times R\ln(2s+1) \approx 6.2R$ (see Fig 7.11).

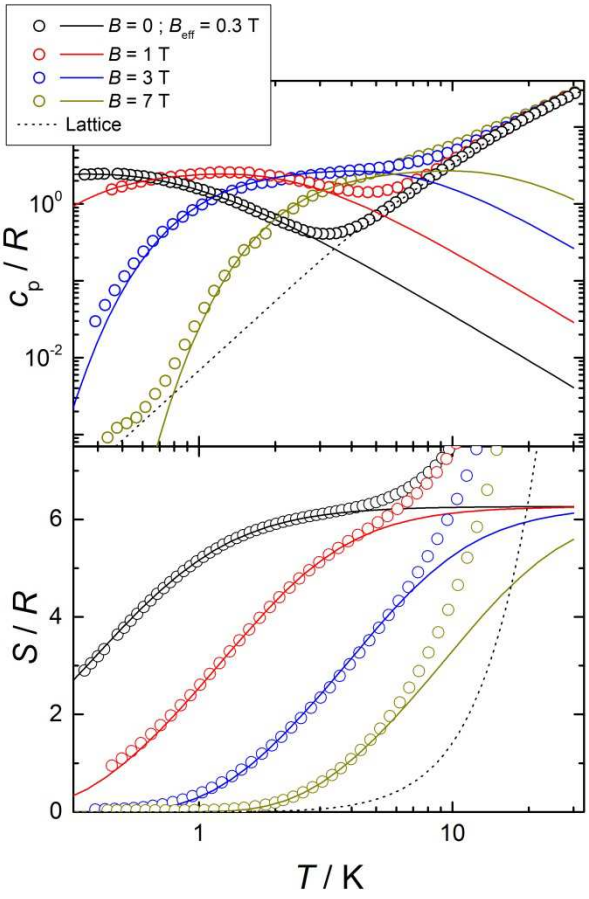

Fig 7.11 Top: Temperature dependence of the heat capacity, normalized to the gas constant, c_p/R for **23** for selected applied fields, as labelled. Bottom: Temperature dependence of the entropy, normalized to the gas constant, S/R for **23** for selected applied fields, as labelled. The dotted line is the lattice contribution, while the solid lines correspond to the magnetic modelling (see text for details).

Next, we evaluate ΔS_m and ΔT_{ad}, following a change of the applied magnetic field ΔB. The temperature dependencies of both ΔS_m and ΔT_{ad} can be calculated straightforwardly from the experimental entropy (Fig 7.11, bottom panel).[34]

Likewise, ΔS_m can also be calculated from the magnetisation data (Fig 7.9) by making use of the Maxwell relation shown in Eq. 7.2.

Eq. 7.2 $$\Delta S_m = \int \left[\frac{\partial M}{\partial T}\right]_B dB$$

Figure 7.12 shows the so-obtained dependence of ΔS_m and ΔT_{ad} for **23** versus temperature for selected ΔB values. Note the nice agreement between the ΔS_m results obtained through both methods, thus validating the approaches employed. For the largest applied field change ΔB = (7–0) T, *i.e.*, after a full demagnetization from 7 T, the maximum value of $-\Delta S_m$ is 5.6*R* at T = 1.9 K, which corresponds to 90% of the available entropy content and is equivalent to 23.6 $J \cdot kg^{-1} \cdot K^{-1}$ per unit mass. Concomitantly, we obtain ΔT_{ad} = 10.7 K at T = 1.5 K for the same field change, that is, the temperature decreases down to a final temperature T_f = 1.5 K, on demagnetizing adiabatically from B = 7 T and an initial temperature $T_i = T_f + \Delta T_{ad}$ = 12.2 K. Note that ΔT_{ad} is limited in T_f by sources of magnetic ordering (spin-spin interactions and magnetic anisotropies) and in T_i by the lattice entropy, which soon becomes the dominating contribution on increasing the temperature (see Fig 7.12).

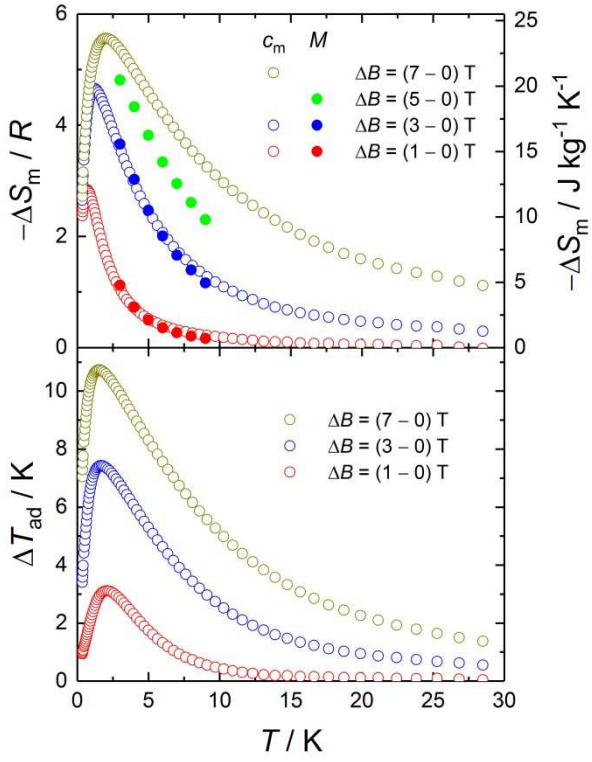

Fig 7.12 Temperature dependence of the magnetic entropy change ΔS_m (top) and adiabatic temperature change ΔT_{ad} (bottom) for **23** for selected changes of the applied magnetic field ΔB, as labelled. Values of ΔS_m are reported per unit mole (left) and mass (right), and are obtained from heat capacity (empty dots) and magnetisation (filled dots) data.

7.3. Concluding remarks

The metallo-organic precursor [$Co(H_6L)(CH_3COO)_2$] (**22**) has successfully directed the molecular assembly in [$Co^{III}_3Gd^{III}_3(H_2L)_3(acac)_2(CH_3COO)_4(H_2O)_2$] (**23**), so that the Gd(III) ions are isolated, thus promoting the discussed magnetocaloric properties. Several Co(II)/Gd(III) molecular coolers have been studied so far.[1, 38-43] The biggest hindrance to a large MCE in those compounds is the large magnetic anisotropy brought in by the Co(II) ions.[32, 34, 44] In **23** we circumvent this impediment by oxidising Co(II) to Co(III) during the synthesis, thus leaving only the Gd(III) ions to contribute magnetically. In terms of the magnetocaloric properties of **23**, the diamagnetic Co(III) ions still play a role, though passively. On the one hand, they influence negatively on the entropy change per unit mass. The lower the magnetic:non-magnetic ions ratio, the lower are the magnetic heat capacity and entropy per unit mass. The maximum value observed of $-\Delta S_m$ = 23.6 $J \cdot kg^{-1} \cdot K^{-1}$ at T = 1.9 K for **23** is large, though not outstanding. However, the key point is that the Co(III) centres impact positively on the adiabatic temperature change. In the molecular-ring structure, Co(III) and Gd(III) ions alternate with respect to one another. Therefore, the intermediate presence of the Co(III) ions weakens extremely the magnetic interaction between the Gd(III) ions, so the temperature-dependence of ΔT_{ad} has a maximum at a relatively lower temperature than usually found for pure-Gd molecular complexes. Among the few known systems that have a ΔT_{ad} maximum below, *e.g.*, 2 K for 7 T, complex **23** with ΔT_{ad} = 10.7 K at T = 1.5 K lags behind only the extraordinary {Gd_2-ac} with ΔT_{ad} = 12.6 K at T = 1.4 K,[45] while it outdoes {Zn_2Gd_2} with ΔT_{ad} = 9.6 K at T = 1.4 K,[46] and {Gd_7} with ΔT_{ad} = 9.4 K at T = 1.8 K.[47]

References

1. Y.−Z. Zheng, M. Evangelisti, F. Tuna and R. E. P. Winpenny, *J. Am. Chem. Soc.*, **2012**, *134*, 1057.
2. J.−B. Peng, Q.−C. Zhang, X.−J. Kong, Y.−Z. Zheng, Y.−P. Ren, L.−S. Long, R.−B. Huang, L.−S. Zheng and Z. Zheng, *J. Am. Chem. Soc.*, **2012**, *134*, 3314.
3. S. K. Gupta, A. A. Dar, T. Rajeshkumar, S. Kuppuswamy, S. K. Langley, K. S. Murray, G. Rajaraman and R. Murugavel, *Dalton Trans.*, **2015**, *44*, 5961.
4. J. A. Sheikh and A. Clearfield, *Inorg. Chem.*, **2016**, *55*, 8254−8256.
5. V. A. Milway, F. Tuna, A. R. Farrell, L. E. Sharp, S. Parsons and M. Murrie, *Angew. Chem. Int. Ed.*, **2013**, *52*, 1949.
6. K. Nakamoto, *Applications in Inorganic Chemistry, in Infrared and Raman Spectra of Inorganic and Coordination Compounds: Part A: Theory and Applications in Inorganic Chemistry*, John Wiley & Sons, Inc., Hoboken, NJ, USA, **1986**.
7. G. B. Deacon and R. J. Phillips, *Coord. Chem. Rev.*, **1980**, *33*, 227.
8. M. Heras Ojea, C. Wilson, S. J. Coles, F. Tuna and M. Murrie, *Dalton Trans.*, **2015**, *44*, 19275.
9. M. Heras Ojea, V. A. Milway, G. Velmurugan, L. H. Thomas, S. J. Coles, C. Wilson, W. Wernsdorfer, G. Rajaraman and M. Murrie, *Chem. Eur. J.*, **2016**, *22*, 12839.
10. M. Heras Ojea, C. Wilson, M. Murrie, *Unpublished work*.
11. D. R. Armstrong, R. Fortune and P. G. Perkins, *Dalton Trans.*, **1976**, 753−757.
12. P. van der Sluis and A. L. Spek, *Acta Crystallog. Sect. A*, **1990**, *46*, 194.
13. A. Spek, *J. Appl. Cryst.*, **2003**, 36, 7.
14. I. D. Brown and D. Altermatt, *Acta Crystallog. Sect. B*, **1985**, *41*, 244.
15. N. E. Brese and M. O'Keeffe, *Acta Crystallog. Sect. B*, **1991**, *47*, 192.
16. R. M. Wood and G. J. Palenik, *Inorg. Chem.*, **1998**, *37*, 4149.
17. M. Pinsky and D. Avnir, *Inorg. Chem.*, **1998**, *37*, 5575.
18. D. Casanova, J. Cirera, M. Llunell, P. Alemany, D. Avnir and S. Alvarez, *J. Am. Chem. Soc.*, **2004**, *126*, 1755.
19. D. Casanova, M. Llunell, P. Alemany and S. Alvarez, *Chem. Eur. J.*, **2005**, *11*, 1479.
20. M. Li, A. M. Ako, Y. Lan, W. Wernsdorfer, G. Buth, C. E. Anson, A. K. Powell, Z. Wang and S. Gao, *Dalton Trans.*, **2010**, *39*, 3375.
21. A. Baniodeh, C. E. Anson and A. K. Powell, *Chem. Sci.*, **2013**, *4*, 4354.
22. K. R. Vignesh, S. K. Langley, B. Moubaraki, K. S. Murray and G. Rajaraman, *Chem. Eur. J.*, **2015**, *21*, 16364.
23. Y.−Z. Zhang, S. Gomez−Coca, A. J. Brown, M. R. Saber, X. Zhang and K. R. Dunbar, *Chem. Sci.*, **2016**, *7*, 6519.
24. N. F. Chilton, R. P. Anderson, L. D. Turner, A. Soncini and K. S. Murray, *J. Comput. Chem.*, **2013**, *34*, 1164.
25. A. Bino, D. C. Johnston, D. P. Goshorn, T. R. Halbert and E. I. Stiefel, *Science*, **1988**, *241*, 1479.
26. A. Morello, F. L. Mettes, F. Luis, J. F. Fernández, J. Krzystek, G. Aromí, G. Christou and L. J. de Jongh, *Phys. Rev. Lett.*, **2003**, *90*, 017206.
27. M. Evangelisti, A. Candini, A. Ghirri, M. Affronte, G. W. Powell, I. A. Gass, P. A. Wood, S. Parsons, E. K. Brechin, D. Collison and S. L. Heath, *Phys. Rev. Lett.*, **2006**, *97*, 167202.
28. F. Luis, in *Molecular Magnets: Physics and Applications*, Springer−Verlag, Berlin, Heidelberg, **2014**, pp. 161.
29. C. Lampropoulos, T. C. Stamatatos, K. A. Abboud and G Christou, *Inorg. Chem.*, **2009**, *48*, 429.
30. C. Y. Chow, H. Bolvin, V. E. Campbell, R. Guillot, J. W. Kampf, W. Wernsdorfer, F. Gendron, J. Autschbach, V. L. Pecoraro and T. Mallah, *Chem. Sci.*, **2015**, *6*, 4148.

31. K. Wang, Z.−L. Chen, H.−H. Zou, K. Hu, H.−Y. Li, Z. Zhang, W.−Y. Sun and F.−P. Liang, *Chem. Commun.*, **2016**, *52*, 8297.
32. F. Luis and M. Evangelisti, *Struct. Bond.*, **2015**, *164*, 431−460.
33. S. A. Stoian, C. Paraschiv, N. Kiritsakas, F. Lloret, E. Münck, E. L. Bominaar and M. Andruh, *Inorg. Chem.*, **2010**, *49*, 3387.
34. M. Evangelisti and E. K. Brechin, *Dalton Trans.*, **2010**, *39*, 4672.
35. R. Sessoli, *Angew. Chem. Int. Ed.*, **2012**, *51*, 43.
36. Y.−Z. Zheng, E. M. Pineda, M. Helliwell and R. E. P. Winpenny, *Chem. Eur. J.*, **2012**, *18*, 4161.
37. M. Evangelisti, F. Luis, L. J. de Jongh and M. Affronte, *J. Mat. Chem.*, **2006**, *16*, 2534.
38. Y.−Z. Zheng, M. Evangelisti and R. E. P. Winpenny, *Chem. Sci.*, **2011**, *2*, 99.
39. J.−B. Peng, Q.−C. Zhang, X.−J. Kong, Y.−P. Ren, L.−S. Long, R.−B. Huang, L.−S. Zheng and Z. Zheng, *Angew. Chem. Int. Ed.*, **2011**, *50*, 10649.
40. R. Sibille, T. Mazet, B. Malaman, T. Gaudisson and M. François, *Inorg. Chem.*, **2012**, *51*, 2885.
41. E. Moreno Pineda, F. Tuna, R. G. Pritchard, A. C. Regan, R. E. P. Winpenny and E. J. L. McInnes, *Chem. Commun.*, **2013**, *49*, 3522.
42. D. I. Alexandropoulos, L. Cunha−Silva, G. Lorusso, M. Evangelisti, J. Tang and T. C. Stamatatos, *Chem. Commun.*, **2016**, *52*, 1693.
43. T. N. Hooper, R. Inglis, G. Lorusso, J. Ujma, P. E. Barran, D. Uhrin, J. Schnack, S. Piligkos, M. Evangelisti and E. K. Brechin, *Inorg. Chem.*, **2016**, *55*, 10535.
44. G. Karotsis, M. Evangelisti, S. J. Dalgarno and E. K. Brechin, *Angew. Chem. Int. Ed.*, **2009**, *48*, 9928.
45. M. Evangelisti, O. Roubeau, E. Palacios, A. Camón, T. N. Hooper, E. K. Brechin and J. J. Alonso, *Angew. Chem. Int. Ed.*, **2011**, *50*, 6606.
46. J. Ruiz, G. Lorusso, M. Evangelisti, E. K. Brechin, S. J. A. Pope and E. Colacio, *Inorg. Chem.*, **2014**, *53*, 3586.
47. E. M. Pineda, G. Lorusso, K. H. Zangana, E. Palacios, J. Schnack, M. Evangelisti, R. E. P. Winpenny and E. J. L. McInnes, *Chem. Sci.*, **2016**, *7*, 4891.

Chapter 8

Contents

8. Effect of ligand modification on the SMM properties in {$Ln_2Ni_2(L2)_2$} Schiff base derivatives

8. Effect of ligand modification on the SMM properties in $\{Ln_2Ni_2(L2)_2\}$ Schiff base derivatives

The final experimental chapter is related to the use of Schiff base ligands as an alternative to bis−tris propane. As was previously explained, valen−type derivatives have been widely employed in the rational design of 3*d*−4*f* SMMs, given consideration to their ability for encapsulating simultaneously both metal ions.[1, 2] Some studies performed on valen−type complexes have been extremely useful in molecular magnetism, such as those developed by Costes that shed light on the factors influencing the nature and strength of the Cu···Ln interaction in dinuclear {CuLn} complexes.[3-5] A diagram of the deprotonated *N,N′*−bis(2−Hydroxy−3−methoxyphenylmethylidene)−2,6−pyridinediamine[6] (referred to as H_2L2) is shown in Figure 8.1. The O, N–donor atoms in H_2L2 define different coordination pockets, which we believe can help to direct the assembly of 3*d*/4*f* polymetallic complexes. Therefore, the investigation of the coordination chemistry of H_2L2 with Ln(III) ions in the presence of nickel is herein proposed. As a result, five new complexes have been isolated, with formula $[Ln_2Ni_2(L2)_2(CH_3COO)_6(H_2O)_2]$ (where Gd **24**, Tb **25**, Dy **26**, Ho **27**, Y **28**). It should be noted that the $\{Ln_2Ni_2(L2)_2\}$ compounds are the first structures obtained with H_2L2 to date, to the best of our knowledge. The reported examples of H_2L2-derivatives found in the literature did not specify any CCDC code, so it was assumed they were not characterised by SXRD.[7, 8]

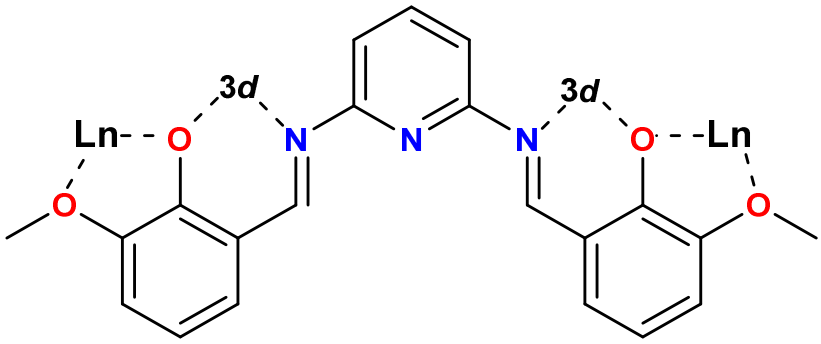

Figure 8.1 Diagram of $L2^{2-}$ displaying the different coordination sites (3*d*, Ln).

The topology displayed by the compounds is quite unusual, but not unique (CSD 5.37, January 2017), as a very similar $\{Ln_2Ni_2(Sal)_2\}$ family has been recently reported, where Ln = Gd, Dy, Y and Sal = *N,N′*−bis(3−methoxysalicylidene)-1,3−diaminobenzene (see Fig 8.2).[9]

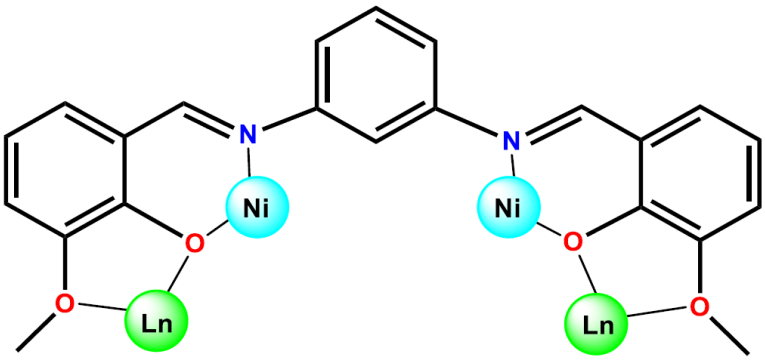

Figure 8.2 Structure and coordination sites of the ligand Sal^{2-}. Reprinted with permission from Ref. 9. Copyright 2014 American Chemical Society.

Even though both families are much alike, there are certain structural differences. Those most remarkable are related to the replacement of the ligand and co−ligands used in the synthesis, such as the presence of the pyridyl N−atom in H_2L2. The effects that such structural modifications have on the magnetic properties exhibited by $[Ln_2Ni_2(L2)_2(CH_3COO)_6(H_2O)_2]$ are discussed. The dc susceptibility experiments performed on $\{Y_2Ni_2\}$ (**28**) clarify the nature of the Ni···Ni interaction, and the axial anisotropy related to the Ni(II) ions (D_{Ni}). The study of the relaxation dynamics for $\{Ln_2Ni_2(L2)_2\}$ reveals a relationship between the type of lanthanide ion and the presence of slow magnetic relaxation.

8.1. Synthesis

N,N′−bis(2−Hydroxy−3−methoxyphenylmethylidene)−2,6−pyridinediamine (H_2L2) was prepared according to the reported procedure.[6] The crystallisation process was avoided though, and the product obtained as precipitate was used without further purification. A few drops of piperidine (~ 3−5 mL) were added to a brown suspension of 2,6−pyridinediamine (2.19 g, 20 mmol) and *o*−vanillin (6.09 g, 40 mmol) in EtOH (150 mL). The initial brown suspension turned orange after refluxing for one half hour. Once cooled, the precipitate was filtered, washed with EtOH and dried with Et_2O. Yield 89% (6.70 mg). The ligand was characterised by ^{1}H−NMR ($CDCl_3$), IR, elemental analysis and ESI−MS. ^{1}H−NMR ($CDCl_3$, see scheme below for assignment of H), δ (ppm): 13.85 (s, 2H, −OH), 9.45 (s, 2H, −CH=N−), 7.81 (t, 1H, Ar–He), 7.21 (d, 2H, Ar–Hc), 7.14 (d, 4H, Ar–Ha, Ar−Hd), 6.88 (t, 2H, Ar–Hb), 3.90 (s, 6H, $-OCH_3$). The assignment of H was performed considering that reported in Ref. 10. IR ($\bar{\upsilon}$ in cm^{-1}): 2994, 1603, 1547, 1464, 1433, 1258, 1017, 727, 602. Elemental analysis (H_2L2) [%], found: C 66.41, H 5.12, N 11.02; calc: C 66.83, H 5.07, N 11.13. MS (ESI^+, *m*/*z*): 378 $[H_2L2+H]^+$, 400 $[H_2L2+Na]^+$.

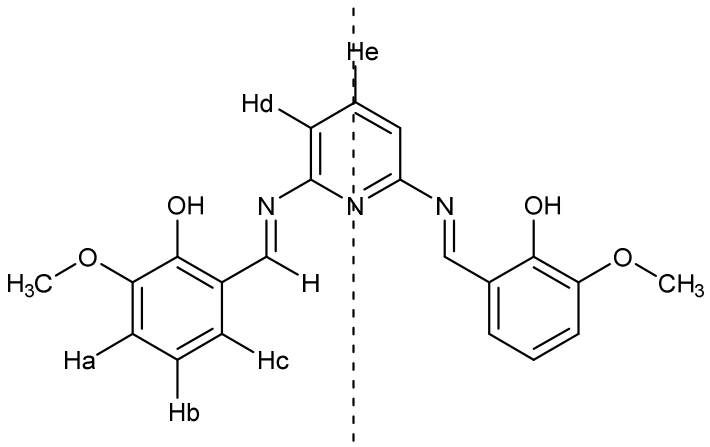

$[Gd_2Ni_2(L2)_2(CH_3COO)_6(H_2O)_2]\cdot 2CH_3CN\cdot 2H_2O$ (**24**): To a suspension of H_2L2 (0.07 g, 0.2 mmol) in MeCN (25 mL), Et_3N (0.06 ml, 0.4 mmol), $Ni(CH_3COO)_2\cdot 4H_2O$ (0.05 g, 0.2 mmol), and $Gd(CH_3COO)_3\cdot H_2O$ (0.06 g, 0.2 mmol) were sequentially added. The resulting orange suspension was heating under reflux for 4h. The final green−yellow solution was stirred overnight at room temperature. Single green rod−like crystals suitable for X−ray diffraction were obtained by slow evaporation over ~7−10 days. Yield 27% (40 mg). IR ($\bar{\upsilon}$ in cm^{-1}): 3277, 1611, 1545, 1414, 1308, 1236, 1200, 741, 658. Elemental analysis ($[Gd_2Ni_2(L2)_2$-

−$(CH_3COO)_6(H_2O)_2]\cdot 2CH_3CN\cdot 2.5H_2O$) [%], found: C 40.96, H 3.90, N 6.66; calc: C 40.98, H 3.97, N 6.59.

$[Tb_2Ni_2(L2)_2(CH_3COO)_6(H_2O)_2]\cdot 4CH_3CN\cdot 5H_2O$ (**25**): The same synthetic procedure described for **24** was followed, but using $Tb(CH_3COO)_3\cdot H_2O$ instead of $Gd(CH_3COO)_3\cdot H_2O$. Single green rod−like crystals suitable for X−ray diffraction were obtained by slow evaporation over ~7−10 days. Yield 21% (33 mg). IR ($\bar{\upsilon}$ in cm^{-1}): 3371, 1611, 1549, 1418, 1306, 1235, 1198, 750, 660. Elemental analysis ($[Tb_2Ni_2(L2)_2(CH_3COO)_6(H_2O)_2]\cdot 3CH_3CN\cdot 5.5H_2O$) [%], found: C 39.97, H 4.01, N 6.76; calc: C 40.07, H 4.26, N 7.01.

$[Dy_2Ni_2(L2)_2(CH_3COO)_6(H_2O)_2]\cdot 4CH_3CN\cdot 5H_2O$ (**26**): The same synthetic procedure described for **24** was followed, but using $Dy(CH_3COO)_3\cdot H_2O$ instead of $Gd(CH_3COO)_3\cdot H_2O$. Single green rod−like crystals suitable for X−ray diffraction were obtained by slow evaporation over ~7−10 days. Yield 55% (88 mg). IR ($\bar{\upsilon}$ in cm^{-1}): 3277, 1613, 1545, 1418, 1310, 1238, 1200, 750, 658. Elemental analysis ($[Dy_2Ni_2(L2)_2(CH_3COO)_6(H_2O)_2]\cdot 1.75CH_3CN\cdot 3.25H_2O$) [%], found: C 39.94, H 4.11, N 6.69; calc: C 40.30, H 3.98, N 6.33.

$[Ho_2Ni_2(L2)_2(CH_3COO)_6(H_2O)_2]\cdot 2CH_3CN\cdot 2H_2O$ (**27**): The same synthetic procedure described for **24** was followed, but using $Ho(CH_3COO)_3\cdot H_2O$ instead of $Gd(CH_3COO)_3\cdot H_2O$. Single green rod−like crystals suitable for X−ray diffraction were obtained by slow evaporation over ~7−10 days. Yield 32% (65 mg). IR ($\bar{\upsilon}$ in cm^{-1}): 3273, 1613, 1545, 1456, 1418, 1310, 1238, 1200, 750. Elemental analysis ($[Ho_2Ni_2(L2)_2(CH_3COO)_6(H_2O)_2]\cdot 0.75CH_3CN\cdot 3.25H_2O$) [%], found: C 39.71, H 3.76, N 5.75; calc: C 39.73, H 3.81, N 5.64.

$[Y_2Ni_2(L2)_2(CH_3COO)_6(H_2O)_2]\cdot 2CH_3CN\cdot 2H_2O$ (**28**): The same synthetic procedure described for **24** was followed, but using $Y(CH_3COO)_3\cdot H_2O$ instead of $Gd(CH_3COO)_3\cdot H_2O$. Single green rod−like crystals suitable for X−ray diffraction were obtained by slow evaporation over ~7−10 days. Yield 24% (35 mg). IR ($\bar{\upsilon}$ in cm^{-1}): 3457, 2971, 1613, 1545, 1435, 1366, 1231, 1204, 835. Elemental analysis ($[Y_2Ni_2(L2)_2(CH_3COO)_6(H_2O)_2]\cdot 5.5H_2O$) [%], found: C 41.83, H 4.45, N 5.49; calc: C 42.24, H 4.40, N 5.47.

8.2. Results and discussion

The ligand H_2L2 was prepared from the characteristic condensation reaction between the R−NH_2 groups of the 2,6−pyridinediamine and the R−CHO from the *o*−vanillin precursors in ethanol.[6] As can be observed in Scheme 8.1, the ligand has multiple binding positions that may promote different environments. There are two outer, less hindered $\{O_2O_2'\}$ pockets predisposed to the coordination of lanthanide ions, and two inner $\{N_2O_2\}$ ones that are likely to encapsulate transition metal centres. The reaction of H_2L2 with nickel and lanthanide acetates leads to the assembly of five isostructural complexes $[Ln_2Ni_2(L2)_2(CH_3COO)_6(H_2O)_2]$, proving the ability of the ligand to control the topology in 3*d*/4*f* systems. Variations in the heat source employed in the synthetic route (*e.g.* aerobic RT or ~75°C reactions) gave rise to the partial decomposition of the ligand by hydrolysis of the iminic bonds, and thus to monomeric impurities (*i.e.* Ni(II)−based compounds, see Fig A8.1 in the appendix) additional to the main $\{Ln_2Ni_2(L2)_2\}$ product. That may be caused by a competition of different final products during the synthesis of $\{Ln_2Ni_2(L2)_2\}$. Hence, relatively harsh conditions such as reflux are needed in order to promote pure $\{Ln_2Ni_2(L2)_2\}$ products. Alternative solvothermal and microwave assisted reactions were performed, most of them yielding precipitate and/or polycrystalline powders but none providing crystals suitable for SXRD characterisation.

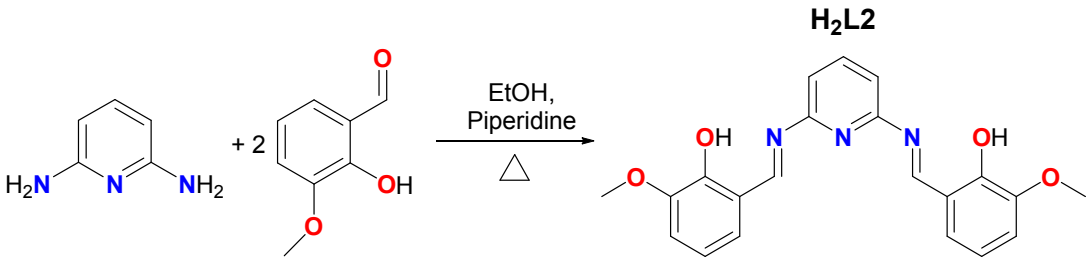

Scheme 8.1 The ligand *N,N'*−bis(2−Hydroxy−3−methoxyphenylmethylidene)−2,6-pyridinediamine (H_2L2).

X−ray crystallographic analysis

Selected crystallographic experimental details for **24**−**28** are shown in Table 8.3. Complexes **24**, **27** and **28** crystallise in the monoclinic space group $P2_1/c$, whereas **25** and **26** crystallise in triclinic *P*−1. The asymmetric unit of all of them contain a molecule of $[Ln_2Ni_2(L2)_2(CH_3COO)_6(H_2O)_2]$, molecules of acetonitrile (two for **24**, **27**, **28**; four for **25**, **26**), and molecules of water (two for **24**, **27**, **28**; five for **25**, **26**). As the complexes are isostructural, the following description of **24** could be applied to

all of them. The crystal structure of $[Gd_2Ni_2(L2)_2(CH_3COO)_6(H_2O)_2]$ displays two pairs of {GdNi} dimers linked by two doubly deprotonated $L2^{2-}$ ligand units in an *E*−configuration (see Fig 8.3). The two different $L2^{2-}$ units are distinguished by colour code (yellow and violet). As expected, Ni(II) ions occupy the inner pocket, whereas the Gd(III) ions are in the outer position defined exclusively by oxygen atoms. Each dimer has a *syn–syn* bidentate acetate group acting as a bridge between the Ni and Gd centres. These ions are additionally bridged by two O−phenoxo atoms (see Fig 8.4). Each nickel ion completes its coordination environment with a water molecule in the apical position of a distorted octahedron, while two chelating acetates do so for each nona−coordinated Gd(III) ion (Fig 8.4).

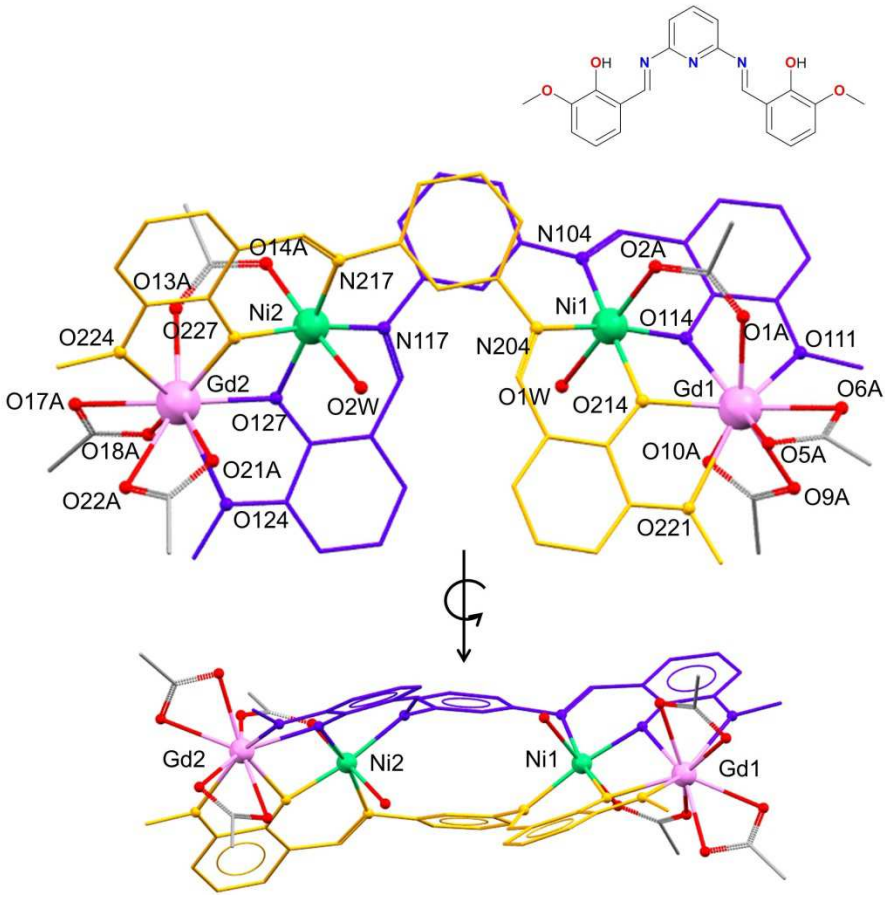

Fig 8.3. Structure of **24**. The chemically inequivalent ligand units are identified in a different colour code. C, grey; Gd, pink; Ni, green; O, red. Hydrogen atoms and lattice solvents are omitted for clarity.

A search based on structures including hexacoordinate−Ni(II) ions displaying a similar environment to that seen in $\{Ln_2Ni_2(L2)_2\}$ (*i.e.* $\{NiN_2O_2O_2'\}$ Schiff base derivatives) was carried out in order to investigate the distortion seen in **24**−**28** (CSD 5.36, February 2017). The reported structures show Ni−N bond distances that range from 1.994 to 2.236 Å, with an average value of $\bar{d}_{(Ni-N)}$ = 2.081 Å.[11-21] Since

the average Ni−N length in **24**−**28** (2.117(5) Å) is moderately bigger than 2.081 Å, the distortion of the octahedral Ni(II) geometry can be described as a *cis*−elongation of the Ni−N bonds of the equatorial plane (see Table A8.3 in the appendix). Note that the deviation from the ideal geometry seen in $\{Ln_2Ni_2(L2)_2\}$ must be taken into consideration during the magnetic analysis of the complexes (*vide infra*), as it is closely related to the anisotropic parameter D_{str}.[22]

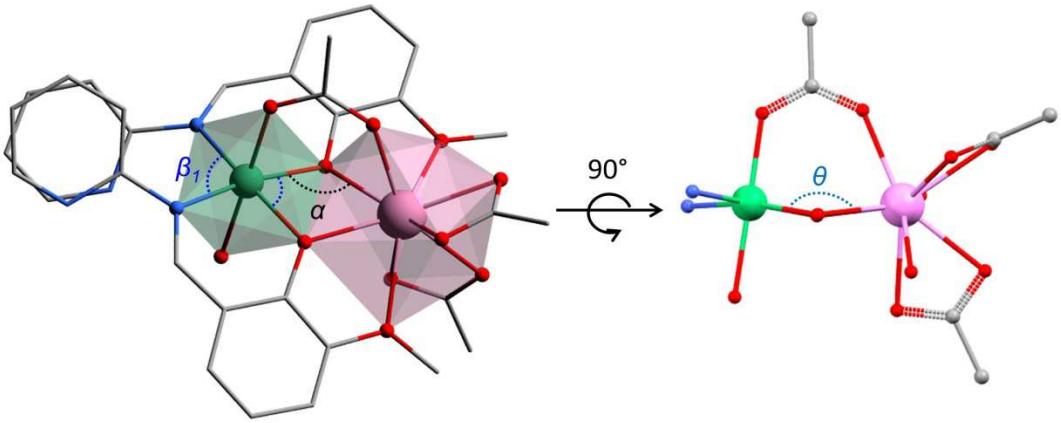

Fig 8.4. Detail of the {LnNi} dimer. Polyhedra around metal ions are shown in green (Ni) and pink (Ln). C, grey; Ln, pink; N, blue; Ni, green; O, red. *α* is displayed in black, β_1 in blue, and *θ* in pale blue.

The closest symmetry for both Ln(III) ions in **24**−**28** proposed by Shape[23-25] is spherical capped square antiprism (C_{4v}; see Tables A8.1, A8.2 of the appendix). The calculated CShMs values for the Ln ions, however, are substantially far from the ideal C_{4v} geometry (CShMs = 1.569–2.252). That may be caused by the different coordinating O−atoms (phenoxo, alkoxo and acetate), and can be observed in the wide range of Ln−O lengths values (from 2.318(2) to 2.540(4) Å, see Table 8.1). It should be noted that the analyses also suggest the muffin−like shape (C_s) as a possible second option, since the resulting CShMs values are fairly close to those related to C_{4v}.

Table 8.1 Average Ln−O bond lengths in $\{LnO_9\}$ for **24**−**28**. *μ*OAc refers to the bridging acetate, OAc to the chelating acetate, OPh and OMe to, respectively, the phenoxo and the methoxo group from the *o*−vanillin.

	24	**25**	**26**	**27**	**28**
$\mathbf{d_{(Ln-\mu OAc)}}$/Å	2.359(4)	2.365(5)	2.362(5)	2.327(4)	2.318(2)
$\mathbf{d_{(Ln-OAc)}}$/Å	2.457(4)	2.436(5)	2.427(5)	2.419(4)	2.418(2)
$\mathbf{d_{(Ln-OPh)}}$/Å	2.358(4)	2.333(5)	2.325(5)	2.327(3)	2.321(2)
$\mathbf{d_{(Ln-OMe)}}$/Å	2.540(4)	2.521(5)	2.571(5)	2.528(4)	2.528(2)

Considering the structure shown in Figure 8.3, one may think that Ni and Ln lie in the same plane. However, the torsion angles clearly indicate that these {NiOO'Ln} dimeric units are not planar ($\theta^{Avg}_{(NiOO'Ln)}$ ~ 163.3(4)°). The average intramolecular Ni···M distances (M = Ni, Ln) are $d_{(Ni\cdots Nl)}$ = 6.634(4) Å, and $d_{(Ni\cdots Ln)}$ = 3.428(6) Å, and the average angle ($\alpha_{(NiOLn)}$) is 103.1(3)° (see Fig 8.4 and Table 8.2).

Table 8.2 Summary of the intramolecular distances, average angles (*α)* and torsions (*θ*) defined for between metal ions in **24**–**28** (see Fig 8.4).

Complex	$d_{(Ni\cdots Ni)}$	$d_{(Ni\cdots Ln)}$	$\alpha_{(NiOLn)}$	$\theta_{(NiOOLn)}$
24 (Gd)	6.627(1) Å	3.451(7) Å	103.2(1)°	163.6(2)°
25 (Tb)	6.637(1) Å	3.421(6) Å	102.7(2)°	162.7(2)°
26 (Dy)	6.640(1) Å	3.416(6) Å	102.7(2)°	162.9(2)°
27 (Ho)	6.636(8) Å	3.428(7) Å	103.4(1)°	163.6(2)°
28 (Y)	6.629(5) Å	3.423(5) Å	103.4(7)°	163.5(8)°

As previously commented, complexes **24**−**28** present an unusual topology, and only the reported $\{Ln_2Ni_2(Sal)_2\}$ systems are structurally comparable. Since the magnetic properties in 3*d*/4*f* systems can be very sensitive to changes in the environment of the Ln ions, different magnetic features between both families are expected. The main structural modifications from $\{Ln_2Ni_2(L2)_2\}$ compared to $\{Ln_2Ni_2(Sal)_2\}$ are listed below.

1. Differences in the Schiff base: the additional N atom of the pyridyl ring in H_2L2 could modify the Ni···Ni, Ni···Ln intramolecularinteractions.
2. Dissimilar coordination environment around the metal ions, partly due to the co−ligands used in the synthesis (AcO^- in **24**−**28** *vs.* NO_3^- in $\{Ln_2Ni_2(Sal)_2\}$).
3. The {LnNi} dimeric units are equivalent within the same structure in **24**−**28**, whereas they are not in $\{Ln_2Ni_2(Sal)_2\}$.
4. Slightly different symmetry proposed for the Ln ions.

Having said that, the characteristic magnetic properties observed along the $\{Ln_2Ni_2(L2)_2\}$ family (**24**−**28**) are discussed in the following section, as well as a comparison with those shown by the published compounds (*i.e*. $\{Ln_2Ni_2(Sal)_2\}$).

Table 8.3. Crystal Data and Structure Refinement Parameters of **24**−**28**.*

Complex	**24**	**25**	**26**	**27**	**28**
T/K	100(2)	100(2)	100(2)	100(2)	100(2)
Crystal system	monoclinic	triclinic	triclinic	monoclinic	monoclinic
Space group	$P2_1/c$	$P\bar{1}$	$P\bar{1}$	$P2_1/c$	$P2_1/c$
a/Å, *b*/Å, *c*/Å	20.535(2), 19.924(2), 16.408(2)	14.675(2), 16.523(2), 17.823(3)	14.684(2), 16.548(2), 17.838(3)	20.5951(12), 19.8612(10), 16.4179(8)	20.5676(3), 19.8900(3), 16.3988(3)
α/°	90	62.965(4)	62.957(4)	90	90
β/°	109.529(4)	81.034(4)	81.000(4)	109.7422(18)	109.7074(17)
γ/°	90	72.374(4)	72.361(4)	90	90
V/Å^3	6326.7(13)	3667.8(9)	3678.2(9)	6320.9(6)	6315.67(18)
Z	4	2	2	4	4
ρ_{calc}/mg/m^3	1.775	1.658	1.659	1.790	1.635
μ/mm^{-1}	2.743	2.496	2.598	3.150	2.494
F(000)	3384.0	1844.0	1848.0	3396.0	3184.0
2θ range for data collection	2.104 to 55.24°	2.566 to 55.146°	2.864 to 54.968°	4.604 to 56.466°	4.396 to 54.968°
Index ranges	$-26 \le h \le 22$, $-19 \le k \le 25$, $-21 \le l \le 21$	$-18 \le h \le 19$, $-18 \le k \le 21$, $0 \le l \le 23$	$-18 \le h \le 19$, $-18 \le k \le 21$, $0 \le l \le 23$	$-27 \le h \le 19$, $-26 \le k \le 24$, $-20 \le l \le 21$	$-26 \le h \le 25$, $-16 \le k \le 25$, $-21 \le l \le 16$
Reflections collected	121042	16829	16837	40054	41793
Data/restraints/parameters	14546/1199/865	16829/1215/940	16837/1579/952	15472/1/860	14396/1198/882
GOF on F^2	1.163	1.042	1.101	1.082	1.025
Final *R* indexes [$I \ge 2\sigma(I)$]	R_1 = 0.0423, wR_2 = 0.0908	R_1 = 0.0439, wR_2 = 0.0953	R_1 = 0.0351, wR_2 = 0.0931	R_1 = 0.0422, wR_2 = 0.1265	R_1 = 0.0329, wR_2 = 0.0701
Final *R* indexes [all data]	R_1 = 0.0802, wR_2 = 0.1123	R_1 = 0.0710, wR_2 = 0.1117	R_1 = 0.0457, wR_2 = 0.1040	R_1 = 0.0544, wR_2 = 0.1335	R_1 = 0.0467, wR_2 = 0.0746
Largest diff. peak/hole/e Å^{-3}	1.77/−1.43	1.44/−1.71	1.89/−1.34	1.27/−2.61	0.70/−0.42

* $[Ln_2Ni_2(L2)_2(CH_3COO)_6(H_2O)_2]$ systems; Ln being Gd for **24**, Tb for **25**, Dy for **26**, Ho for **27** and Y for **28**.

Magnetic properties

The dc magnetic properties of **24**–**28** were investigated in the temperature range of 290–2 K in an applied field of 1000 Oe (Fig 8.5), and at 2, 4, 6 K in the field range of 0–5 T (Fig 8.6, Fig A8.2 Appendix). At room temperature, the $\chi_M T$ products correspond to those expected for two non−interacting Ni(II) (S_{Ni} = 1, g_{Ni} = 2.15) and two Ln(III) ions (see Table 8.4). The g_{Ni} = 2.15 value used for Ni(II) ions is reasonable considering similar reported compounds.[26-28] As the temperature is lowered though, the complexes display different tendencies. Both **24** (Gd) and **25** (Tb) display ferromagnetic coupling, as their $\chi_M T$ products increase with

temperature reaching a maximum of 22.43 $cm^3 \cdot mol^{-1} \cdot K$ at 3.6 K and 28.28 $cm^3 \cdot mol^{-1} \cdot K$ at 3.8 K, respectively. Then, the susceptibilities decrease to 21.93 $cm^3 \cdot mol^{-1} \cdot K$ (**24**) and 27.51 $cm^3 \cdot mol^{-1} \cdot K$ (**25**) at 2 K. The $\chi_M T$ experimental maximum for **24** (Gd), however, is considerably smaller than the calculated one for a molecule with *S* = 18/2, and an average g_{Avg} value of 2.08 (48.44 $cm^3 \cdot mol^{-1} \cdot K$). Note that g_{Avg} is calculated by considering $g_{Avg} = \frac{2 \times g_{Ni} + 2 \times g_{Gd}}{4}$, where g_{Gd} = 2. As the anisotropy for Gd(III) ions is usually discarded, the difference in $\chi_M T$ at low temperature can be related to zero−field splitting from the Ni(II) ions or to intra/intermolecular antiferromagnetic interactions. Conversely, the drop in the $\chi_M T$ values with temperature seen for **26** (Dy) and **27** (Ho) mainly arise from the depopulation of the Stark levels of the Ln(III) ions, reaching a minimum of 25.74 $cm^3 \cdot mol^{-1} \cdot K$ (**26**) and 10.22 $cm^3 \cdot mol^{-1} \cdot K$ (**27**) at 2 K.

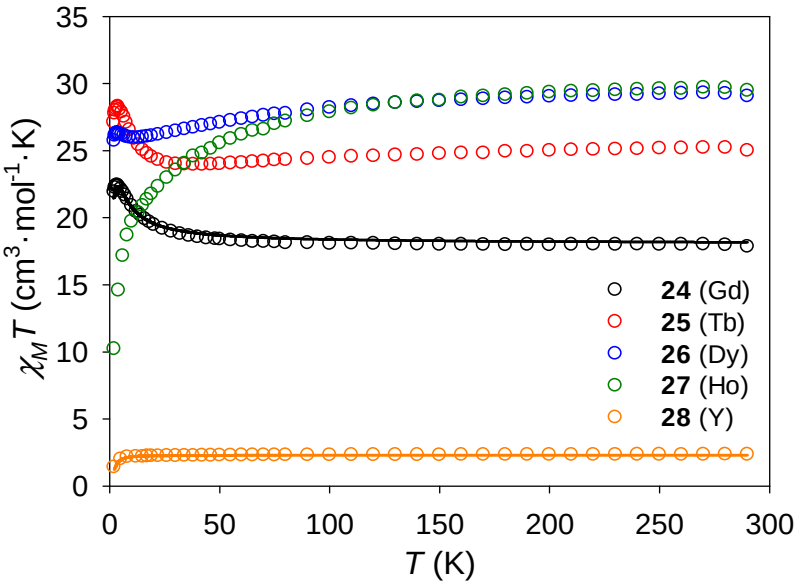

Fig 8.5 Temperature dependence of $\chi_M T$ for **24**–**28** in an applied field of 1000 Oe. Solid lines correspond to the fit for **24** and **28** (see text for details).

Table 8.4 Summary of the calculated ($\chi_M T_{calc}$) and experimental ($\chi_M T_{exp}$) susceptibility values for **20**–**24** (at room temperature).

Complex	Ln ion	*L*	*S*	g_J	GS term symbol	$\chi_M T_{exp}$ {Ln_2Ni_2} ($cm^3 \cdot mol^{-1} \cdot K$)	$\chi_M T_{calc}$ {Ln_2Ni_2} ($cm^3 \cdot mol^{-1} \cdot K$)
24	Gd	0	7/2	2	$^8S_{7/2}$	17.85	18.06
25	Tb	3	3	3/2	$^7F_6$	24.99	25.95
26	Dy	5	5/2	4/3	$^6H_{15/2}$	29.06	30.65
27	Ho	6	2	5/4	$^5I_8$	29.47	30.45
28	Y	–	–	–	–	2.35	2.31

Note that the modest increase of the susceptibility for **26** around 11 K may indicate weak ferromagnetic interactions between Ni and Dy centres. The different magnetic properties observed for **24**–**27** suggest that the interaction between metal ions is dependent on the Ln ion. For **28**, the susceptibility steadily decreases until 2.21 $cm^3 \cdot mol^{-1} \cdot K$ at 11 K, then sharply drops to 1.42 $cm^3 \cdot mol^{-1} \cdot K$ at 2 K. As Y(III) ions are diamagnetic, the observed trend may be a consequence of a ZFS contribution along with weak antiferromagnetic Ni···Ni interactions. An intramolecular Ni···Ni interaction is more likely to occur, as the Ni(II) ions are relatively close to each other compared to those between different molecules. The charge density provided by the N–atoms from the ligand can also promote the spin delocalisation, and therefore the magnetic coupling.[29-31] In addition, the results previously reported by Colacio and co–workers on the {$Ln_2Ni_2(Sal)_2$} family were taken into consideration.[9] The isothermal field dependence magnetisation experiments for **24**–**28** (Fig 8.6, Fig A8.2 in the Appendix) show that the values at 5 T are notably lower than the expected saturation, especially for **25** (Tb), **26** (Dy) and **27** (Ho), suggesting the presence of significant magnetic anisotropy.

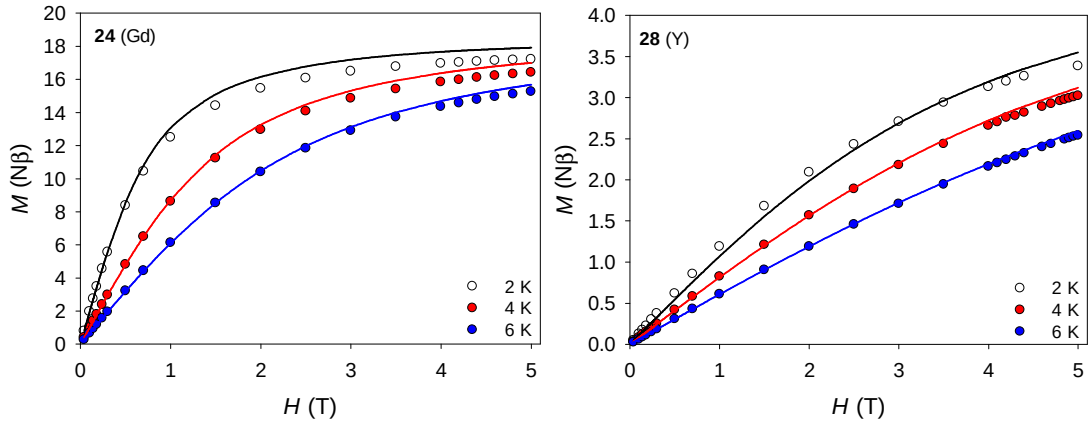

Fig 8.6 Magnetisation *vs*. field at 2, 4, and 6 K for **24** (Gd) and **28** (Y). Solid lines correspond to the fit (see text for details).

The dc magnetic data (susceptibility and magnetisation) for **28** (Y) and **24** (Gd) were simultaneously fit in order to analyse the axial zero–field splitting for Ni(II) ions (D_{Ni}), and the intramolecular Ni···Ni, Ni···Ln interactions. The Hamiltonian proposed for the analysis of **28** (see Eq 8.1) takes into account the coupling between the Ni(II) ions ($\mathcal{J}_1$), and the single–ion ZFS in Ni(II) ions D_{Ni} (see model in Fig 8.7, discarding the Ni···Gd interaction labeled as $\mathcal{J}_2$). The use of the rhombic contribution to the ZFS (E_{Ni}) is excluded to avoid overparameterisation.

Eq 8.1 $$\hat{\mathcal{H}} = -2\mathcal{J}_1(\hat{S}_1 \cdot \hat{S}_2) + g_{Ni}\mu_B\vec{B}\sum_{i=1}^{2}\vec{s}_i + D_{Ni}\sum_{i=1}^{2}\left(\hat{S}_{iz}^2 - \frac{1}{3}S_i(S_i+1)\right)$$

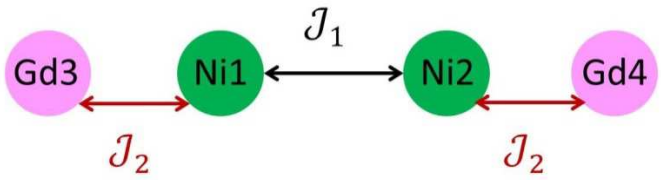

Fig 8.7 Magnetic model used for the fit of **24**. The model is also applied to **28**, considering Y is diamagnetic, therefore discarding $\mathcal{J}_2$.

Since the above-mentioned parameters to be fitted could display different values depending on many factors (*e.g*. type of geometry/distortion),[22] a survey of g_{Ni}, D_{Ni} and $\mathcal{J}_1$ is performed prior to the fit to establish some initial values. The survey suggests a weak, but not negligible antiferromagnetic interaction between Ni(II) ions, a g_{Ni} value of ~ 2.16, and multiple options for D_{Ni} (from ~ −4 to ~ +4 cm^{-1}). Theoretical studies have demonstrated the correlation between the magnitude and sign of D_{Ni} and the distortions in octahedral mononuclear Ni(II) complexes.[22, 32, 33] The first magneto−structural correlation is related to the Ni−N *cis*−bond elongation and $D_{Ni.}$ Then, compounds displaying a *cis*−bond elongation (thus positive D_{str}) led to positive D_{Ni} parameters.[22] Note that D_{str} is a tetragonality distortion parameter related to the difference between the axial (*z*) and equatorial (*x*, *y*) bond lengths of octahedral complexes.[22, 34] Furthermore, D_{Ni} increases in magnitude with D_{str}. Since **24**−**28** can be classified as $\{NiN_2O_2O_2'\}$ (Group IV), the formula shown in Eq 8.2 is used for the calculation of D_{str}.[34]

Eq 8.2 $$D_{str} = \Delta_z - \frac{(\Delta_x - \Delta_y)}{2}; \quad \Delta_i = d_i - \bar{d}_i$$

Where d_i are the experimental Ni−L bond distances, and $\bar{d}_i$ the average bond lengths relative to complexes with an homogeneous ligand sphere (*i.e*. $[Ni(NH_3)_6]^{2+}$, $[Ni(H_2O)_6]^{2+}$).[22]

In the case of **28** (Y) both Ni(II) ions display similar positive D_{str} values ($\overline{D}_{str}$ = 0.48) in good agreement with a Ni−N *cis*−bond elongation, therefore a positive D_{Ni} is expected. The second correlation shows that D_{Ni} increases in magnitude with $\Delta\beta$. The $\Delta\beta$ parameter gives information about the deviation of the *cis* angles within the coordination environment of a particular complex compared to those for an ideal $\{NiL_6\}$ sphere (see Fig 8.8).[22] Note that $\Delta\beta$ influence the strength, but not the sign of the D value (*i.e*. the larger $\Delta\beta$, the larger $|D_{Ni}|$). For **28**, the β_1 angles are defined by

the two equatorial N atoms and the two O−phenoxo atoms (see Fig 8.4). The analysis reveals that both Ni(II) ions display a substantial angular distortion ($\overline{\Delta\beta}$ = 3.28), which contributes to increase the ZFS parameter D_{Ni}.

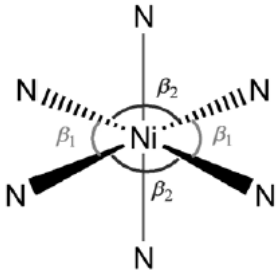

$$\Delta\beta = \frac{(\beta_1 + \beta_1)}{2} - \frac{(\beta_2 + \beta_2)}{2}$$

Fig 8.8 Schematic illustration of the $\Delta\beta$ parameters present for a O_h−Ni(II) mononuclear complex (left), and formula for the calculation of $\Delta\beta$. Picture adapted from the literature.[22]

Given consideration to D_{str}, a positive D_{Ni} is proposed as a starting fitting value. The best fit gives g_{Ni} = 2.15, D_{Ni} = 4.34 cm^{-1} and $\mathcal{J}_1$ = −0.15 cm^{-1} (*R* = 99.8%; see solid lines in Fig 8.5, 8.6 right). The value found for D_{Ni} is in accord with the previously discussed magneto−structural correlations.[22] Since the Ni centres are not directly linked, and are 6.634(4) Å apart, a weak interaction is expected. Therefore, the resulting g_{Ni}, D_{Ni} and $\mathcal{J}_1$ for **28** are reasonable. It must be stressed that alternative fits discarding the magnetic exchange between Ni(II) ions did not reproduce the low temperature $\chi_M T\ vs. T$ data as well as the fit including $\mathcal{J}_1$. In addition, the previous magnetic study of a dinuclear [$Cu_2(L2)_2$] complex with H_2L2 (note these results are not included in this report), showing an intramolecular Cu···Cu' distance equal to 7.275(1) Å, revealed antiferromagnetic coupling between Cu(II) ions (~−10 cm^{-1}). Thus, the coupling constant $\mathcal{J}_1$ was included as a variable parameter in the fit of the magnetic data for both **28** (6.629(5) Å) and **24** (6.627(1) Å).

The fit of **24** (Gd) is carried out by applying the magnetic model displayed in Figure 8.7, and the Hamiltonian from Eq 8.3. In this case, g_{Gd} = 2, g_{Ni} = 2.15 and D_{Ni} = 4.34 cm^{-1} values are fixed during the fit, since the Ni(II) environment for **24** (Gd) and **28** (Y) show a fairly similar distortion ($\overline{D}_{str}$ (**24**) = 0.54, $\overline{\Delta\beta}$ (**24**) = 4.06). Note that $\mathcal{J}_2$ is included as a term related to the Gd···Ni interaction. This new interaction could have an influence on the magnitude of the Ni···Ni ($\mathcal{J}_1$) interaction, therefore, two approaches were investigated to fit the experimental data for **24**. The first one (A) assumes the Ni···Ni coupling is equivalent for both **28** and **24**, and then $\mathcal{J}_1$ = −0.15 cm^{-1} is fixed during the analysis, whereas the second one (B) considers that $\mathcal{J}_1$ could differ from **28** to **24** and it is included as a variable term. Both fits give

very similar results, giving $\mathcal{J}_2$ = 0.50 cm^{-1} for A (R = 98.6%), and $\mathcal{J}_1$ = −0.12 cm^{-1}, $\mathcal{J}_2$ = 0.48 cm^{-1} for B (R = 99.1%). That suggests that the Gd···Ni interaction does not have a strong impact on the Ni···Ni coupling, thus the results from the simplest approach named A were chosen as final values (see solid lines in Fig 8.5, 8.6 left).

Eq 8.3
$$\hat{\mathcal{H}} = -2\mathcal{J}_1(\hat{S}_1 \cdot \hat{S}_2) - 2\mathcal{J}_2(\hat{S}_1 \cdot \hat{S}_3 + \hat{S}_2 \cdot \hat{S}_4) + g_{Ni}\mu_B\vec{B}\sum_{i=1}^{2}\vec{s}_i + g_{Gd}\mu_B\vec{B}\sum_{j=3}^{4}\vec{s}_j + D_{Ni}\sum_{i=1}^{2}\left(\hat{S}_{zi}^2 - \frac{1}{3}S_i(S_i+1)\right)$$

Theoretical studies have established some correlations between the magnetic exchange between Gd···Ni in Ni/Gd dinuclear complexes and the bond angle (*i.e.* $\alpha_{(NiOGd)}$) and/or the hinge angle (*i.e.* Ni−O···O−Gd, defined as 180°− $\theta_{(NiOO'Gd)}$).[35, 36] Therefore, larger torsion angles ($\theta_{(NiOO'Gd)} \longrightarrow 120°$), and small hinge angles, favour ferromagnetic interaction. The value calculated for $\mathcal{J}_2$ (0.50 cm^{-1}) is then reasonable, considering that **24** displays a relatively large average Ni−O−Gd angle ($\alpha_{(NiOGd)}$ = 103.2(1) Å) and a small hinge angle (16.4°). The different calculated values for the coupling between Ni(II) ions ($\mathcal{J}_1$) in **24** (−0.15 cm^{-1}) and the reported $\{Gd_2Ni_2(Sal)_2\}$ complex (0.38−0.42 cm^{-1}; see Table 8.5) suggest a switch from antiferromagnetic to ferromagnetic interaction, which may be related to structural differences (*vide supra*). That result must, however, be interpreted with caution, as the magnetic exchange parameters $\mathcal{J}_1$ for **24** and $\{Gd_2Ni_2(Sal)_2\}$ extracted from the fit are very small and close in absolute value. Therefore, the suggested change in the sign of $\mathcal{J}_1$ may be simply due to errors associated with the program used for the calculations (*i.e.* PHI).

The dynamic properties of **24**–**27** were investigated, by ac experiments as a function of the frequency over the temperature range 2−10 K, in the absence of a dc field and at 2000 Oe. The dynamics for **24** (Gd) and **28** (Y) were studied to see if any slow relaxation comes from the ZFS of the Ni(II), taking into account that Gd(III) is isotropic and Y(III) is diamagnetic (see Fig 8.9). As expected, no signal was observed in the out−of−phase susceptibility, and neither was there frequency dependence in the in−phase component for **24** or **28** in the absence of field nor under the influence of an external dc field.

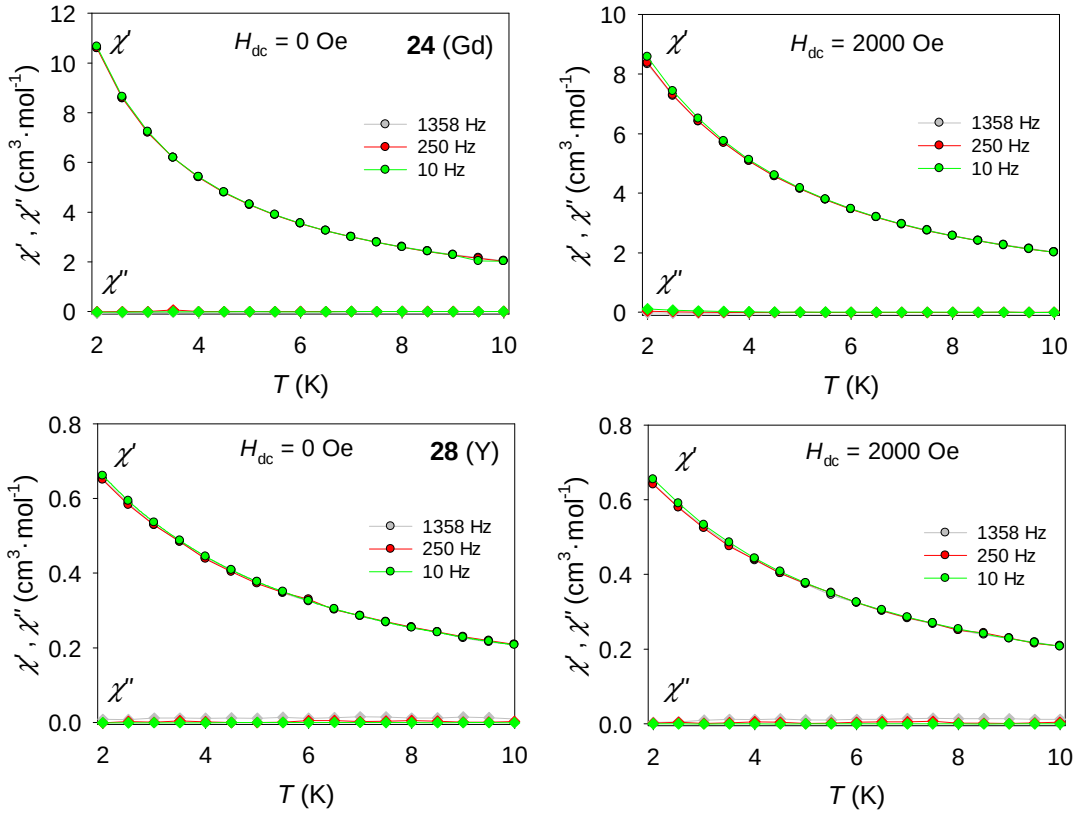

Fig 8.9 Ac susceptibility of **24** (Gd; top) and **28** (Y; bottom) as a function of the temperature (T = 2.0−10 K) at zero field (left), and in an external field of H_{dc} = 2000 Oe (right) at selected frequencies (υ = 10, 250, 1358 Hz).

As discussed in previous chapters, the high−magnetic anisotropy Ln(III) ions, such as Tb^{3+} (in **25**), Dy^{3+} (**26**), and Ho^{3+} (**27**) are more prone to display the out−of−phase, frequency dependent ac signals characteristic of single−molecule magnets. It must be stressed, though, that the ac studies reveal that none of the complexes (**25**−**27**) display slow reversal of the magnetisation in the absence of an external field (see Fig 8.10 and 8.11, left), suggesting the presence of a strong quantum−tunnelling mechanism within the molecule. However, under the influence of an external field the complexes behave slightly differently: **26** displays the onset of a very weak χ" signal (see inset in Fig 8.10 top, right), while **27** does not show any change compared to the zero−field experiment (Fig 8.10 bottom, right). Note also that the in−phase susceptibly signals for both **26** and **27** complexes are relatively frequency−dependent, as the data for the different frequency values do not overlap at low temperatures (~ below 4 K). That could be related to a possible anisotropy of the lanthanide ions along with the nickel contribution. Additional isothermal field sweep ac susceptibility experiments were not performed for **26** though, as we do not expect to see any significant improvement considering the fairly weak χ" signal.

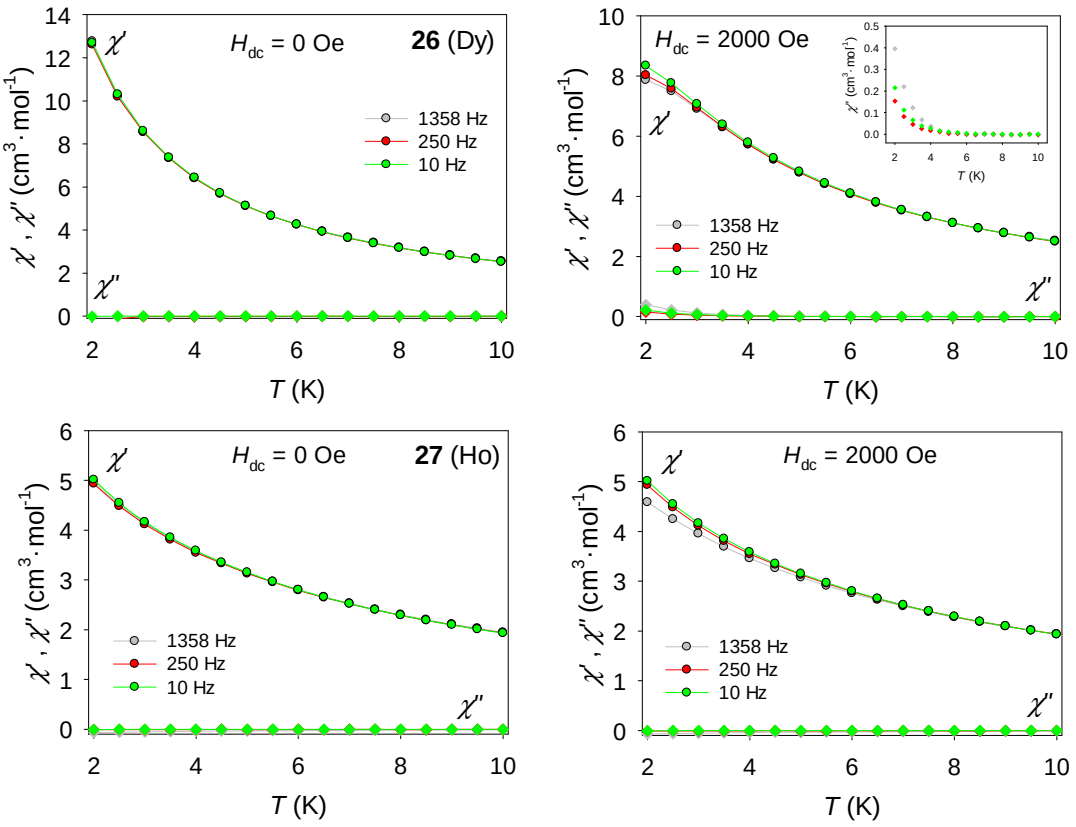

Fig 8.10 Ac susceptibility of **26** (Dy; top) and **27** (Ho; bottom) as a function of the temperature (T = 2.0−10 K) at zero field (left), and in an external field of H_{dc} = 2000 Oe (right) at selected frequencies (υ = 10, 250, 1358 Hz). The inset shows a zoom of the χ'' *vs.* T for **26**.

In the case of **25** (Tb), the complex exhibits a field−induced slow magnetic relaxation behaviour, since the application of a relatively small dc field causes a considerable improvement on the dynamic properties (Fig 8.11, right). To investigate the optimum conditions to inhibit the tunnelling, the effect of various field strengths on the dynamics of **25** was investigated (Fig 8.12). The ac susceptibility plots show out−of−phase maxima for applied fields greater than 1000 Oe. However, the Cole−Cole plots suggest multiple field−dependent processes competing for the reversal of the magnetisation. That may be a consequence of the two structurally inequivalent Tb(III) ions (Tb1, Tb2) in **25**. Also it can be seen how the secondary process becomes more important at high fields, as the semi−circle displays a more asymmetrical shape (Fig 8.12 right, top). Generalised one− or two−component Debye models were used for fitting the experimental data, however, none of them gave reasonable results. Although the field dependence of the relaxation rate τ −extracted from the experimental χ"(ω) maxima− showed no clear local maximum, the field promoting the larger τ is expected to be in−between 1500 and 2000 Oe (Fig 8.12 right, bottom).

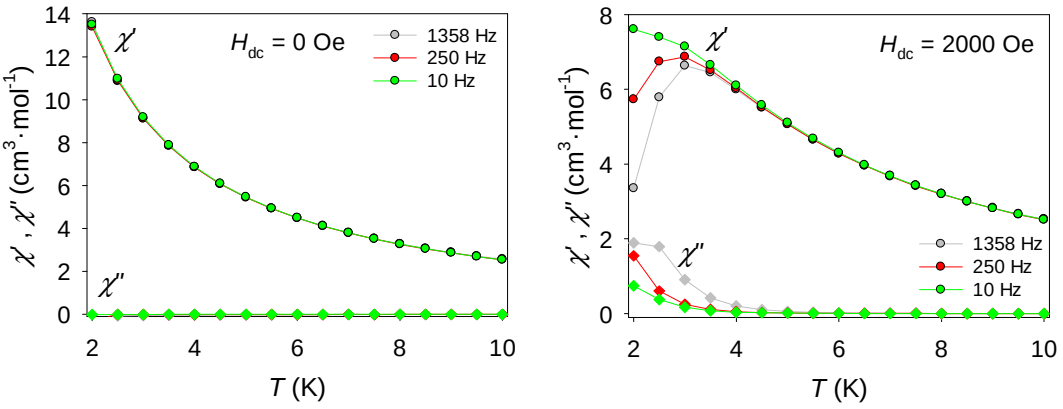

Fig 8.11 Ac susceptibility of **25** (Tb) as a function of the temperature (T = 2.0−10 K) at zero field (left), and in an external field of H_{dc} = 2000 Oe (right) at selected frequencies (υ = 10, 250, 1358 Hz).

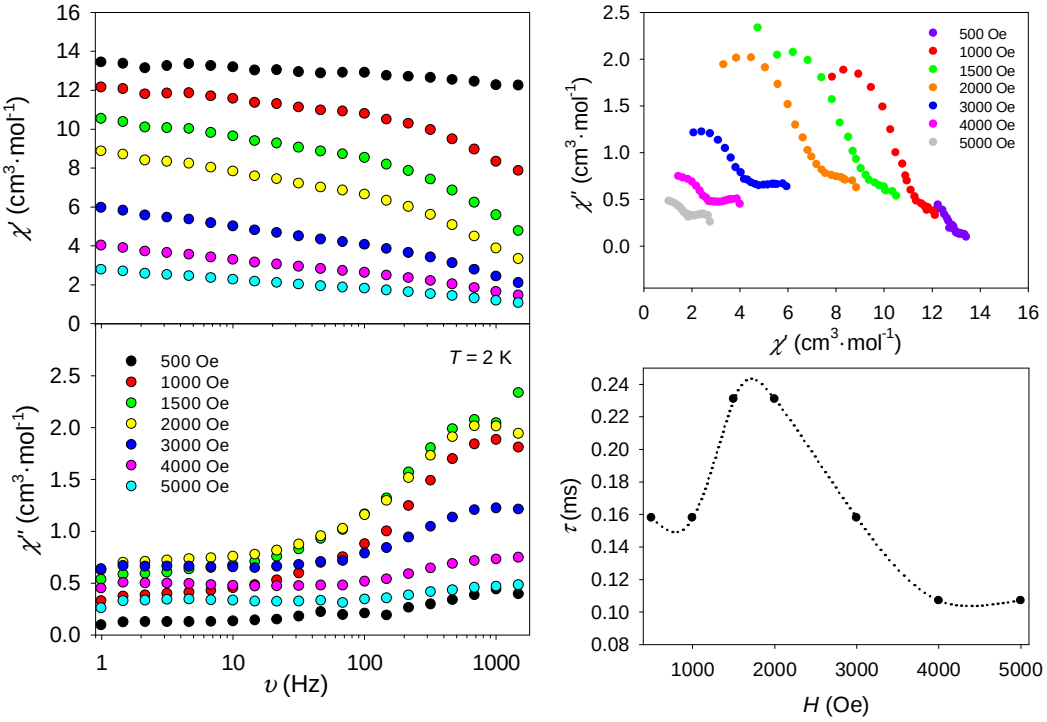

Fig 8.12 Ac magnetic susceptibility of **25** (Tb), at T = 2 K in applied fields over 0–5000 Oe (left); Argand plots from the susceptibility data (right, top), and field dependence of the magnetic relaxation time (right, bottom). The dotted line in τ *vs*. H is a guide for the eye.

In light of this, the ac susceptibility was measured over the temperature range 1.8−5 K, as a function of the frequency in applied dc field of 1700 Oe (Fig 8.13). The ac studies at 1700 Oe show slow magnetic relaxation, associated with the presence of frequency−dependent out−of−phase maxima (Fig 8.13). Cole–Cole plots display considerable asymmetrical semi−circular shapes, in good agreement with the multiple relaxation processes previously suggested by the field sweep experiments (Fig 8.13 right, top). The Argand plots (1.8−3 K) were then modelled

considering a relaxation process with two time constants, τ_1 and τ_2. Note that the single relaxation time equation gave a poor quality data fit (α = 0.47−0.76), and thus was discarded as a possible model. The results display clearly two branches (see Fig 8.13 right, bottom). The calculated data for τ_2 does not look quite reliable, since it does certainly deviate from the Arrhenius behaviour. In addition, none of the Argand plots display a semicircle −not even a half−semicircle− for the secondary process involving τ_2 (note that the τ_i parameters are related to the maximum; see section 1.3). Hence, only the part of the semicircle related to τ_1 (α = 0.01−0.33) was analysed by the Arrhenius law, $\tau = \tau_0 \exp(\Delta E/k_B T)$. Then, the different relaxation times for τ_1 were used to extract the pre−exponential factor τ_0 and the energy barrier $\Delta E/k_B$, yielding τ_0 = 6.5·10^{-8} s and $\Delta E/k_B$ = 15.8 ± 0.4 K. The estimated parameters are in the same order of magnitude as other reported {LnNi} SMMs.[37]

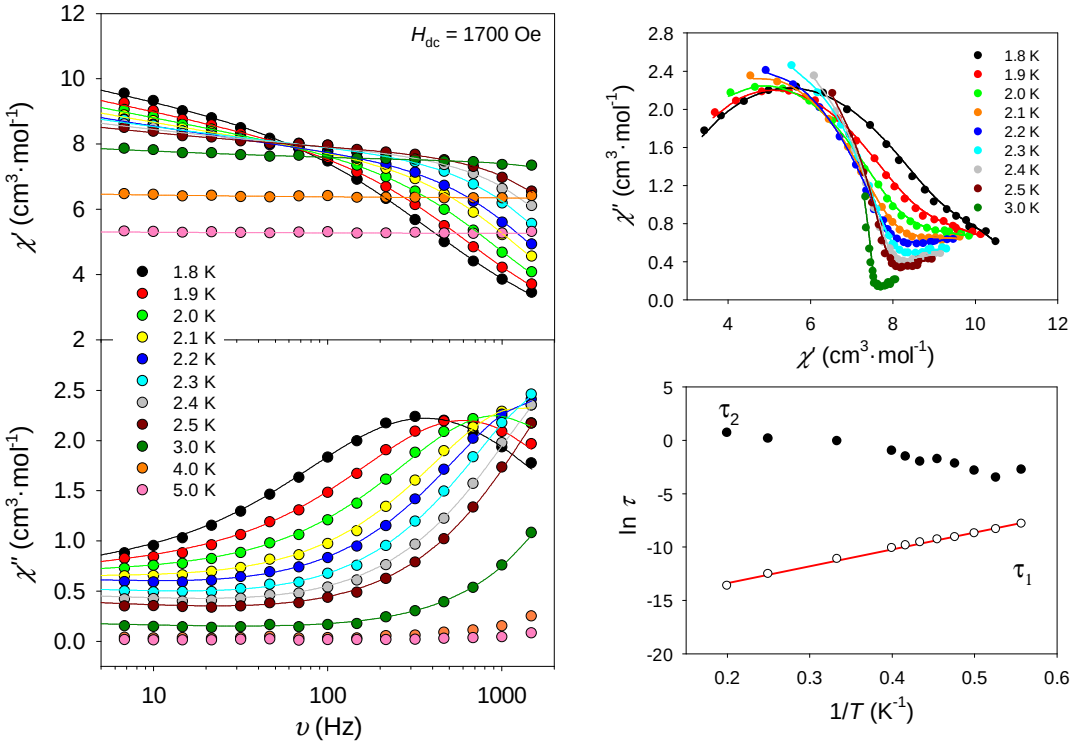

Fig 8.13 Dynamic magnetic properties for **25** (Tb). Left: ac magnetic susceptibility data at different frequencies at H_{dc} = 1700 Oe. Right: Cole–Cole plots (top) and Arrhenius plot (bottom) from the ac susceptibility data. The solid lines correspond to the fit (see text for details).

It must be stressed that, surprisingly, slow magnetic relaxation was observed for the Tb analogue (**25**), but not for the Dy one (**26**), especially if we consider the dynamic properties displayed by {$Dy_2Ni_2(Sal)_2$}.[9] Dy is the most common lanthanide used in the design of SMMs, as it is a Kramer's ion and thus displays a doubly

degenerate ground state independent of the crystal field created by the surrounding ligands. In contrast, Tb is a non−Kramer's ion, so that bistability in the ground state is subject to certain ligand fields (*i.e*. axial symmetry).[38] Therefore, one possible explanation for that might be related to the ligands present in the coordination sphere of the Ln ion in the $\{Ln_2Ni_2(L2)_2\}$ family (*i.e*. $L2^{2-}$, CH_3COO^-, H_2O), since they may alter the crystal field so as to promote SMM properties for Tb while inhibiting them for Dy.[39] It is worth noting that the dc magnetic studies (see above Fig 8.5) display different features for complexes **25** (Tb) and **26** (Dy) at low temperatures (~ below 25 K). That suggests a change in the magnetic interactions (*i.e*. Ni···Ni and/or Ln···Ni) related to the replacement of the Ln(III) ion. Some empirical studies performed on acetato− and diphenolato−bridged dinuclear Ni−4*f* complexes similar to those here introduced shed light on the displayed SMM behaviour depending on the strength of the Ni···4*f* interaction.[38] The ac susceptibility measurements on Ni^{II}−Tb^{III} and Ni^{II}−Dy^{III} show that both complexes display slow magnetic relaxation. However, Ni^{II}−Tb^{III} is clearly the most promising candidate, since the Dy(III) analogue shows a small dependence only at very low temperature. The studies correlate the above mentioned different ac properties with the fact that $J_{NiTb}>J_{NiDy}$ (J_i extracted from the fit of the dc data). Given consideration to these studies, the small differences in the M···Ni intramolecular distances (*i.e*. $d_{(Ni\cdots Ni)}$, $d_{(Ni\cdots Ln)}$) between **25** (Tb) and **26** (Dy) could maybe lead to a change in the magnetic interactions (*i.e*. J_{NiNi}, $J_{NiLn)}$) and therefore to the SMM features. Another possible explanation for the different dynamics seen for **25** and **26** is related to a change in the orientation of the anisotropic axes of the Ln(III) ions, and thus with the alignment with the Ni(II)-axes, since recent studies show the anisotropy orientation is related to the number of the 4*f* electrons.[40] However, this hypothesis needs to be supported by additional studies (*e.g*. theoretical calculations about the nature of the exchange interactions and the magnetic anisotropy).

In conclusion, the geometrical and structural differences between **24**−**28** and the published $\{Ln_2Ni_2(Sal)_2\}$ do modify the magnetic behaviour of the final complexes. Table 8.5 (*vide supra*) shows some factors related to the static and dynamic properties of **24**−**28** and $\{Ln_2Ni_2(Sal)_2\}$ (Ln = Gd, Dy, Y). As Gd, Dy, and Y analogues are common to both families, a comparative analysis is performed between these structures. As previously discussed, the symmetry of the Ln ions, the nature of the Ni···Ni exchange interaction (AF for **24**, **28**, F for $\{Ln_2Ni_2(Sal)_2\}$), and the magnitude of Gd···Ni are different between the two families. This may involve changes related to crystal−field environment (*e.g*. a different splitting of

energy levels), the exchange interactions and/or the magnetic anisotropy axis alignment, thus modifying the static and dynamic properties of the different complexes. Furthermore, the study of the relaxation dynamics for $\{Ln_2Ni_2(L2)_2\}$ suggest that a contribution of 4*f* ions to the anisotropy in addition to that from the Ni(II) ions is required in order to display slow magnetisation reversal.

Table 8.5 Symmetry of the lanthanide ions, Ni···Ni, Gd···Ni interaction, axial parameter D_{Ni} and dynamic properties for **24**, **26**, **28** and $\{Ln_2Ni_2(Sal)_2\}$ (Ln = Gd, Dy, Y).

Complex	Symmetry Ln	Ni···Ni ($\boldsymbol{J_1}$)	Gd···Ni ($\boldsymbol{J_2}$)	$\boldsymbol{D_{Ni}}$	Slow magnetic relaxation
24 (Gd)	C_{4v}	−0.15 cm^{-1}	0.50 cm^{-1}	4.34 cm^{-1}	No
$\{Gd_2Ni_2(Sal)_2\}$[9]	C_s	0.42 cm^{-1}	1.80 cm^{-1}	4.63 cm^{-1}	No
26 (Dy)	C_{4v}	–	–	–	~No
$\{Dy_2Ni_2(Sal)_2\}$[9]	C_s	–	–	–	Yes
28 (Y)	C_{4v}	−0.15 cm^{-1}	–	4.34 cm^{-1}	No
$\{Y_2Ni_2(Sal)_2\}$[9]	C_s	0.38 cm^{-1}	–	4.63 cm^{-1}	No

8.3. Concluding remarks

The exploration of the chemistry of the Schiff base derivative *N,N′*−bis(2−Hydroxy−3−methoxyphenylmethylidene)−2,6−pyridinediamine (H_2L2) with Ni/Ln salts proved its potential as a ligand in the directed synthesis of heterometallic 3*d*/4*f* complexes. Ni(II) ions tend to be encapsulated in the $\{N_2O_2\}$ pocket, whereas *4f* ions occupy the less−hindered position, which is defined solely by oxygen atoms. The synthesis, structure, and the magnetic properties of $[Ln_2Ni_2(L2)_2(CH_3COO)_6(H_2O)_2]$ (Ln = Gd, Tb, Dy, Ho, Y) have been discussed and compared to the reported family named $\{Ln_2Ni_2(Sal)_2\}$. The investigation of the static properties suggests that maybe the Ni centres are weakly antiferromagnetically coupled, despite being relatively far apart. Even though the analysis of the dc data proposes an anisotropic contribution arising from the single−ion ZFS in Ni(II), the results from the ac studies suggest that anisotropy is not enough to promote slow relaxation within the molecule. The dynamic properties change drastically depending on the Ln used, with **25** (Tb) being the only compound that presents field−induced slow relaxation. The absence of out−of−phase ac susceptibility signals in the zero dc field experiments for complexes **25**−**27** suggests the presence of significant quantum tunnelling. As mentioned before, the inhibition of the spin−reversal seen in the ac experiments under the influence of an external dc field in compounds containing high−magnetic anisotropy Dy (**26**) or Ho (**27**) ions may be a consequence of several factors. These could involve changes in the crystal field, in the magnetic exchange interactions and/or the magnetic anisotropy. Theoretical calculations on the complexes of the $\{Ln_2Ni_2(L2)_2\}$ family will be performed in order to elucidate the differences observed in the dynamic properties for **25**–**27**. To conclude, the comparison between $\{Ln_2Ni_2(L2)_2\}$ and $\{Ln_2Ni_2(Sal)_2\}$ (Ln = Gd, Dy, Y) discussed throughout the chapter shows the effect of ligand modification on the observed magnetic features of the final complexes.

References

1. M. Andruh, *Dalton Trans.*, **2015**, *44,* 16633.
2. K. Liu, W. Shi and P. Cheng, *Coord. Chem. Rev.*, **2015**, *289–290*, 74.
3. J.−P. Costes, F. Dahan, A. Dupuis and J.−P. Laurent, *Inorg. Chem.*, **1996**, *35*, 2400.
4. J.−P. Costes, F. Dahan, A. Dupuis and J.−P. Laurent, *Inorg. Chem.*, **1997**, *36*, 3429.
5. J.−P. Costes, F. Dahan and A. Dupuis, *Inorg. Chem.*, **2000**, *39*, 5994.
6. N. Galić, D. Matković-Čalogović and Z. Cimerman, *Struct. Chem.*, **2000**, *11*, 361.
7. H.-J. Bai, F.-G. Xing, Z.-L. Wang, *J. Shaanxi Normal Univ. (Nat. Sci. Ed.)*, **2008**, *6*, 47.
8. L. Lei, G.-X. Xiong; Y.-Z. Wang, *Fine Chemicals*, **2012**, *2*, 155.
9. C. Meseguer, S. Titos-Padilla, M. M. Hänninen, R. Navarrete, A. J. Mota, M. Evangelisti, J. Ruiz and E. Colacio, *Inorg. Chem.*, **2014**, *53*, 12092.
10. İ. Kaya, F. Doğan and A. Bilici, *Polym. Int.*, **2009**, *58*, 570.
11. A. Chakraborty, P. Bag, E. Riviere, T. Mallah and V. Chandrasekhar, *Dalton Trans.*, **2014**, *43*, 8921.
12. A. R. Paital, M. Mikuriya and D. Ray, *Eur. J. Inorg. Chem.*, **2007**, *2007*, 5360.
13. M. Fondo, N. Ocampo, A. M. Garcia-Deibe, J. Cano and J. Sanmartin, *Dalton Trans.*, **2010**, *39*, 10888.
14. H. Adams, S. Clunas, D. E. Fenton, T. J. Gregson, P. E. McHugh and S. E. Spey, *Inorg. Chim. Acta*, **2003**, *346*, 239.
15. P. Mukherjee, M. G. B. Drew, V. Tangoulis, M. Estrader, C. Diaz and A. Ghosh, *Polyhedron*, **2009**, *28*, 2989.
16. S. Akine and T. Nabeshima, *Inorg. Chem.*, **2005**, *44*, 1205.
17. H. Adams, D. E. Fenton, L. R. Cummings, P. E. McHugh, M. Ohba, H. Okawa, H. Sakiyama and T. Shiga, *Inorg. Chim. Acta*, **2004**, *357*, 3648.
18. J.-W. Ran, S.-Y. Zhang, B. Hu, B. Xu and Y. Li, *Inorg. Chem. Commun.*, **2008**, *11*, 1474.
19. X. Yang, C. Chan, D. Lam, D. Schipper, J. M. Stanley, X. Chen, R. A. Jones, B. J. Holliday, W.-K. Wong, S. Chen and Q. Chen, *Dalton Trans.*, **2012**, *41*, 11449.
20. M. Fondo, A. M. Garcia-Deibe, N. Ocampo, J. Sanmartin, M. R. Bermejo and A. L. Llamas-Saiz, *Dalton Trans.*, **2006**, *35*, 4260.
21. M. Fondo, A. M. Garcia-Deibe, N. Ocampo, J. Sanmartin and M. R. Bermejo, *Dalton Trans.*, **2007**, *45*, 414.
22. S. K. Singh, T. Gupta, P. Badkur and G. Rajaraman, *Chem. Eur. J.*, **2014**, *20*, 10305.
23. M. Pinsky and D. Avnir, *Inorg. Chem.*, **1998**, 37, 5575.
24. A. Ruiz-Martinez, D. Casanova and S. Alvarez, *Dalton Trans.*, **2008**, *19*, 2583.
25. A. Ruiz-Martínez, D. Casanova and S. Alvarez, *Chem. Eur. J.*, **2008**, *14*, 1291.
26. E. Pardo, I. Morales-Osorio, M. Julve, F. Lloret, J. Cano, R. Ruiz-García, J. Pasán, C. Ruiz-Pérez, X. Ottenwaelder and Y. Journaux, *Inorg. Chem.*, **2004**, *43*, 7594.
27. A. Escuer, J. Esteban, J. Mayans and M. Font-Bardia, *Eur. J. Inorg. Chem.*, **2014**, *31*, 5443.
28. H. Arora, J. Cano, F. Lloret and R. Mukherjee, *Dalton Trans.*, **2016**, *45*, 14174.
29. I. Fernández, R. Ruiz, J. Faus, M. Julve, F. Lloret, J. Cano, X. Ottenwaelder, Y. Journaux and M. C. Muñoz, *Angew. Chem. Int. Ed.*, **2001**, *40*, 3039.
30. A. R. Paital, A. Q. Wu, Guo, G. Aromí, J. Ribas-Ariño and D. Ray, *Inorg. Chem.*, **2007**, *46*, 2947.
31. Y. Pang, S. Cui, B. Li, J. Zhang, Y. Wang and H. Zhang, *Inorg. Chem.*, **2008**, *47*, 10317.
32. J. Titiš and R. Boča, *Inorg. Chem.*, **2010**, *49*, 3971.
33. A. Packová, J. Miklovič, J. Titiš, M. Koman and R. Boča, *Inorg. Chem. Commun.*, **2013**, *32*, 9.
34. J. Miklovič, P. Baran and R. Boča, *Nova Biotechnol. Chim.,* **2016**, *15*, 182.

35. E. Cremades, S. Gómez-Coca, D. Aravena, S. Alvarez and E. Ruiz, *J. Am. Chem. Soc.*, **2012**, *134*, 10532.
36. S. K. Singh, N. K. Tibrewal and G. Rajaraman, *Dalton Trans.*, **2011**, *40*, 10897.
37. L. Rosado Piquer and E. C. Sañudo, *Dalton Trans.*, **2015**, *44*, 8771.
38. M. Towatari, K. Nishi, T. Fujinami, N. Matsumoto, Y. Sunatsuki, M. Kojima, N. Mochida, T. Ishida, N. Re and J. Mrozinski, *Inorg. Chem.*, **2013**, *52*, 6160.
39. J. D. Rinehart and J. R. Long, *Chem. Sci.*, **2011**, *2*, 2078.
40. M.-E. Boulon, G. Cucinotta, J. Luzon, C. Degl'Innocenti, M. Perfetti, K. Bernot, G. Calvez, A. Caneschi and R. Sessoli, *Angew. Chem. Int. Ed.*, **2013**, *52*, 350.

Chapter 9

9. Conclusions

The results discussed throughout this thesis prove the capability of 2,2'−(propane−1,3−diyldiimino)bis[2−(hydroxymethyl)−propane−1,3−diol] (Bis−tris propane, H_6L) or *N,N′*−bis(2−Hydroxy−3−methoxyphenylmethylidene)-2,6−pyridinediamine (H_2L2) for directing the synthesis of heterometallic complexes with potential applications in molecular magnetism (*i.e*. SMMs, magnetic molecular refrigerants). The development of a synthetic approach halfway between serendipitous and rational design has been used in favour of controlling the assembly of new 3*d* and/or 4*f* polynuclear systems that are of structural and magnetic interest.

The flexible polydentate ligand H_6L shows a rich coordination chemistry, having generated twenty-three new coordination complexes by means of “one-pot” reactions, which have been sub-classified into five groups.

The use of 3*d*-based metallo-ligands proved to be highly effective in the synthesis of heteronuclear systems. The reaction of $[Ni(H_6L)]Cl_2$ (**1**) or $[Cu_2(H_5L)_2(CH_3COO)_2]$ (**2**) with manganese salts (ClO_4^-, CH_3COO^-, $HCOO^-$) allows the formation of the “butterfly-type" complexes $[Mn_2Ni_2(OH)_2(H_3L)_2(H_2O)_2]Cl_2$ (**3**), $[Mn_2Cu_2(CH_3O)_2(H_3L)_2(CH_3COO)_2]$ (**4**) and $[Mn_2^{III}Mn^{II}Cu_2O(HCOO)(H_4L)(H_2L)(CH_3COO)_3]$ (**5**). The magnetic properties of **3**−**4** were easily tuned by small modifications in the reaction conditions (*i.e* metal precursor, co−ligands). Therefore, the combined use of Cu (from **2**) and $Mn(CH_3COO)_2$ instead of Ni (**1**) and $Mn(ClO_4)_2$ modifies the resulting dc magnetic properties, and may induce the slow relaxation in applied dc field in **4**. The reaction of **2** with $Mn(HCOO)_2$, otherwise, led to the synthesis of a higher nuclearity Cu/Mn system (**5**), which unfortunately did not present similar properties to those shown by **4**. It should be noted that the slow relaxation seen for **4** is rare, since, to the best of our knowledge, there is only one other reported Cu/Mn structure displaying SMM properties.

The second approach used to control the assembly process of 3*d*/4*f* systems benefits from the tendency of H_6L to chelate 3*d* ions in its inner $\{N_2O_2\}$ position. As a common feature for all the structures, the transition metal ion occupies the internal $\{N_2O_2\}$ pocket defining $\{M(H_nL)\}$ units (M = Cu, Co; n = 2, 3, 4), which are also coordinated to lanthanide ions by multiple alkoxo/hydroxo groups. Note that the absence of oxygen-donor co−ligands in the reaction media results in the

encapsulation of the 4*f* ions by the {M(H_nL)} moieties. This may be due to the oxophilic nature of the lanthanides. In addition, different Ln elements (Y, La, Gd, Tb, Dy, Ho, Er or Yb) were explored to see how the topological and physical properties of the final complexes varies along the *f*−block.

The Cu/4*f* combination provides the families {$Ln_2Cu_3(H_3L)_2X_n$} (**6**−**12**; Ln = Gd, Tb, Dy, Ho, Er; X = CH_3COO^-, NO_3^-) and [$LnCu_4(H_4L)_4$]$(Cl)_2(ClO_4)$ (**13**−**16**; Ln = Gd, Tb, Dy, La). The substitution of acetate by nitrates in {$Ln_2Cu_3(H_3L)_2X_n$} results in changes in the symmetry of the Ln, the crystal field and the exchange interactions (*i.e*. Cu···Ln, Cu···Cu), which considerably modify the global magnetic properties. The comparison between the dc and ac data for the Tb analogues (**7** and **9**) shows how these subtle alterations cause a great improvement of the SMM performance (*i.e*. increase of the effective energy barrier $\Delta E/k_B$). *Ab initio* CASSCF calculations indicate that the above mentioned changes may quench differently the tunnelling of the magnetisation, and hence influence the $\Delta E/k_B$ parameter. It is worth noting that **9** has the largest reported energy barrier for Tb/Cu−based SMMs (in zero−dc field).

The unusual topology shown by {$LnCu_4$} prompted us to perform a magneto-structural analysis by SXRD, magnetic (dc and ac) studies and theoretical (DFT) calculations, in order to better understand the nature of the Cu···Ln interactions. DFT calculations support the results obtained from the fit of the dc data and the hypothesis proposed by the analysis of the CuOOLn dihedral angles (*α*): the greater the CuOOLn distortion (larger *α*), the greater tendency to be (weakly) antiferromagnetically coupled, and vice versa. The theoretical studies suggest also a relationship between the type of Ln ion and the Cu···Cu interaction, considering that the delocalisation of the spin density in the structure depends on the electronic configuration for each 4*f* trivalent ion. It should be noted that the nature of the Cu···Gd magnetic interaction has been carefully studied in the recent years, since, as formerly explained, this seems to play an important role in the dynamics of 3*d*/4*f* systems. The results presented here are intended to complement these studies, and help in the design of Cu/Ln−SMMs.

Reactions involving the combination of H_6L and Co(II) starting materials display the tendency of Co(II) to be oxidised to Co(III) under mild conditions in the presence of 4*f* ions. Therefore, since low-spin octahedral Co(III) ions are diamagnetic, the static and dynamic magnetic properties of the final complexes are defined predominantly by the Ln ions.

A new series of $[Co_3Ln(H_2L)_2(H_3L)](ClO_4)$ (**17**−**21**, Ln = Tb, Dy, Ho, Er, Yb) has been successfully isolated by using a similar methodology to that used in the synthesis of $\{LnCu_4\}$. Static and dynamic magnetic experiments performed on **17**−**21** show that the magnetic properties are relatively dependent on the electronic structure of the Ln(III) ion. Therefore, only Kramer's ion derivatives (*i.e*. **18** Dy, **20** Er) display slow relaxation induced by the application of an external dc field.

The magnetic studies performed on $[Co^{III}_3Gd^{III}_3(H_2L)_3(acac)_2(CH_3COO)_4(H_2O)_2]$ (**23**) shows that the Co(III) ions do not play a totally passive role in the magnetic properties in **23**, as they partially influence the magnetocaloric properties. In addition, the pre-formation of the metallo-organic precursor $[Co(H_6L)(CH_3COO)_2]$ (**22**) seems to be essential for the assembly of **23**, and thus to promote the magnetocaloric effect. $\{Co^{III}_3Gd^{III}_3\}$ has a unique star-shaped ring, where diamagnetic Co ions alternate with Gd ions. That helps to minimise the Gd···Gd exchange interactions, thus improving the adiabatic temperature change (ΔT_{ad}) in the system. It must be stressed that the maximum value of ΔT_{ad} (10.7 K at T = 1.5 K) displayed by **23** is comparable to those previously reported for some of the most promising Gd−based magnetic cooler candidates.

The coordination chemistry of the polycompartmental ligand H_2L2 was investigated in the presence of nickel and lanthanides, resulting in the synthesis of $[Ln_2Ni_2(L2)_2(CH_3COO)_6(H_2O)_2]$ (**24**−**28**, Ln = Gd, Tb, Dy, Ho, Y). As predicted, the Ni(II) ions occupy the less hindered inner position defined by $\{N_2O_2\}$, while the 4*f* ions are placed in the outer $\{O_2O_2'\}$ pocket. The analysis of the experimental dc data for **28** (Y) suggests a contribution from the ZFS of the Ni(II) ions to the $\{Ln_2Ni_2\}$ systems. However, the dynamics for **24**−**28** strongly depends on the lanthanide present in the structure, where the Tb analogue (**25**) is the only complex presenting field-induced slow relaxation of the magnetisation. This may arise from changes in the crystalline field related to the substitution of the 4*f* ion, or due to a possible re−orientation of the individual magnetic anisotropies of each metal ion (*i.e*. Ni, Ln).

As future work, DFT theoretical calculations that provide insight into the nature of the different exchange interactions in the $\{Mn_2M_n\}$ family (especially that between Mn(III) ions) should be performed to establish, if possible, a relationship with the differences displayed in the dc and ac susceptibility experiments for **3** and **4**. Inelastic neutron scattering (INS) spectroscopic experiments on $[TbCu_4(H_4L)_4](Cl)_2(ClO_4)$ are currently underway to determine the magnetic

interactions within the molecule by interpreting the observable transitions between exchange-split components of the ground state. Furthermore, electron paramagnetic resonance and optical spectroscopic studies will be carried out on the {Co_3Ln} systems in order to determine the optimal parameters of those complexes which showed attractive SMM magnetic features (**18** Dy and **20** Er), since the magnetic properties such 4*f* systems are closely related to the crystal-field splitting of the ground state of the lanthanide ions. In addition, *ab initio* CASSCF calculations on the single−ion magnetic anisotropy orientation of the Ni and Ln centres in **25** (Tb), **26** (Dy) and **27** (Ho) are proposed to shed light on the absence of slow magnetic relaxation in the ac susceptibility studies for the {Ln_2Ni_2} series.

To conclude, the results presented in this PhD thesis show that our methodology based on a bottom-up approach to synthetically control the assembly and physical properties of polynuclear heterometallic complexes is a promising strategy towards the synthesis of new molecular nanomagnets and molecule-based magnetic refrigerants.

Appendix

Appendix

3. Promoting single−molecule magnet properties in a 3*d*/3*d*' butterfly family

Single crystal X−ray data collection and refinement details

Hydrogen atoms were placed in geometrically calculated positions and refined as part of a riding model except some solvent and/or hydroxyl hydrogens which were located in difference Fourier maps and refined as part of a rigid rotating group. For **3**, these were water hydrogens (H1WA, H1WB, H2WA, H2WB, H3WA, H3WB) and some hydroxyl groups (H1, H106, H110, H111). For **4**, these were the hydrogen atoms for all the MeO/MeOH molecules (H1MA,H1MB,H1MC; H2, H2A,H2B,H2C; H1, H1A,H1B,H1C), those for the acetate group (H2AA,H2AB,H2AC), and for two hydroxyl groups (O106, O111).

$[Mn_2^{III}Mn^{II}Cu_2O(HCOO)(H_4L)(H_2L)(CH_3COO)_3]\cdot 4.5CH_3OH\cdot 3.5H_2O$ (**5**): The crystals grew as stacks of very thin plates which could not be separated. Several attempts of processing the data considering a multiple component twin did not show any improvement of the refinement parameters, therefore the data was treated considering just one single component. The relatively large peak of residual electron density (1.8 electrons) could possibly be due to further twin components which have not been accounted for.

Magnetic susceptibility measurements

Fig A3.1 Temperature dependence of $\chi_M T$ (left) and molar magnetic susceptibility (χ_M) *vs*. temperature (T) (right) for $[Cu_2(H_5L)_2(CH_3COO)_2]$ (**2**) in an applied field of 1000 Oe. The red solid lines correspond to the fit (see below details).[1]

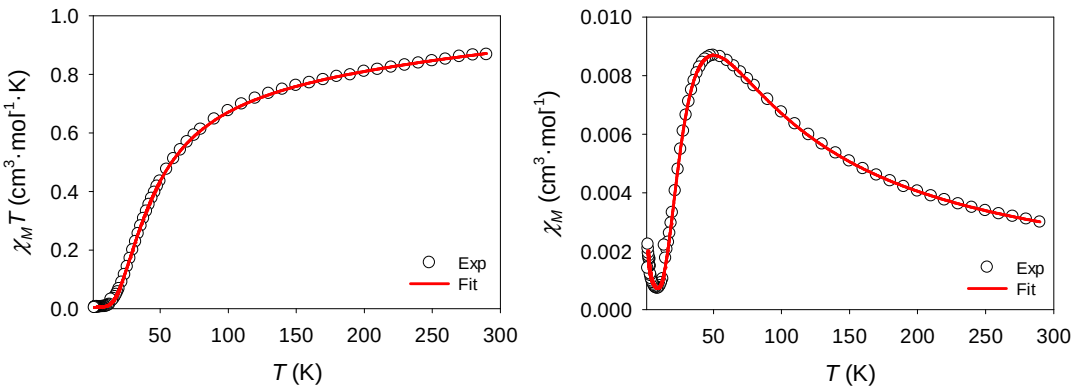

Note that the molecular weight used for calculating the molar susceptibility values corresponds to $[Cu_2(H_5L)_2(CH_3COO)_2]$ (*MW* = 807.84 g/mol). The experimental value of $\chi_M T$ at 290 K of 0.87 $cm^3 \cdot mol^{-1} \cdot K$ is similar to that expected for two non−interacting Cu(II) ions (0.75 $cm^3 \cdot mol^{-1} \cdot K$, S = 1/2, g = 2). The $\chi_M T$ versus T data was fitted (red solid line) by applying the spin Hamiltonian shown above, to give $\mathcal{J}$ = −28.9 ± 0.1 cm^{-1} and g = 2.18 ± 0.002.[1] A small monomeric impurity of IMP = 1.5% and a temperature−independent paramagnetism term of TIP = $1.2 \cdot 10^{-4}$ $cm^3 \cdot mol^{-1}$ were also included.

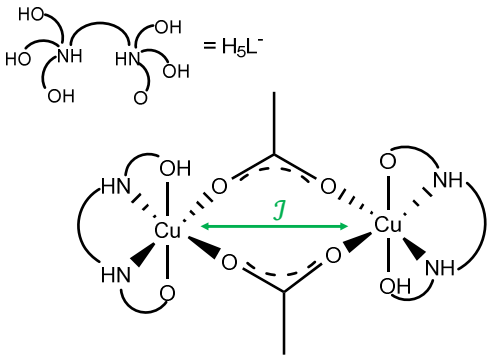

$$\hat{\mathcal{H}} = -2\mathcal{J}(\hat{S}_1 \cdot \hat{S}_2) + g\mu_B \vec{B} \sum_{i=1}^{2} \vec{s_i}$$

Magnetic model and spin Hamiltonian used to fit the magnetic data for **2** with a single parameter $\mathcal{J}$ describing the exchange interaction between Cu(II) centres ($\vec{s}$ denotes the spin operator). The second term is the Zeeman interaction, with g the isotropic single−ion g factor, μ_B the Bohr magneton and $\vec{B}$ the magnetic field.

Fig A3.2 Five−coordinate system $\{CuN_2O_3\}$ and equation for the structural parameter τ. The *α* angle (corresponding to the smaller basal plane angle) is shown in red, whereas the *β* angle (corresponding to the bigger one) is displayed in blue. Cu, turquoise; N, blue; O, red.

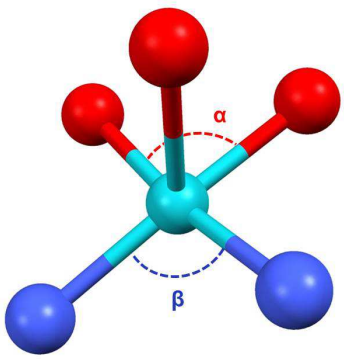

$$\tau = \frac{(\beta - \alpha)}{60}$$

Fig A3.3 Intermolecular hydrogen bonding interactions (dashed black lines) in complex **3**. C, grey; Cu, turquoise; H, white; Mn, lilac; N, blue; O, red. Only the shortest interaction between Cu(II) ions in which the CH_3COO^- group is involved is highlighted (7.369(1) Å). These interactions occurs via $CH_3COO^-\cdots HO(H_3L^{3-})$ and $CH_3COO^-\cdots H(C-N)$ hydrogen bonds.

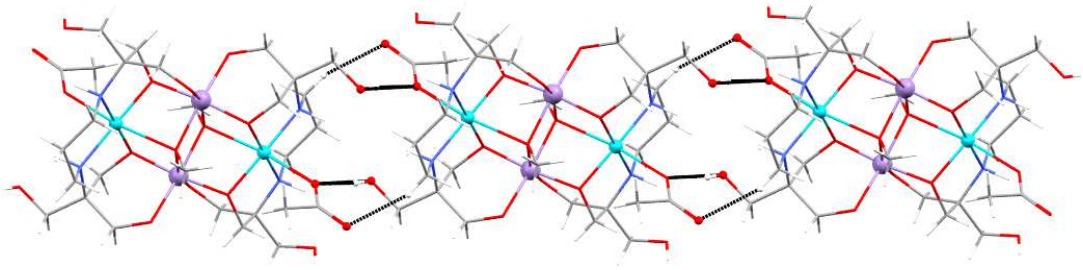

Fig A3.4 Temperature dependence ac plots of χ' and χ'' of **4** in the absence of an applied dc field (right) and in an external field of H_{dc} = 2000 Oe, measured with a small alternating field of 3 Oe and at υ = 10, 250, 1359 Hz.

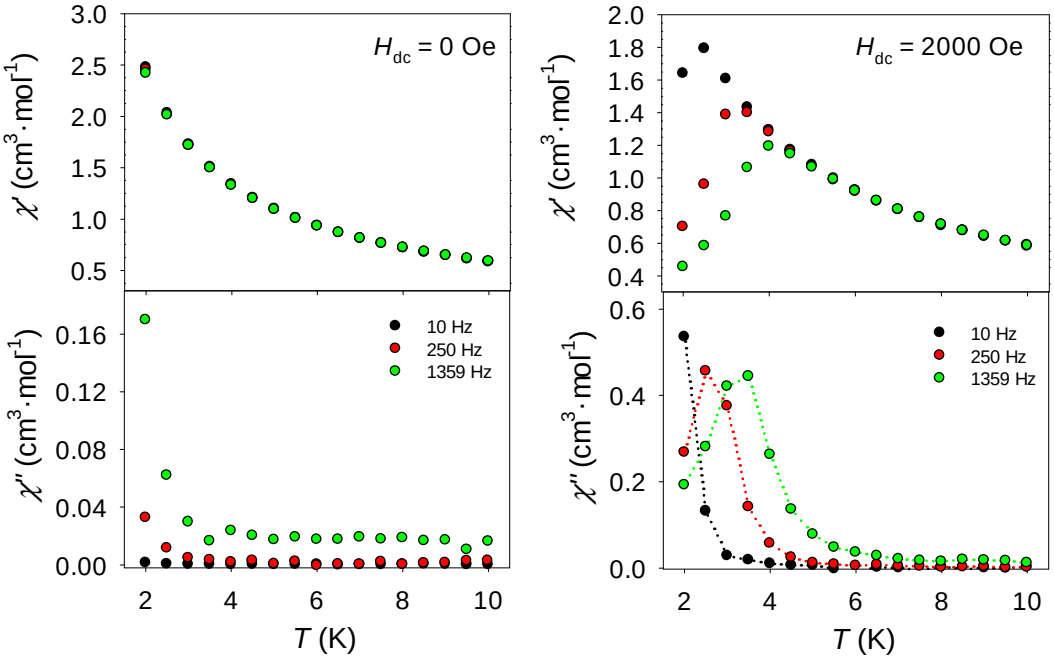

Fig A3.5 Left: Variable−field ac plots of χ' and χ'' *vs.* frequency (υ) of **4**, at T = 1.8 K under applied dc fields in the range H_{dc} = 0 − 5000 Oe. Right: Field dependence of τ. The dotted line in τ *vs*. H is a guide for the eye.

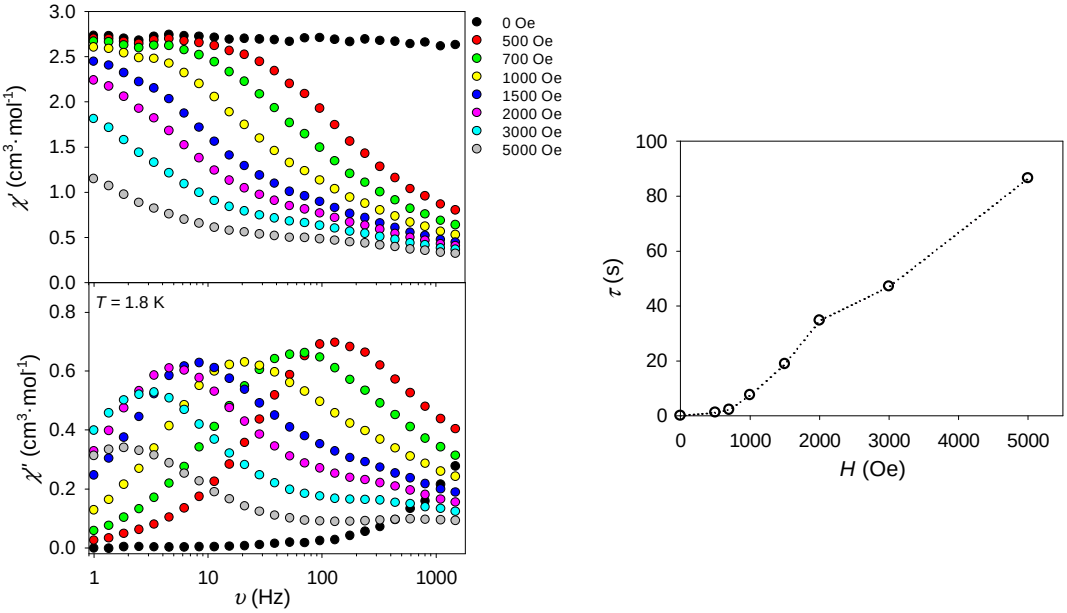

Fig A3.6 Magnetisation *vs*. field at 2 and 5 K for **5**.

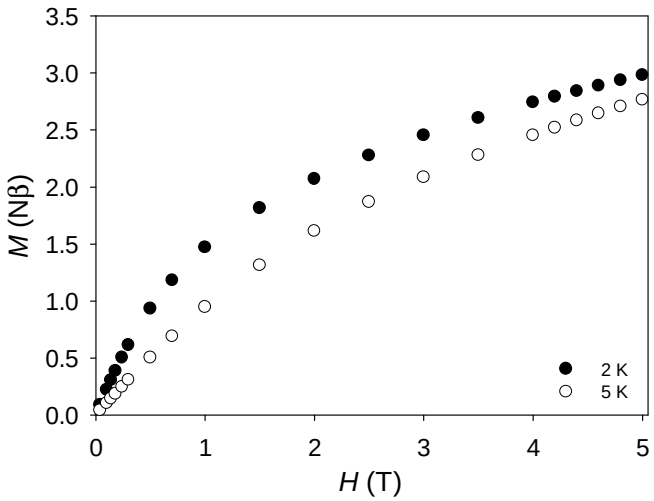

Fig A3.7 Variable−field ac plots of χ' and χ'' vs υ of **4**, at T = 1.8 K under applied dc fields in the range H_{dc} = 0 − 5000 Oe.

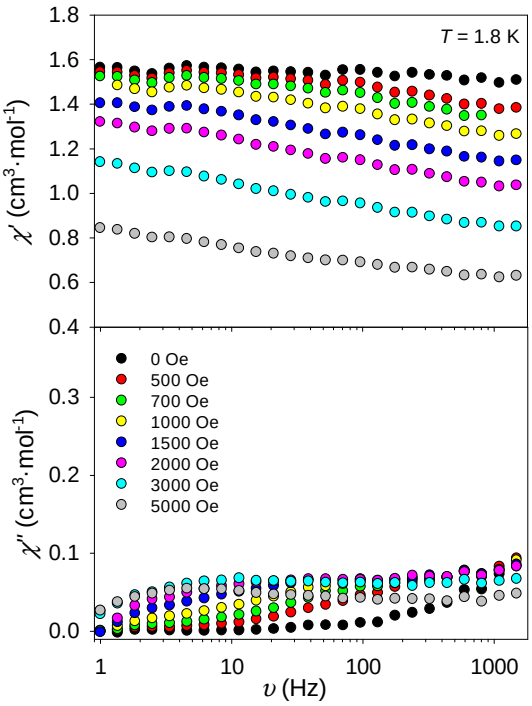

References

1. N. F. Chilton, R. P. Anderson, L. D. Turner, A. Soncini and K. S. Murray, *J. Comput. Chem.*, **2013**, *34*, 1164.

4. Enhancement of Tb^{III}–Cu^{II} SMM performance through structural modification

Single crystal X−ray data collection and refinement details

Hydrogen atoms were placed in geometrically calculated positions and refined as part of a riding model except some solvent and/or hydroxyl hydrogens which were located in difference Fourier maps and refined as part of a rigid rotating group.

$[Tb_2Cu_3(H_3L)_2(CH_3COO)_6]\cdot CH_3OH\cdot 2H_2O$ (**7**): The crystal for complex **7** showed signs of a twin (2−fold rotation about 1 0 0) which we attempted to account for. There is approx. 18% overlap between the two twin components so a hklf4 format file corresponding to only one component was around 80% complete but did reduce the residual electron density to approx. 2 $e^-/Å^3$. An hklf5 format file with both components gave worse agreement factors and did not improve the residual electron density. All results are for the data as processed without this twinning taken into account.

$(NMe_4)_2[Tb_2Cu_3(H_3L)_2(NO_3)_7(CH_3OH)_2](NO_3)$ (**9**): Disorder was modelled in one of the NMe_4^+ cations as a rotation about the N−C101 axis and the remaining 3 CH_3−carbons were modelled over 2 partially occupied sites with occupancies of 0.72/0.28. Distance similarity restraints were applied to all N−C distance in the NMe_4^+ and the minor component was modelled with isotropic *adps*. One nitrate ion also has an oxygen atom disordered over two partially occupied sites with occupancy 0.75/0.25 and the minor component modelled with isotropic *adp*.

$(NMe_4)_2[Ho_2Cu_3(H_3L)_2(NO_3)_7(CH_3OH)_2](NO_3)$ (**11**): Disorder was present in one nitrate anion where one oxygen atom is modelled over two partially occupied sites with occupancies 0.85:0.15. The minor component is modelled with isotropic *adps* and distance restraints were applied to all N−O distances.

Table A4.1 Shape measures of $\{Ln_2Cu_3\}$ relative to the ideal 9−vertex polyhedra shown of complexes $[Ln_2Cu_3(H_3L)_2(CH_3COO)_6]$ (**9**−**7**) (Gd^{3+}, Tb^{3+}), $(NMe_4)_2[Gd_2Cu_3(H_3L)_2(NO_3)_8(CH_3CH_2OH)_2]\cdot 2H_2O$ (**8**), and $(NMe_4)_2[Tb_2Cu_3(H_3L)_2(NO_3)_7(CH_3OH)_2](NO_3)$ (**9**). The lowest CShMs value, and thus the closest geometry is highlighted in pink.[1-3]

	6	**7**	**8**	**9**, Tb1	**9**, Tb2	**Symmetry**	**Ideal shape**
EP-9	36.757	36.630	30.410	31.370	32.088	D_{9h}	Enneagon
OPY-9	21.989	22.101	19.543	20.489	19.743	C_{8v}	Octagonal pyramid
HBPY-9	19.715	19.598	16.358	17.143	17.281	D_{7h}	Heptagonal bipyramid
JTC-9	13.828	13.772	13.601	13.135	13.524	C_{3v}	Johnson triangular cupola J3
JCCU-9	10.750	10.841	8.866	9.196	10.310	C_{4v}	Capped cube J8
CCU-9	9.463	9.677	7.920	8.490	9.534	C_{4v}	Spherical-relaxed capped cube
JCSAPR-9	2.878	2.820	3.502	2.931	2.944	C_{4v}	Capped square antiprism J10
CSAPR-9	**1.889**	**1.937**	2.608	2.144	**2.043**	C_{4v}	**Spherical capped square antiprism**
JTCTPR-9	3.469	3.310	2.457	2.333	2.363	D_{3h}	Tricapped trigonal prism J51
TCTPR-9	2.195	2.171	2.649	2.609	2.189	D_{3h}	Spherical tricapped trigonal prism
JTDIC-9	11.492	11.689	12.607	14.190	13.421	C_{3v}	Tridiminished icosahedron J63
HH-9	12.344	12.360	9.034	9.245	10.373	C_{2v}	Hula-hoop
MFF-9	2.252	2.377	**2.271**	**1.766**	2.174	C_s	**Muffin**

Table A4.2 Shape measures of $\{Ln_2Cu_3\}$ relative to the ideal 9−vertex polyhedra shown of complexes $(NMe_4)_2[Ln_2Cu_3(H_3L)_2(NO_3)_7(CH_3OH)_2](NO_3)$ (**10**−**12**) (Ln = Dy^{3+}, Ho^{3+}, Er^{3+}). The lowest CShMs value, and thus the closest geometry is highlighted in pink.[1-3]

	10, Dy1	**10**, Dy2	**11**, Ho1	**11**, Ho2	**12**, Er1	**12**, Er2	**Symmetry**	**Ideal shape**
EP-9	31.389	31.976	31.381	31.956	31.362	31.953	D_{9h}	Enneagon
OPY-9	20.633	19.859	20.764	19.914	20.851	19.952	C_{8v}	Octagonal pyramid
HBPY-9	17.253	17.391	17.289	17.383	17.400	17.444	D_{7h}	Heptagonal bipyramid
JTC-9	13.256	13.462	13.284	13.443	13.270	13.450	C_{3v}	Johnson triangular cupola J3
JCCU-9	9.206	10.332	9.050	10.232	9.038	10.258	C_{4v}	Capped cube J8
CCU-9	8.540	9.584	8.458	9.515	8.515	9.558	C_{4v}	Spherical-relaxed capped cube
JCSAPR-9	2.886	2.937	2.895	2.919	2.871	2.868	C_{4v}	Capped square antiprism J10
CSAPR-9	2.106	**2.037**	2.106	**2.025**	2.101	**1.984**	C_{4v}	**Spherical capped square antiprism**
JTCTPR-9	2.281	2.284	2.246	2.237	2.191	2.192	D_{3h}	Tricapped trigonal prism J51
TCTPR-9	2.586	2.168	2.587	2.146	2.603	2.122	D_{3h}	Spherical tricapped trigonal prism
JTDIC-9	14.131	13.438	14.127	13.482	14.095	13.528	C_{3v}	Tridiminished icosahedron J63
HH-9	9.325	10.443	9.305	10.404	9.346	10.436	C_{2v}	Hula-hoop
MFF-9	**1.740**	2.165	**1.733**	2.160	**1.733**	2.127	C_s	**Muffin**

Magnetic susceptibility measurements

Fig A4.1 Magnetisation *vs*. field at 2, 4, 5 and/or 6 K for **7** − **12**.

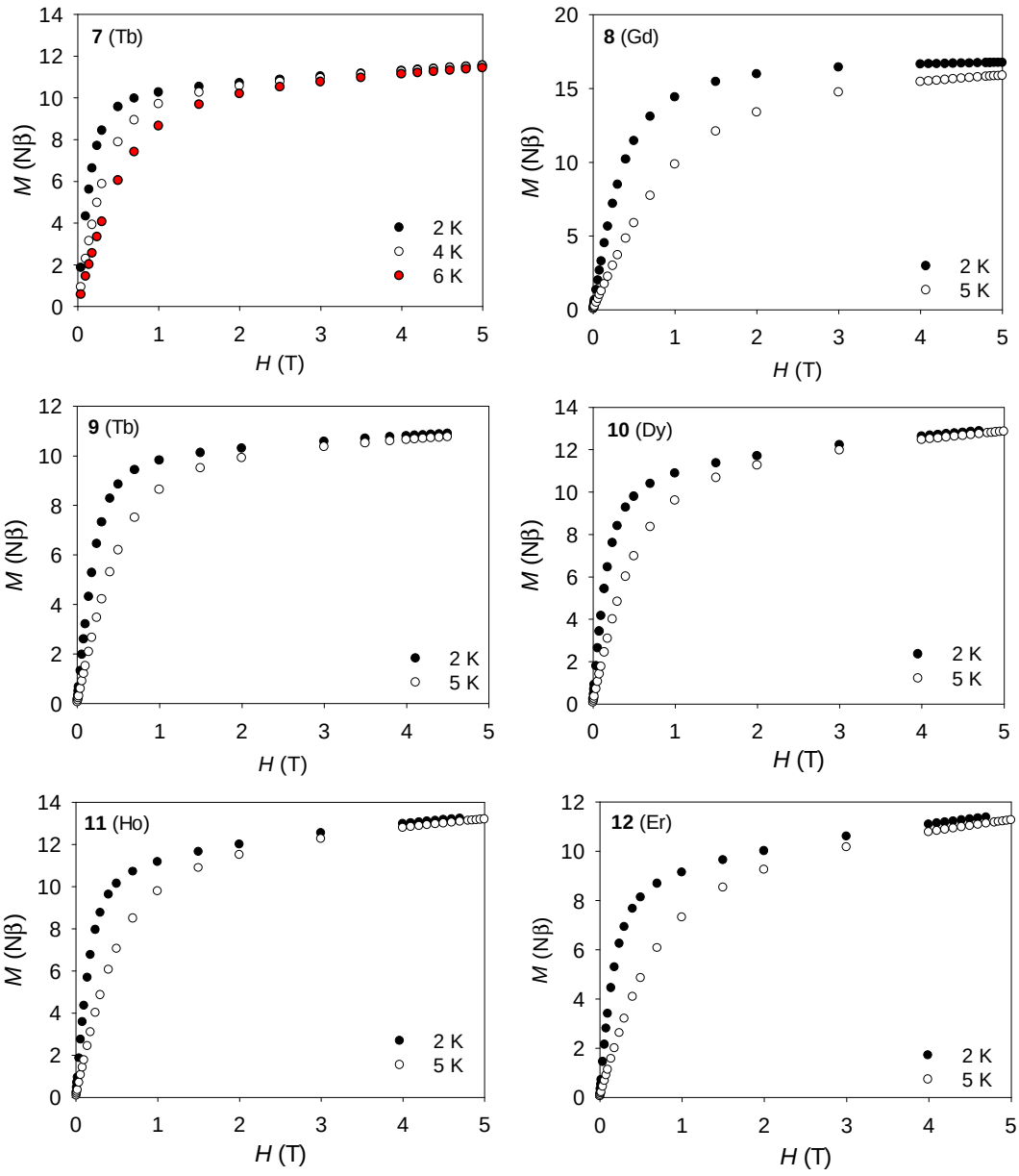

Table A4.3 Summary of Cu/4*f* SMMs based on the structures reported in the Cambridge Structural Database (CSD 5.36 version, February 2016). Energy barrier, pre−exponential factor, and magnetic dc field are indicated as $\Delta E/k_B$, τ_0, and H_{dc} respectively.

	Complex	$\Delta E/k_B$ / K (applied H_{dc}/Oe)	τ_0/s	Ref
1	$[L^4CuTb(NO_3)_2]_2(CH_3OH)_2$	4.2 (0)	$1\cdot10^{-5}$	[4]
2	$[Dy^{III}{}_3Cu^{II}{}_6L_6(\mu_3\text{-}OH)_6(H_2O)_{10}]Cl_2\cdot ClO_4\cdot 3.5H_2O$	25 (0)	$1.5\cdot10^{-7}$	[5]
3	$[LCu(O_2COMe)Tb(thd)_2]$	13.8 (1000)	$3\cdot10^{-7}$	[6]
4	$[\{Dy(hfac)_3\}_2\{Cu(dpk)_2\}]$	47 (0)	$1.1\cdot10^{-7}$	[7]
5	$[\{Cu^{II}LTb^{III}(o\text{-}van)(CH_3COO)(MeOH)\}_2]\cdot 2H_2O$	20.4 (1000)	$7.1\cdot10^{-8}$	[8]
6	$[LCuDy(hfa)_2(dmf)_2]_2$	14.7 (0)	$1.7\cdot10^{-7}$	[9]
7	$C_{24}H_{32}N_5O_{15}CuTb$	16.6 (0)	–	[10]
8	$[\{TbCu(L4)(L5)(NO_3)_2\}_2]$	17 (0)	–	[11]
9	$[TbCu(L3)(NO_3)_3(H_2O)]$	29 (1000)	–	[12]
10	[TbCu(L3)(*O*-vanilate)(NO_3)(MeOH)]NO_3	32.2 (1000)	–	[12]
11	$[H_3O][Cu_{24}Dy_8(Ph_3C\text{–}PO_3)_6(Ph_3C\text{–}PO_3H)_6(MeCO_2)_{12}(MeCO_2H)_6(OH)_{42}$	4.6 (0)	$2.1\cdot10^{-8}$	[13]
12	$[TbCu(sal)(NO_3)_2(L)(MeOH)]$	32.9 (1000)	$3.0\cdot10^{-8}$	[14]
13	$[DyCu(sal)(NO_3)_2(L)(MeOH)]$	26.0 (1000)	$1.02\cdot10^{-5}$	[14]
14	$[Cu^{II}{}_5Tb^{III}{}_4O_2(teaH)_4\{O_2CC(CH_3)_3\}_2(NO_3)_4(OMe)_4]\cdot 2MeOH\cdot 2Et_2O$	7 (0)	$1.3\cdot10^{-5}$	[15]
15	$[Cu^{II}{}_5Dy^{III}{}_4O_2(teaH)_4\{O_2CC(CH_3)_3\}_2(NO_3)_4(OMe)_4]\cdot 2MeOH\cdot 2Et_2O$	11.9 (0)	$9\cdot10^{-6}$	[15]
16	$[Cu^{II}{}_5Ho^{III}{}_4O_2(teaH)_4\{O_2CC(CH_3)_3\}_2(NO_3)_4(OMe)_4]\cdot 2MeOH\cdot 2Et_2O$	10 (0)	$3\cdot10^{-6}$	[15]
17	$[Cu_2Tb_2(L)_2(dae\text{-}o)_2(NO_3)_2]\cdot 2(n\text{-}BuOH)$	14.91 (0)	$2.39\cdot10^{-7}$	[16]
		23.76 (1000)	$7\cdot10^{-8}$	
18	$\{[CuTb(L)(n\text{-}BuOH)_{0.5}]_2(daec)_3\}\cdot 5(DMF)\cdot 4(n\text{-}BuOH)\cdot 2(H_2O)$	12.13 (0)	$3.03\cdot10^{-6}$	[16]
		22.04 (1000)	$2.11\cdot10^{-7}$	
19	$[TbCu_4(L)_2(\mu_3\text{-}OH)_4(H_2O)_8(NO_3)](ClO_4)_2\cdot 6H_2O$	25.0 (3000)	$8.1\cdot10^{-8}$	[17]

	Complex	$\Delta E/k_B$ / K (applied H_{dc}/Oe)	τ_0/s	Ref
20	$[SmCu_4(L)_2(\mu_3\text{-}OH)_4(H_2O)_8(NO_3)](ClO_4)_2\cdot 6H_2O$	14.1 (3000)	$4.7\cdot10^{-7}$	[17]
21	$[Cu(L)(C_3H_6O)Tb(NO_3)_3]$	42.3 (1000)	$7.1\cdot10^{-10}$	[18]
22	$[Cu(L)(C_3H_6O)Dy(NO_3)_3]$	11.5 (1000)	$4\cdot10^{-10}$	[18]
23	$[Dy^{III}_2Cu^{II}_7(OH)_2(L^2)_2(L^3)_2(OAc)_8(NO_3)_2(H_2O)_4](NO_3)_2\cdot 8.5H_2O$	18.0 (0)	$5.61\cdot10^{-8}$	[19]
24	$[Dy^{III}_9Cu^{II}_8(NO_3)_2(OH)_{10}(L^3)_4(OAc)_{18}(H_2O)_4](NO_3)_2(OH)_3\cdot 16H_2O\cdot 10MeOH$	11.5 (0)	$1.86\cdot10^{-6}$	[20]
25	$[Dy_2Cu_8(\mu_2\text{-}OH)_2(\mu_3\text{-}OH)_2(ClO_4)_2(HTMHSA)_4(H_2O)10]\cdot 15H_2O$	0.82 (0)	$8.02\cdot10^{-6}$	[21]
26	$[Cu_5Dy_2(L)_2(\mu_3\text{-}OH)_4(\mu\text{-}OH_2)_2(\mu\text{-}OAc)_2(OAc)_2(OH_2)_2](NO_3)_2(H_2O)_2$	4 (0)	$3\cdot10^{-6}$	[22]
27	$[Cu_5Ho_2(L)_2(\mu_3\text{-}OH)_4(\mu\text{-}OH_2)_2(\mu\text{-}OAc)_2(OAc)_2(OH_2)_2](NO_3)_2(H_2O)_2$	6 (900)	$3\cdot10^{-6}$	[22]
28	$[Cu_2(valpn)_2Tb_2(N_3)_6]\cdot 2CH_3OH$	30.1 (0)	$1.1\cdot10^{-6}$	[23]
29	$[Cu^{II}_4Dy^{III}_4(vanox)_6(Hvanox)_2(NO_3)_4(\mu\text{-}HOMe)_2]\cdot 6MeOH$	41.6 (0)	$2.1\cdot10^{-5}$	[24]
30	$[(CuL)_2Tb(H_2O)(NO_3)_3]\cdot MeOH\cdot H_2O$	20.3 (1000)	$1.5\cdot10^{-7}$	[25]
31	$[\{(CuL)_2Tb(H_2O)(NO_3)_3\}2bpy]\cdot 2MeOH\cdot 4H_2O$	18.0 (1000)	$1.2\cdot10^{-8}$	[25]
32	$[Cu_6Dy_2(L^{3-})_4(NO_3)_3(OAc)(CH_3OH)_6]\cdot NO_3\cdot OAc\cdot 3CH_3OH\cdot 2H_2O$	5.2 (0)	$6.5\cdot10^{-6}$	[26]
33	$[Cu_6Tb_2(L^{3-})_4(NO_3)_3(OAc)_2(CH_3OH)_5]\cdot NO_3\cdot CH_3OH\cdot 6H_2O$	15.6 (0)	$6.9\cdot10^{-7}$	[26]

Computational details

All *ab initio* calculations on the model complexes were performed with the MOLCAS 8.0 suite.[27-33] Spin−free wave functions were generated using the complete active space self−consistent field (CASSCF) method. These multiconfigurational wave functions have been used as input states to account for spin−orbit coupling via the Restricted Active Space Spin State Interaction−Spin Orbit (RASSI−SO) methodology.[33,34] The resulting spin−orbit eigenstates were used for the calculation of the anisotropic magnetic properties and *g* tensors of the lowest state using a specially designed routine SINGLE_ANISO.[35] All the atoms were represented by ANO−RCC basis sets from the ANO−RCC basis library included in the MOLCAS 8.0 suite. We have employed the [ANO−RCC...8s7p5d3f2g1h.] basis set for Tb^{III}, and [ANO−RCC...4s3p2d1f.] basis set for C, N and O and [ANO−RCC...2s.] basis

set for H throughout our calculations. The active space of (8,7) is used for all the models. In the configurational Interaction (CI) procedure, 7 septets, 140 quintets and 195 triplets are considered. The singlet states were not included due to computational limitations. In the RASSI module, 7 septets, 105 quintets and 112 triplets are mixed by spin−orbit coupling within the energy window of about 40,000 cm^{-1}.

The two Tb(III) ions in complex **7** are isostructural with spherical capped square antiprismatic geometry, therefore only one Tb(III) ion core (model−1) is considered for *ab initio* calculations. However, the Tb(III) ions present in complex **9** are different, hence two Tb(III) ions (model−2 and model−3) are considered for the calculations. To understand the magnetic properties of these complexes, we performed *ab initio* calculations of each Tb(III) centre of the complexes. In these calculations, the effect of neighbouring Cu(II) ions are not included and the ligands which bridge to the corresponding Cu(II) ions are approximated. The structures of the calculated models are shown in Figures 4.14 and 4.15.

Table A4.4 Calculated energy spectrum, *g* tensors and angles (θ) of the principal anisotropy axes of excited states (ES) with respect to the ground state (GS) for model−1.

Level	Energy (cm^{-1})	g_z	Δ_{tun} (cm^{-1})	Angle (°)
1	0.00	17.79	0.45	-
2	0.45			
3	54.03	15.18	2.11	153.62
4	56.14			
5	96.95	12.33	7.14	137.79
6	104.09			
7	141.33	-	-	-
8	160.30	-	-	-
9	181.78	-	-	-
10	203.87	12.59	9.26	100.93
11	213.13			
12	309.73	17.35	0.92	100.58
13	310.65			

Table A4.5 Calculated energy spectrum, *g* tensors and angles (*θ*) of the principal anisotropy axes of excited states (ES) with respect to the ground state (GS) for model−2.

Level	Energy (cm^{-1})	g_z	Δ_{tun} (cm^{-1})	Angle (°)
1	0.00	17.80	0.08	-
2	0.08			
3	58.07	16.63	1.40	56.48
4	59.47			
5	115.66	12.13	3.73	24.12
6	119.39			
7	178.52	-	-	-
8	186.68	-	-	-
9	212.73	-	-	-
10	233.20	12.20	6.93	62.58
11	240.13			
12	295.48	17.15	3.41	94.42
13	298.89			

Table A4.6 Calculated energy spectrum, *g* tensors and angles (*θ*) of the principal anisotropy axes of excited states (ES) with respect to the ground state (GS) for complex model−3.

Level	Energy (cm^{-1})	g_z	Δ_{tun} (cm^{-1})	Angle (°)
1	0.00	17.72	0.32	-
2	0.32			
3	58.93	16.33	5.00	86.29
4	63.93			
5	98.94	-	-	-
6	125.34	-	-	-
7	134.39	-	-	-
8	184.73	11.81	5.05	77.73
9	189.78			
10	256.14	14.57	1.34	79.76
11	257.48			
12	371.81	17.59	0.75	92.65
13	372.56			

Table A4.7 SINGLE_ANISO computed crystal field parameters for model−1, model−2 and model−3. The major components in the Table are in bold. B_k^q is the crystal field parameter and O_k^q is the extended Stevens operator. The quantization axis is chosen to be the main magnetic axis of the ground pseudo−doublet.

k	q	Model−1	Model−2	Model−3
		B_k^q	B_k^q	B_k^q
2	-2	-1.459	0.893	-3.752
	-1	**1.420**	**1.159**	**-0.912**
	0	**-2.016**	**-1.877**	**-1.996**
	1	**2.526**	**-2.667**	**-0.406**
	2	1.094	-1.672	-0.456
4	-4	-0.228×10^{-1}	-0.548×10^{-2}	0.184×10^{-1}
	-3	0.435×10^{-1}	-0.311×10^{-1}	0.104
	-2	0.167×10^{-1}	-0.822×10^{-2}	0.176×10^{-1}
	-1	-0.121×10^{-1}	-0.586×10^{-2}	0.619×10^{-2}
	0	-0.147×10^{-2}	-0.472×10^{-2}	-0.353×10^{-2}
	1	-0.293×10^{-1}	0.279×10^{-1}	0.430×10^{-3}
	2	0.163×10^{-2}	0.179×10^{-1}	-0.161×10^{-1}
	3	0.437×10^{-1}	-0.104	0.463×10^{-1}
	4	0.517×10^{-2}	-0.174×10^{-1}	0.299×10^{-2}
6	-6	0.218×10^{-3}	0.143×10^{-3}	0.222×10^{-3}
	-5	0.214×10^{-3}	0.523×10^{-3}	0.161×10^{-3}
	-4	0.887×10^{-5}	-0.190×10^{-4}	0.832×10^{-4}
	-3	0.255×10^{-3}	-0.862×10^{-4}	-0.175×10^{-3}
	-2	0.255×10^{-4}	0.137×10^{-3}	-0.415×10^{-4}
	-1	-0.131×10^{-3}	-0.291×10^{-3}	0.762×10^{-4}
	0	0.271×10^{-4}	0.581×10^{-6}	-0.342×10^{-4}
	1	0.151×10^{-3}	0.145×10^{-3}	0.803×10^{-5}
	2	0.109×10^{-3}	0.115×10^{-4}	0.139×10^{-3}
	3	-0.581×10^{-4}	0.328×10^{-3}	-0.224×10^{-3}
	4	0.109×10^{-3}	-0.669×10^{-4}	-0.120×10^{-3}
	5	0.764×10^{-3}	0.747×10^{-3}	0.948×10^{-3}
	6	-0.311×10^{-3}	0.204×10^{-4}	0.141×10^{-3}

Fig A4.2 The structure of the calculated models (model−1, model−2 and model−3).

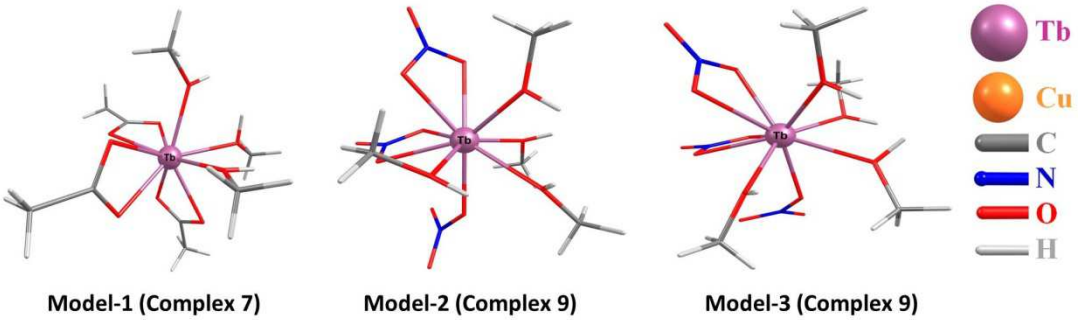

References

1. M. Pinsky and D. Avnir, *Inorg. Chem.*, **1998**, *37*, 5575.
2. A. Ruiz-Martínez, D. Casanova and S. Alvarez, *Chem. Eur. J.*, **2008**, *14*, 1291.
3. A. Ruiz-Martinez, D. Casanova and S. Alvarez, *Dalton Trans.*, **2008**, 2583.
4. J.-P. Costes, M. Auchel, F. Dahan, V. Peyrou, S. Shova and W. Wernsdorfer, *Inorg. Chem.*, **2006**, *45*, 1924.
5. C. Aronica, G. Pilet, G. Chastanet, W. Wernsdorfer, J.-F. Jacquot, D. Luneau, *Angew. Chem. Int. Ed.*, **2006**, *45*, 4659.
6. J.-P. Costes, F. Dahan, W. Wernsdorfer, *Inorg. Chem.*, **2006**, *45*, 5.
7. F. Mori, T. Nyui, T. Ishida, T. Nogami, K.-Y. Choi, H. Nojiri, *J. Am. Chem. Soc.*, **2006**, *128*, 1440.
8. T. Hamamatsu, K. Yabe, M. Towatari, N. Matsumoto, N. Re, A. Pochaba, J. Mrozinski, *Bull. Chem. Soc. Jpn.*, **2007**, *80*, 523.
9. J.-P. Costes, S. Shova, W. Wernsdorfer, *Dalton Trans.*, **2008**, *14*, 1843.
10. T. Kajiwara, M. Nakano, S. Takaishi, M. Yamashita, *Inorg. Chem.*, **2008**, *47*, 8604.
11. T. Kajiwara, K. Takahashi, T. Hiraizumi, S. Takaishi, M. Yamashita, *Cryst. Eng. Comm*, **2009**, *11*, 2110.
12. T. Kajiwara, K. Takahashi, T. Hiraizumi, S. Takaishi, M. Yamashita, *Polyhedron*, **2009**, *28*, 1860.
13. V. Baskar, K. Gopal, M. Helliwell, F. Tuna, W. Wernsdorfer, R. E. P. Winpenny, *Dalton Trans.*, **2010**, *39*, 4747.
14. T. Kajiwara, M. Nakano, K. Takahashi, S. Takaishi, M. Yamashita, *Chem. Eur. J.*, **2011**, *17*, 196.
15. S. K. Langley, L. Ungur, N. F. Chilton, B. Moubaraki, L. F. Chibotaru, K. S. Murray, *Chem. Eur. J.*, **2011**, *17*, 9209.
16. T. Shiga, H. Miyasaka, M. Yamashita, M. Morimoto, M. Irie, *Dalton Trans.*, **2011**, *40*, 2275.
17. Q. Zhu, S. Xiang, T. Sheng, D. Yuan, C. Shen, C. Tan, S. Hu and X. Wu, *Chem. Commun.*, **2012**, *48*, 10736.
18. T. Ishida, R. Watanabe, K. Fujiwara, A. Okazawa, N. Kojima, G. Tanaka, S. Yoshii, H. Nojiri, *Dalton Trans.*, **2012**, *41*, 13609.
19. J.-L. Liu, Y.-C. Chen, Q.-W. Li, S. Gomez-Coca, D. Aravena, E. Ruiz, W.-Q. Lin, J.-D. Leng, M.-L. Tong, *Chem. Commun.*, **2013**, *49*, 6549.
20. J.-L. Liu, W.-Q. Lin, Y.-C. Chen, S. Gómez-Coca, D. Aravena, E. Ruiz, J.-D. Leng, M.-L. Tong, *Chem. Eur. J.*, **2013**, *19*, 17567.

21. H. Zhang, G.-L. Zhuang, X.-J. Kong, Y.-P. Ren, L.-S. Long, R.-B. Huang and L.-S. Zheng, *Cryst. Growth Des.*, **2013**, *13*, 2493.
22. V. Chandrasekhar, A. Dey, S. Das, M. Rouzières, R. Clérac, *Inorg. Chem.*, **2013**, *52*, 2588.
23. X.-C. Huang, C. Zhou, H.-Y. Wei, X.-Y. Wang, *Inorg. Chem.*, **2013**, *52*, 7314.
24. I. A. Kuhne, N. Magnani, V. Mereacre, W. Wernsdorfer, C. E. Anson, A. K. Powell, *Chem. Commun.*, **2014**, *50*, 1882.
25. S. Ghosh, Y. Ida, T. Ishida, A. Ghosh, *Cryst. Growth Des.*, **2014**, *14*, 2588.
26. S. Xue, Y.-N. Guo, L. Zhao, H. Zhang, J. Tang, *Inorg. Chem.*, **2014**, *53*, 8165.
27. F. Aquilante, J. Autschbach, R. K. Carlson, L. F. Chibotaru, M. G. Delcey, L. De Vico, I. Fdez. Galván, N. Ferré, L. M. Frutos, L. Gagliardi, M. Garavelli, A. Giussani, C. E. Hoyer, G. Li Manni, H. Lischka, D. Ma, P. Å. Malmqvist, T. Müller, A. Nenov, M. Olivucci, T. B. Pedersen, D. Peng, F. Plasser, B. Pritchard, M. Reiher, I. Rivalta, I. Schapiro, J. Segarra-Martí, M. Stenrup, D. G. Truhlar, L. Ungur, A. Valentini, S. Vancoillie, V. Veryazov, V. P. Vysotskiy, O. Weingart, F. Zapata and R. Lindh, *J. Comput. Chem.*, **2016**, *37*, 506.
28. F. Aquilante, L. De Vico, N. Ferre, G. Ghigo, P. A. Malmqvist, P. Neogrady, T. B. Pedersen, M. Pitonak, M. Reiher, B. O. Roos, L. Serrano-Andres, M. Urban, V. Veryazov and R. Lindh, *J. Comput. Chem.*, **2010**, *31*, 224.
29. J. A. Duncan, *J. Am. Chem. Soc.*, **2009**, 131, 2416.
30. B. Swerts, L. F. Chibotaru, R. Lindh, L. Seijo, Z. Barandiaran, S. Clima, K. Pierloot and M. F. A. Hendrickx, *J. Chem. Theory Comput.*, **2008**, *4*, 586.
31. V. Veryazov, P. O. Widmark, L. Serrano-Andres, R. Lindh and B. O. Roos, *Int. J. Quantum Chem.*, **2004**, *100*, 626.
32. G. Karlstrom, R. Lindh, P. A. Malmqvist, B. O. Roos, U. Ryde, V. Veryazov, P. O. Widmark, M. Cossi, B. Schimmelpfennig, P. Neogrady and L. Seijo, *Comp Mater Sci*, **2003**, *28*, 222.
33. P. A. Malmqvist, B. O. Roos and B. Schimmelpfennig, *Chem. Phys. Lett.*, **2002**, *357*, 230.
34. L. F. Chibotaru and L. Ungur, *J. Chem. Phys.*, **2012**, *137*, 064112.
35. L. Ungur and L. F. Chibotaru, in *http://www.molcas.org/documentation/manual/node95.html*.

5. Elucidating the nature of the spin interactions in a structurally exceptional Ln^{III}–Cu^{II} family

Single crystal X−ray data collection and refinement details

Hydrogen atoms were placed in geometrically calculated positions and refined as part of a riding model, except those from molecules of methanol and from the uncoordinated OH groups of the H_4L^{2-} ligands, which were refined as part of a rigid rotating group. The perchlorate anion is half occupied and overlaps with a half occupied MeOH molecule, with one of the oxygen atoms forming part of both the perchlorate (O4) and the MeOH oxygen (O5). These were constrained to have the same position and *adps*. One other MeOH is also half occupied. In addition, the O1S atom of one of the methanol molecules in **16** was modelled over two partially occupied sites with competitively refined occupancies of 0.9(9):0.1(1).

Table A5.1 Shape measures of {$LnCu_4$} relative to ideal 8-vertex polyhedra shown of complexes $[LnCu_4(H_4L)_4](Cl)_2(ClO_4)\cdot 4CH_3OH$ (Gd **13**, Tb **14**, Dy **15** and La **16**). The lowest CShMs value, and thus most coincident geometry is highlighted in pink.[1, 2]

	13	14	15	16	Symmetry	Ideal shape
OP-8	33.263	33.124	32.973	33.997	D_{8h}	Octagon
HPY-8	22.159	22.271	22.220	21.998	C_{7v}	Heptagonal pyramid
HBPY-8	15.297	15.268	15.410	14.966	D_{6h}	Hexagonal bipyramid
CU-8	7.811	7.740	7.914	7.482	*Oh*	Cube
SAPR-8	**1.125**	**1.081**	**1.060**	**1.371**	$\boldsymbol{D_{4d}}$	**Square antiprism**
TDD-8	1.973	1.878	1.909	2.019	D_{2d}	Triangular dodecahedron
JGBF-8	16.888	16.872	16.928	16.861	D_{2d}	Johnson gyrobifastigium J26
JETBPY-	28.557	28.696	28.476	28.315	D_{3h}	Johnson elongated triangular bipyramid J14
JBTPR-8	3.563	3.535	3.506	3.874	C_{2v}	Biaugmented trigonal prism J50
BTPR-8	3.020	2.952	2.930	3.259	C_{2v}	Biaugmented trigonal prism
JSD-8	5.371	5.348	5.324	5.696	D_{2d}	Snub diphenoid J84
TT-8	8.364	8.362	8.518	8.090	*Td*	Triakis tetrahedron
ETBPY-8	23.386	23.509	23.453	23.095	D_{3h}	Elongated trigonal bipyramid

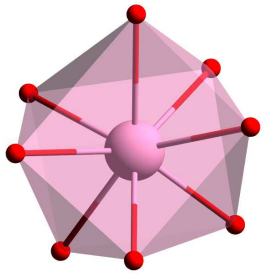

Magnetic susceptibility measurements

Figure A5.1 Magnetisation *vs*. field at 2, 4, 5 and/or 6 K for **13**−**16**.

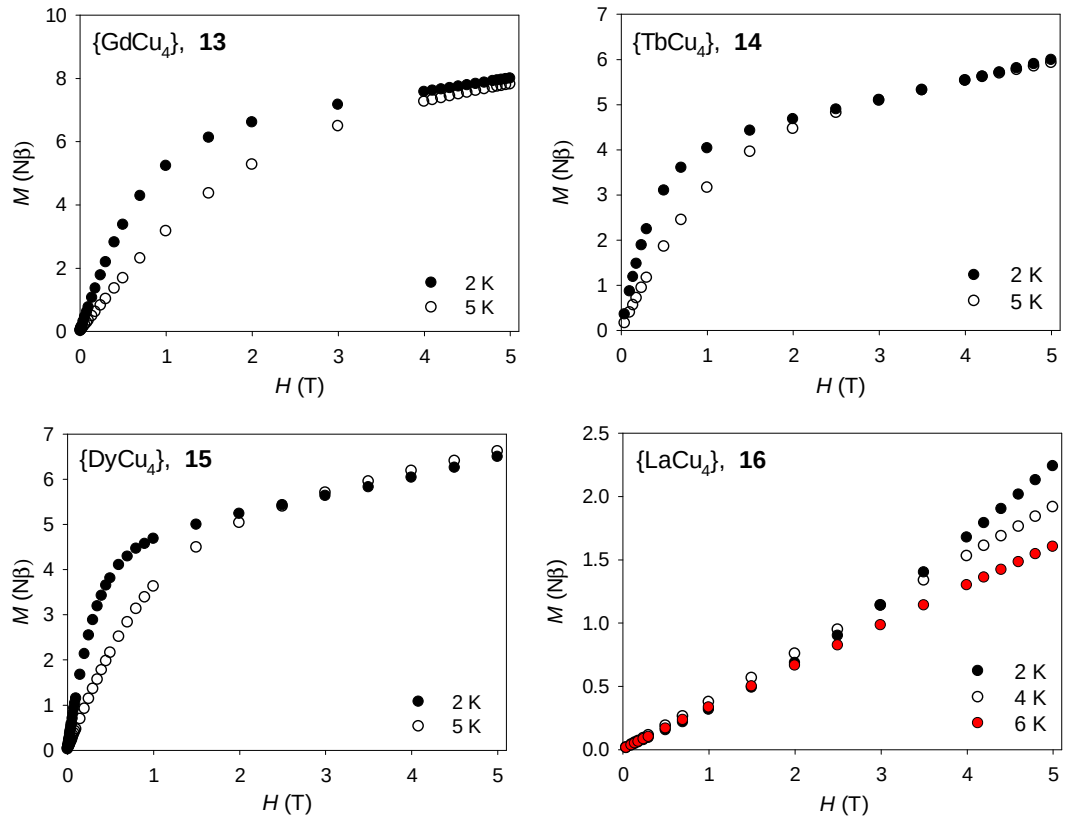

Figure A5.2 Field−sweep ac susceptibility measurements for **14** (left) and **15** (right) at T = 2 K.

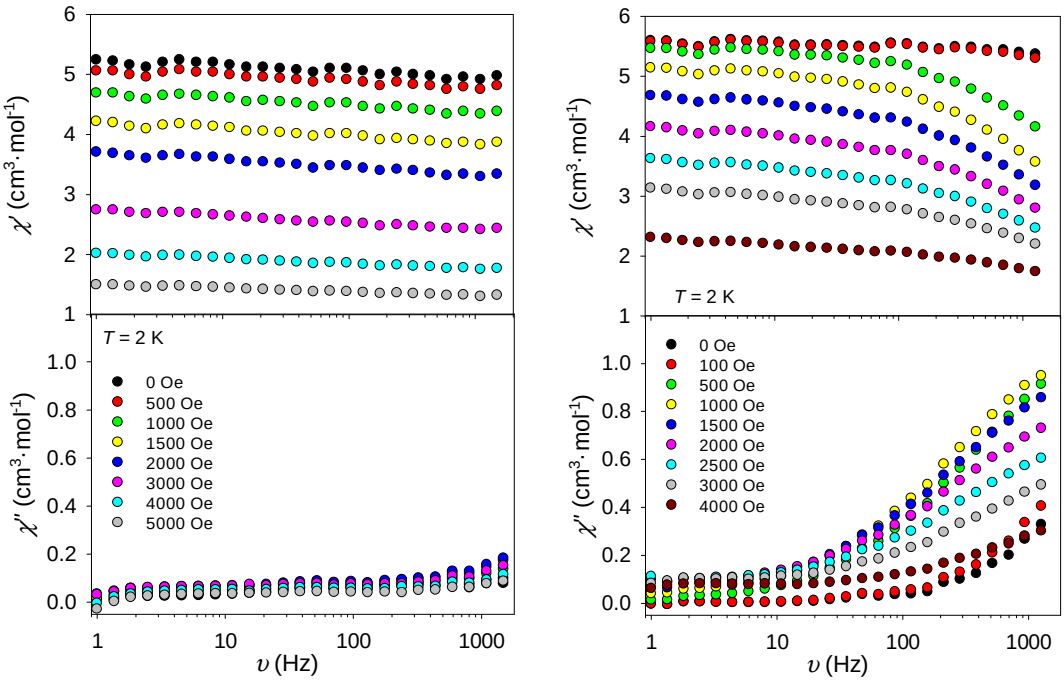

Figure A5.3 Top: Ac dynamic measurements for **15** under dc fields of 1500 Oe (left) and 2000 Oe (right) at various temperatures in the range 1.8 – 5.0 K. Bottom: fit of the experimental ac susceptibility by the Kramer's−Kronig−derivate equation of the Arrhenius law.[3]

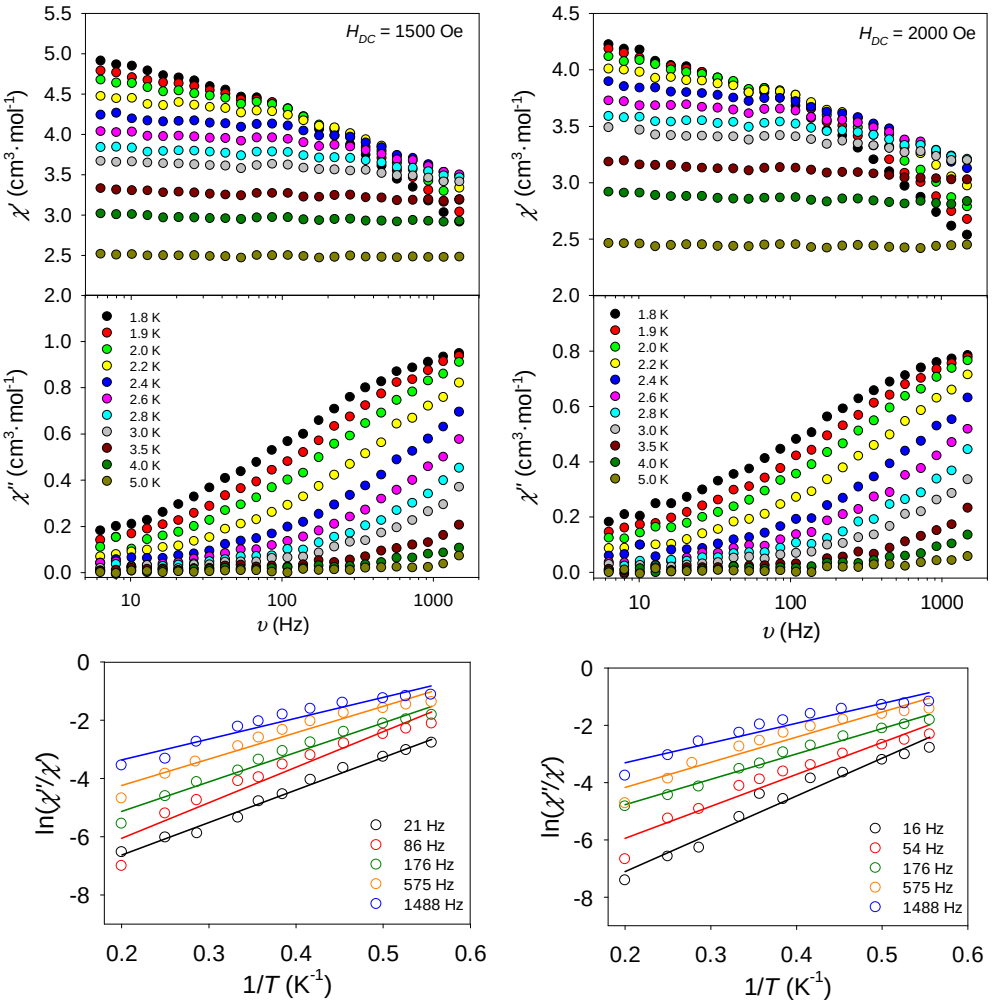

Table A5.2 Table with the relaxation rate (τ_0) and the energy barrier ($\Delta E/k_B$) parameters extracted from the fit of the ac experiments at different dc fields for **15**.

Applied H_{dc}	$\Delta E/k_B$ (K)	τ_0 (s)
1000 Oe	9.7 ± 0.2	7.2×10^{-7}
1500 Oe	9.9 ± 0.3	7.4×10^{-7}
2000 Oe	9.8 ± 0.3	8.8×10^{-7}

Computational Details

To calculate the exchange interactions,[4-6] a phenomenological Heisenberg Hamiltonian was used, excluding the terms related to magnetic anisotropy (*D* and *E* zero−field splitting parameters) to describe the exchange coupling in the polynuclear complex.

$$\hat{\mathcal{H}} = -\sum_{a<b} J_{ab} \hat{S}_a \cdot \hat{S}_b \qquad [1]$$

where $\hat{S}_a$ and $\hat{S}_b$ are the spin operators of the different magnetic centers. The J_{ab} parameters are the pairwise coupling constants between the paramagnetic centers of the molecule. In order to solve the system, we need to calculate the energy of *n + 1* spin distributions for a given system with *n* different exchange coupling constants. These energy values allowed us to build a system of *n* equations in which the *J* values are the unknowns. All calculations were performed using Gaussian09 (rev D01)[7] with the hybrid functional B3LYP,[8] using a guess function generated with the help of the fragments option, which employs a procedure that allows us to individually assign local electronic structures to atoms and/or ligands. A triple−ζ all electron Gaussian basis set was used for all the atoms, including polarization functions for the Cu centers.[9] An all electron basis set was also used for the Gd and La atoms. In order to include 2nd order scalar relativistic effects in the calculations, a Douglas−Kroll−Hess Hamiltonian (DKH) was used.[10, 11]

Figure A5.4 Intermolecular hydrogen bonding interactions (highlighted in green) in $[GdCu_4(H_4L)_4](Cl)_2(ClO_4)$ (**13**). C, grey; Cu, turquoise; Gd, pink; H, white; N, blue; O, red. Shortest intermolecular Cu···Cu distance is 7.821(1) Å.

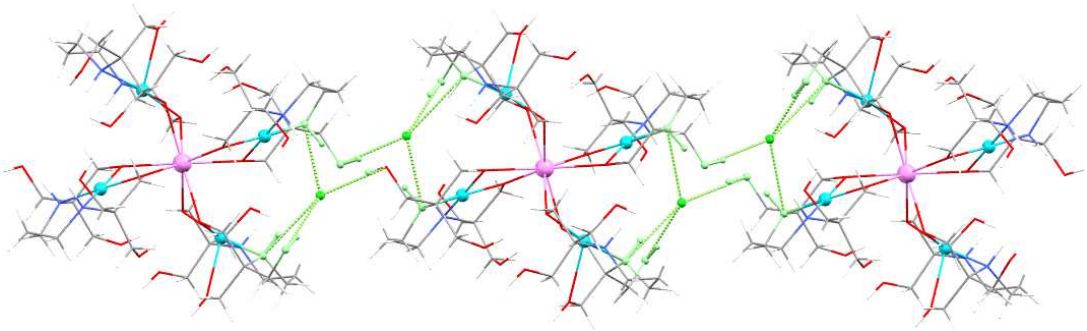

Figure A5.5 Intermolecular hydrogen bonding interactions (highlighted in orange) in $[LaCu_4(H_4L)_4](Cl)_2(ClO_4)$ (**16**). C, grey; Cu, turquoise; H, white; La, pink; N, blue; O, red. Shortest intermolecular Cu···Cu distance is 7.436(1) Å.

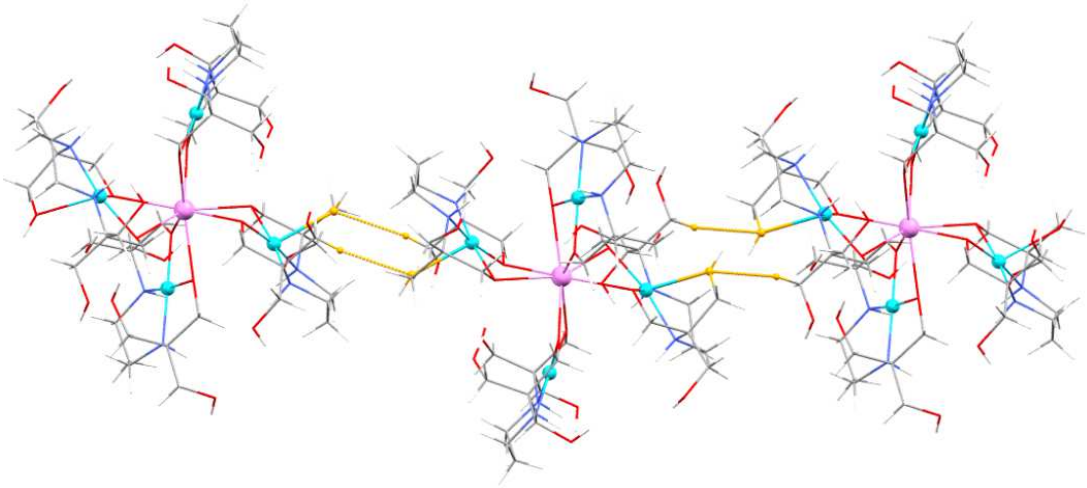

References

1. M. Pinsky and D. Avnir, *Inorg. Chem.*, **1998**, *37*, 5575.
2. D. Casanova, M. Llunell, P. Alemany and S. Alvarez, *Chem. Eur. J.*, **2005**, *11*, 1479.
3. J. Bartolomé, G. Filoti, V. Kuncser, G. Schinteie, V. Mereacre, C. E. Anson, A. K. Powell, D. Prodius and C. Turta, *Phys. Rev. B*, **2009**, *80*, 014430.
4. E. Ruiz, P. Alemany, S. Alvarez and J. Cano, *J. Am. Chem. Soc.*, **1997**, *119*, 1297.
5. E. Ruiz, J. Cano, S. Alvarez and P. Alemany, *J. Comp. Chem.*, **1999**, *20*, 1391.
6. E. Ruiz, A. Rodriguez-Fortea, J. Cano, S. Alvarez and P. Alemany, *J. Comp. Chem.*, **2003**, *24*, 982.
7. M. J. Frisch, G. W. Trucks, H. B. Schlegel, G. E. Scuseria, M. A. Robb, J. R. Cheeseman, G. Scalmani, V. Barone, B. Mennucci, G. A. Petersson, H. Nakatsuji, M. Caricato, X. Li, H. P. Hratchian, A. F. Izmaylov, J. Bloino, G. Zheng, J. L. Sonnenberg, M. Hada, M. Ehara, K. Toyota, R. Fukuda, J. Hasegawa, M. Ishida, T. Nakajima, Y. Honda, O. Kitao, H. Nakai, T. Vreven, J. A. Montgomery Jr., J. E. Peralta, F. Ogliaro, M. J. Bearpark, J. Heyd, E. N. Brothers, K. N. Kudin, V. N. Staroverov, R. Kobayashi, J. Normand, K. Raghavachari, A. P. Rendell, J. C. Burant, S. S. Iyengar, J. Tomasi, M. Cossi, N. Rega, N. J. Millam, M. Klene, J. E. Knox, J. B. Cross, V. Bakken, C. Adamo, J. Jaramillo, R. Gomperts, R. E. Stratmann, O. Yazyev, A. J. Austin, R. Cammi, C. Pomelli, J. W. Ochterski, R. L. Martin, K. Morokuma, V. G. Zakrzewski, G. A. Voth, P. Salvador, J. J. Dannenberg, S. Dapprich, A. D. Daniels, Ö. Farkas, J. B. Foresman, J. V. Ortiz, J. Cioslowski and D. J. Fox, Gaussian, Inc., Wallingford, CT, USA, **2009**.
8. A. D. Becke, *J. Chem. Phys.*, **1993**, *98*, 5648.
9. A. Schafer, C. Huber and R. Ahlrichs, *J. Chem. Phys.*, **1994**, *100*, 5829.
10. M. Douglas and N. M. Kroll, *Ann. Phys.*, **1974**, *82*, 89.
11. B. A. Hess, *Phys. Rev. A*, **1985**, *32*, 756.

6. Towards the synthesis of pseudo−single−ion magnets

Single crystal X−ray data collection and refinement details

$[Co_3Tb(H_2L)_2(H_3L)](ClO_4)\cdot 5.5H_2O$ (**17**): The structure contains significant solvent accessible voids containing water. This was accounted for using SQUEEZE (in PLATON),[1, 2] which calculated as 2 voids of 109 e^- each per unit cell corresponding to approximately 5.5 molecules of H_2O per complex, giving consideration to the elemental analysis results. The perchlorate anion is modelled over 3 partially occupied sites, two of which are overlapped, with one site of 0.25 occupancy and a second of 0.75 modelled as 0.50 and 0.25 overlapped anions. Distance and angle restraints were applied, and the oxygen and one of the 0.25 occupied Cl^- were refined with isotropic *adps*. From charge considerations one of the coordinated oxygen atoms needs to be protonated. O304 and O204 are the most likely candidates, and O304 was selected as it has a longer Co−O bond length. Hydrogen atoms refined as part of a rigid rotating OH−group: H106, H111, H206, H211, H306, H311.

$[Co_3Dy(H_2L)_2(H_3L)](ClO_4)\cdot 5.5CH_3OH\cdot 1.5H_2O$ (**18**): Lattice solvent was modelled as an overlapping 0.5 H_2O and 0.5 CH_3OH with the oxygen common to both. The *adps* were modelled as isotropic, hydrogen atoms were not included in the model but are included in the formula. Remaining solvent was accounted for using SQUEEZE (in PLATON),[1, 2] which calculated as 2 voids of 202 e^- each per unit cell corresponding to approximately 5 molecules of CH_3OH and one of H_2O per complex, giving consideration to the elemental analysis results. One $-CH_2OH$ arm from the ligand was modelled over two partially occupied sites with competitively refined occupancies of 0.7(2):0.3(2) and suitable distance restraints applied. Two central $-CH_2$ groups of the ligands also showed disorder, and were refined over 2 sites. In one case the occupancies refined to 0.5 and were then fixed at this. For the other the occupancies refined to approximately 0.6:0.4. For both of these groups the partially occupied atoms were refined with anisotropic *adps*. Hydrogen atoms refined as part of a rigid rotating OH−group: H211, H206, H111, H306, H311, H106, H6B.

$[Co_3Ho(H_2L)_2(H_3L)](ClO_4)\cdot 4.5CH_3OH\cdot 5.5H_2O$ (**19**): Several parts of the structure show disorder. Two central $-CH_2$ groups of two ligands showed disorder and were refined over 2 sites. In one case the occupancies refined to approximately 0.75:0.25, for the other the occupancies refined to approximately 0.60:0.40. The

third ligand shows more disorder with a significant part of it modelled over two partial positions, refined to approximately 0.70:0.30. All the partially occupied atoms from the three ligands were refined with anisotropic *adps*, and suitable distance restraints applied. The structure contains significant solvent accessible voids containing water. This was accounted for using SQUEEZE (in PLATON),[1, 2] which calculated as 2 voids of 273 e^- each per unit cell corresponding to approximately 5.5 molecules of H_2O and 4.5 molecules of CH_3OH per complex, giving consideration to the elemental analysis results. Hydrogen atoms refined as part of a rigid rotating OH−group: H111, H206, H211, H306, H311.

$[Co_3Er(H_2L)_2(H_3L)](ClO_4)\cdot 0.75CH_3OH\cdot 5H_2O$ (**20**): Several parts of the structure show disorder. The central $-CH_2$ groups of two ligands are disordered and modelled over two partially occupied sites. The third ligand shows more disorder with a significant part of it modelled over two partial positions. Suitable distance restraints were applied. A region containing poorly defined solvent was accounted for using SQUEEZE (in PLATON),[1, 2] which calculated 2 voids of 211 e^- per unit cell corresponding to 5 H_2O per complex, giving consideration to the elemental analysis results. Hydrogen atoms refined as part of a rigid rotating group: CH_3OH molecule – H2SA, H2SB, H2SC; OH groups – H106, H111, H206, H306, H311.

$[Co_3Yb(H_2L)_2(H_3L)](ClO_4)\cdot 4CH_3OH\cdot 5H_2O\cdot 5(CH_3CH_2)_2O$ (**21**): The same disorder model to that applied for **20** was used. A region containing poorly defined solvent was accounted for using SQUEEZE (in PLATON),[1, 2] which calculated 2 voids of 493 e^- each per unit cell. This could correspond to 5 molecules of H_2O, 4 molecules of CH_3OH and 3 molecules of Et_2O giving consideration to the elemental analysis results. Hydrogen atoms refined as part of a rigid rotating OH−group: H106, H111, H206, H211, H216, H311.

Table A6.1 Shape measures for the Ln ions relative to the ideal 8-vertex polyhedra for **17** - **21**. The lowest CShMs value, and thus the closest geometry is highlighted in pink.[3, 4]

	17, Tb	**18**, Dy	**19**, Ho	**20**, Er	**21**, Yb	**Symmetry**	**Ideal shape**
OP-8	26.501	26.651	26.937	26.820	27.031	D_{8h}	Octagon
HPY-8	20.850	20.502	21.247	20.253	20.582	C_{7v}	Heptagonal pyramid
HBPY-8	16.785	17.117	16.924	16.956	17.039	D_{6h}	Hexagonal bipyramid
CU-8	11.994	11.680	11.411	11.418	11.363	*Oh*	Cube
SAPR-8	**1.096**	**1.015**	**1.054**	**0.919**	**0.888**	$\boldsymbol{D_{4d}}$	**Square antiprism**
TDD-8	3.003	3.125	2.874	3.079	2.996	D_{2d}	Triangular dodecahedron
JGBF-8	15.989	16.786	15.688	16.639	16.680	D_{2d}	Johnson gyrobifastigium J26
JETBPY-8	25.026	26.158	25.375	26.136	26.090	D_{3h}	Johnson elongated triangular bipyramid J14
JBTPR-8	3.121	3.319	2.889	3.322	3.256	C_{2v}	Biaugmented trigonal prism J50
BTPR-8	2.554	2.752	2.244	2.670	2.647	C_{2v}	Biaugmented trigonal prism
JSD-8	5.318	5.515	5.196	5.417	5.368	D_{2d}	Snub diphenoid J84
TT-8	12.574	12.422	12.152	12.200	12.121	*Td*	Triakis tetrahedron
ETBPY-8	21.672	22.762	21.906	22.714	22.714	D_{3h}	Elongated trigonal bipyramid

Table A6.2 Ln−O bond lengths displayed by the {LnO_8} square antiprism polyhedra for **17** – **21**.

17	**18**	**19**	**20**	**21**
Tb−O bond length (Å)	Dy−O bond length (Å)	Ho−O bond length (Å)	Er−O bond length (Å)	Yb−O bond length (Å)
2.331(6)	2.382(7)	2.243(5)	2.304(4)	2.410(6)
2.280(7)	2.311(9)	2.309(4)	2.233(4)	2.364(4)
2.472(7)	2.481(9)	2.369(3)	2.361(3)	2.235(4)
2.417(6)	2.240(1)	2.466(3)	2.448(4)	2.274(4)
2.327(7)	2.440(1)	2.426(5)	2.297(3)	2.211(6)
2.375(5)	2.396(8)	2.400(3)	2.412(5)	2.280(4)
2.519(7)	2.328(8)	2.268(4)	2.385(4)	2.349(4)
2.263(8)	2.261(9)	2.310(3)	2.255(4)	2.443(4)

Table A6.3 Structural parameters related to the symmetry described by the {LnO_8} units for **17** – **21**: Φ is the angle between the diagonals of the squares; α is the angle between the S_8 axis and a Ln–O bond direction; d_{in} is the shortest intraplanar O–O distance in a {O_4} square; d_{pp} is the shortest interplanar distance between oxygen donor atoms of different {O_4} squares.

	Avg Φ (°)	Avg α (°)	d_{in} (Å)	d_{pp} (Å)
20 (Tb)	45.03	59.21	2.552(9)	2.660(1)
21 (Dy)	45.01	59.18	2.550(1)	2.620(1)
22 (Ho)	45.00	59.02	2.540(6)	2.652(5)
23 (Er)	45.01	59.08	2.544(6)	2.645(6)
24 (Yb)	45.01	58.94	2.533(6)	2.619(6)

Magnetic susceptibility measurements

Table A6.4 Crystal field parameter sets (CFPs), and related energy levels resulting from the fit of the dc susceptibility data for **18** (Dy).[5]

CFPs A	CFPs B	CFPs C	CFPs D	CFPs E	CFPs F	CFPs G	CFPs H
B_0^2, B_0^4, B_4^4							
236.8, 236.8, 2437.2	236.8, 236.8, -2437.2	289.5, 184.2, 2487.4	289.5, 184.2, -2487.4	394.7, 131.6, 2788.9	394.7, 131.6, -2788.9	79.0, 394.7, 2135.7	79.0, 394.7, -2135.7
Energy levels (cm^{-1})							
0	0	0	0	0	0	0	0
73	73	73	73	78	78	65	65
92	92	98	98	115	115	77	77
361	361	316	316	286	286	479	479
548	548	502	502	494	494	648	648
559	559	520	520	523	523	660	660
785	785	792	792	890	890	816	816
811	811	811	811	901	901	834	834

Fig A6.1 Isothermal field sweep ac susceptibility experiments as a function of frequency for **17**.

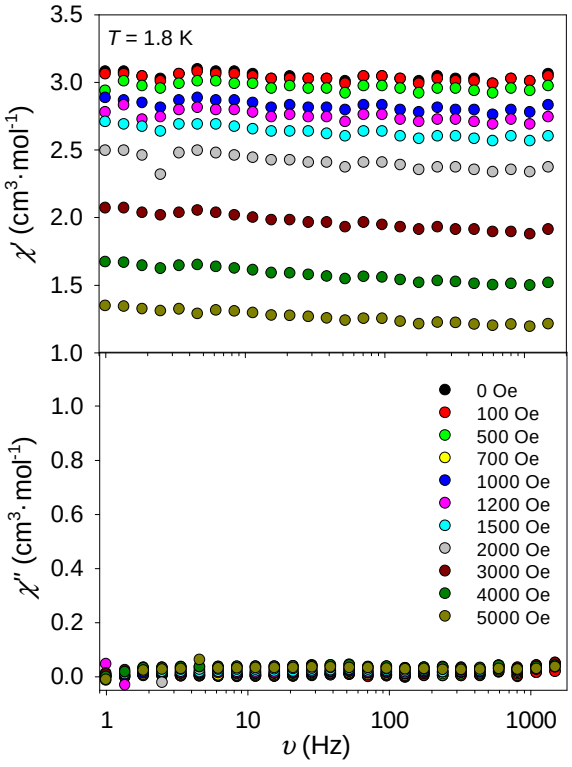

Fig A6.2 Estimation of the τ_0 and $\Delta E/k_B$ parameters from the ac magnetic experiments performed on **18** (Dy). The model applied to the higher temperature range data, considering solely the Orbach contribution, is shown below.

$$\tau^{-1} = \tau_0^{-1} \cdot \exp(-\Delta E/k_B T)$$

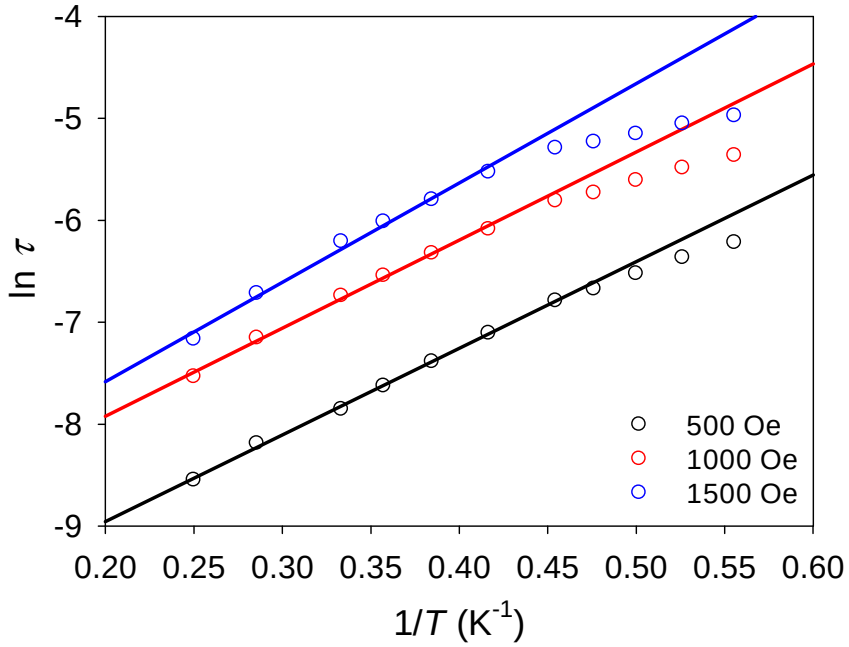

Summary of resulting τ_0, $\Delta E/k_B$ values

		H_{dc} = 500 Oe	H_{dc} = 1000 Oe	H_{dc} = 1500 Oe
$T \geq 2.4$ K	$\Delta E/k_B$	8.5 ± 0.2 K	8.6 ± 0.3 K	9.7 ± 0.5 K
	τ_0	$2.4 \cdot 10^{-5}$ s	$6.4 \cdot 10^{-5}$ s	$7.3 \cdot 10^{-5}$ s

Fig A6.3 Estimation of τ_0, $\Delta E/k_B$, *A* and *m* parameters from the ac magnetic experiments performed on **18** (Dy). The model includes Orbach and direct contributions (see equation below).

$$\tau^{-1} = AH^m T + \tau_0^{-1} \cdot \exp(-\Delta E/k_B T)$$

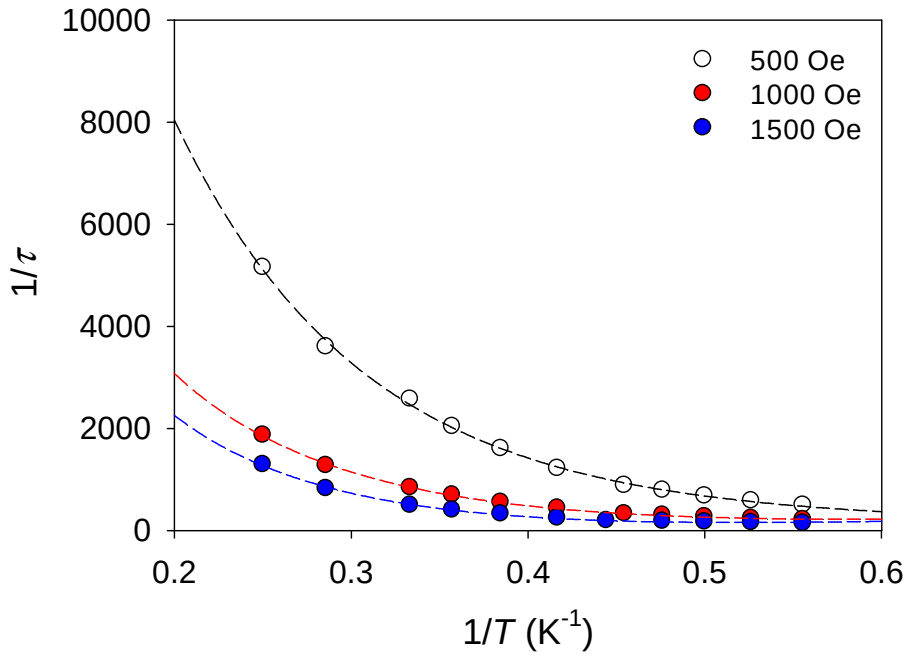

Summary of resulting τ_0, $\Delta E/k_B$, A, m values

	H_{dc} = 500 Oe	H_{dc} = 1000 Oe	H_{dc} = 1500 Oe
A	$8.7\cdot10^{-5}$ $s^{-1}\cdot K^{-1}$ $Oe^{-2.3}$	$2.0\cdot10^{-5}$ $s^{-1}\cdot K^{-1}$ $Oe^{-2.6}$	$4.1\cdot10^{-5}$ $s^{-1}\cdot K^{-1}$ $Oe^{-1.7}$
*m**	2.3	2.6	1.7
τ_0	$2.0\cdot10^{-5}$ s^{-1}	$-1.3\cdot10^{-4}$ s^{-1}	$-1.3\cdot10^{-4}$ s^{-1}
$\Delta E/k_B$	9.5 K	1.8 K	2.0 K

*Note *m* should be 4 for a Kramer's ion (except in the presence of hyperfine interactions, when *m* = 2).[6]

Fig A6.4 Natural logarithm of χ'/χ'' $vs.\, 1/T$ for **20**.

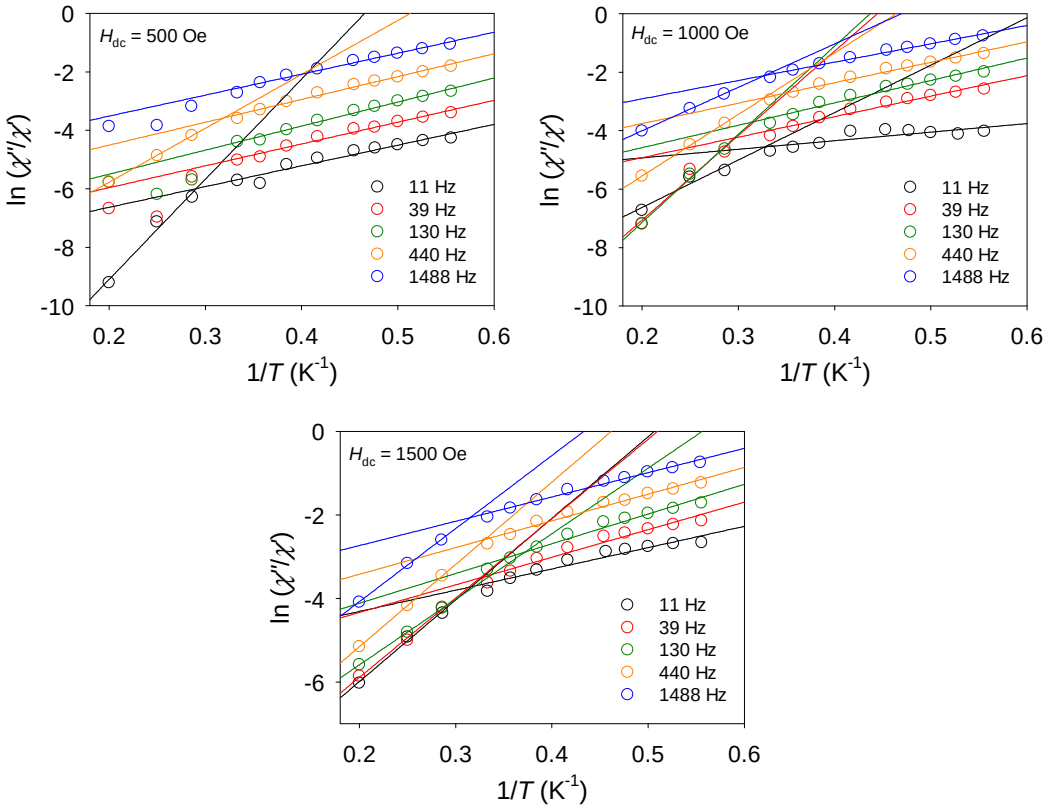

The fit of the data was performed considering two different temperature regions. The extracted τ_0, $\Delta E/k_B$ parameters are shown in Table A6.5.

Table A6.5 Estimated energy barrier ($\Delta E/k_B$) and pre−exponential factor (τ_0) parameters for **20** (Er) calculated by the Kramer's−Kronig−derivate equation of the Arrhenius law[7] at different frequencies (11−1488 Hz), temperature ranges (T ≥ 3.5 K and T ≤ 3.0 K), and fields (500, 1000, 1500 Oe). The average values for each dc field and temperature region are highlighted in grey.

		T ≥ 3.5 K		T ≤ 3.0 K	
H_{dc}	υ	$\Delta E/k_B$	τ_0	$\Delta E/k_B$	τ_0
500 Oe	11 Hz	34.3 ± 5.2 K	$1.6\cdot10^{-9}$ s	7.1 ± 0.7 K	$4.4\cdot10^{-6}$ s
	39 Hz	-	-	7.5 ± 0.4 K	$2.4\cdot10^{-6}$ s
	130 Hz	-	-	8.2 ± 0.3 K	$9.6\cdot10^{-7}$ s
	440 Hz	18.4 ± 0.4 K	$2.8\cdot10^{-8}$ s	7.8 ± 0.4 K	$8.4\cdot10^{-7}$ s
	1488 Hz	-	-	7.2 ± 0.4 K	$7.6\cdot10^{-7}$ s
Avg		**26.4 ± 3.7 K**	**$1.5\cdot10^{-8}$ s**	**7.6 ± 0.5 K**	**$1.9\cdot10^{-6}$ s**

		$T \geq 3.5$ K		$T \leq 3.0$ K	
H_{dc}	υ	$\Delta E/k_B$	τ_0	$\Delta E/k_B$	τ_0
1000 Oe	11 Hz	16.2 ± 4.7 K	$7.2 \cdot 10^{-7}$ s	2.9 ± 0.8 K	$5.6 \cdot 10^{-5}$ s
	39 Hz	28.9 ± 5.8 K	$1.1 \cdot 10^{-8}$ s	7.0 ± 0.6 K	$7.4 \cdot 10^{-6}$ s
	130 Hz	30.2 ± 2.9 K	$2.3 \cdot 10^{-9}$ s	7.7 ± 0.6 K	$2.7 \cdot 10^{-6}$ s
	440 Hz	21.0 ± 0.4 K	$2.1 \cdot 10^{-8}$ s	7.0 ± 0.4 K	$2.1 \cdot 10^{-6}$ s
	1488 Hz	14.9 ± 0.3 K	$1.0 \cdot 10^{-7}$ s	6.3 ± 0.3 K	$1.7 \cdot 10^{-6}$ s
Avg		**22.2 ± 3.6 K**	**$1.7 \cdot 10^{-7}$ s**	**6.2 ± 0.6 K**	**$1.4 \cdot 10^{-5}$ s**
1500 Oe	11 Hz	19.5 ± 1.8 K	$7.0 \cdot 10^{-7}$ s	5.1 ± 0.6 K	$6.8 \cdot 10^{-5}$ s
	39 Hz	19.0 ± 1.3 K	$2.6 \cdot 10^{-7}$ s	6.6 ± 0.6 K	$1.4 \cdot 10^{-5}$ s
	130 Hz	15.7 ± 0.1 K	$2.0 \cdot 10^{-7}$ s	7.1 ± 0.5 K	$4.8 \cdot 10^{-6}$ s
	440 Hz	19.7 ± 0.1 K	$4.1 \cdot 10^{-8}$ s	6.4 ± 0.4 K	$3.2 \cdot 10^{-6}$ s
	1488 Hz	17.5 ± 0.8 K	$5.5 \cdot 10^{-8}$ s	5.8 ± 0.3 K	$2.2 \cdot 10^{-6}$ s
Avg		**18.3 ± 1.1 K**	**$2.5 \cdot 10^{-7}$ s**	**6.2 ± 0.5 K**	**$1.8 \cdot 10^{-5}$ s**

References

1. P. van der Sluis and A. L. Spek, *Acta Crystallog. Sect. A*, **1990**, *46*, 194.
2. A. Spek, *J. Appl. Cryst.*, **2003**, *36*, 7.
3. M. Pinsky and D. Avnir, *Inorg. Chem.*, **1998**, 37, 5575.
4. D. Casanova, M. Llunell, P. Alemany and S. Alvarez, *Chem. Eur. J.*, **2005**, *11*, 1479.
5. N. F. Chilton, R. P. Anderson, L. D. Turner, A. Soncini and K. S. Murray, *J. Comput. Chem.*, **2013**, *34*, 1164.
6. S. T. Liddle and J. van Slageren, *Chem. Soc. Rev.*, **2015**, *44*, 6655.
7. J. Bartolomé, G. Filoti, V. Kuncser, G. Schinteie, V. Mereacre, C. E. Anson, A. K. Powell, D. Prodius and C. Turta, *Phys. Rev. B*, **2009**, *80*, 014430.

7. A topologically unique alternating {$Co^{III}_3Gd^{III}_3$} magnetocaloric ring

Single crystal X−ray data collection and refinement details

The central carbon atom of one of the H_2L^{4-} ligand units (C201) was modelled over 2 half occupied positions related by a 2−fold rotation and together with one of the terminal carbon sites of the $acac^-$ group (C5A) it was refined with an isotropic *adps*. Hydrogen atoms were placed in geometrically calculated positions and refined as part of a riding model except OH^-, H_2O, CH_3COO^- and $acac^-$ (H1AA, H1AB, H1AC, H5AA, H5AB, H5AC) hydrogens which were refined as part of a rigid rotating group.

Fig A7.1 Structure of $[Co^{III}_4Co^{II}_4(H_2L)_2(H_3L)_2(CH_3COO)_4](CH_3COO)$. C, grey; Co^{II}, purple; Co^{III}, fuchsia; N, blue; O, red; Hydrogen atoms and crystallisation molecules are omitted for clarity. The crystals grew by vapour diffusion of Et_2O into a concentrated methanolic solution of the precipitate. Data collected in NCS facilities.

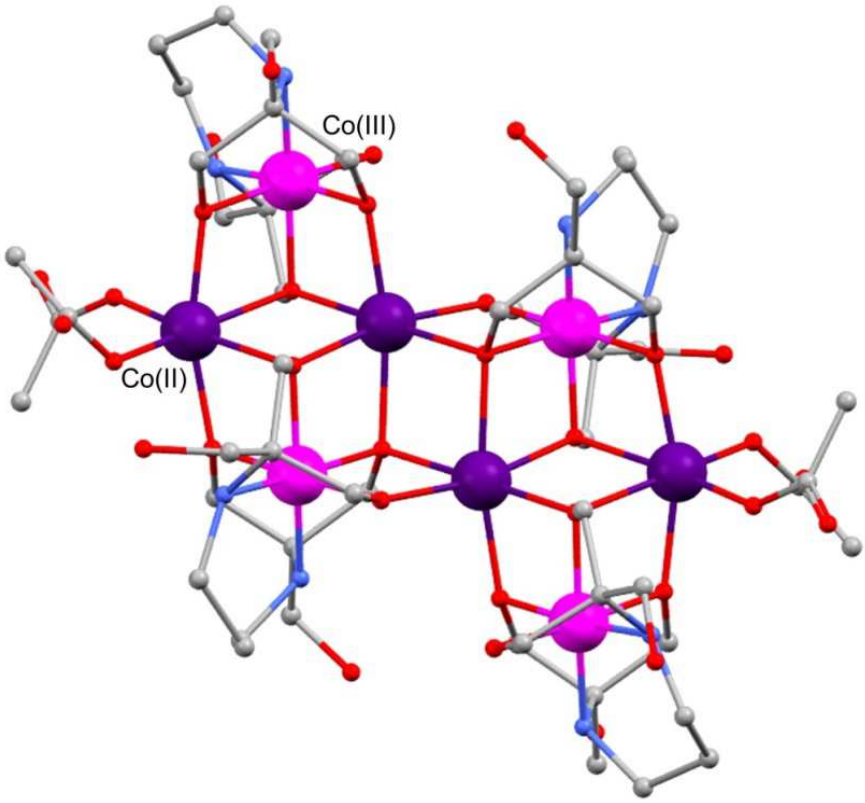

Table A7.1 Shape measures of **23**, $\{Co^{III}_3Gd^{III}_3\}$ relative to ideal 8-vertex polyhedra. The lowest CShMs value, and thus most coincident geometry is highlighted in pink.[1, 2]

	Gd1	Gd2	Symmetry	Ideal shape
OP-8	36.266	29.523	D_{8h}	Octagon
HPY-8	23.975	23.435	C_{7v}	Heptagonal pyramid
HBPY-8	14.977	16.887	D_{6h}	Hexagonal bipyramid
CU-8	11.482	11.757	Oh	Cube
SAPR-8	4.715	2.558	D_{4d}	Square antiprism
TDD-8	**2.895**	**0.990**	$\boldsymbol{D_{2d}}$	**Triangular dodecahedron**
JGBF-8	12.597	13.317	D_{2d}	Johnson gyrobifastigium J26
JETBPY-8	28.056	27.988	D_{3h}	Johnson elongated triangular bipyramid J14
JBTPR-8	5.123	2.250	C_{2v}	Biaugmented trigonal prism J50
BTPR-8	4.423	1.689	C_{2v}	Biaugmented trigonal prism
JSD-8	4.968	2.788	D_{2d}	Snub diphenoid J84
TT-8	12.302	12.569	Td	Triakis tetrahedron
ETBPY-8	23.595	24.091	D_{3h}	Elongated trigonal bipyramid

Magnetic measurements

Fig A7.2 Temperature dependence of $\chi_M T$ for **22** in an applied field of 1000 Oe.

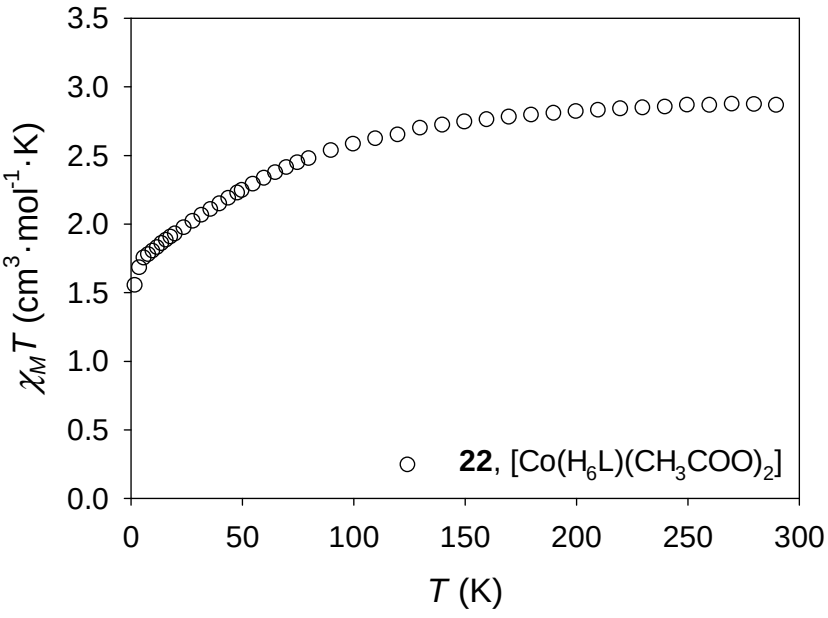

Fig A7.3 Intermolecular hydrogen bonding interactions (dashed black lines) in complex **23**. C, grey; Co, fuchsia; Gd, green; H, white; N, blue; O, red All the interactions involve $CH_3COO^{-}\cdots(HO)R$ hydrogen bonds. The average intermolecular Gd···Gd distance is 10.200(1) Å.

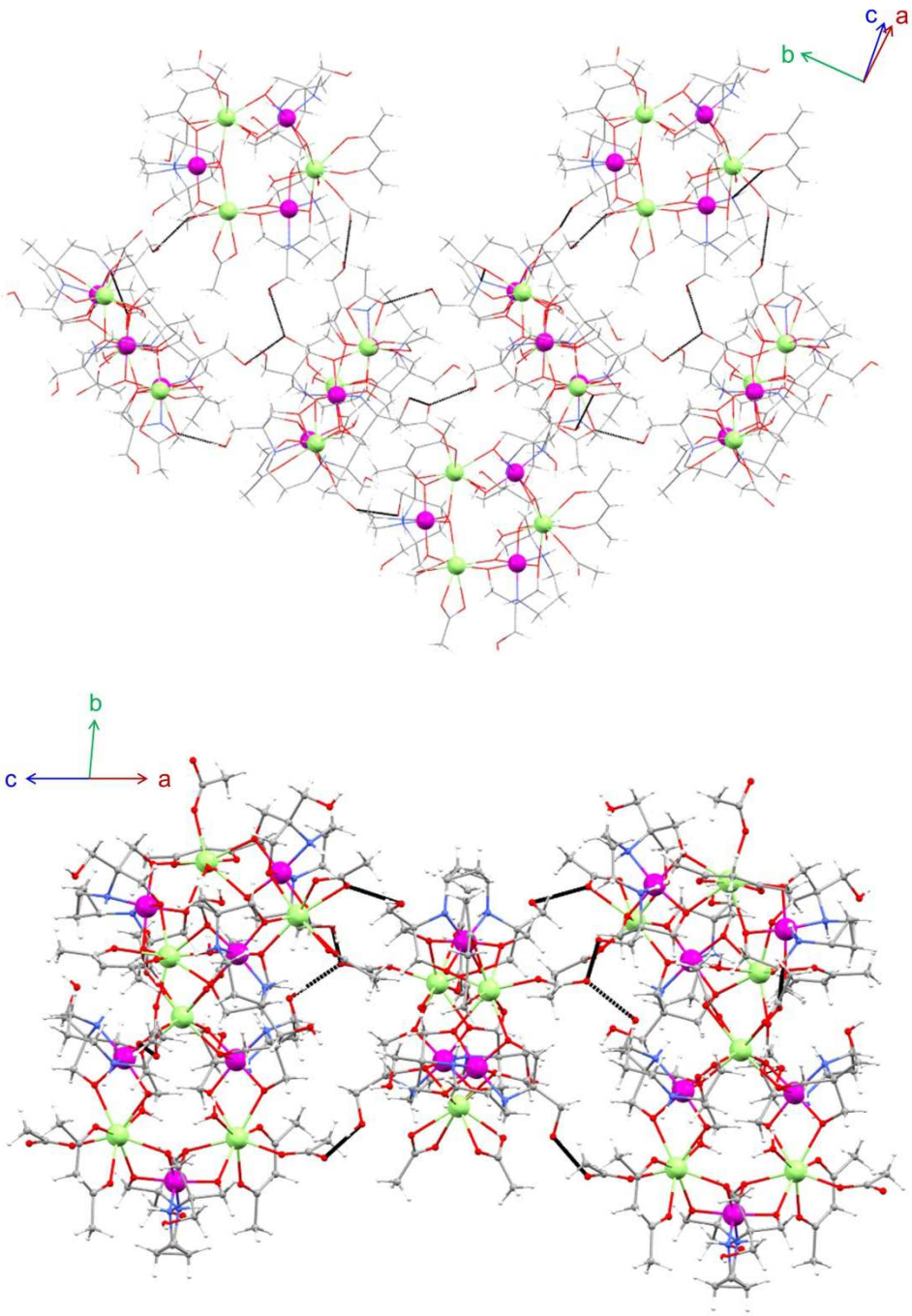

References

1. M. Pinsky and D. Avnir, *Inorg. Chem.*, **1998**, *37*, 5575.
2. D. Casanova, M. Llunell, P. Alemany and S. Alvarez, *Chem. Eur. J.*, **2005**, *11*, 1479.

8. Effect of ligand modification on the SMM properties in {$Ln_2Ni_2(L2)_2$} Schiff base derivatives

Single crystal X−ray data collection and refinement details

Hydrogen atoms were placed in geometrically calculated positions and refined as part of a riding model, except those ones indicated below. In all the complexes (except for **25**) one of the acetonitrile molecules is modelled over two partially occupied sites, refined to approximately 0.50:0.50.

$[Gd_2Ni_2(L2)_2(CH_3COO)_6(H_2O)_2]\cdot 2CH_3CN\cdot 2H_2O$ (**24**): Hydrogen atoms for water molecules (O1W, O2W, O8S), some acetate groups (C4AC, C8AC, C12A, C16A, C20A, C24A), and the carbon atoms of the methoxide groups (C112, C125, C212, C225) were refined as part of a rigid rotating group.

$[Tb_2Ni_2(L2)_2(CH_3COO)_6(H_2O)_2]\cdot 4CH_3CN\cdot 5H_2O$ (**25**): The data was collected from a twinned crystal and was integrated as a 2−component twin, using 2−orientation matrices related by a 180° rotation about [0 0 1]. The twin component factor was refined to 0.6822(6) and 0.3178(6). One acetonitrile molecule was refined with an isotropic *adps*. Hydrogen atoms for water molecules (O1WS, O2WS, O3WS, O4WS, O5WS, O1W, O2W), acetonitrile molecules (C12S, C3S, C9S, C6S) some acetate groups (C4A, C4B, C8A, C8B, C12A, C16A), and the carbon atoms of the methoxide groups (C110, C122, C210, C222) were refined as part of a rigid rotating group.

$[Dy_2Ni_2(L2)_2(CH_3COO)_6(H_2O)_2]\cdot 4CH_3CN\cdot 5H_2O$ (**26**): The data was collected from a twinned crystal and was integrated as a 2−component twin, using 2−orientation matrices related by a 180° rotation about [−1 1 −1]. The twin component factor was refined to 0.5718(6) and 0.4282(6). Hydrogen atoms for water molecules (O1W, O2W, O13S, O15S, O17S), acetonitrile molecules (C9S, C3S, C6S) some acetate groups (C14A, C18A, C22A, C24A, C28A, C32A), and the carbon atoms of the methoxide groups (C110, C125, C210, C225) were refined as part of a rigid rotating group.

$[Ho_2Ni_2(L2)_2(CH_3COO)_6(H_2O)_2]\cdot 2CH_3CN\cdot 2H_2O$ (**27**): Hydrogen atoms for water molecules (O1W, O2W, O1S, O2S), acetonitrile molecules (C5S) some acetate groups (C1, C2, C5, C6, C112, C113), and the carbon atoms of the methoxide groups (C125, C210, C212, C226) were refined as part of a rigid rotating group.

$[Y_2Ni_2(L2)_2(CH_3COO)_6(H_2O)_2]\cdot 2CH_3CN\cdot 2H_2O$ (**28**): One of the acetonitrile molecules is modelled over two partially occupied sites, refined to approximately 0.50:0.50. Hydrogen atoms for water molecules (O8S, O1W, O2W), acetonitrile molecules (C6S) some acetate groups (C12A, C16A, C20A, C24A, C4AC, C8AC), and the carbon atoms of the methoxide groups (C112, C125, C212, C225) were refined as part of a rigid rotating group.

Fig A8.1 Structure of a monomeric Ni(II) complex. The new Schiff base units were obtained as a result of the decomposition of the ligand H_2L2 by hydrolysis of the C=N bonds.

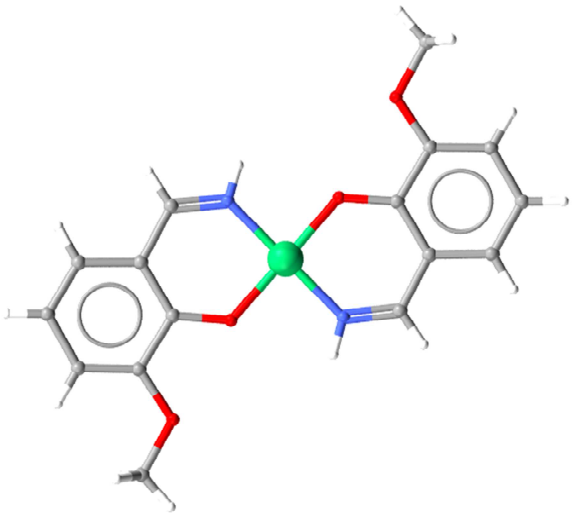

Table A8.1 Shape measures for the Ln ions relative to the ideal 9−vertex polyhedra for **24** − **26**. The lowest CShMs value, and thus the closest geometry for the Ln centre is highlighted in pink. The subsequent CShMs value close to the lowest one is also highlighted in grey.[1-3]

	24, Gd1	**24**, Gd2	**25**, Tb1	**25**, Tb2	**26**, Dy1	**Symmetry**	**Ideal shape**
EP-9	34.616	34.689	35.915	34.918	36.100	D_{9h}	Enneagon
OPY-9	23.481	23.411	22.211	23.227	22.280	C_{8v}	Octagonal pyramid
HBPY-9	16.193	16.144	16.252	16.078	16.297	D_{7h}	Heptagonal bipyramid
JTC-9	14.722	14.410	15.785	15.400	15.723	C_{3v}	Johnson triangular cupola J3
JCCU-9	8.356	8.767	8.663	8.239	8.726	C_{4v}	Capped cube J8
CCU-9	6.969	7.319	7.192	6.707	7.255	C_{4v}	Spherical-relaxed capped cube
JCSAPR-9	3.136	3.392	2.739	3.018	2.693	C_{4v}	Capped square antiprism J10
CSAPR-9	**2.039**	**2.252**	**1.621**	**1.870**	**1.569**	$\boldsymbol{C_{4v}}$	**Spherical capped square antiprism**
JTCTPR-9	3.598	3.493	4.360	3.667	4.241	D_{3h}	Tricapped trigonal prism J51
TCTPR-9	2.568	2.391	2.431	2.445	2.335	D_{3h}	Spherical tricapped trigonal prism
JTDIC-9	11.688	11.822	10.316	10.908	10.379	C_{3v}	Tridiminished icosahedron J63
HH-9	8.549	8.425	9.931	8.675	10.089	C_{2v}	Hula-hoop
MFF-9	2.087	2.316	1.954	2.213	1.882	C_s	Muffin

Table A8.2 Shape measures for the Ln ions relative to the ideal 9−vertex polyhedra for **26** − **28**. The lowest CShMs value, and thus the closest geometry for the Ln centre is highlighted in pink. The subsequent CShMs value close to the lowest one is also highlighted in grey.[1-3]

	26, Dy2	**27**, Ho1	**27**, Ho2	**28**, Y1	**28**, Y2	**Symmetry**	**Ideal shape**
EP-9	35.087	34.584	34.770	34.553	34.721	D_{9h}	Enneagon
OPY-9	23.137	23.525	23.450	23.484	23.486	C_{8v}	Octagonal pyramid
HBPY-9	16.171	16.468	16.313	16.544	16.316	D_{7h}	Heptagonal bipyramid
JTC-9	15.484	14.660	14.585	14.652	14.553	C_{3v}	Johnson triangular cupola J3
JCCU-9	8.327	8.527	8.839	8.556	8.813	C_{4v}	Capped cube J8
CCU-9	6.817	7.119	7.388	7.154	7.373	C_{4v}	Spherical-relaxed capped cube
JCSAPR-9	2.881	2.986	3.157	2.995	3.169	C_{4v}	Capped square antiprism J10
CSAPR-9	**1.742**	**1.860**	**2.008**	**1.872**	**2.030**	$\mathbf{C_{4v}}$	**Spherical capped square antiprism**
JTCTPR-9	3.654	3.280	3.246	3.263	3.231	D_{3h}	Tricapped trigonal prism J51
TCTPR-9	2.412	2.341	2.199	2.330	2.215	D_{3h}	Spherical tricapped trigonal prism
JTDIC-9	10.932	11.919	11.939	11.988	11.942	C_{3v}	Tridiminished icosahedron J63
HH-9	8.897	8.793	8.674	8.835	8.681	C_{2v}	Hula-hoop
MFF-9	2.080	1.921	2.084	1.935	2.113	C_s	Muffin

Table A8.3 Bond lengths for Ni−O and Ni−N in **24** − **28**. Ni−O_{ax} refers to the heteroatoms occupying the axial positions of the {$NiN_2O_2O_2$'} octahedron; whereas Ni−O_{eq} and Ni−N are those in the equatorial plane.

Complex	Atom	$d_{(Ni-Oax)}$/Å	$d_{(Ni-Oeq)}$/Å	$d_{(Ni-N)}$/Å
24	Ni1	2.087(3)	2.053(3)	2.141(5)
		2.033(3)	2.024(4)	2.112(5)
	Ni2	2.134(3)	2.042(4)	2.122(4)
		2.045(3)	2.027(4)	2.099(5)
25	Ni1	2.093(4)	2.056(4)	2.121(8)
		2.055(4)	2.031(6)	2.103(6)
	Ni2	2.096(6)	2.041(4)	2.126(6)
		2.047(6)	2.040(4)	2.126(5)
26	Ni1	2.097(4)	2.058(4)	2.117(6)
		2.056(4)	2.037(5)	2.101(4)
	Ni2	2.101(5)	2.041(4)	2.129(4)
		2.039(6)	2.040(4)	2.115(4)
27	Ni1	2.090(3)	2.049(3)	2.137(4)
		2.031(3)	2.029(4)	2.106(4)
	Ni2	2.143(3)	2.047(3)	2.120(4)
		2.046(3)	2.017(4)	2.096(5)
28	Ni1	2.091(2)	2.053(2)	2.132(2)
		2.030(2)	2.022(2)	2.111(2)
	Ni2	2.135(2)	2.048(2)	2.123(2)
		2.041(2)	2.018(2)	2.093(2)
Avg		**2.075(4)**	**2.039(4)**	**2.117(5)**

Magnetic measurements

Fig A8.2 Magnetisation *vs*. field at 2, 4, 6 K for **25** − **27**.

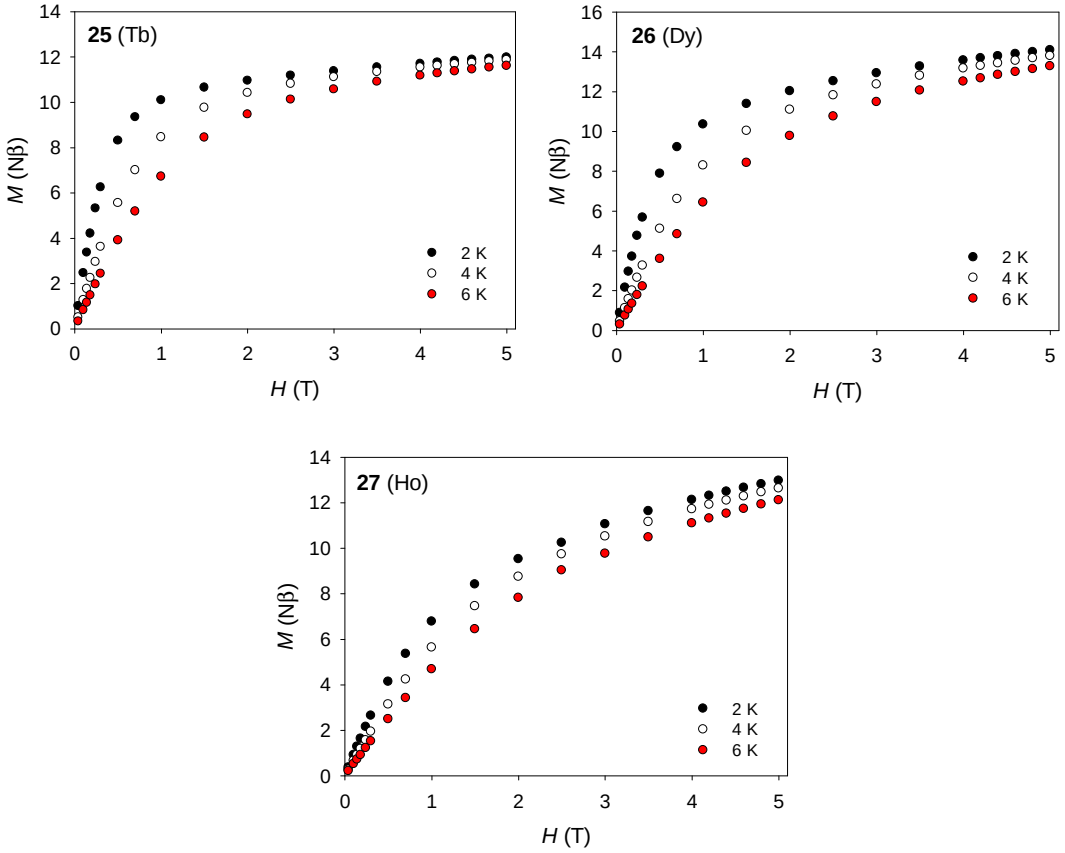

References

1. M. Pinsky and D. Avnir, *Inorg. Chem.*, **1998**, *37*, 5575.
2. A. Ruiz-Martínez, D. Casanova and S. Alvarez, *Chem. Eur. J.*, **2008**, *14*, 1291.
3. A. Ruiz-Martinez, D. Casanova and S. Alvarez, *Dalton Trans.*, **2008**, 2583.

⇨ Summary of the simulated ground state (GS) configuration for **2**−**4**, **6**, **8**, **13**, **16**, **23**, **24**, **28** given consideration to the parameters proposed by the fit of the corresponding magnetic data. See more details in the main text.

Complexes	**2**	**3**	**4**	**6**	**8**	**13**	**16**	**23**	**24**	**28**
GS	0	0	3	17/2	17/2	7/2	0	21/2	12/2	0

Publication list

1. “Directed synthesis of $\{Cu^{II}_2Zn^{II}_2\}$ and $\{Cu^{II}_8Zn^{II}_8\}$ heterometallic complexes”

María José Heras Ojea, Claire Wilson, Simon J. Coles, Floriana Tuna and Mark Murrie. *Dalton Trans.*, **2015**, *44*, 19275. DOI: 10.1039/C5DT03344F.

2. “Enhancement of Tb^{III}-Cu^{II} single-molecule magnet performance through structural modification” **Highlighted as VIP**

María José Heras Ojea, Victoria A. Milway, Gunasekaran Velmurugan, Lynne H. Thomas, Simon J. Coles, Claire Wilson, Wolfgang Wernsdorfer, Gopalan Rajaraman and Mark Murrie. *Chem. Eur. J.*, **2016**, *22*, 12839. DOI: 10.1002/chem.201601971 (*See Chapter 4*).

3. "Dangling and Hydrolyzed Ligand Arms in $[Mn_3]$ and $[Mn_6]$ Coordination Assemblies: Synthesis, Characterization and Functional Activity" **Collaboration**

Krishna Chattopadhyay, Gavin A. Craig, María José Heras Ojea, Moumita Pait, Animesh Kundu, Junseong Lee, Mark Murrie and Debashis Ray. *Inorg. Chem.*, **2017**, *56*, 2639. DOI: 10.1021/acs.inorgchem.6b02813.

4. “A topologically unique alternating $\{Co^{III}_3Gd^{III}_3\}$ magnetocaloric ring”

María José Heras Ojea, Giulia Lorusso, Gavin A. Craig, Claire Wilson, Marco Evangelisti and Mark Murrie. *Chem. Commun.*, **2017**, *53*, 4799. DOI: 10.1039/C7CC02243C (*See Chapter 7*).